The Development of a Wide Field UV Imager for Planetary Space Missions

Thesis submitted for the degree of
Doctor of Philosophy
at the University of Leicester.

by

Philippa Mary Molyneux

Space Research Centre
Department of Physics and Astronomy
University of Leicester

February 2012

Abstract

This thesis describes the development of the Jupiter system Ultraviolet Dynamics Experiment (JUDE): a far ultraviolet (FUV) imager designed for the *JUICE* mission to Jupiter and Ganymede. To date the only in situ UV instruments to study Jupiter's aurora have been spectrographs or spectral imagers, which are unable to provide instantaneous large-scale images. JUDE will obtain such images, thus providing information on highly variable, small scale features in Jupiter's auroral regions, allowing models of the global magnetospheric dynamics that produce the emissions to be refined. The imager will also observe Ganymede's FUV auroral emissions, which have not yet been comprehensively studied.

Two preliminary designs for the JUDE optics have been proposed: one based on reflective optics (developed at the University of Liège, Belgium) and one based on novel microchannel plate (MCP) optics. An overview of both optical designs is given in Chapter 2, along with a description of the detector and readout electronics that will complete the instrument. Chapters 3 and 4 then detail a feasibility study for the MCP optic version, based on sequential ray tracing modelling of the system and laboratory tests of similar optics. The results of the modelling suggest that diffraction effects would severely limit the achievable resolution of the MCP optic. Similarly, images obtained by real MCP optics of two different specifications indicate that the theoretical resolution of each optic is not achievable, although in this case problems in the optic manufacturing process are more to blame than diffraction. Hence, the MCP optic version of JUDE would be unable to produce high quality images of small auroral features at Jupiter, and is rejected in favour of the reflective optic design.

JUDE is a broadband instrument, but the isolation of two FUV emission lines at 130.4 nm and 135.6 nm is desirable, as the relative intensity of these lines at Ganymede provides information on the moon's atmosphere. Chapter 5 outlines an investigation into the possibility of isolating these emissions using a combination of reflective multilayer coatings and commercially available transmission filters. The results are promising: in the absence of significant background emissions in the FUV region, the ratio of the two lines was calculated using simultaneous equations to within $\sim$1% of the known value.

Although MCP optics were found to be unsuitable for JUDE, they are ideal for other applications with less stringent resolution requirements. A summary of potential imagers based on variations of the JUDE MCP optic design is given in Chapter 6.

Declaration

I hereby declare that no part of this thesis has been previously submitted to this or any other university as part of the requirement for a higher degree. The work described herein was conducted solely by the undersigned except for those colleagues and other workers acknowledged in the text.

Philippa Mary Molyneux

February 8, 2012

Acknowledgements

There are many people who have helped me over the course of my PhD, without whom this thesis would not have been written, and I would like to express my thanks to all of them. I'm particularly grateful to my supervisors Nigel Bannister and Emma Bunce for all their advice and guidance, for always being willing to make time for me and for their comments and suggestions as I wrote this thesis. Thanks also to everyone in the Space Research Centre and the Physics department who has helped me over the last few years, particularly Adrian Martindale for helping me understand ray-tracing results and MCP optic images, Jon Nichols for helping with data extraction from Hubble files, and Charly Feldman for general advice and friendliness. I am also grateful for the input of the Liège JUDE team, especially Jean-Claude Gérard for his help with Chapter 5.

Thanks to the other physics postgrads, for pub trips and friendship, especially those who I managed to coerce into fancy dress (special mention to Owen the triceratops). Special thanks to Nishad for her appreciation of cake and her brilliant taste in TV shows, and to everyone who has kept me company in the corner of the office since I started. I should also mention my ex-housemates from physics, Amy 'Efficiency' Scott and Vicky 'Cherrybomb' Heard, who each manage to be both incredibly sensible and brilliantly silly– living with them was a pleasure.

I am eternally grateful to my family for all their support and encouragement. To Tom, Fran, Anna, Ed, Molly (+ Monkey) and Iggy, and especially to Mum and Dad, I couldn't have got this far without you.

Finally thanks to Adam, for making me breakfast, making my code better, and making me smile.

Contents

List of Figures

List of Tables

CHAPTER 1

Introduction

1.1 A brief history of auroral science

The aurora is the visible evidence of the interaction between a planet's atmosphere and its magnetosphere, generated by the excitation of upper atmospheric molecules and atoms by charged particles that precipitate down into the auroral region along magnetic field lines. Studies of a planet's aurora can therefore provide information about both its atmospheric composition and the global magnetospheric dynamics at the time the aurora was produced. Auroras are produced in various spectral regions: at Earth, Jupiter and Saturn, the three bodies with the most studied aurora, emissions have been observed at ultraviolet, visible, infrared and radio wavelengths, and X-ray emissions have been observed at both Earth and Jupiter.

Earth's aurora, along with other meteorological effects, was considered by early communities to be the work of spirits, and the phenomenon features particularly prominently in the mythology and literature of Scandinavian countries and other northern societies. The first scientific theory of auroral production is often considered to be an explanation found in Aristotle's *Meteorologica*, but modern auroral science really has its roots in 18th and 19th century observations. It was at this time that the aurora first became linked to geomagnetism, with the discovery by Olof Hiorter and Anders Celcius that the appearance of the northern lights was accompanied by a 'great deviation' in the direction of a magnetic compass needle. In 1820, Hans Ørsted discovered that a magnetic needle would move from its normal position when it was brought close to electrical wires, with the direction of the needles deviation dependent on the direction of the current carried in the wires. Hence, the behaviour of a compass in the vicinity of the aurora could be explained by the presence of electric currents along the auroral arcs. Within the next few decades, the first clues of a solar influence to the aurora were uncovered: in 1843, Heinrich Schwabe published 17 years worth of sunspot observations, suggesting there was a ten year cycle (later refined to eleven years) with which the number of spots rose and fell; nine years later, Edward Sabine announced that the average magnetic disturbance, i.e. geomagnetic activity, varied from year to year in parallel with the sunspot cycle. In the 1860s, the first auroral spectrum was produced by Anders Ångström, although he was unable to identify the gases responsible for the emissions.

From the late 19th century onwards, scientific expeditions to the polar regions led to a vast increase in the amount of data available concerning the aurora. The Norwegian scientist Kristian Birkeland, for example, organised several expeditions to the arctic regions of Norway and founded a network of observatories to collect magnetic field data, allowing him to deduce the global system of electric currents in the region using his knowledge of electromagnetism (see e.g. Birkeland [1908]). Birkeland's main motivation in undertaking the expeditions was to collect the data necessary to test a theory of auroral production he had developed through laboratory studies of the behaviour of 'cathode rays' (beams of electrons) under the influence of magnetic fields: he proposed that cathode rays from the Sun move towards the Earth and are guided towards its poles, where they interact with the gases of the upper atmosphere to produce the visible aurora. Hence, the separate fields related to auroral science were combined to give a detailed theory of a solar-terrestrial connection. Birkeland went on to simulate aurora in a laboratory environment, firing electrons at a magnetised sphere, known as a 'terrella' (meaning 'little Earth'), with a phosphorescent coating (see Figure 1.1).

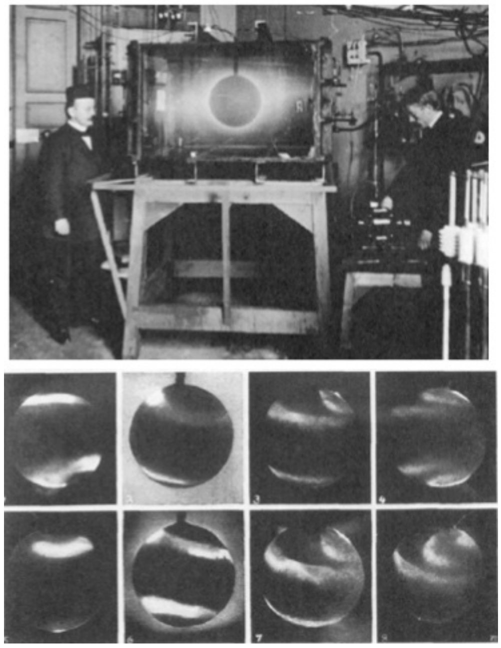

Figure 1.1 *— Top: Birkeland (left) with his 'terrella' equipment, used to simulate various phenomena including sunspots, auroras and the rings of Saturn. Bottom: Photographs of auroral simulations carried out using Birkeland's terrella. All images from [Rypdal and Brundtland, 1997].*

Birkeland's terrella simulations allowed him to argue by analogy that the aurora was caused by a solar-terrestrial interaction, but investigations of this connection were limited until the start of the space age, when satellite observations became possible, leading to a more accurate and thorough understanding of the processes involved.

1.1.1 Auroral science in the space age

Ground-based auroral imagers are only capable of viewing a small fraction of the auroral oval at once, owing to the close proximity of the emissions. Large-scale images of the aurora therefore only became obtainable in the space age, with imagers being flown on satellites in eccentric orbits that took them high above one of the Earth's poles; starting in 1973 with the Canadian *ISIS-2* satellite, which carried two scanning photometers for auroral observations [Anger et al., 1973]. The initial images were not truly global, as the intense visible background on the dayside of the Earth meant that they were limited to observing the nightside only. Hence, it became more common for satellites aimed at solar-terrestrial investigations to carry far ultraviolet (FUV: $\sim$100–200 nm) imagers. The first UV auroral images were taken by the Auroral Television (ATV) camera on the Japanese *KYOKKO* satellite, launched in 1978. Other spacecraft carrying UV auroral imagers have included NASA's Dynamics Explorer 1 (*DE 1*) (active 1981–1991), *Polar* (1996–2008) and *IMAGE* (2000–2005), and the Swedish Space Corporation's *Viking* (1986–1987) and *Freja* (1992–1995). The imagers carried by these missions have produced results that have contributed much to our knowledge of the aurora. For example, *DE 1* was able to observe auroral substorms – in which a large and previously quiet portion of the auroral oval becomes active and then returns to its quiet state, all within a few hours – from their onset through to recovery, enabling substorm models to be refined [Frank and Craven, 1988]. Meanwhile, *Viking* discovered a consistent pattern for substorm development [Anger et al., 1987]. *Viking*, *Freja* and *IMAGE* were each capable of simultaneous imaging in two (*Viking*, *Freja*) or three (*IMAGE*) wavebands, with the aim of determining the energies of the particles responsible for the emissions. O_2 in the atmosphere absorbs at some FUV wavelengths but not others and O_2 density increases with decreasing altitude, leading to more absorption for emissions produced lower down, so the intensity ratio of a non-absorbed emission to one that is absorbed is diagnostic of the altitude reached by the incoming particles, and therefore their energy. *IMAGE* was also responsible for the first global images of the proton aurora [Mende et al., 2003]. Examples of images produced by the UV instruments discussed above can be found in Figure 1.2.

As satellite technology improved since the 1950s, missions exploring the solar system began to provide the opportunity to study aurora at planets other than Earth. The first evidence of extraterrestrial auroral emissions came from ground-based radio observations which discovered that Jupiter was an intense radio source, implying that it possessed a

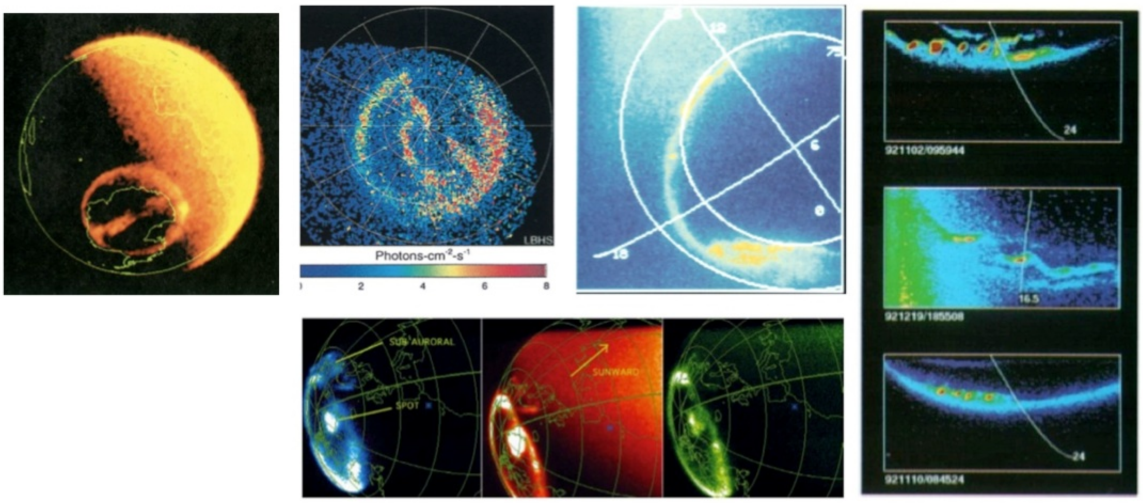

Figure 1.2 — *Clockwise from top left: An image of a theta aurora taken by the ultraviolet SAI photometer on* DE1 *(this auroral form was discovered by* DE1*) [Frank and Craven, 1988]; A POLAR UVI image of a rare double-θ aurora [Newell et al., 1999]; a Viking image showing a large portion of the auroral oval [Lui et al., 1987]; Freja images showing examples of periodic distortions in the aurora (red areas are the most intense) [Murphree et al., 1994]; Images obtained simultaneously by the two UV IMAGE instruments– the spectral imager (SI) and the wideband imaging camera (WIC) (left: SI-12 channel, centre: WIC, right: SI-13 channel) [Mende et al., 2003].*

strong magnetic field. Based on these observations, attempts were made to detect Hα (656.28 nm) emissions at the planet (e.g. Smith et al. [1963]), but the eventual discovery of the aurora was made by an ultraviolet instrument on the *Voyager 1* spacecraft, which performed a flyby of Jupiter in 1979. Although aurora have since been detected in various spectral regions at all of the giant planets (as summarised in Bhardwaj and Gladstone [2000]), Jupiter's emissions remain the most well studied of these, owing mainly to the relative closeness of the planet to Earth and the brightness of the emissions.

1.1.2 UV spectroscopy and imaging of the jovian aurora

Jupiter's aurora consists of three main emission regions, which will be discussed fully in Section 1.2.2: the main oval, the polar emissions and the satellite footprints. The main jovian aurora were first detected in 1979 by the *Voyager* Ultraviolet Spectrometer experiment (UVS), which covered the region 500 – 1700 Å. Further observations were performed by the Short – Wavelength Primary (SWP) spectrograph on the International Ultraviolet Explorer (IUE), an Earth-orbiting satellite; the Hopkins Ultraviolet Telescope (HUT), a spectrographic telescope flown on the Space Shuttle; and *Galileo* UVS. Each of these instruments measured an auroral emission spectrum very similar to those obtained in laboratory studies of electron collisional excitation of H_2, with the bulk of the emissions concentrated in the H_2 Lyman and Werner band series and the H Lyman-α line. Other features in the spectrum are due to fast proton and H atom collisional excitation [Clarke et al., 2004]. The IUE observations also showed that the aurora are almost always active, although they vary slightly from day to day, and that the emission regions rotate with Jupiter's system III period[1]. This is in contrast to the Earth's aurora, which remain fixed with the direction of the solar wind, and therefore suggests different production mechanisms for each of the two planets' aurora.

More recently, spectra were obtained by the Ultraviolet Imaging Spectrometer (UVIS) on *Cassini*, during its flyby of the jovian system between October 2000 and March 2001 [Ajello et al., 2005]. At the time, the *Galileo* spacecraft was still actively collecting data within the system, and a campaign to investigate the aurora was undertaken involving the two spacecraft, as well as the Far Ultraviolet Spectrometer Explorer (*FUSE*), *Chandra* X-

[1]The rotation rate of Jupiter's interior is not trivial to determine, since the planet has no solid surface from which the rate can be measured. The earliest attempts to establish a period of rotation were based on observing the motion of visible features in Jupiter's atmosphere, either near the equator (to give the System I period) or in the temperate regions (for the System II period) [Higgins et al., 1997]. In the 1950s, Jupiter was found to be an intense source of non-thermal radio emissions. Following on from this, the System III period was defined as the mean rotational period of decametric radio sources. The decametric emissions are generated at close to the local electron gyrofrequency, and are beamed in cones aligned on magnetic field lines. Hence, the System III period is the period of rotation of Jupiter's magnetic field.

ray observatory, the Infrared Telescope Facility (*IRTF*) and the Hubble Space Telescope (*HST*) Space Telescope Imaging Spectrograph (STIS). During this campaign, auroral images were obtained concurrently with measurements of the precipitating particles responsible for the emissions imaged. This was the first time any such simultaneous measurements had been performed at any planet other than the Earth [Clarke et al., 2004]. There has been one more recent Jupiter flyby – the *New Horizons* mission to Pluto passed Jupiter in 2007. Its ALICE UV imaging spectrograph measured aurora on Io and aurora and nightside airglow on Jupiter, and found that there was a surprising lack of nightglow at Jupiter compared to the substantial amount seen in *Voyager* UVS observations [Gladstone et al., 2007]. A UV spectrograph based on the ALICE design is also included on the Juno mission, which will arrive at Jupiter in 2016 [Retherford et al., 2009]. Juno UVS will observe the jovian UV aurora from an eccentric polar orbit (1.06×39 R_J [Matousek, 2007]), where it will avoid the bulk of Jupiter's radiation environment.

The most complete and detailed images of Jupiter's UV aurora to date have been captured by the various UV instruments on the Hubble Space Telescope. The emissions were imaged first by the Faint Object Camera (FOC) in the early 1990s, and then, after the first *HST* servicing mission in 1993, by the Wide Field and Planetary Camera 2 (WFPC2). The FOC observations first showed the high latitude of the main auroral oval, while the WFPC2 is the only *HST* camera to have imaged both of Jupiter's poles in the same frame (see, for example, Plate 1 in [Clarke et al., 1998]) . The Io footprint was detected at least once by FOC and consistently by WFPC2. WFPC2 images clearly showed the three main emission regions within the aurora and indicated that there was conjugacy between the northern and southern emissions. They also showed that dawn storms (see Section 1.2.2.1), which had been previously detected by FOC, occurred along the main oval. Between June 1996 and July 1997, WFPC2 images were obtained at similar times to UV spectra and *in situ* measurements of particles, fields and plasma waves obtained from the *Galileo* platform [Clarke et al., 1998].

More recently, detailed images of the jovian UV aurora have been obtained using the Space Telescope Imaging Spectrograph (STIS), which has operated since 1997, with a break between 2004 and 2009 due to a power supply failure. STIS is sensitive to emissions of $\sim$1 kR (compared to limiting sensitivities for FOC and WFPC2 of 50–100 kR and 10 kR respectively, where one Rayleigh, R, is equal to $10^6/4\pi$ photons s^{-1} cm^{-2} sr^{-1}), and is able to provide much more detailed images of the diffuse emissions either side of the main auroral oval than the other UV *HST* instruments [Clarke et al., 2004]. It was through STIS observations that the Io tail emissions (see Section 1.2.2.3) were first observed, along with the footprint aurora of Ganymede and Europa. STIS images have shown that the Io footprint actually consists of multiple spots [Clarke et al., 2002, Gérard et al., 2006], the number, brightness and position of which vary on short timescales [Bonfond et al., 2007]. Ganymede's footprint emission has similarly been found to show significant temporal variations [Grodent et al., 2009].

Since 2002, further FUV imaging has been possible using *HST*'s Advanced Camera for Surveys (ACS), the solar blind channel (SBC) of which is more sensitive than STIS at wavelengths below 200 nm [STScI., 2011]. ACS has been used, for example, to collect a comprehensive dataset of FUV images of Jupiter's aurora obtained within a $\sim$4 month period (21 February – 11 June 2007). Each set of observations within this dataset lasted $\sim$45 minutes, with images taken every 2–3 minutes [Radioti et al., 2008], making it possible to study the temporal variations of auroral features such as spots in the polar dawn region over periods ranging from a few minutes to a few days.

A summary of the characteristics of instruments previously used to study Jupiter's UV aurora can be found in Tables 1.1 (instruments used within the Jupiter system) and 1.2 (instruments viewing Jupiter from Earth orbit).

As suggested by Table 1.1, UV instruments flown on missions to Jupiter or on spacecraft performing Jupiter flybys have tended to be spectrographs or spectral imagers. Spectrographs have no spatial resolution and can therefore provide only very limited information about the distribution of the aurora (e.g. whether there are emissions within the instrument field of view), while the narrow field of view of spectral imagers means that they must scan over the auroral region to build up an image and so are unable to provide an insight into the short-timescale global variability of the aurora. The Earth-orbiting imagers and spectral imagers on *HST* have obtained the most detailed images of the jovian aurora to date. The angular size of Jupiter is clearly much smaller for these instruments, so they do not have to scan the auroral region, but their exposure times are still on the order of hundreds of seconds due to the reduced throughput at this distance. Additionally, there is no dedicated solar system imager on *HST* and the process of gaining observing time with any of its instruments is competitive. *HST* is nearing the end of its lifetime, and its successor, the James Webb Space Telescope, will not have UV imaging capability. A wide-field UV imager, capable of viewing a large fraction of Jupiter from within the jovian system to produce short exposure images with good spatial resolution, would be extremely useful for increasing our knowledge of Jupiter's aurora, particularly if combined with *in situ* field and plasma data from the same platform.

1.2 Overview of UV auroral emissions at Jupiter

Jupiter has the brightest and most energetic aurora in the solar system, 100 times more energetic than the Earth's, and with a surface brightness up to ten times higher [Clarke et al., 2004]. It is the huge jovian magnetosphere- produced by the planets strong internal field and rapid rotation, combined with a large internal source of plasma from Io- that is responsible for the vast energy and complexity of the emissions. The main atmospheric constituent of Jupiter is hydrogen, and this can be seen in the similarity of Jupiter's auroral spectrum to laboratory spectra of excited H_2 (see Figure 1.3 for an example of this similarity). In the UV and visible regions of the spectrum, auroral emissions are produced by H_2 that has been electronically excited by electron impact, while infrared emissions are due to vibrationally excited H_2 and $H_3{}^+$. X-ray and radio auroras differ from those in other spectral regions as their emissions are the result of excitation of the precipitating particles rather than the species that these collide with (see for example Bhardwaj and Gladstone [2000]).

Table 1.1 — *Comparison of UV spectrographs and imaging spectrographs which have previously viewed the jovian aurora from within the Jupiter system / Jupiter flybys, or are scheduled to do so within the next 5 years.*

Instrument	Description	Year(s) active at Jupiter	Wavelength range (Å)	Spectral resolution (Å)	Field of View
Voyager UVS [a]	Spectrograph	1979	535 – 1702	33 (extended source)	0.1° × 0.87°
Galileo UVS [b]	Spectrograph	1995–2003	1130 – 4320	from 6.7 (below 1900 Å) to 12.7 (above 2820 Å) (point source)	1.0° × 0.1° (1130 – 1920 Å); 0.4° × 0.1° (1620 – 3230 Å)
Cassini UVIS: EUV channel [c]	Imaging spectrograph	2000	560 – 1180	2.75, 4.8, 19.4 (extended source, three slits)	(1, 2, 8) × 60 mrad
Cassini UVIS: FUV channel [c]	Imaging spectrograph	2000	1100 – 1900	2.75, 4.8, 24.9 (extended source, three slits)	(0.75, 1.5, 8) × 60 mrad
New Horizons ALICE [d]	Imaging spectrograph	2007	520 – 1870	<18	0.1° × 4.0° (Airglow slit)
Juno UVS [e]	Imaging spectrograph	2016–2017	700 – 2050	4 – 6 (point source) 10 – 12 (extended)	0.2° × 2.5 + 0.05° × 2.0 + 0.2° × 2.5° [f]

[a] [Broadfoot et al., 1977] [b] [Hord et al., 1992]

[c] [Esposito et al., 2004] [d] [Stern et al., 2008]

[e] [Retherford et al., 2009] [f] [Gladstone, 2012]

1.2.1 UV Science at Jupiter

The main features visible in an FUV spectrum of Jupiter's aurora are the Lyman and Werner bands of H_2 and the Lyman-α spectral line of H. Lyman-α radiation is produced at Jupiter mainly by dissociative excitation of H_2 and dissociative ionisation and excitation of H_2. Dissociative excitation is described by the following equations (e.g. Bhardwaj and Gladstone [2000]):

$$e_p + H_2 \rightarrow H(2p, 2s) + H + e_p; \tag{1.1}$$

$$H(2p, 2s) \rightarrow H + h\nu. \tag{1.2}$$

Table 1.2 — *Comparison of UV spectrographs and imagers previously used to view the jovian aurora from the near-Earth environment, showing specifications of the best available instruments for jovian auroral imaging campaigns at present.*

Instrument	Type	Years active	Wavelength range (Å)	Spectral resolution (Å)	Field of View	Spatial resolution
Copernicus PEP[a] (Princeton Experiment Package)	Spectrograph	1972 – 1982	912 – 3275	Minimum of 0.05 between 950 and 1450 Å	39” × 0.314”	
IUE SWP[b] (Short-Wavelength Prime camera)	Spectrograph	1978 – 1996	1150 – 1970	11 (extended source) [c]	∼23” × ∼10” ellipse [b] (large entrance aperture)	∼6” [b]
HUT[d]	Spectrograph	1990; 1995	814 – 1876 (1st order); 407 – 938 (2nd order)	4 – 12 (extended source, various apertures)	from 12” diameter to 19” × 197” (various apertures)	
HST FOC[e] (imaging mode)	Imager	1990 – 2002	1150 – 6500		Low res: between 3.6” × 3.6” and 28” × 28”; Medium res: between 1.8” × 1.8” and 14” × 14”	0.028” per pixel (low res); 0.014” per pixel (medium res)
HST WFPC[f]	Imager	1993 – 2009	1150 – 10500		150” × 150” L-shaped region + 34” × 34” square	0.1” per pixel (L-shaped region); 0.046” per pixel (square region)
HST STIS[g] (imaging mode)	Imaging spectrograph	1997 – 2004; 2009 –	1150 – 10300	dependent on filters	25” × 25”	∼0.0246” per pixel
FUSE [h]	spectrograph	1999 – 2007	905 – 1187	∼0.22 [i]	between 1.25” × 20” and 30” × 30” depending on aperture used	
HST ACS (SBC) [j]	imager (low res spectroscopy also possible)	2002 –	1150 – 1700		34.6” × 30.8”	0.034” × 0.03” per pixel

[a] [Rogerson et al., 1973] [b] [ESA, 2005] [c] [Clarke et al., 1980]

[d] [Durrance et al., 1994] [e] [Nota et al., 1996] [f] [McMaster et al., 2008]

[g] [Bostroem et al., 2010] [h] [Andersson, 2006] [i] [Gustin et al., 2004]

[j] [Maybhate et al., 2010]

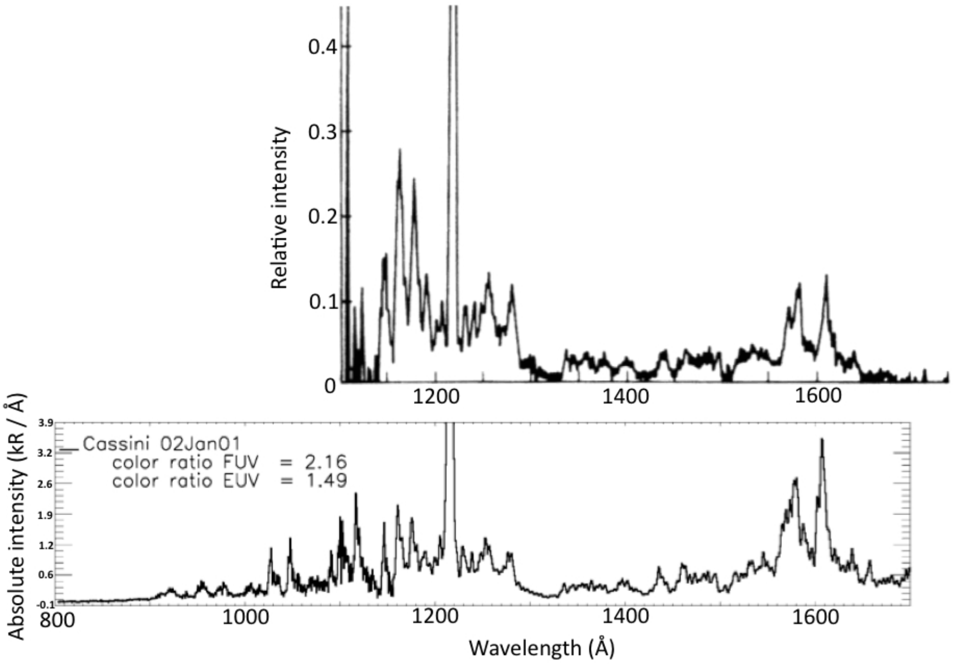

Figure 1.3 — *Top: Laboratory spectrum of UV emissions of H_2 by electron impact (300 keV electrons, 0.4 nm resolution) [Ajello et al., 1982]. Bottom: Cassini spectrum of the jovian aurora, recorded on 2 January 2001 (0.8 Å channels smoothed by a 5-channel box car algorithm, giving a spectral resolution of 0.4 nm) [Ajello et al., 2005].*

A primary electron, e_p[2], collides with a molecule of H_2, causing the H_2 molecule to split into one ground state H atom and one electronically excited atom in either of the n=2 quantum states (2p or 2s). As the excited atom returns to the ground state, it emits a photon, $h\nu$, at the Lyman-α wavelength (121.6 nm). Dissociative ionisation and excitation of H_2 is similar, but in this case the H_2 molecule splits into electronically excited H atom and one H^+ ion with the release of a secondary electron, e_s [Bhardwaj and Gladstone, 2000]:

$$e_p + H_2 \rightarrow H(2p, 2s) + H^+ + e_s + e_p; \tag{1.3}$$

$$H(2p, 2s) \rightarrow H + h\nu. \tag{1.4}$$

[2]The precipitating particle does not necessarily need to be an electron – protons and ions are capable of exciting similar emissions either directly or through the production of secondary electrons [Bhardwaj and Gladstone, 2000].

The Lyman band (distributed over the entire FUV region) and Werner band (∼90–130 nm [Liu and Dalgarno, 1996]) emissions are produced by electronic excitation of H_2 as described by the following equations [Bhardwaj and Gladstone, 2000]:

$$e_p + H_2 \rightarrow H_2(B, C) + e_p; \tag{1.5}$$

$$H_2(B, C) \rightarrow H_2 + h\nu. \tag{1.6}$$

In this scenario, the collision between the primary electron and the H_2 molecule excites the H_2 to the upper electronic level of either the Lyman (B) or the Werner (C) band system. Since H_2 is a molecule rather than an atom, within each of its electronic energy states are a number of allowed vibrational and rotational levels. As the molecule returns to the ground state, it emits a photon, $h\nu$. These transitions do not occur at a precise wavelength because vibrational and rotational transitions occur along with the electronic transitions [Tennyson, 2005]: molecules excited to different vibrational and rotational levels will emit photons of different energies.

A comparison of the relative intensities of different FUV emissions can provide information about the energy of the precipitating particles responsible for the emissions. More energetic particles penetrate deeper into Jupiter's atmosphere, which contains increasing densities of hydrocarbons at decreasing altitudes. The hydrocarbons absorb some of the UV auroral emissions. Hence, a comparison of UV intensity in a wavelength band where there is little absorption to that in a band with high absorption can allow the precipitating particle energy to be estimated. The ratio calculated is known as the auroral colour ratio [Yung et al., 1982].

1.2.2 Auroral Morphology

Spectral studies of the aurora can provide some information about Jupiter's atmosphere and the particles impinging on it but in order to gain a thorough understanding of the interaction between the atmosphere and magnetosphere, it is vital to investigate the morphology of the emissions and the spatial and temporal variations they undergo as a result of changing magnetospheric conditions. Jupiter's ultraviolet aurora exhibits three distinct emission regions, as discussed below (and shown in Figure 1.4).

1.2.2.1 The main auroral oval

Jupiter's main auroral ovals can be seen in bands around each of the planets magnetic poles, at $\sim$15° magnetic co-latitude. The ovals are narrow and bright, with widths of $\sim$100–500 km and brightnesses exceeding $\sim$100 kR in the visible and UV, peaking at up to a few MR [Prangè et al., 1998, Vasavada et al., 1999]. Emission features within the ovals corotate with the planet at the System III rotation period [Ballester et al., 1996], which indicates that they are controlled by the magnetic field. This corotation implies that the emissions map to a region of the jovian magnetosphere where the plasma is also close to corotation. Since plasma in the magnetodisk begins to fall behind corotation with the jovian magnetic field at 20–30 R_J, this imposes an outer limit of $\sim$30 R_J on the mapping region [Clarke et al., 2002]. An inner limit on the mapping region can be determined by looking at the position of Ganymede's footprint aurora (see Section 1.2.2.3) relative to the main oval. The oval is almost always poleward of the Ganymede footprint[3]; since Ganymede orbits at 15 R_J, and the oval is almost always clearly separated from the Ganymede footprint and at a higher latitude, the inner limit of the main oval mapping region is believed to lie at $\sim$20 R_J. This corresponds well to the theory that the main oval emissions are produced by a large-scale current system induced within Jupiter's magnetosphere and ionosphere to accelerate sub-corotating plasma at $\sim$20–30 R_J back up to corotation with the planet (e.g. Cowley and Bunce [2001]). The ovals are mainly stable, with the brightness not varying much from the mean on any given day, but dynamical features such as dawn storms are sometimes present. These storms begin as faint, structured emissions in the dawn local time sector, and then intensify over the

[3]Bonfond et al. [2012] compare STIS images of Jupiter's aurora from Febraury 27th and May 21st 2007. In the second of these observations, Ganymede's footprint is $\sim$500 km more equatorward, while the main oval is $\sim$3000 km equatorward – such a significant shift that the Ganymede footprint now lies inside the main oval. Bonfond et al. [2012] suggest that the movement was triggered by changes in Io's volcanic activity.

course of approximately an hour, reaching brightnesses of several MR [Gérard et al., 1994, Ballester et al., 1996].

The emission altitude and the UV spectra of the main oval aurora suggest that the principal precipitating particles responsible for the emissions are electrons ranging in energy up to many tens of keV [Ajello et al., 1998]: energetic sulphur or oxygen ions from Io (see Sections 1.4.3 and 1.4.4) would be capable of producing auroral emissions, but no UV emission lines from these elements have been observed [Waite Jr. et al., 1988]; neither is there any Doppler-shifted Lyman-α present that would indicate the presence of fast precipitating protons [Clarke et al., 1989, Rego et al., 1999]. The main oval aurora is associated with large-scale coupling between the ionosphere and magnetosphere, and the transfer of angular momentum from the ionosphere to the plasma in the middle magnetosphere, which accelerates sub-corotating plasma up to corotation with the ionosphere [Cowley and Bunce, 2001, Hill, 2001, Southwood and Kivelson, 2001]. While this accounts for the general shape of the emissions, it is unable to describe smaller-scale structures within the emission region, and many unexplained local time effects can be seen. For example, the dawn storms have not yet been explained: Cowley et al. [2003] suggest they may be related to reconnection in the magnetotail. Variations in the location of the main auroral emissions over long periods of time (i.e. several years) have been reported by Grodent et al. [2008], with a similar trend seen in the position of the Ganymede footprint aurora. High resolution UV imaging of the main auroral region, combined with magnetospheric and plasma measurements, will enhance our understanding of the processes governing the behaviour of the emissions here.

1.2.2.2 The polar aurora

The polar aurora consist of diffuse emissions, appearing poleward of the main auroral oval. They are the most variable of Jupiter's auroral emissions, varying independently and much more rapidly than the main oval and satellite footprint emissions: Waite Jr. et al. [2001] describe *HST* STIS observations of the jovian aurora in which a rapidly evolving, very bright and localised emission was seen in the northern polar auroral region, with the intensity of the emission increasing by a factor of 30 within 70 s up to a peak brightness of 37 MR, and then decreasing on a somewhat longer timescale. The polar emissions appear at high latitudes and lag behind corotation with the planets magnetic field, indicating mapping to distances of greater than ~30 R_J [Grodent et al., 2003].

The UV polar aurora can be divided into three distinct regions, each fixed in local magnetic time. The dark region is a crescent-shaped area in the dawn sector characterised by faint emissions which rarely exceed a few kR above the disk background [Grodent et al., 2003]. Brighter emissions can be seen in the swirl region. The region is named for the turbulent, swirling motions of the aurora that are found there. Although brighter than the dark region aurora, the swirl region emissions are relatively dim, with UV intensities of up to 200 kR, and last for just tens of seconds [Grodent et al., 2003]. The swirl region is located near the centre of the polar region, and fills approximately a third of the area poleward of the main oval. On average it is responsible for around half of the total UV polar emission. The remainder of the polar area is filled by the active region, which is confined to the noon and post-noon sector. Two types of emission feature can be seen here: a steady arc-like feature, and occasional bright, transient events called polar flares [Grodent et al., 2003].

The origin of the polar emissions is under debate: current magnetic field models are accurate only within ~30 R_J of Jupiter in the equatorial plane [Vogt et al., 2011], and the polar emissions map to the poorly constrained region beyond this. The swirl region is generally believed to map to open field lines [Vogt et al., 2011], but interpretations of the other regions vary. Pallier and Prangè [2001] suggest that the bright spots in the active region are either the footprint of the northern jovian polar cusp or transient dayside aurora. The same authors observed faint arcs in the dark region, which they suggest map to closed field lines in the outer magnetosphere (~70 R_J) [Pallier and Prangè, 2001]. Grodent et al. [2003], meanwhile, associate the dark region with the rotating Dark Polar Region (r-DPR) deduced from ground-based Doppler observations in the infrared [Stallard et al., 2001] and interpret polar flares in the active region as the signature of explosive magnetopause reconnection on the day side. Vogt et al. [2011] conclude that the polar auroral active region maps to field lines beyond the dayside magnetopause that can be interpreted as Jupiters polar cusp; the swirl region maps to lobe field lines on the night side and can be interpreted as Jupiters polar cap; and the dark region spans both open and closed field lines and must be explained by multiple processes.

Delamere and Bagenal [2010] disagree with the view that the polar swirl region maps to open field lines, suggesting that it instead corresponds to tailward flows in the cushion region[4] and the region of viscous interaction between the solar wind and Jupiter's magnetospheric flanks. They link the dark polar region to dawn sector corotational flows between 20 and 60 R_J and suggest that bright polar emissions may be the signature of decoupling between the corotating ionospheric flows and subcorotating magnetospheric flows in the dusk region. Future UV observations, in combination with field and particle measurements in the regions beyond 30 R_J from an in situ spacecraft, will allow the origins of each of the polar emission regions to be constrained further, for example by observing any changes in the auroral forms that occur simultaneously with changes in the plasma or field environment surrounding the spacecraft.

1.2.2.3 The satellite footprint aurora

The satellite footprint aurora are the result of electromagnetic interactions between Jupiter and the Galilean moons Io, Europa and Ganymede, and are seen as emissions at or near the point where each satellite's magnetic flux tube is incident on the planet, equatorward of the main oval. Callisto may also produce a UV footprint, but since the moon orbits at $\sim$26 R_J the footprint aurora would overlap the main oval and hence has not been observed. A comparison of the characteristics of the three satellite footprint auroras can be found in Table 1.3. The exact mechanism of the interaction causing the satellite footprints is not well understood as yet. Additionally, Ganymede's intrinsic magnetic field and magnetosphere (see Section 1.3) may lead to different interactions between this moon and Jupiter than for the other satellites. UV observations of Io's auroral footprint have shown that it consists of multiple temporally and spatially varying spots [Clarke

[4] a region of extremely disturbed plasma found at $\sim$15 R_J on Jupiter's dayside

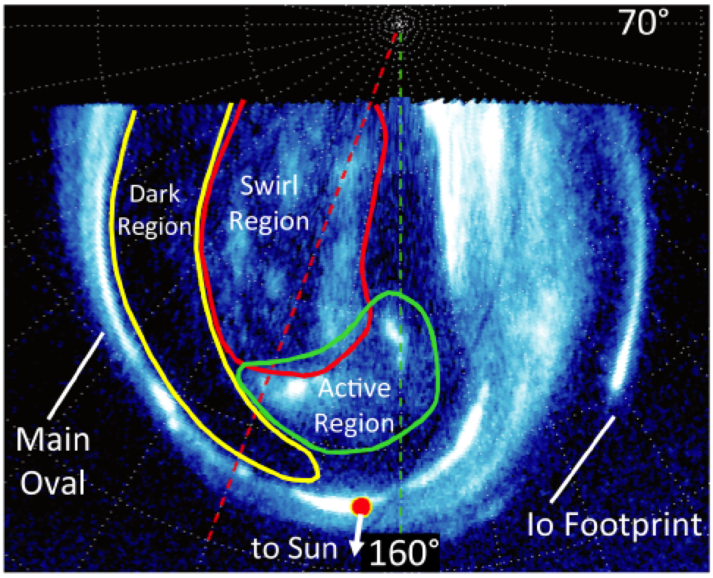

Figure 1.4 — HST *STIS image of Jupiter's northern auroral region, with the positions of the main oval, Io footprint, and the three distinct regions of the polar aurora indicated (from Vogt et al. [2011], adapted from Figure 5 in Grodent et al. [2003]).*

Table 1.3 — *Comparison of satellite footprint characteristics [Clarke et al., 2004].*

	UV Brightness (kR)	Power (mW m^2)	Total power (W)
Io	several $\times$ 100	tens	$< 10^{11}$ (plus half this again in tail)
Ganymede	few $\times$ 10	1 – 5	1 – 5 $\times$ 10^8
Europa	few $\times$ 10	1 – 5	1 – 5 $\times$ 10^8

et al., 2002, Gérard et al., 2006, Bonfond, 2009]. Recently, variations in Ganymede's footprint aurora have also been observed [Grodent et al., 2009]. A dedicated Jupiter UV imager will investigate the footprint fluctuations and may be able to resolve the Callisto footprint for the first time.

1.3 Ultraviolet aurora at Ganymede

Although most UV images of the jovian system obtained to date have focused on Jupiter itself, other objects in the system also merit investigation at UV wavelengths. Ganymede is particularly interesting as it possesses its own magnetosphere and its emissions show a morphology that suggests they are auroral in nature. A description of the UV emissions at Ganymede and the science that can be inferred by studying them follows. A brief summary of other UV emitters within the Jupiter system can be found in Section 1.4.

1.3.1 Ganymede's Magnetosphere

Ganymede is the only moon in our Solar System known to possess an intrinsic magnetosphere. Magnetometer measurements from *Galileo* flybys of the satellite indicated the presence of a magnetic field, and the plasma wave experiment detected a population of trapped charged particles near Ganymede, suggesting the presence of a miniature magnetosphere residing within the jovian magnetosphere. Ganymede's magnetic field is believed to be the sum of a permanent dipole field, and a second dipole component induced within a sub-surface conducting shell, which is driven by the time-varying component of Jupiter's magnetosphere [Kivelson et al., 2002] (although this model has not been proven). At Ganymede orbit, the ambient plasma flow is sub-Alfvénic and sub-sonic, so no bow shock forms [Jia et al., 2008]. Due to the limited number of *in-situ* measurements made to date, Ganymede's magnetosphere is not well characterised and many questions remain about its size and structure, its spatial and temporal variations, and its interaction with Jupiter's magnetosphere. However, by observing the auroral emissions generated by the interaction of Ganymede's magnetosphere with the surrounding charged particle environment, remote observations can be used to address many of these important questions.

1.3.2 Ganymede's Auroral Emissions

In 1996, the Goddard High Resolution Spectrograph (GHRS) onboard *HST* was used to observe the FUV airglow of Ganymede's trailing hemisphere, and revealed atomic oxygen emissions around 130.4 nm and 135.6 nm. These emissions were interpreted as airglow from an oxygen atmosphere – a conclusion that was supported by charged particle measurements from the *Galileo* spacecraft, which discovered an outflow of protons at Ganymede, suggesting ongoing gas production [Hall et al., 1998]. The shape of the spectral peaks measured by GHRS suggested that the emissions were not uniformly distributed across the satellite, but concentrated in the two regions near its poles. This was later confirmed by *HST* Space Telescope Imaging Spectrograph (STIS) observations performed in 1998 [Feldman et al., 2000]. The Feldman observations also showed that the brightest emission regions corresponded to the boundaries of Ganymede's polar caps, implying that the emissions are auroral in nature (see Figure 1.5).

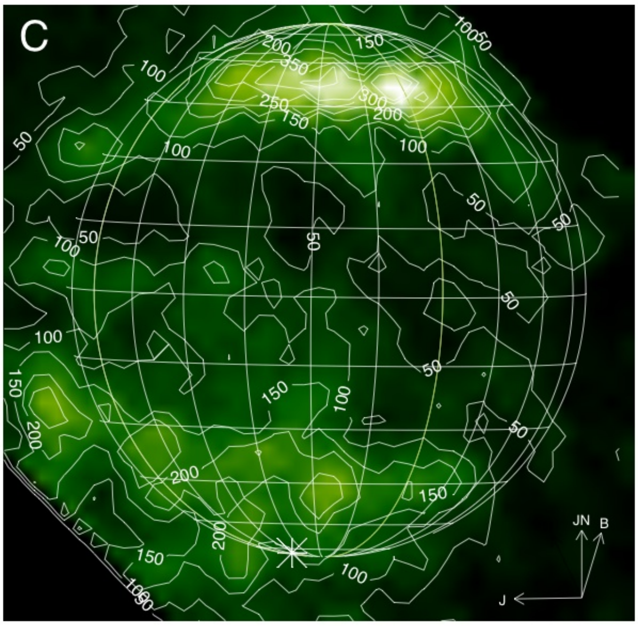

Figure 1.5 — HST *STIS image of Ganymede at 135.6 nm, showing increased intensity in the polar regions (from Fig. 3 in Feldman et al. [2000]).*

Ganymede's magnetic field is tilted 10° from its spin axis [Kivelson et al., 1997], so the orientation of its magnetic field relative to the jovian magnetic field varies considerably as it orbits the planet. This variation leads to a shift in the position of the polar caps on Ganymede's surface, which accounts for differences in O I flux and distribution between the STIS images. The processes that give rise to the aurora at Ganymede are not well understood, although models have been proposed to explain the oxygen emissions [Eviatar et al., 2001]. Information about the O I emission flux from future observations will help to constrain these models, and provide information of the relationship between the structure and distribution of the aurora and the magnetospheric conditions responsible for it. Measurement of the relative strength of the O I 130.4 nm and O I 135.6 nm emissions will also provide a method of refining our understanding of the composition of Ganymede's atmosphere.

1.3.3 The Connection between O I Emissions and Ganymede's Atmospheric Composition

The composition of Ganymede's atmosphere can be inferred from its spectrum, specifically from the ratio of O I 130.4 nm to O I 135.6 nm emissions. It is possible to estimate the relative abundances of O and O_2 (or other species containing oxygen, such as H_2O and O_3) within the atmosphere by considering the main excitation mechanisms responsible for the observed emissions. Assuming that Ganymede's atmosphere is too thin to absorb a significant number of photons from the incident solar flux, particularly considering the weakness of the flux at that distance from the Sun, the two most probable excitation processes are electron-impact excitation of oxygen atoms, i.e.

$$e + O \rightarrow e + O^*, \tag{1.7}$$

and electron-impact dissociative excitation of O_2:

$$e + O_2 \rightarrow e + O + O^*, \tag{1.8}$$

where O^* represents an excited oxygen atom that will go on to emit a photon [Hall et al., 1995]. The expected 130.4 nm / 135.6 nm ratio for an atmosphere composed either entirely of O or entirely of O_2 can be determined by laboratory measurements of emission cross-sections from electron impact on oxygen at the two wavelengths, as the cross-sections are proportional to the integrated intensities of the emissions [Noren et al., 2001]. Feldman calculated that the ratio O I 135.6 nm / O I 130.4 nm ranges from 1.6 to 2.0 for electron temperatures, T_e, of 1-100 eV in an O_2 atmosphere with an electron density of 370 cm^{-3}, a value that was extrapolated from measurements taken by *Galileo* during a Ganymede flyby [Feldman et al., 2000]. In a pure atomic oxygen atmosphere with the same electron density, the ratio decreases from 1.2 at $T_e = 4$ eV to $\sim$0.35 at $T_e = 20$ eV. Analysis of Hubble STIS images suggests that the actual ratio at Ganymede varies between 1.2 $\pm$ 0.2 and 3.2 $\pm$ 1.6 [Feldman et al., 2000]. This result implies that the atmosphere is dominated by O_2, but the errors on the ratios extracted from the STIS files are generally high; between 13% and 50% for each of the eight images acquired during the observation period. By making new observations of Ganymede with enhanced spectral resolution, more accurate measurements of the O I emission ratio will be obtained, leading to an improved model of the satellite's atmospheric composition.

1.3.4 Variations in Ganymede's Atmosphere between the Leading and Trailing Hemispheres

Ganymede is tidally locked to Jupiter, so the same hemisphere (the leading hemisphere) always points in the direction of orbital motion. The orbital velocity of the satellite is less than the co-rotation velocity of plasma in Jupiter's magnetosphere, so that Ganymede's trailing hemisphere receives a larger flux of ions from the plasma than its leading hemisphere [Noll et al., 1996]. Two emission bands of O_2 in the visible wavelength region have been shown to exist with enhanced intensity on the trailing hemisphere relative to the leading hemisphere [Spencer et al., 1995]. Observations of both hemispheres in the FUV will determine whether this enhancement is also present in the 130.4 nm and 135.6 nm emissions, and will provide data necessary to facilitate a comparison of the O I 130.4 nm / O I 135.6 nm ratio in each hemisphere. These data will help to constrain models of the composition of Ganymede's atmosphere, and the production mechanisms which sustain it.

1.4 Other UV emissions in the Jupiter system

1.4.1 Europa

Europa's thin oxygen atmosphere was discovered through *HST* GHRS observations [Hall et al., 1995], which observed O I 130.4 nm and O I 135.6 nm emission lines with intensities well above those that could be explained by reflected sunlight. The intensity ratio I (135.6 nm) / I (130.4 nm) was $\sim$1.9:1, which implies that the atmosphere at Europa is predominantly O_2 rather than O (see Section 1.3.3) [Hall et al., 1998]. The total UV intensity of the Europa emissions is up to $\sim$100 R (Saur et al. [1998]; based on observations described in Hall et al. [1998]). *HST* STIS images at 135.6 nm show that the UV emissions are in the form of a limb glow around the disk of the satellite, plus a region of significantly brighter emission in the anti-jovian northern quadrant [McGrath et al., 2004]. The limb glow fits well with the expected result of plasma interaction with an optically thin atmosphere [McGrath et al., 2004], but the cause of the more intense region is not yet understood. McGrath et al. [2004] suggest that perhaps the surface of Europa is not icy everywhere: it is thought that the atmosphere is created by magnetospheric thermal ion sputtering of O_2 from the icy surface [Ip, 1996], so variations in the surface ice may lead to inhomogeneity of the atmosphere. Further UV imaging of the satellite will determine whether the enhanced region is temporally or spatially variable, and help to explain its origin.

1.4.2 Callisto

Callisto's atmosphere is not well understood at present. A thin CO_2 atmosphere has been detected [Carlson, 1999] but denser O_2 contributions to the atmosphere have only been indirectly inferred [Kliore et al., 2002]. *HST* STIS imaging has failed to detect UV emission from Callisto. The inability to detect UV emissions is thought to be due to the combination of Callisto's thin atmosphere and substantial ionosphere and the small magnitude of the background magnetic field of Jupiter at Callisto orbit ($\sim$35 nT, compared to $\sim$500 nT at Europa). These factors lead to a strong electrodynamic interaction between Callisto's ionosphere and the jovian magnetosphere, resulting in shielding that reduces the net electron impact emission rate by a factor of $\sim$1500 [Strobel et al., 2002]. An upper limit of 15 R for the O I 130.4 nm, O I 135.6 nm, C I 133.5 nm and C I 156.1 nm lines and the CO UV bands has been derived by Strobel et al. [2002]. A UV imager dedicated to imaging the jovian system may detect these emissions and, with measurements of the oxygen lines, provide the first direct evidence of Callisto's O_2 atmosphere.

1.4.3 Io

Io is the most volcanically active object in the solar system, with more than 100 known active volcanoes [McGrath et al., 2004]. It has a thin, predominantly SO_2 atmosphere, which is confined to a region towards the equator, extending to around $\pm$30–45° latitude [Roesler et al., 1999]. Buffer gases such as SO and O_2 may also be present in significant quantities, increasing the atmospheric pressure [Laver et al., 2007]. Io's atmosphere believed to be created by volcanism or sublimation, but the relative importance of these processes is currently unclear. The decrease in SO_2 concentration with increasing latitude can be explained as either due to a lower surface temperature at the poles suppressing a sublimation-dominated atmosphere, or due to a majority of the satellite's volcanoes being located in the equatorial region [McGrath et al., 2004]. As SO_2 gas absorbs strongly in the UV wavelength region, UV imaging can be useful for monitoring the atmosphere: the extent to which solar UV radiation is absorbed rather than reflected provides information on the concentration and distribution of SO_2. A comparison of dayside and nightside UV images would reveal the source of the atmosphere, as a low surface temperature on the nightside will suppress a sublimation driven atmosphere, resulting in much weaker UV emissions here. *HST* STIS images [Roesler et al., 1999] have shown that the brightest atomic oxygen and sulphur emissions from Io's atmosphere are seen in two peaks of the limb of the magnetic equator. These bright spots can be as intense as 2.5 kR and are produced by electron impact dissociation (as described by Equation 1.8). This means that the emissions are dependent on the local electron density and temperature, which is strongly controlled by the local plasma environment and magnetic field. Hence, UV images of the satellite's atmosphere are able to provide information about the environment surrounding the satellite.

1.4.4 Io Torus

Io's atmosphere is continuously losing matter into the jovian magnetosphere. This matter is initially part ionised and mostly neutral, but the neutral components become ionised through excitation by UV radiation or through electron impact. The ions and electrons become concentrated around Io's orbit and form the Io plasma torus [Thomas et al., 2004]. The plasma torus consists mainly of the ions of SO_2 (e.g. ionised oxygen and sulphur). Many of these produce emission lines in the extreme ultraviolet (EUV) region, but there are also emissions in the FUV region, with the strongest being S III 119.1 nm, S III 120.1 nm and S III 172.9 nm [Saur et al., 2004] (see Figure 1.6). UV observations with *Voyager* have led to a value of 1 ton s^{-1} for the mass loss rate from Io into the torus. A significant variation in this rate was observed during the Cassini flyby of Jupiter (October 2000 – March 2001), falling from >1.8 ton s^{-1} to 0.7 ton s^{-1} [Delamere et al., 2004], with the larger value most likely due to volcanic plume activity. The Cassini UVIS instrument detected both long-term and short-term ("twinkling") variations in the total EUV luminosity of the torus, as well as significant changes in the intensities of individual EUV emission lines, implying significant compositional changes [Steffl et al.,

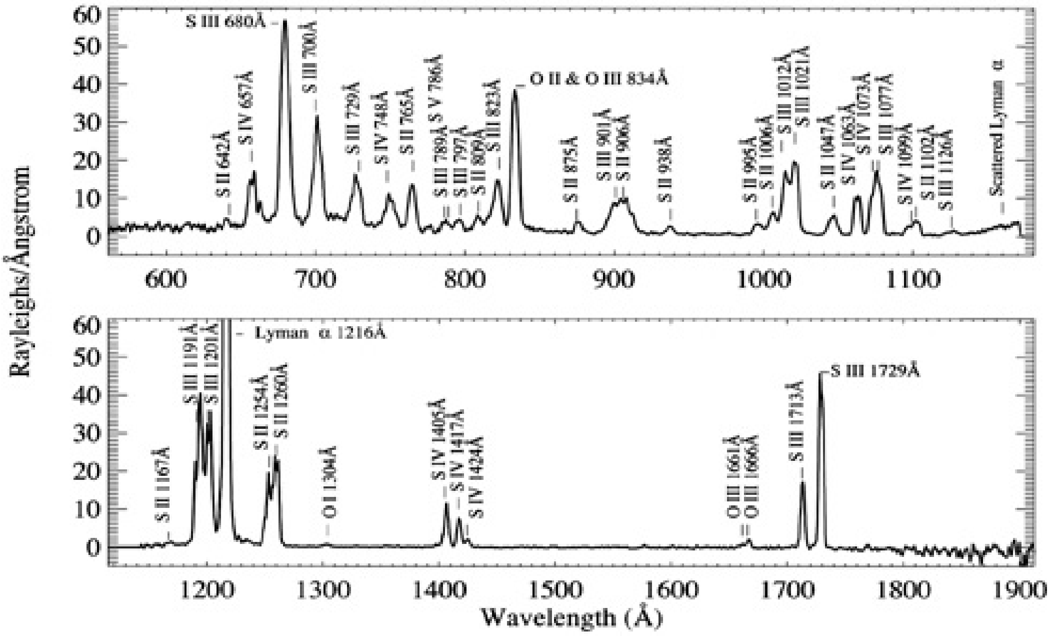

Figure 1.6 — Cassini *UVIS spectrum of the Io torus on January 14, 2001 [Thomas et al., 2004]. The intensities given are the average intensity of each feature in the region 4 to 8* R_J.

2004]. Further UV studies will add to the current available dataset and allow stronger conclusions about the torus variability and the processes governing this to be drawn.

1.5 A UV Imager for Jupiter missions

In 2008, NASA and ESA began joint studies of two possible missions to the outer planets: the Europa Jupiter System Mission (EJSM) to the Jupiter system and the Titan Saturn System Mission (TSSM) to the Saturn system. In 2009 it was announced that EJSM would take priority over TSSM, with a planned launch in 2020.

1.5.1 Overview of the Europa Jupiter System Mission

EJSM was designed as a dual-spacecraft, joint NASA–ESA mission to Jupiter. The two constituent spacecraft would have separate but complimentary science goals, and together would conduct a thorough investigation of the entire Jupiter system, with a particular emphasis on the Galilean satellites. Each spacecraft would undertake a tour of the jovian system, during which atmospheric, magnetospheric and satellite science questions would be addressed. The spacecraft would use gravity assists of the Galilean moons to shape their trajectories, and take advantage of these assists to study all four of Jupiter's major moons. A satellite-to-satellite communication capability would allow synergistic science to be performed by the two orbiters. For NASA's Jupiter Europa Orbiter (JEO), the tour would be followed by insertion into a 200 km circular orbit around Europa, and then a transfer to a 100 km circular orbit approximately one month later, with the mission ending with impact onto Europa once the fuel had run out or the orbiter had been irrevocably damaged by the surrounding radiation environment [Clark et al., 2009]. ESA's Jupiter Ganymede Orbiter (JGO) was proposed as one of three L class (large) mission candidates competing for launch in the early 2020s as part of ESA's Cosmic Vision – a long-term plan for European space science missions between 2015 and 2025. The spacecraft would follow its tour of the main jovian system with insertion into an elliptical orbit around Ganymede, which would evolve in to a 500 km circular orbit and then be reduced to a 200 km orbit, and the mission would end with the orbiter impacting Ganymede.

EJSM was designed to build on *Galileo's* discovery of sub-surface oceans at Europa, Ganymede, and Callisto, and of Ganymede's magnetosphere [EJSM-Laplace Joint Science Definition Team, 2011]. These discoveries greatly increase the potential habitability of the moons, making them an exciting target for further missions. EJSM aimed to confirm the presence of the oceans and determine their characteristics, as well as investigating whether the satellites possess the conditions necessary to sustain life. In addition to specific satellite science, the mission would perform a comprehensive study of the entire jovian system. Jupiter and its moons can be compared to a miniature solar system, and by investigating the properties of the major objects therein and the interactions between them, an understanding of the formation and evolution of the system can be obtained which can be applied to other gas giant systems and to the solar system as a whole.

JEO and JGO were originally scheduled for independent launches in February and March 2020 respectively, arriving at Jupiter in December 2025 and February 2026 [Clark et al., 2009]. The staggered arrival would allow JEO to conduct measurements of the jovian magnetosphere while JGO was in the solar wind – the first of many synergistic science opportunities arising during the mission. While the two orbiters had the same overarching science goals, they differed in significant ways. JEO would be powered by radioisotopes, while JGO would get its power from solar panels, limiting its power budget and placing constraints on its trajectory so that it would not spend too much time in eclipse. The solar panels would take up a considerable fraction of the mass budget for the orbiter. JEO would be exposed to more intense radiation than JGO, as it was designed to explore the inner region of Jupiter's magnetosphere, and so would require extremely effective shielding to protect its instruments. The radiation dose encountered by JGO, although smaller, is still significant, and shielding and the use of radiation hard components would be important for it to perform effectively. JEO would also face stricter planetary protection rules than JGO as impact on Europa meant that JEO was classified as category III [5] mission [Clark et al., 2009], while JGO was a category II [6] mission with a few extra requirements identified [EJSM-Laplace Joint Science Definition Team, 2011].

[5]Category III missions are *"certain types of missions (mostly flyby and orbiter) to a target planet of chemical evolution and/or origin of life interest or for which scientific opinion provides a significant chance of contamination which could jeopardize a future biological experiment"* [Rummel et al., 2002]. Documentation is required, including an overview of controls put in place to avoid contamination of the target, and cleanrooms must be used during the assembly and testing of the spacecraft.

[6]A category II mission is one to targeting a body where *"there is significant interest relative to the process of chemical evolution and the origin of life, but where there is only a remote chance that contamination carried by a spacecraft could jeopardize future exploration"* [Rummel et al., 2002]. These missions require brief documentation including an outline of any intended impacts. Additional requirements for JGO were concerned with reducing the likelihood of any collateral contamination of other bodies like Europa or Mars, and with limiting the chance of any organism from Earth reaching Ganymede [EJSM-Laplace Joint Science Definition Team, 2011].

The Jupiter Europa Orbiter was named as the second highest priority Flagship mission by the National Research Council's decadal survey of planetary missions [Committee on the Planetary Science Decadal Survey, 2011]. However, its projected cost of $4.7 billion was considered to be prohibitively high, and the Council recommended that *"it should fly in the decade 2013-2022 only if changes to both the mission and the NASA planetary budget make it affordable without eliminating any other recommended missions"*. Since JGO was completely independent of JEO, its development has continued in a slightly altered form as the JUpiter ICy moon Explorer (*JUICE*).

1.5.2 JUICE overview and timeline

The evolution of EJSM into the reformulated, ESA-alone *JUICE* mission has allowed it to remain one of the three L class mission candidates competing for launch in the early 2020s as part of ESA's Cosmic Vision. In its original guise as JGO, it was slated for launch from Kourou on Ariane 5 on 11th March 2020, allowing the spacecraft to directly escape Earth orbit towards Venus. The orbiter would undergo a Venus-Earth-Earth gravity assist sequence and arrive at Jupiter on 4th February 2026 [Boutonnet et al., 2010]. The currently envisaged launch date for *JUICE* is June 2022, followed by an Earth-Venus-Earth-Earth gravity assist sequence, with the spacecraft reaching the Jupiter system in January 2030 [JUICE Science Study Team, 2011].

On arrival at Jupiter, the spacecraft will perform a Ganymede gravity assist followed by a Jupiter orbit insertion manoeuvre which will insert the spacecraft into a 13 $\times$ 243 R_J orbit. This orbit will be gradually reduced to 41 $\times$ 11.6 R_J and the inclination reduced from 9° with respect to the orbital plane of the jovian system to zero, with the use of four further Ganymede swing-bys and small correction manoeuvres near the apojove of each orbit [JUICE Science Study Team, 2011]. This phase will be followed by two Europa flybys: these were not part of the original JGO orbital design and have been included to recover some of the science opportunities lost through the removal of JEO from the mission. The spacecraft will then be brought into a Callisto resonant orbit through a sequence of Callisto-Ganymede-Callisto gravity assists [JUICE Science Study Team, 2011].

The next phase of the mission is the Jupiter high latitude phase, which will involve a sequence of repetitive Callisto gravity assists to increase the inclination of the orbit to 29°. Each Callisto flyby has a preliminary altitude of 200 km, although a lower altitude may be considered for the later flybys to allow in situ measurements in the moon's exosphere [JUICE Science Study Team, 2011]. This phase is another addition to the original JGO orbital design, with the aim of enhancing the spatial and temporal coverage of the jovian atmosphere and magnetosphere to compensate for the loss of the second spacecraft. The high latitude phase will be followed by further Callisto-Ganymede-Callisto gravity assists to reduce the spacecraft velocity in preparation for transfer to Ganymede.

At Ganymede, the orbiter will be injected into a 200 $\times$ 10000 km orbit, which will experience significant perturbation from Jupiter, causing it to evolve into a 5000 km circular orbit within about 30 days. This altitude will be maintained for around 90 days and the orbit will gradually become more eccentric, until a suitable altitude is reached for a manoeuvre to insert the spacecraft into a 500 km circular orbit. The mission phase up to this point is called the Ganymede elliptical orbit (GEO) phase. It is followed by the Ganymede circular orbit (GCO) phase, which consists of approximately 102 days in the 500 km circular orbit, and a final 200 km circular orbit lasting for at least 30 days, and longer if the spacecraft health and fuel supply allow. The main science driver during GEO is analysis of Ganymede's magnetosphere, followed by a global mapping of the satellite during the lower altitude GCO phase [Boutonnet et al., 2010]. Studies of the moon's atmosphere and interior are also important and, as in the earlier phases, remote sensing of other objects is possible. Once the spacecraft ceases to operate, its orbit will become more eccentric, leading to impact on Ganymede's surface [JUICE Science Study Team, 2011].

1.5.3 Requirements for a dedicated UV imager on board JUICE

As already mentioned, a UV imager dedicated to observing Jupiter's aurora from within the jovian system has manifold advantages over both the Earth-orbiting imagers and *in situ* spectral imagers that are the current state of the art. The inverse square law dictates that the flux an imager encounters falls with the square of its distance from the emitting object, so an instrument within the jovian system will detect considerably fainter emissions than an imager with the same sensitivity observing the same region from Earth, and will require shorter integration times for stronger emissions. Similarly, an imager capable of observing the entire auroral region in a single frame will have a significantly higher time resolution than an imaging spectrograph that has to scan over the region to create an image. A dedicated auroral imager represents an opportunity to implement the first continuous observation of the auroral ovals over a solar rotation (∼25 days), which, combined with magnetospheric and plasma measurements from other *JUICE* instruments, would allow all the expected variability of the solar wind-magnetosphere-ionosphere-atmosphere coupling processes in the jovian system to be monitored, vastly increasing our knowledge of the system.

Although there is clearly a strong case for future UV imaging at Jupiter, the development of an imager for *JUICE* does face a number of challenges. The spacecraft will not encounter the extreme radiation environment within Jupiter's inner radiation belts, which exist well within Ganymede's orbit (∼15 R_J), in regions within ∼5 R_J of Jupiter, but even as far out as Ganymede a significant number of high energy (<1 GeV) electrons can be found [JUICE Science Study Team, 2011]. The addition of the Europa flybys to the mission orbital design will increase the radiation dose relative to the original dose estimated for JGO. In light of this, instruments carried by the spacecraft should be constructed from radiation tolerant components (the entire payload vault will also be shielded to some extent). Power will be supplied by solar panels, but the large distance from the Sun means this will be limited to a worst case solar constant of 46 W/m^2 [JUICE Science Study Team, 2011]. The size of the panels will be limited by the launch mass available, to around 60 – 75 m^2, so instruments with a low power requirement will be favoured, as will those with a small mass and volume. The limited power budget will also result in limited data storage and downlink capabilities, so the imager's telemetry rate should be as low as possible while still providing the required data. In order to maximise the solar flux incident on the solar panels, they will be kept close to normal to the Sun direction, using rotation of both the panels and the spacecraft body. The imager must be designed in such a way that the effects of the spacecraft rotation (yaw steering) can be removed from images so that the data is not compromised.

The novel UV imager will compete for space on *JUICE* with other UV instruments, most likely spectral imagers, which will make use of technology that has already been proven to be reliable on previous missions. In order for the new design to be favoured it must be shown to have a good level of technology readiness, must be competitive in terms of mass, volume and power and should be able to provide better scientific results than the competing instruments. The current paragon of UV imaging is the Hubble Space Telescope so, ideally, any future UV imagers should improve on the *HST* instruments. *HST* STIS has a pixel size of 0.0246" [Bostroem et al., 2010] but the resolution of its FUV-MAMA detector is limited by its point spread function of ∼0.1" at 143 nm [Walsh, 1997]. Jupiter's orbit has an aphelion of ∼5.46 AU and a perihelion of ∼4.95 AU, so the Earth-Jupiter distance can vary between ∼3.95 AU and ∼6.46 AU. Hence the best possible spatial resolution achievable by the STIS FUV-MAMA is ∼286 km. An imager within the jovian system with a spatial resolution of around 100 km will therefore allow substantially smaller auroral features to be resolved than is currently possible.

The huge variation in the intensities of the UV emitters within the jovian system poses another problem for the imager. In order to maximise scientific returns, the instrument should be capable of providing high resolution images of both Ganymede and Jupiter. The instrument will therefore need to respond well to UV emissions as dim as tens of Rayleighs, and as intense as a few MR. A summary of the main science requirements for a UV imager on *JUICE* can be found in Table 1.4.

Table 1.4 — *JUICE UV Imager Science Requirements*

Imaging parameter	Required value
Spatial Resolution	$\sim$100 km
Exposure Time	$\sim$10 sec – 1 min
Spectral Range	FUV: 90–165 nm
Wavelength Discrimination	H_2 (90–165 nm), Ly-α ($>$121.6 nm), O (135.5 nm), reject/retain long-wavelength ($>$165 nm)
Dynamic Range	10s R to few MR
Observation Duration	$\sim$1 solar rotation (25 days)
Spatial Precision	$\sim$500 km
Field of View	To include entire auroral emission region in one or both of Jupiter's hemisphere; global satellite views; long range Io torus images

1.6 Thesis structure

In March 2009, ESA issued a call for declarations of interest in science instrumentation for the Europa Jupiter System Mission, which has now been superseded by *JUICE*. In response to this, a consortium of researchers from various institutions across Europe, the US and Canada was formed to perform a UV imager instrument study to determine the science case for such an instrument, and to describe the technology that would be able to fulfil the science requirements. Two alternative design approaches for the instruments optics were initially considered: one based on novel microchannel plate (MCP) optics, lead by the University of Leicester, UK; and one using conventional reflective UV optics designed at the Centre Spatial de Liège, Belgium. A detailed description of the Leicester design can be found in Chapter 2, along with a brief overview of the alternative Liège optics.

A thorough feasibility study of the MCP based instrument was carried out, using Sequential Ray Tracing (SRT) models to determine the instrument's response to UV radiation from Jupiter and Ganymede (Chapter 3), backed up by laboratory testing of two MCP optics with different characteristics (described in Chapter 4). The response to both point sources and extended sources was considered, with the model eventually being able to accept black and white images as a source, allowing the user to input images of Ganymede and Jupiter obtained by *HST* STIS to produce more realistic results. While the models suggested that the instrument would perform well in many ways, it was determined that diffraction effects would severely compromise the resolution of the optics in reality, as the wavelengths of interest are of a similar magnitude to the width of the pores used to focus the light in the MCP optic. This is particularly problematic for this specific MCP optic application, as JUDE has a stringent resolution requirement set to match that of *HST* STIS. Laboratory tests were also unable to recreate the theoretical resolution of the optics tested, although this was due to a number of factors, including one of the optics being poorly fused.

As a result of the feasibility study, it was therefore decided that the Liège reflective optics would be more suitable for this particular mission. A study of possible filters to include within this design is discussed in Chapter 5. The aim of this study was to determine whether it would be possible to determine the O I 135.6 nm / O I 130.4 nm ratio of the Ganymede emissions, with the use of two commercially available filters and a good knowledge of the transmission curves of both these and the coatings used on the UV optics. It was found that the ratio derived for a number of input spectra was very accurate.

The development of the UV imager as a whole is ongoing. The next hurdle will come after a down-selection of ESA's L-class missions due to take place in April 2012 (at the time of writing). If *JUICE* is selected, an Announcement of Opportunity (AO) will follow, calling for proposals for instruments to be included on the spacecrafts payload. Chapter 6 summarises the future development work that will take place, and outlines other targets which the initial MCP optic imager (or a modified version thereof) may be more suitable for.

1.7 Summary

Satellite-based ultraviolet auroral imagers provide an instantaneous, global view of the Earth's aurora, enabling researchers to learn much about the emissions and, when combined with simultaneous particle and field data, the processes that influence them. While UV imagers have been included on numerous Earth-orbiting solar-terrestrial science satellites, no such instruments have been carried on planetary missions, and the best FUV planetary images obtained to date have been produced by the Hubble Space Telescope. HST is nearing the end of its mission, and no UV-sensitive instruments will be included on its successor.

Jupiter's UV aurora exhibits three separate emission regions. The origins of the three regions can be broadly explained by current theories, but further observations are needed to study fluctuations and fine-structure within the emissions. The processes producing the polar emissions are particularly unclear. High-resolution images of Jupiter's aurora by a dedicated imager would have the potential to refine current models of all three emission groups.

Jupiter is not the only UV emitter in the jovian system. Ganymede in particular displays interesting atmospheric FUV features that appear to be auroral in nature. Studies of the Ganymede emissions provide information about the moon's atmosphere and the interaction between its magnetosphere and Jupiter's, but there have been very few observations to date, all with limited spatial resolution.

JUICE is one of three ESA L-Class missions competing for launch in 2020. The spacecraft could potentially provide a platform for the first UV imager to operate within the jovian system. Such an imager would greatly enhance our understanding of the solar wind-magnetosphere-ionosphere-atmosphere coupling processes occurring in the system, and of the nature of FUV emissions from the Galilean satellites. This thesis describes a feasibility study of an imager designed for this purpose.

CHAPTER 2

The Jupiter system Ultraviolet Dynamics Experiment (JUDE): Baseline Design

The Jupiter system Ultraviolet Dynamics Experiment (JUDE) is a far-ultraviolet imager designed for *JUICE*, with the aim of producing global, high-resolution images of Jupiter's aurora, and the UV emissions of its Galilean satellites. Two different optic systems were originally proposed for the instrument: one based on novel microchannel plate (MCP) optics, and one using more conventional reflective optics. The two options are discussed in this chapter, with a particular emphasis on the MCP optic design. Either one of the optical designs would be used in combination with an MCP detector and a novel readout anode, as described in Section 2.3.

2.1 Design option 1: MCP optics

2.1.1 Microchannel Plates

Microchannel plates are small lead glass sheets with closely packed, parallel, microscopic pores chemically etched through them (Figure 2.1). MCPs were originally used in image intensifiers for military applications, but since their declassification in the late 1960s they have been used as photon or particle detectors (see Section 2.3.1) in numerous scientific instruments, including astronomical instruments such as the *Chandra* High Resolution Camera (HRC) [Kenter et al., 1997]. The impact of a particle or photon on a channel wall within an MCP causes an electron to be released, which is accelerated down the channel by an applied bias voltage, liberating more electrons on its way through further collisions with the wall. In this way a charge cloud builds up so that a single photon can produce a detectable signal at the focal plane: the gain of a detector MCP is typically $\sim 10^4$ - 10^7 [Wiza, 1979] (see Section 2.3.1). MCPs were used as signal intensifiers in some of the UV instruments mentioned in Section 1.1.1, namely those flown on *Viking*, *Freja* and *Polar*, and the Wideband Imaging Camera on *IMAGE*. More recently, MCPs with square pores (in contrast to the circular pores that are generally used for detectors) have been developed for use as X-ray optics (a theoretical discussion of such optics is given by Chapman et al. [1991] and early laboratory tests are described by Fraser et al. [1993a]). The manufacture of MCPs in general, and the operation of MCP optics in particular, are described below.

2.1.1.1 Manufacture

A schematic of MCP manufacture is given in Figure 2.2. A cylindrical (for circular pore MCPs) or square cross-sectioned (for square pore plates) stick of chemically etchable ‘core’ glass is placed inside a tube of lead glass cladding. The cladding will later make up the matrix of the finished MCP, with the purpose of the core glass being to provide support during the manufacturing process. The combination of cladding and core glass, known

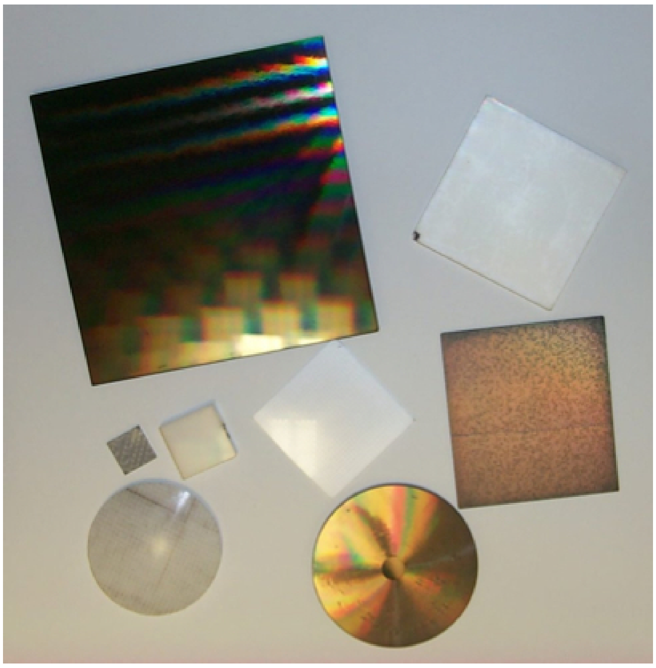

Figure 2.1 — *A selection of MCPs, both detector plates and optics. Diffraction patterns can be seen on some due to their small pore widths. For scale, the largest plate is 100 × 100 mm [Price, 2001].*

as a ‘couple’, is hung in a drawing tower and heated and drawn to produce a fibre ∼1 mm in diameter. This is cut into lengths of ∼50 cm, which are then stacked into bundles. The shape of the stack varies depending on the cross-section of the fibres. Cylindrical fibres stack well in a hexagonal arrangement, while fibres with a square cross-section are stacked into a square, with the fibres aligned along rows and columns. The bundle of fibres is then drawn in the same manner as the first draw to produce a ‘multifibre’. This process can be repeated as necessary to create multifibres containing channels of the required size (generally on the order of tens of microns).

Once suitable multifibres have been produced, they are stacked once more, into a ‘boule’. Again, the stacking geometry varies with multifibre cross-section. Hexagonal multifibres, containing circular pores, are stacked hexagonally, while square multifibres can be stacked either into a square block, to give ‘square-pack’ MCPs, or in a curved block to produce radially-packed plates. The boule is then fused and sliced to the required thickness. If the plate is to be used as a detector, it may be cut at an angle so the channels

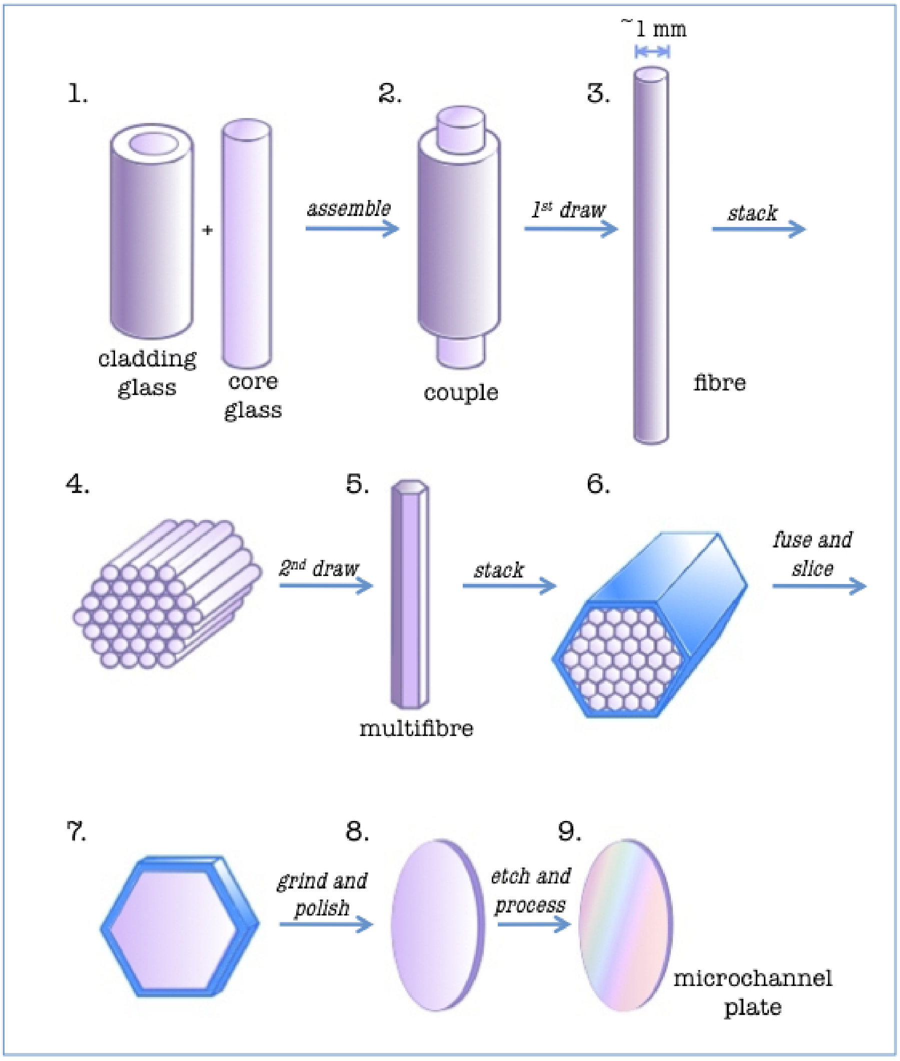

Figure 2.2 — *Illustration of MCP production, after Fig. 3.3 in [Fraser, 1989].*

have a particular bias (see Section 2.3.1). The plates are polished and etched with acid or alkali to remove the core glass. Detector plates are then reduced in hydrogen to create a semiconducting surface in the channels which will release electrons on particle or photon impact, and electrodes are deposited on each face of the plates. MCP optics do not need to be reduced but may have a reflective coating deposited on their channel walls to increase their efficiencies. Both optic and detector MCPs can be ‘slumped’ to a spherical profile (see Section 2.1.1.2) by sandwiching the plate between one concave and one convex section of a spherical surface, in a device known as a “mandrel”, and applying pressure.

2.1.1.2 MCP optics

Microchannel plate optics focus light by grazing-incidence reflection from the channel walls. They are particularly useful for focusing X-rays, as these cannot be focused by refraction or by normal-incidence reflective optics. In 1960, Giacconi and Rossi described an X-ray telescope design that made use of a parabolic mirror to focus rays at grazing incidence [Giacconi and Rossi, 1960]. However, this system does not meet the Abbè sine condition, which must be fulfilled in order for an optical system to produce a true image (see textbooks such as Hecht [2002]). For a source at infinity (so that all rays reaching the optical system from the source are parallel), the Abbè sine condition can be expressed as

$$\frac{h}{\sin\alpha} = r, \tag{2.1}$$

where h is the distance between the incoming ray and the optical axis of the system, α is the angle at which the focused ray meets the optical axis, and r is a constant. This means that the principal surface[1] of the optical system must be a sphere of radius r around the focal point for a true image to be obtained. The principal surface of a single parabola is the parabola itself (see Figure 2.4a). This deviation from the Abbè sine condition leads to aberrations in the image a parabolic lens produces: while on-axis rays are focused to a point, off-axis radiation produces an image in the form of a ring centred on the optical axis [Giacconi and Rossi, 1960]. In order to produce a true image, X-ray telescopes often use a Wolter type I design, in which rays are focused by glancing reflection off two coaxial elements, the first paraboloid and the second hyperboloid [Wolter, 1952]. The mirrors can be nested to increase the telescope's collecting area. This system is able to more closely obey the Abbè sine condition (see Figure 2.4b) than a system based on parabolic mirrors [Willingale, 1984].

[1]The principal surface is the theoretical surface at which rays are focused by a lens or mirror. For example, when a ray is focused by a typical lens, it is refracted twice, once for each surface of the lens. The principal surface is an imaginary surface within the lens at which we can consider an equivalent focusing of the ray to occur through a single refraction. We can draw the principal surface on a ray diagram by extending the initial and final paths of rays to the points where they intersect and joining up these points (see Figure 2.3). The principal surface of a single mirror is the mirror itself, as an incident ray is only reflected once.

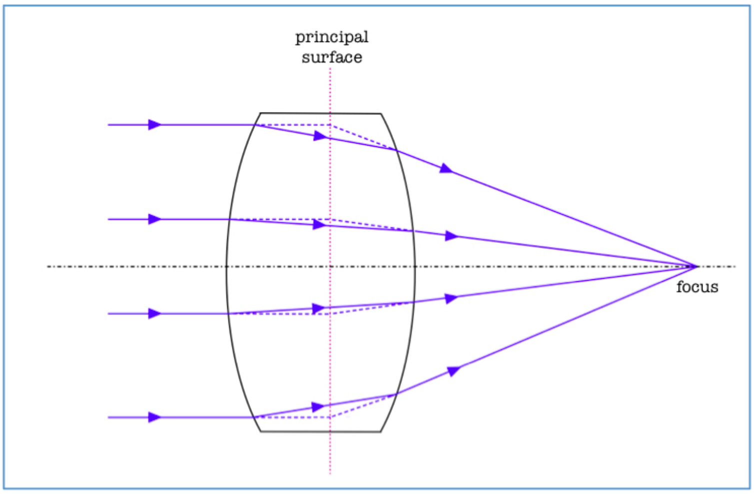

Figure 2.3 — *Ray diagram of a lens, showing how the initial and final paths of rays can be used to define the principal surface of the lens.*

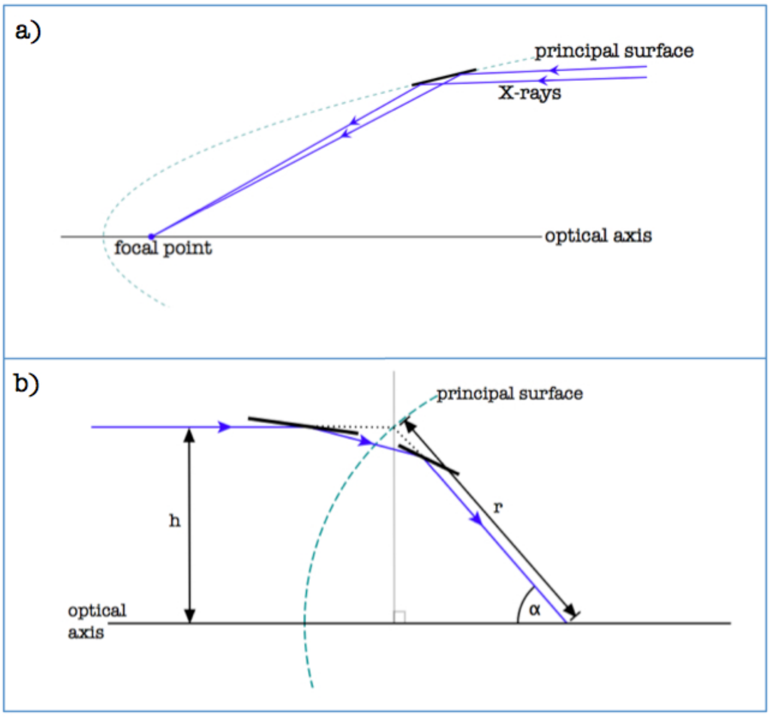

Figure 2.4 — *Diagram showing: a) the principal surface of a parabolic mirror; b) the principal surface of a Wolter type 1 mirror system (based on Figure 3 in [Willingale, 1984]). According to the Abbè sine rule, the principal surface should be spherical for the mirror to produce a true image. The Wolter type 1 design is able to approximately meet this condition [Willingale, 1984].*

Although optics with a Wolter type I design have been used successfully in missions such as *ROSAT*, *Chandra* and *XMM-Newton* to provide high-resolution X-ray images, the design has several limitations, with one of the most critical being the size of the telescope required. *XMM-Newton*, for example, carries three sets of mirrors, each consisting of 58 nesting mirror shells. The shells are 600 mm long, with a maximum diameter of 700 mm, and each mirror module has a mass of 430 kg, with 350 kg of this in the mirrors themselves and the rest in the supporting structure [Buzzi et al., 2001]. The X-rays are focused at grazing incidence, i.e. narrow angles, so their paths are only altered by a small angle, meaning they must travel for a substantial distance before coming to a focus (see Figure 2.5): *XMM-Newton* has a focal length of 7.5 m. The combination of high-mass optics and the large telescope structures required to hold both the optics and the detectors several metres behind them makes X-ray astronomy missions such as *XMM-Newton* very costly. Additionally, the field of view of the Wolter type I optical system is limited by its geometry, to e.g. 30' for *XMM-Newton* [Ehle et al., 2003].

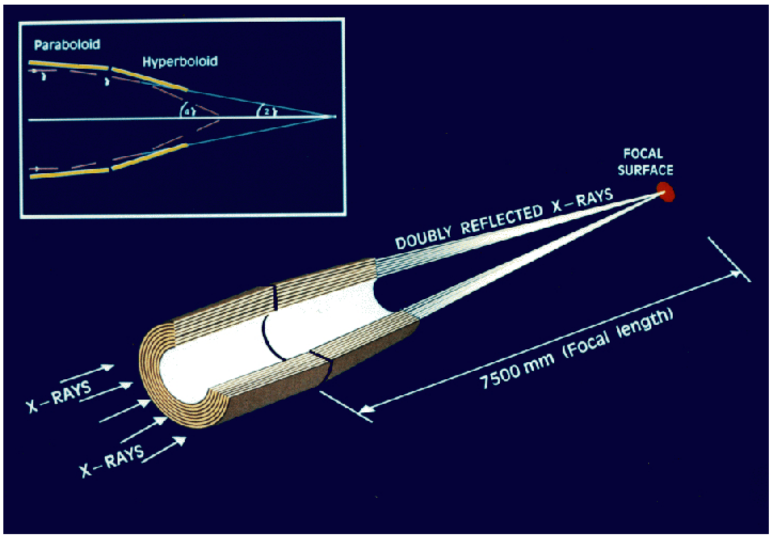

Figure 2.5 **—** *Diagram of the Wolter type I optics on XMM-Newton (from [Ehle et al., 2003]).*

The idea of developing an optic based on grazing-incidence reflection from the walls of an array of channels was first set out by Angel [1979], who took inspiration from the eyes of certain crustaceans, including lobsters, shrimps and crayfish. A comparison between a crustacean eye and the preliminary optic designs given by Angel is shown in Figure

2.6. Early tests of MCPs in this application are described by Chapman et al. [1990]. The MCPs used in these experiments were two hexagonally-packed, circular pore plates, one flat and one slumped to a radius of curvature of 160 mm. While X-ray focusing was achieved by both plates, circular pores are unable to provide a true image of a source, as reflection from most points on their walls results in X-rays being diverted away from the optical axis [Chapman et al., 1991]. The image produced by a circular pore MCP viewing a point source is a ring in the focal plane, as shown in Figure 2.7 [Chapman et al., 1990].

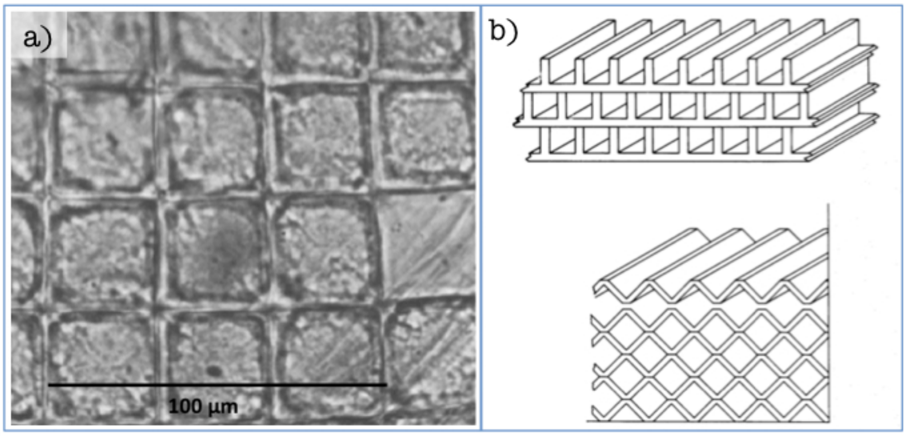

Figure 2.6 *— a) The cornea of a squat lobster, from Land et al. [1979]; b) Possible arrangements for the square cells in an X-ray telescope based on the lobster eye, as suggested by Angel [1979].*

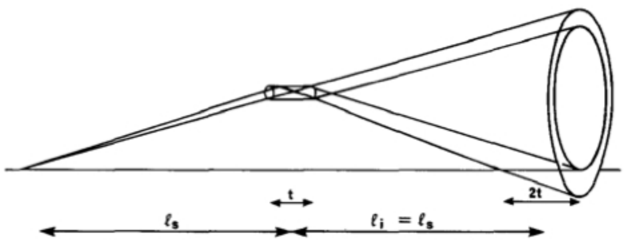

Figure 2.7 *— Ray diagram showing how a ring-shaped image is produced by a circular pore MCP optic imaging a point source (Fig. 3 in Chapman et al. [1990]).*

The problem of obtaining a true image with an MCP optic can be solved by using square pore plates: a reflection at each of two orthogonal walls within a square channel will direct an incoming ray back towards the optical axis. A discussion of X-ray focusing by square pore MCPs is given by Chapman et al. [1991], and the results of early laboratory tests of these optics are described by Fraser et al. [1993a].

The method by which MCPs are able to focus X-rays (and UV light or particles) is shown in Figure 2.8. Rays hitting the wall of a channel are reflected if they strike at an angle less than the critical angle of reflection, θ_c (degrees), for their energy:

$$\theta_c(E) = aE^{-1.04}. \tag{2.2}$$

Equation 2.2 is an empirical relation given by Willingale et al. [1998] for hard X-rays encountering lead glass MCPs. If the energy of the X-rays, E, is in keV then the constant, a, has a value of 2.4. The critical angle for X-rays is small, and reflection at the MCP wall changes the path of a ray by just 2 $\times$ the angle of incidence, so for a flat MCP the source distance is equal to the image distance. Clearly this is not practical for astronomical observations, as the study of distant objects would require a telescope with an infinite focal length. Hence, MCP optics are "slumped" to the shape of a portion of a sphere, such that each of the channels points towards the centre of the sphere. In this scenario, the MCP optic obeys the following lens equation:

$$\frac{1}{l_s} - \frac{1}{l_i} = \frac{2}{R_{MCP}}, \tag{2.3}$$

where l_s is the source distance, l_i is the image distance and R_{MCP} is the radius of curvature (or slump radius) of the MCP, defined as positive when the optic is concave as viewed from the source [Chapman et al., 1990]. Hence, the image distance (i.e. focal length) of a slumped MCP optic viewing an object at infinity is half of the slump radius. Another advantage of slumping is that it gives the MCP optic an intrinsically large field of view. The field of view can be increased further by tiling a number of MCPs so that together they approximate the surface of a sphere. This tiling is possible because a perfectly slumped optic will be spherically symmetrical and thus will exhibit no preferred optical axis. In this way it is theoretically possible to produce a field of view covering the entire sky, minus the area taken up by the telescope structure.

Although the most obviously useful application of MCP optics is for X-ray focusing, as they can achieve much larger fields of view than the alternative Wolter optics at

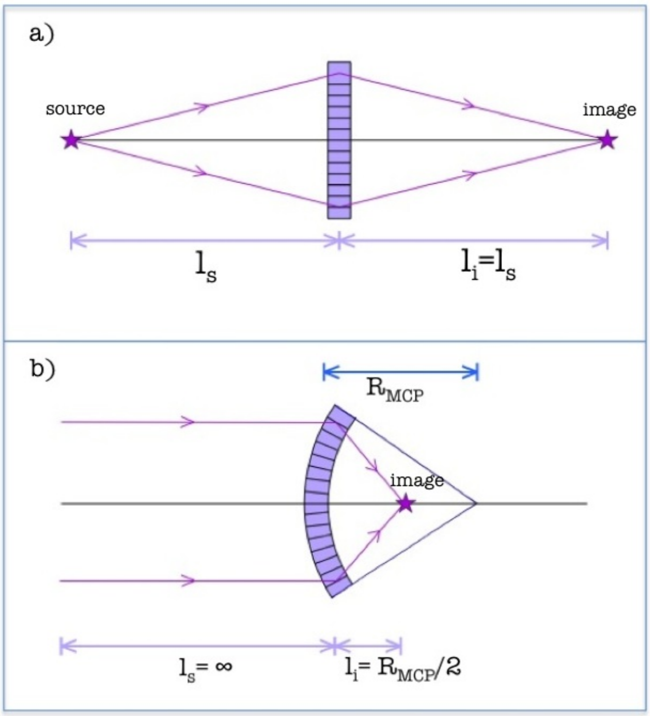

Figure 2.8 — *Diagrams showing focusing of light by MCP optics. a) For a flat MCP optic the image distance is equal to the source distance. b) A slumped MCP observing a source at infinity produces an image at a distance equal to half of the slump radius.*

significantly lower mass and volume requirements, they are also able to focus radiation at extreme and far ultraviolet (EUV and FUV) wavelengths. FUV radiation can be focused by more conventional optics, but MCP optics can provide large fields of view, and the larger critical angles for UV reflection make them well-suited for this application. For missions to Jupiter, which possesses an intense radiation environment, bare MCPs have the added advantage of being radiation hard, although any coatings applied to the plates to increase reflectivity or select spectral regions may be affected by the radiation, so these would need careful consideration. However, as the wavelength of interest increases, so does the magnitude of the diffraction effects seen in images. This problem is due to the small channel size of the optics. Each channel acts as an individual aperture, giving a diffraction-limited angular resolution of λ/D for the optic, where λ is the imaging wavelength and D is the width of a single pore [Angel, 1979]. Hence, high-resolution imaging with MCP optics is easier to achieve in the shorter wavelength portion of the ultraviolet region.

2.1.1.3 Point-Spread Function of MCP optics

Typical MCP optics are made up of square-packed channels with a square cross-section, in contrast to the hexagonally-packed, circular pores found in standard detector MCPs (Figure 2.9). This leads to a characteristic cruxiform point-spread function (PSF) at the focal plane, as shown in Figure 2.10. X-rays encountering an MCP optic are reflected n_x times on one set of parallel walls within a channel and n_y times on the orthogonal set. If a ray is reflected once in each direction (n_x=1, n_y=1), it will be directed back towards the optical axis and focused to the central spot seen in Figure 2.10. Rays reflected once in one direction only (i.e. n_x=1, n_y=0; or n_x=0, n_y=1) will be focused only in that direction, leading to the two orthogonal cross-arms in the PSF. Rays passing through a channel without being incident on any walls (n_x=0, n_y=0) contribute to an unfocused background image [Angel, 1979].

It is possible for photons to undergo multiple reflections at each set of walls within the channel, although at higher energies the smaller critical angles for reflection make this less likely than single reflections, as does the possibility of absorption by the channel glass at each reflection. The general rules for X-ray focusing by an MCP optic are given in Table 2.1.

Another characteristic feature of an MCP optic PSF is the presence of a tiled ‘checkerboard’ pattern of background events within the image, as shown in Figure 2.11. This is due to the geometry of the optic: the lines in which no events are seen correspond to regions of the optic where the channel angle relative to the source is such that all photons undergo an odd number of reflections in one axis and are directed to the relevant PSF cross-arm (see Figure 2.11). The areas in the PSF image where the dark lines of no events cross correspond to regions of the optic where photons are reflected an odd number of times in both the x and y directions, and are therefore directed to the central focus.

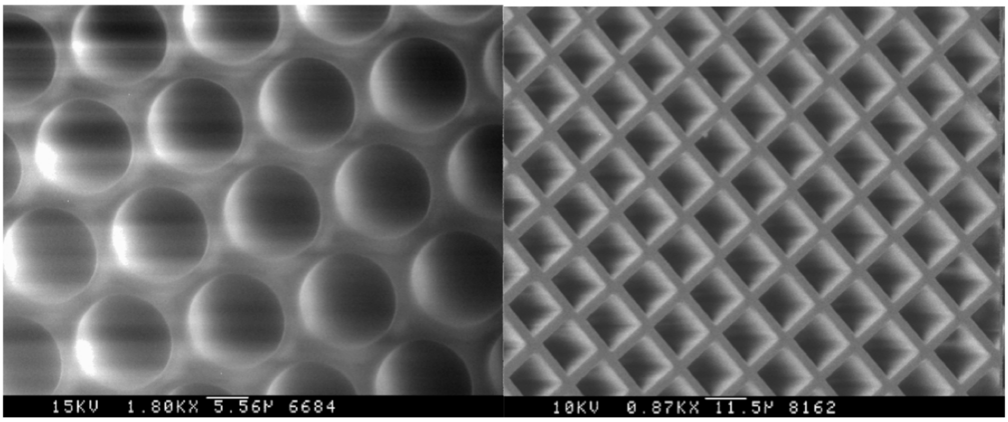

Figure 2.9 — *Electron micrographs of a circular pore, hexagonally-packed MCP (left) and a square pore, square-packed MCP (right). Scale is given by bars at the bottom of each image. From [Price, 2001].*

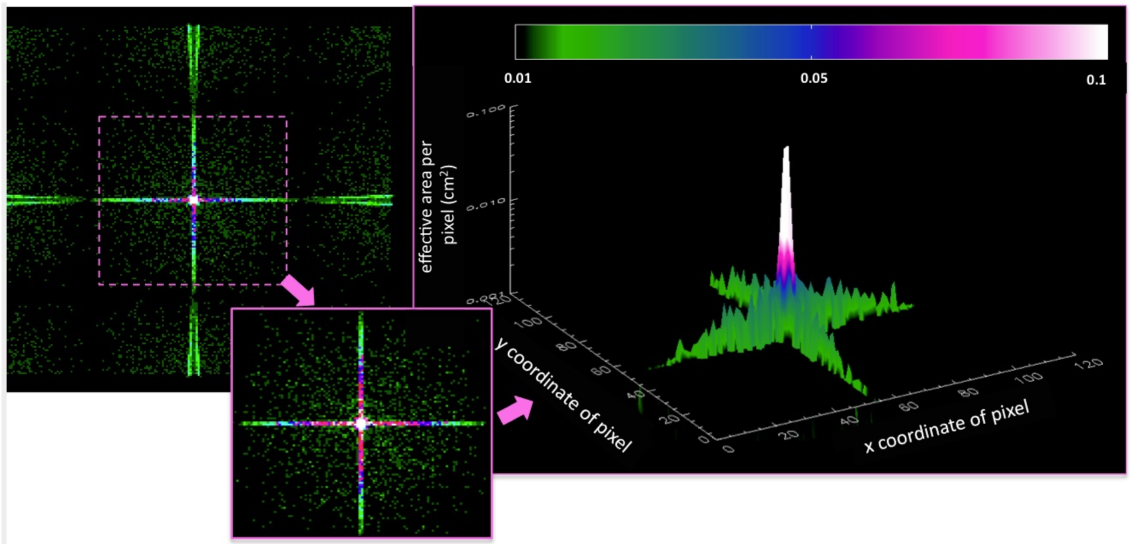

Figure 2.10 — *Left: a ray-traced image of a point source focused by a square-pore, square-packed MCP optic (optic parameters: pore width=100 μm; pitch=120 μm; R_{MCP}=100 mm; plate thickness=0.9 mm; image pixel size=0.2 mm). The focal plane for this simulation was flat rather than slumped to match the curvature of the optic, leading to a distortion in the image which can be seen in the widening of the cross-arms towards the edges. Right: a projection of the central 110 × 110 pixel region (shown in the central inset). The ray-tracing code returns an effective area for each pixel in cm^2 – this is interpreted as the image intensity.*

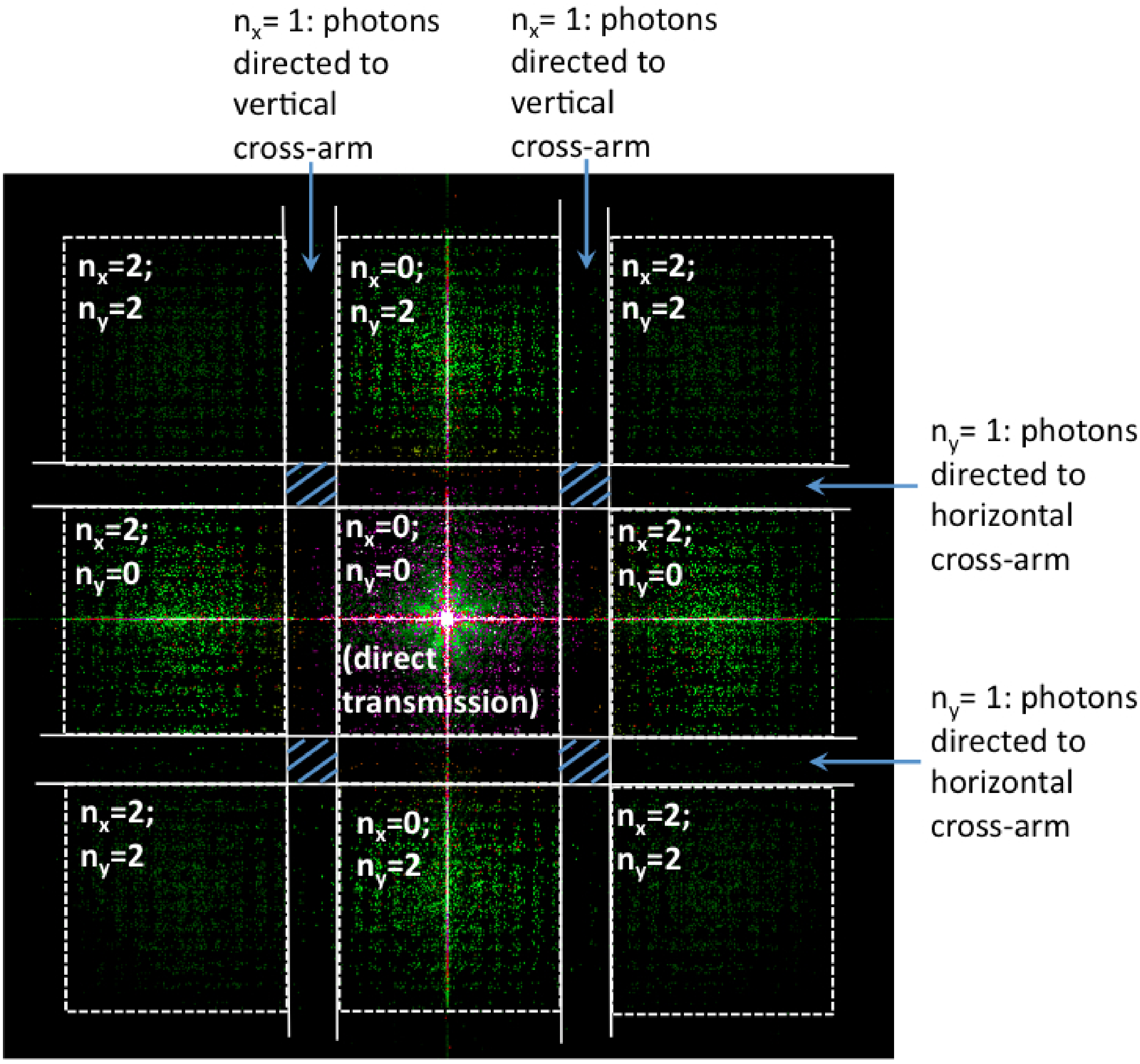

Figure 2.11 — *Simulated MCP optic PSF image showing the tiled appearance of the unfocused background. The number of reflections undergone by photons is shown in each 'tile': these values are for the background photons only, those making up the central focus and cross-arms follow the reflection rules given in Table 2.1. The areas shaded blue correspond to regions of the optic where photons are directed toward the central focus of the PSF.*

Table 2.1 — *Contributions of n_x and n_y to the PSF of an MCP optic [Angel, 1979]*

n_x	n_y	focused?	contribution to PSF
odd	odd	in both x and y directions	central spot
odd	even	in x direction only	vertical cross-arm
even	odd	in y direction only	horizontal cross-arm
even	even	no	unfocused background

2.1.1.4 Resolution

The resolution of a microchannel plate optic is a function of the angle subtended by a channel at the focal plane, so smaller pores provide higher resolution images. However, if the channels are too narrow, this resolution is degraded due to increased diffraction effects. This problem is particularly acute for longer wavelength UV imaging and is considered in more detail in Chapter 3.

Other factors that can degrade the resolution of an MCP optic include misalignments between the channels introduced at the stacking stages of manufacture, and distortions of the channels arising from twisting in the drawing stages. If the optic is slumped, there is scope for more errors to be introduced. For example, channel shear between adjacent multifibres may occur, so the channels do not all point towards the centre of curvature of the slumped optic.

The resolution of the image produced by the optic will also be affected by the resolution of the detector (see Section 2.3.1.3). With all these factors considered, it is unlikely that an image obtained by an MCP optic will achieve the theoretical resolution limit for an ideal optic.

2.1.1.5 Effective area

The effective area of an MCP optic is defined as the area of the impinging beam which contains the same number of counts as lie within the central focus of the image in a fixed exposure time [Martindale, 2008]. Hence, the effective area determines the count rate at the detector when imaging a source of a given intensity. The effective area varies with a number of parameters, including the wavelength of incident light, the slump radius of the MCP and the presence of any reflective coatings on the interior walls of the MCP channels. Another important factor is the channel length to diameter ratio (*L:D*). If the ratio is too small, the reflecting area is small and rays must travel at a large angle relative to the channel to hit the walls; hence most rays pass straight through unfocused, and those that do encounter a wall are likely to be incident at an angle greater than the critical angle and thus will be absorbed. However, if the ratio is too large then more rays will undergo multiple reflections within a channel, increasing the proportion of rays that are absorbed rather than focused. When determining the optimum effective area of an MCP optic, the energy of the incident radiation must also be considered, as more energetic radiation has a narrower critical angle, reducing the effective area. A full consideration of the effective area of an MCP optic can be found in Chapter 3.

2.1.1.6 Field of view

The field of view (FOV) of a square, slumped MCP optic is given by $\tan^{-1}$[(side length of optic)/R_{MCP}]. Hence, the field of view can be maximised by using large plates or a small slump radius. For an MCP with a fixed channel width, a decrease in slump radius (and hence focal length) results in a degradation in angular resolution (see Section 2.1.1.4). The key trade-off between large or tightly slumped MCPs is therefore a trade-off between angular resolution and instrument size: for a fixed channel width, a large MCP optic will provide better resolution but in a bulkier instrument than a smaller MCP slumped to a smaller radius of curvature to provide the same FOV. Additionally, MCPs are delicate, so there is a limit to how small their radius of curvature can be, as the amount of pressure applied by the mandrel during the slumping process increases as the required radius decreases. Large plates are also more likely to break than small ones, so large field of views are built up by ‘tiling’ MCPs with the same slump radius, such that they approximate one large optic. This is the method that will be used to provide the required FOV for JUDE in the case of an MCP optic solution for the instrument.

2.1.2 Instrument Overview

The MCP optic design for JUDE under development at the University of Leicester has its heritage in the *BepiColombo* Mercury Imaging X-Ray Spectrometer (MIXS) instrument [Fraser et al., 2010], and the Wide Field Auroral Imager (WFAI), a UV imager developed to allow large scale images of the Earth’s aurora to be obtained from lower orbits than those generally required [Bannister et al., 2007].

The proposed MCP optic design for JUDE is shown in Figure 2.12. The MCPs used would have a radius of curvature, R_{MCP}, of 1500 mm, implying a focal length of 750 mm. The baseline design uses four 40 $\times$ 40 mm^2 square-packed MCPs, arranged in a 2 $\times$ 2 array, providing a total geometrical optic area of 64 cm^2. The field of view of the optic array is thus $3.06° \times 3.06°$. Although this is smaller than the $6° \times 6°$ FOV specified in the science requirements (Chapter 1 Table 1.4), analysis of this design can be used to assess the suitability of microchannel plate optics in general for a high-resolution UV imager in the jovian system.

The channel walls are uncoated in the preliminary optical design. MCP optics are radiation hard, but a 45° mirror may be introduced into the design so that energetic particles from the jovian environment do not have a direct line-of-sight path to the detector. The detector is slumped to half the radius of the curvature of the optic, in order to fit the curved focal plane (see Section 2.3.1.5), and will have an active area of width 40 mm.

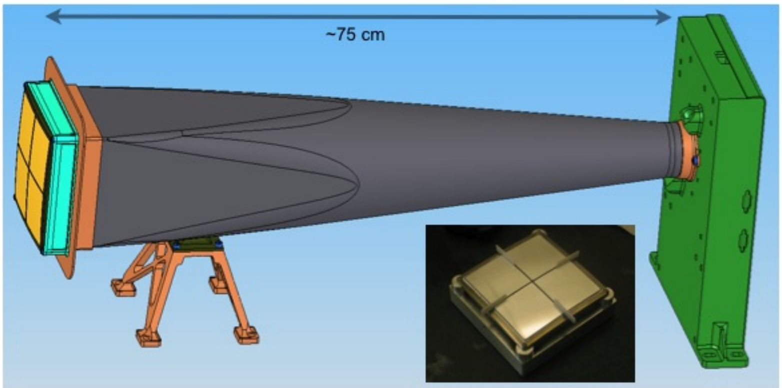

Figure 2.12 — *A preliminary design for the JUDE instrument. Inset: An example of a* 2×2 *MCP optic array with supporting structure (produced for the BepiColombo Mercury Imaging X-ray Spectrometer (MIXS))[Bunce et al., 2009].*

2.1.3 Advantages

The MCP optic design is lightweight and its ability to cope with radiation makes it well-suited for the Jupiter system. Its field of view can be easily modified to match science requirements by increasing the number of MCPs in the optic array. The resolution of the imager can be optimised by considering different channel widths in the optics, to fulfil the requirement to resolve the satellite footprint aurora at Jupiter. However, the reflective optics described in Section 2.2 are able to provide higher resolution images. The MCP optic design contains no moving parts, reducing both the risk of failure and the power requirement for the instrument.

2.1.4 Potential problems

The most critical issue with the MCP optic design is the potential for diffraction effects to severely degrade the resolution of the images. The diffraction is proportional to the observation wavelength, λ, divided by the channel width, D, so it can be limited by using wider channels, but this in itself will degrade the image resolution as the intrinsic MCP resolution is also determined by the angle subtended by a channel at the focal plane. A full simulation of the effect of diffraction on images obtained by the MCP optic version of JUDE can be found in Chapter 3.

2.2 Design option 2: conventional reflective optics

The second optical design option for JUDE uses reflective UV optics developed at the Centre Spatial de Liège (CSL), Belgium. CSL has extensive experience of UV optics, having provided mirrors for the Ultraviolet Spectrograph (UVS) on *JUNO* and the *IMAGE* FUV Spectral Imager (SI), along with various other instruments.

2.2.1 Overview

The reflective optic design for JUDE is shown in Figure 2.13 and consists of a two-mirror off-axis telescope with multilayer filter coatings deposited on the mirror surfaces to allow bandpass selection. The filter bandpass will be optimised to provide the required imaging capabilities at both Jupiter and Ganymede– this will be discussed in Chapter 5. The imager in this configuration has a focal length of 380 mm, and is able to image a field of view of 6° on a circular detector with an active area of diameter 40 mm. The resolution of the optics can be assessed by producing a spot diagram for the system. In the paraxial approximation,[2] the imaging quality of an optical system is ideal, but in practice aberrations in the system degrade its imaging quality [Lindlein and Leuchs, 2007]. The RMS spot size is a measure of image quality, determined by tracing rays through the optical system and measuring the spread of rays around the image centroid position.

The RMS spot size required to match the JUDE angular resolution requirement can be calculated by considering the distance subtended by that angle at the focal length of the instrument. The angular resolution required to resolve features of 100 km within Jupiter's

[2]an approximation to the full equations of optics that is valid in the limit of small angles from the optical axis

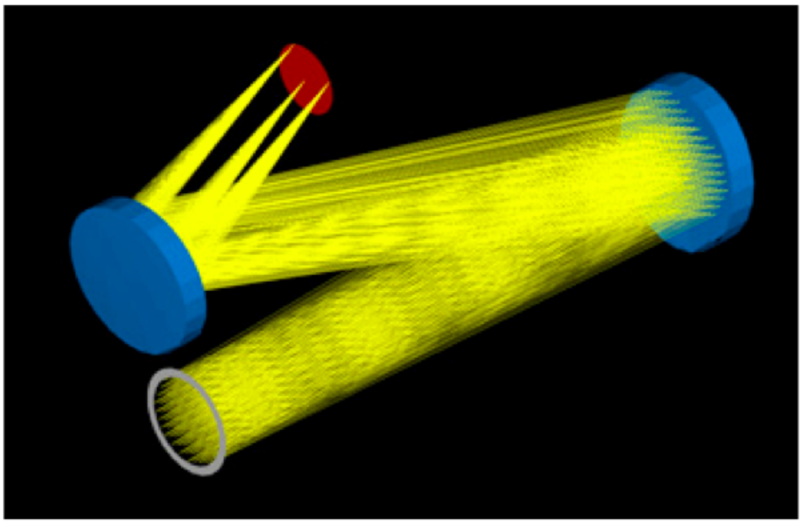

Figure 2.13 — *The Liège optical design for JUDE: Light enters through the aperture (grey ring) and is focused onto the focal plane detector (red circle) by a conic primary mirror of 90 mm diameter and an aspheric secondary mirror of 85 mm diameter (blue objects) [Bannister et al., 2010].*

aurora from a distance of 15 R_J (Ganymede's orbital semi-major axis) is 19.3 arcseconds. This angle subtends a distance of 36 μm at a focal length of 380 mm. Hence, the RMS spot size of the Liège optics should be less than 36 μm to allow the resolution of sub-100 km features at Jupiter from Ganymede orbit.

Figure 2.14 is a plot showing the variation in spot size over the focal plane of the Liège optics, from preliminary ray tracing investigations at CSL. The RMS is below 36 μm at all positions except one, at one edge of the field, showing that the optics are capable of matching the JUDE resolution requirement. Further optimisation of the optics may decrease the edge of field resolution further.

2.2.2 Advantages

As the filters in the Liège design are deposited on the mirrors, there is no need for moving parts. The suggested design has been shown to match the required angular resolution,

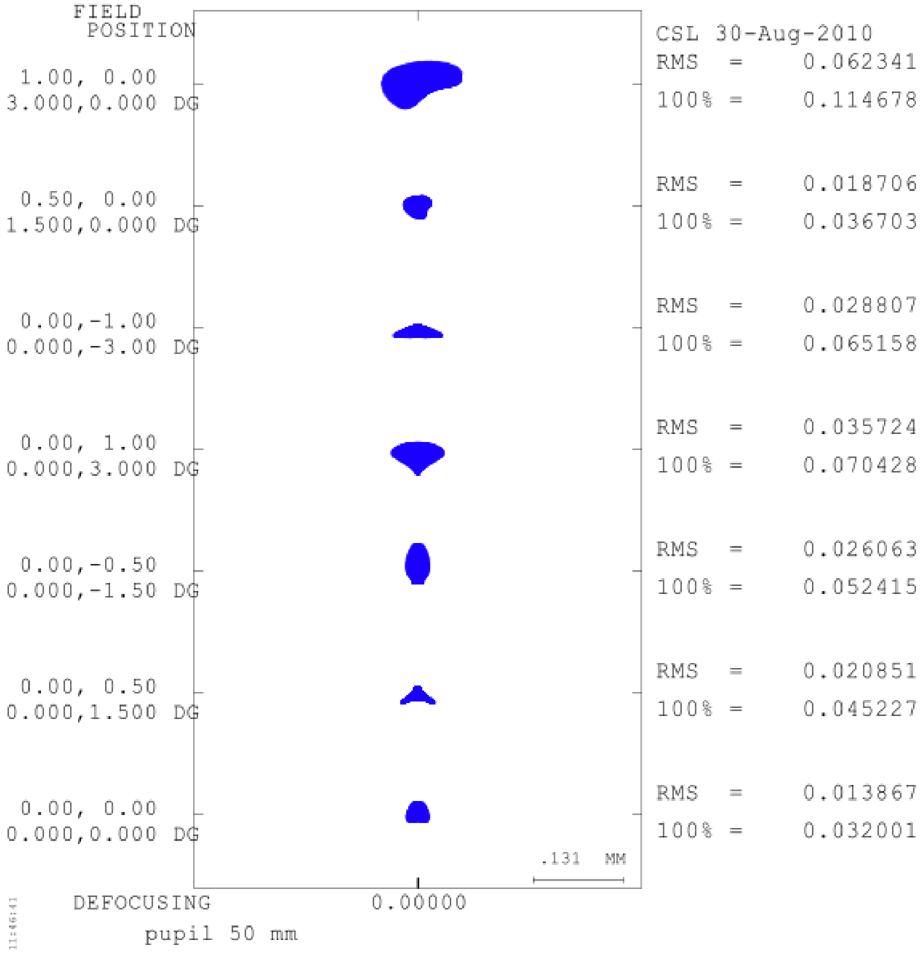

Figure 2.14 — *Spot diagram showing the variation in spot size over the focal plane of the Liège optics [Bannister et al., 2010]. The RMS size in mm is given to the right of each image.*

and the 6° field of view required to view the disk of Jupiter from Ganymede orbit is also achievable. The effects of diffraction on the resolution of the reflective optics should not be as critical as those likely to be experienced by the MCP optics.

2.2.3 Disadvantages

Although still relatively compact, the reflective optics have a greater mass than the MCP optics. A comparison of the predicted mass and volume of the two design options is shown in Table 2.2. The MCP optic mass is based on the preliminary mass estimate of a similar instrument proposed for the *KuaFu* mission [KuaFu Payload Definition Group, 2007] (see Chapter 4, Section 4.1), and the volume estimate is based on the preliminary focal length of the instrument[3] and the optic area required to provide a 6° FOV. The reflective optic estimates of both mass and volume are preliminary values provided for a JUDE design and development report [Bannister et al., 2010].

Table 2.2 — *Preliminary mass and volume estimates for the two proposed JUDE designs.*

	MCP optic design	Reflective optic design
Mass	$\sim$6 kg	$<$10 kg
Volume	160×160×750 mm	400×200×100 mm

Radiation can change the properties of UV filters and coatings, although CSLs experience of producing UV mirrors for *JUNO* should mean that the performance of similar optics in the jovian environment has already been considered to some extent.

2.3 Baseline instrument design

The initial instrument studies presented in this thesis will consider an MCP optic design, with an MCP detector and a novel capacitive readout anode. The detector and readout design are described below.

[3] assuming an MCP optic with a radius of curvature of 1500 mm

2.3.1 MCP detector

MCP detectors are electron multipliers (see Figure 2.15). A particle or photon incident on the internal wall of a channel excites an electron via the photoelectric or Auger effect[4], releasing it into the channel. The electron is accelerated down the channel by a large voltage applied across the plate, until it collides with another section of the channel wall and liberates more electrons which undergo the same process. In this manner a detectable charge cloud is formed at the base of the MCP, the centre of which gives the impact position of the impinging particle responsible for the signal [Fraser, 1989].

The gain of an MCP detector– that is, the number of electrons exiting the end of a channel for each initial electron released from the channel wall– can be controlled by altering the magnitude of the accelerating voltage applied across the plate. MCP detectors that are used for single photon counting are operated in a high gain configuration. In this mode, the magnitude of the charge cloud that results from a channel firing stabilises or 'saturates'. This is due to the electron avalanche within the channel depleting the wall of charge, establishing an electric field in the opposite orientation to that due to the applied voltage. The wall charge field reduces the electron collision energies, limiting the size of the charge cloud produced. The saturation of the charge cloud can be seen in the pulse height distribution (PHD)[5] measured at the detector. The PHD for a high gain ($\sim 10^6$–10^8) detector is a narrow peak, as the saturation means all signals detected will carry a similar charge. This narrow PHD allows noise counts to be more easily rejected and also narrows the dynamic range that must be dealt with by the readout electronics [Fraser, 1989].

A second characteristic PHD shape for an MCP detector is an exponential decay of frequency with increasing charge. This is expected for noise counts, since the noise event

[4]The Auger effect: a photon or particle incident on an atom excites an electron from the atoms inner shell. As another electron falls to fill the gap left, energy is released and transferred to another electron, which is ejected from the atom. This electron is called an Auger electron.

[5]A PHD is a frequency distribution of the amount of charge contained within each pulse exiting the MCP detector.

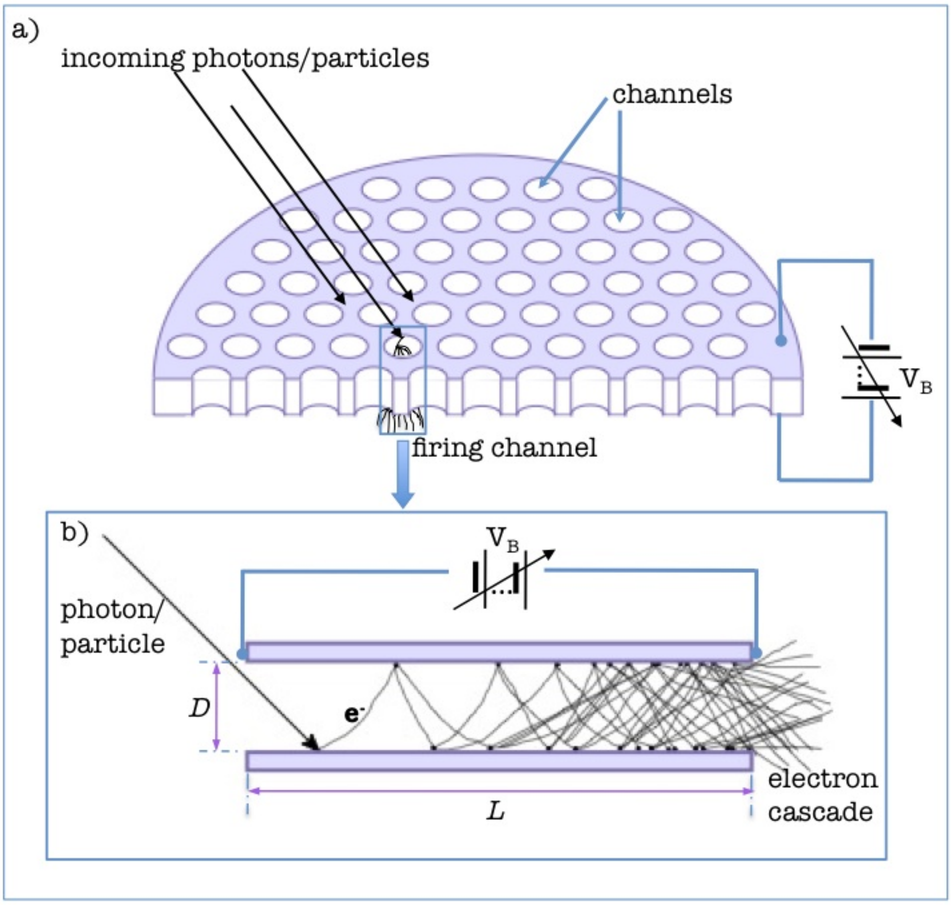

Figure 2.15 — *a) Operation of an MCP detector. Electrodes are deposited on each face of the MCP and a bias voltage, V_B, applied between them. The channel walls possess a semiconducting surface, from which electrons are emitted after photon/particle impact. b) Close up of a single firing channel, showing how the electron avalanche is produced.*

may be generated at any point along the channel length. The exponential decay shape is also seen in PHDs obtained by MCP detectors with low bias voltage, and indicates a lack of pulse saturation.

2.3.1.1 Multiple-MCP detector configurations

When a single MCP detector is run in high gain mode, the expected narrow PHD peak is often not seen, as the large applied voltage causes ion feedback in the plate. MCP detectors are operated at pressures below $\sim 10^{-5}$ Torr, but any gas molecules remaining in a channel can become ionised by electron impact during the detector operation, and can move back up the channel, initiating further electron cascades. These are seen as a high-charge tail in the PHD.

In order to avoid ion feedback, detectors are made up of a number of MCPs in series. The most common detector geometry is the chevron configuration (see Figure 2.16), which consists of two MCP stages with their channels tilted in different directions, and a small ($\sim$0.1 mm) gap between the two plates. The channel angle is created during MCP manufacture by slicing the plates at the required angle (see Section 2.1.1.1). The change in channel direction between the two stages of the detector limits the possible paths taken by any ions created, so they impact the channel wall lower down in the detector and with insufficient energy to create another electron avalanche.

2.3.1.2 Quantum efficiency

The quantum efficiency (QE) of a bare lead-glass MCP at X-ray and extreme UV energies is low, around 1–10%, and varies strongly with photon energy (falling sharply as the energy increases) and with the angle of incidence of the radiation on the detector (e.g. Timothy and Bybee [1975], Fraser [1982]). In order to increase the detection efficiency, a photocathode layer may be deposited on the front of the plate and on the channel walls. Typical photocathode materials include MgF_2 (previously used for X-ray astronomy

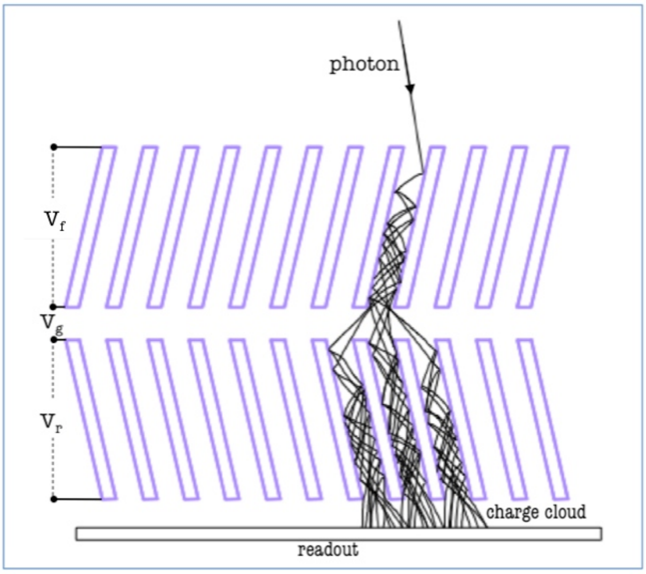

Figure 2.16 — *An MCP detector consisting of two MCPs in a chevron configuration. The voltages V_f, V_g and V_r (f=front MCP; g=gap between MCPs; r=rear MCP) can be controlled to provide the required gain. The potential difference across the gap between the front and rear MCPs is used to constrain the spreading of the charge cloud between the two plates.*

instruments including the *Einstein* High Resolution Imager), CsI (efficient in both the soft X-ray and 2–2000 Å bands; e.g. Martin and Bowyer [1982], Fraser and Pearson [1984]), CsBr (more efficient than CsI in the 20–100 Å region; Fraser et al. [1987]) and KBr (more efficient than CsI in some parts of the 44–1500 Å region; Siegmund et al. [1987]).

Another method of increasing the quantum efficiency of an MCP detector is to place a mesh, or 'repeller grid' in front of it. Ordinarily, any electrons ejected through interactions between radiation and the front surface of an MCP between its channels are lost. A mesh with a potential less negative than that at the plate surface will direct these electrons back towards the MCP, where they may enter a channel and produce a signal. This method does, however, have a detrimental effect on the spatial resolution achieved by the detector, as the electron will not necessarily enter the nearest channel to its site of ejection [Fraser, 1989].

2.3.1.3 Resolution

The spatial resolution of an MCP detector is fundamentally limited by the width of the channels. Other factors affecting the resolution include noise within the signal processing electronics chain and readout. If a repeller grid has been used to increase the detector count rate, the displacement this causes between the electron ejection site and the channel the electron goes on to enter will also contribute to a widening of the FWHM spatial resolution. In detectors with multiple MCPs, any transverse movement of the charge cloud in the inter-plate gap will decrease the resolution, as will any transverse movement of the cloud in the gap between the detector and readout [Fraser, 1989].

Although MCP detectors can offer good spatial resolution, a detector in saturated mode has no energy resolution, as the applied voltage is deliberately set such that all events result in the largest charge cloud possible. Therefore, any spectral selection within the JUDE imager will take place before the incoming radiation reaches the detector.

2.3.1.4 Dark noise

Traditionally, MCPs contain $\sim$5% potassium by weight, some of which is in the form of the beta emitter ^{40}K. This radioactive portion of the potassium is responsible for $>$90% of the dark noise seen in a standard MCP detector (which is evenly distributed across the plate with a density of $\sim$0.2 counts cm^{-2} s^{-1}) [Fraser, 1989]. However, it is now possible to obtain low noise plates, produced without potassium (or rubidium, which can also cause counts through radioactive decay: see e.g. Lees et al. [1997]).

2.3.1.5 Slumping

If an MCP detector is to be used with a slumped MCP optic, it must also be slumped to match the curved focal plane produced by the optics. The detector, placed at a distance of [R_{MCP}(optic)]/2 from the optic, should be slumped to half the radius of curvature of the optic so that the images it produces are not distorted, as shown in Figure 2.17.

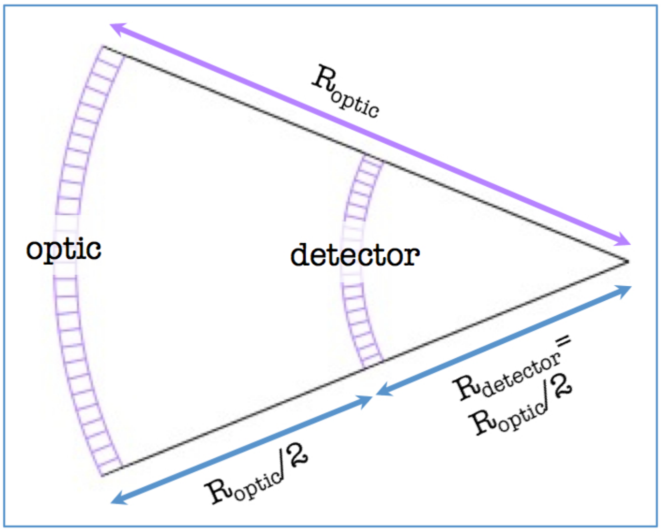

Figure 2.17 — *A slumped optic should be used in conjunction with a detector slumped to match the curvature of its focal plane, to avoid distortions in the image. Since the focal length of an MCP optic is half its radius of curvature, the detector should be slumped to $R_{optic}/2$.*

2.3.2 Signal readout method

2.3.2.1 Resistive anode readout

Resistive anode readouts are commonly used behind MCP detectors to encode the position of events at the detector. A typical readout consists of a square resistive sheet with electrodes either on each edge or each corner, as in Figure 2.18. The charge cloud exiting the detector spreads out through the plate, and its originating position in both the x and y dimensions can be determined either by zero-cross timing or amplitude ratio encoding at pairs of electrodes that lie on the relevant axis. For the anodes shown in Figure 2.18, the amplitude ratios in each direction, $Q_{x,y}$, are given by

$$Q_x = \frac{V_1}{(V_1 + V_3)}; \qquad Q_y = \frac{V_2}{(V_2 + V_4)}, \tag{2.4}$$

where $V_{1,2,3,4}$ are the peak electrode output voltages. The zero-crossing time difference in each direction, $T_{x,y}$ is given by

$$T_x = t_3 - t_1; \qquad T_y = t_4 - t_2, \tag{2.5}$$

where $t_{1,2,3,4}$ are the zero-cross times of the electrode output voltages [Fraser, 1989].

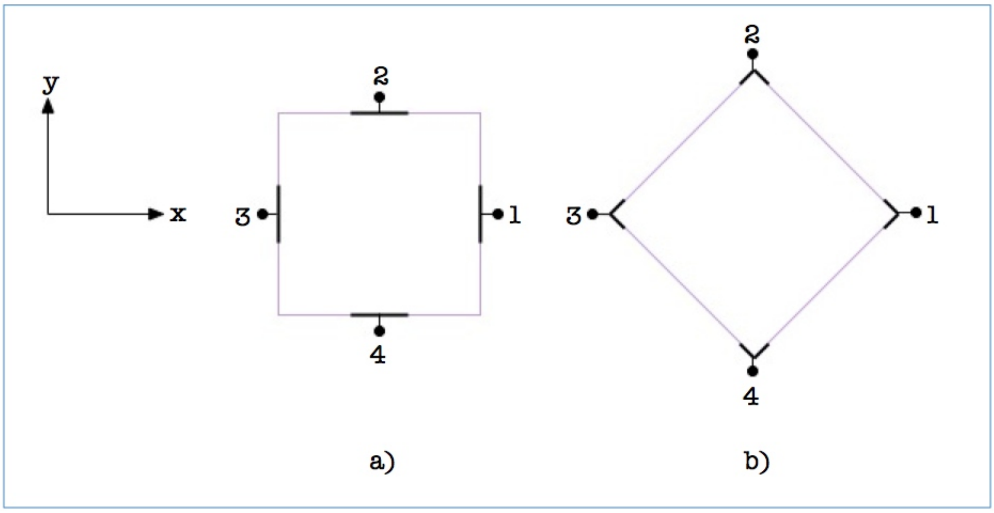

Figure 2.18 — *The two possible square anode designs for which the position of an incident charge cloud can be calculated using Equations 2.4 and 2.5. The numbered features along the edges (a) or at the corners (b) represent electrodes.*

Resistive anode readouts are not divided into pixels in the same way that CCDs, for example, are. However, images produced using a resistive anode readout will have an apparent pixel size corresponding to the limiting resolution of the electronics readout chain.

2.3.2.2 Novel capacitive readout

Rather than a standard resistive anode readout, JUDE will use a novel capacitive readout, called the Capacitive Division Image Readout (C-DIR). This device is made up of three elements. The first element encountered by electrons exiting the back MCP of the detector is a resistive layer, which localises the charge cloud. The resistive layer is deposited onto a dielectric substrate. This element capacitively couples the signal at the resistive layer to the third element: an array of capacitively coupled electrodes. The signal is capacitively distributed through the array to four readout nodes. The charge induced on each of the readout nodes is measured electronically and this provides information about the location of the photon interaction that produced the detected charge cloud, using the same algorithms as for a standard resistive anode [Lapington, 2012].

Resistive anodes suffer from Johnson noise, which is due to the thermal excitation of electrons within a resistor, and limits spatial resolution. C-DIR is purely capacitive and therefore its resolution will not be degraded by Johnson noise. Resistive anodes also suffer from partition noise, which is essentially Poisson noise introduced by physically dividing the electrons that make up the charge cloud among the four readout electrodes. With C-DIR, the charge signal is capacitively induced in the electrode array, rather than the cloud being physically divided, so the partition noise is not seen [Lapington, 2012]. The performance of a resistive anode device is fundamentally limited by a trade-off between spatial resolution and event rate caused by the competing characteristics of signal-to-noise ratio and pulse processing time, and dominated by Johnson noise [Lapington, 2012]. Jupiter's UV auroral emissions can peak at several MR (see Chapter 1, Section 1.2.2), so high count rates are expected at the JUDE detector. Additionally, stringent spatial resolution requirements have been set for JUDE in order to match the performance of *HST* STIS. The decrease in spatial resolution with raised count rates in the resistive anode design therefore makes these devices unsuitable for JUDE.

The purely capacitive nature of C-DIR leads to very fast time response by the detector/electronics and minimises noise, leading to excellent spatial resolution. This device is therefore much better suited for JUDE than a traditional resistive anode readout.

2.3.3 Spectral selection

The baseline JUDE design is a broadband imager, sensitive to radiation over the $\sim$90-160 nm waveband. This will cover many of the Lyman and Werner band emissions from

Jupiter's aurora (see Chapter 1, Section 1.2.1), but for observations of Ganymede, there is a need to isolate the 130.4 nm and 135.6 nm O I emissions, as the relative intensities of these emissions can provide information about the moons atmosphere (see Chapter 1, Section 1.3). This spectral selection will be performed with a combination of filters, either just before the detector or deposited on a mirror at 45° to the optical axis. The mirror would also have the purpose of preventing any high energy electrons or ions in Jupiter's radiation belts from having a direct path to the detector, where they would produce noise counts.

2.3.4 Operating Modes

The large difference in intensity between Jupiter's and Ganymede's auroral emissions ($\sim$ a few hundred R at Ganymede vs. up to a several MR at Jupiter- see Chapter 1) will lead to vastly different count rates at the JUDE detector when imaging each object (estimates of the expected count rates are discussed in Chapter 3, Section 3.4). Hence, it is envisioned that the detector will operate in two principal target modes, one optimised for the high count rate produced by Jupiter's emissions, and one optimised for low count rate observations of Ganymede. It will be possible to switch between these modes by reconfiguring the JUDE signal processing electronics.

Within the two principal modes, there is the possibility of selecting one of a number of planned data modes. The choice of data mode will depend on the spacecraft resources (e.g. data storage and telemetry bandwidth) available and the spatial and temporal requirements for specific observations. The potential modes available are summarised below:

- Consecutive image sequences: regular images of the entire JUDE field of view at the full resolution to provide a general view of auroral emissions.
- Increased time resolution: images obtained at shorter intervals with decreased resolution, to provide sequences of images revealing auroral structures with high

temporal variability.

- Keogram mode: recordings of auroral intensity as a function of time along a cut through the auroral region, providing information about auroral location and intensity with lower storage and telemetry requirements than full images.
- Image burst mode, raw data samples: images will generally be integrated and compressed before being sent to Earth, but in this mode raw samples will be returned to provide detailed information on the detailed dynamics of small scale auroral structures. The raw samples can also be used to check that the on-board data processing is performing as expected.
- Keogram burst mode: keograms made up of raw data samples, allowing the high temporal resolution auroral variability along a cut through the imager focal plane to be investigated.
- Safe mode: the imager is powered down during periods of intense particle background or when spacecraft resources are needed elsewhere.

2.4 Summary

JUDE is an ultraviolet imager designed with the *JUICE* mission in mind. Two different designs were considered for the JUDE optics, one based on microchannel plates, and one using more conventional reflective UV optics. Each design has different strengths: a large field of view is easier to obtain using MCPs, but the reflective optics are capable of providing higher resolution images. The reflective optics are based on a design that was developed for use in the *JUNO* UVS instrument, and hence have a higher technology readiness level, although a programme of MCP optic development for the *BepiColombo* MIXS instrument is also well under way. It was decided that the MCP optic design would be explored first, as their low mass, relatively low cost, radiation tolerance and wide field of view make them an attractive option for the imager. However, there is a possibility that an MCP optic will not be able to achieve the spatial resolution specified in the science requirements, mainly due to diffraction of UV light through the optic's narrow pores.

At the JUDE focal plane, an MCP detector will convert the focused UV light into clouds of electrons. Each charge cloud will then impact a novel readout, where its dispersion through an array of capacitively coupled electrodes to four readout anodes will allow the x and y coordinates of its impact position, and hence the coordinates of the original photon impact, to be determined. In this way an image can be built up.

Chapter 3 describes the results of ray-tracing models of the MCP-based JUDE instruments response to various sources, which will allow a decision to be made as to the suitability of this design for *JUICE*. Complimentary, supporting laboratory experiments are described in Chapter 4.

CHAPTER 3

Modelling the JUDE instrument response (MCP optic design)

This chapter describes models designed to simulate the expected JUDE instrument response using the MCP optic design. A large portion of the work uses Sequential Ray Tracing (SRT) code using the Q data analysis system produced by R. Willingale, Department of Physics and Astronomy, University of Leicester [Willingale, 2009]. The code allows the user to specify the design and composition of the optic used and its position, as well as the size and position of the detector, and characteristics of the source illumination. It is also possible to include apertures, lenses, gratings etc., and deformations of optical elements may be included to allow for imperfections introduced during manufacture of these objects. The detector type is not specified within the model, but it may be planar or spherically curved. SRT modelling has been used to investigate the UV imager's response to both point and extended sources (Section 3.1) and to provide estimates of the JUDE optics effective area at UV wavelengths (Section 3.3). The effective area calculations have been used to determine likely count rates at the detector when imaging both Ganymede and Jupiter (Section 3.4).

3.1 SRT images obtained with the JUDE instrument (MCP optic configuration)

3.1.1 Imaging a point source

SRT templates created by J. Pearson (University of Leicester) for work on the *BepiColombo* Mercury Imaging X-Ray Spectrometer (MIXS) instrument were modified to include parameters specific to the square pack, square-pore MCP optics used in the JUDE imager design, as summarised in Table 3.1. The templates were used to trace 900000 rays with energies of 12.4 eV (λ = 100 nm) though the preliminary imager design, with the code using the form of the Fresnel equations derived by Henke [1972] (see Appendix A) to model the reflection of the rays at the optic channel walls. The imager's optic array was modelled as one large MCP optic rather than 4 individual segments, and the MCP was assumed to be free from any deformations. The supporting structures shown in Figure 2.12 (Chapter 2) were not included within the model, although it is possible to define such structures using Q (see Section 3.3.5 for a discussion of the effect of the supporting structure on the images produced). A point source at infinity was specified, and the resulting image can be seen in Figure 3.1, showing the characteristic cruxiform-shaped point spread function (PSF) produced by all square-pored MCP optics, as described in Section 2.1.1.3. The resolution of the imager may be estimated from the full width at half maximum (FWHM) of the central focus of the PSF. This was found to be $\sim$0.5 mm, which corresponds to an angular resolution of $\sim$2.3 arcminutes[1]. If the instrument was used to image the jovian aurora from Ganymede orbit, which has a semi-major axis of 1070400 km [Weiss, 2004] ($\sim$15R_J), the spatial resolution at Jupiter

[1]The angular resolution is the angle subtended by the FWHM of the PSF at the detector-optic distance: $\tan^{-1}\frac{0.5}{750} = 0.038° = 2.3\text{arcmin}$

would be ∼668 km. The theoretical resolution of the optic, given by the angle subtended by a channel at the focal plane, is ∼0.73 arcminutes, which implies a spatial resolution of ∼214 km when imaging Jupiter from Ganymede orbit (this is greater than the goal specified Table 1.4, but can potentially be reduced by using narrower channels– see Section 3.2 for a discussion of the optimum channel width).

Table 3.1 — *Summary of JUDE parameters used in SRT models.*

Channel pitch (centre-to-centre)	180 μm
Channel width	160 μm
Channel wall thickness	20 μm
MCP coating	SiO_2 (bare glass)
R_{MCP}	1500 mm
Channel length:diameter ratio	50:1
MCP optic size	80×80 mm^2
Detector size	40×40 mm^2
Detector radius of curvature	750 mm
Detector–optic distance	750 mm (optic focal length)

As the resolution of the PSF in Figure 3.1 was larger than expected, further images were produced using optics with different pore sizes, to investigate the relationship between this parameter and the FWHM of the resultant images. A plot of the angular resolution of an MCP optic as a function of pore size, both theoretical and as measured from SRT images, is shown in Figure 3.2 for an MCP with a focal length of 0.75 m. When the FWHM was initially measured for various pore sizes, the results were consistently larger than expected (compare the red line in Figure 3.2, the measured FWHM, to the green line, the theoretical MCP resolution). The focal plane of a slumped MCP optic has a depth: parallel rays hitting different parts of the same wall are reflected at the same angle, which means their path lengths to the optical axis will differ (see Figure 3.3). Hence, although the detector in the SRT model was placed at the theoretical focal plane of the optic, not all of the rays reaching the detector will have been properly focused. SRT includes an option to automatically adjust the position of the detector to minimise the FWHM. The FWHM measurements were repeated with this option selected, and the

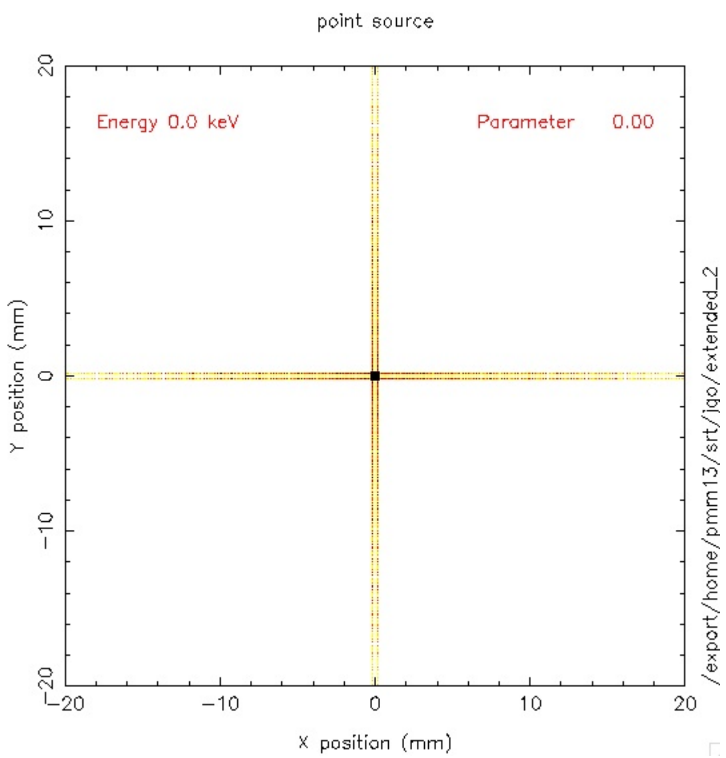

Figure 3.1 — *SRT image of a point source at infinity, produced using JUDE parameters (Table 3.1).*

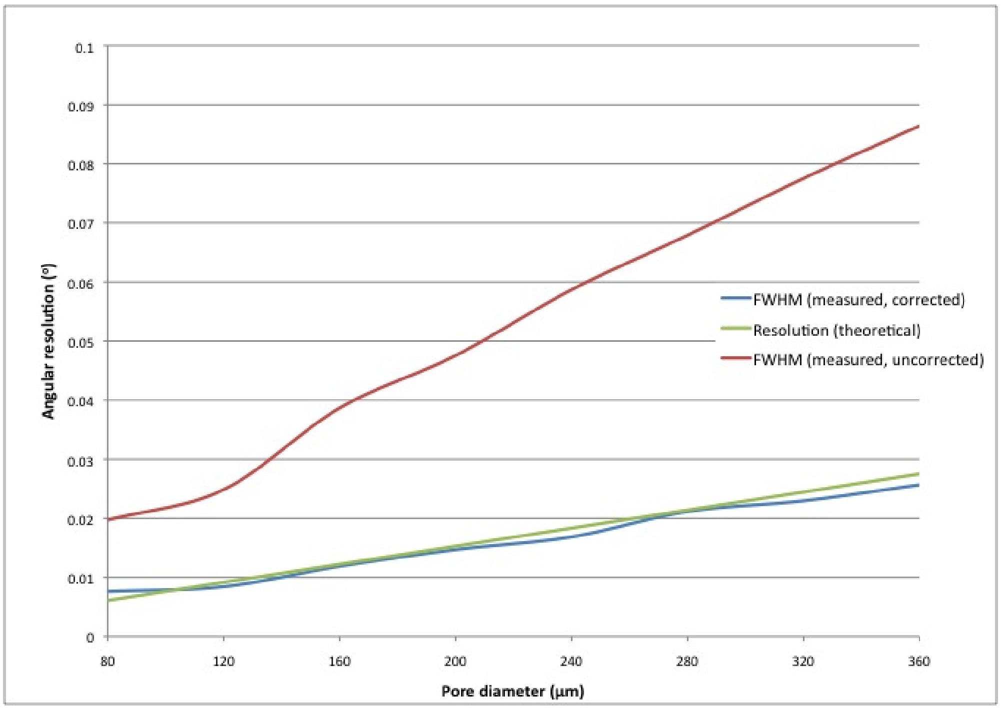

Figure 3.2 — *Angular resolution as a function of pore size for a plate with 0.75 m focal length: comparison of theoretical calculations (green line) with SRT results (blue and red lines). Both the L:D and channel width:wall thickness ratios were kept constant in the SRT models. The red line corresponds to the initial SRT results, while the blue line shows the FWHM measured when automatic focal length adjustment was implemented.*

results are plotted in Figure 3.2 (blue line). The adjustment feature was found to shift the detector position from 750 mm to 753.94 mm. The resolution values measured at the adjusted focal position were very close to the theoretical values. The slight differences may be due to the relatively large pixels of the images (0.05 mm$\approx$0.0038°, so the largest adjusted FWHM measured was under 7 pixels wide) limiting the accuracy at which the FWHM calculation could be performed.

The $\sim$4 mm adjustment in focal position performed by the SRT model may correspond to the position in each channel at which reflection is most likely to occur. Photons are focused by areas of the optic in which the channel angle is steepest relative to the optical axis, i.e. towards the corners of the optic (see Section 3.3.5). At steep channel angles and

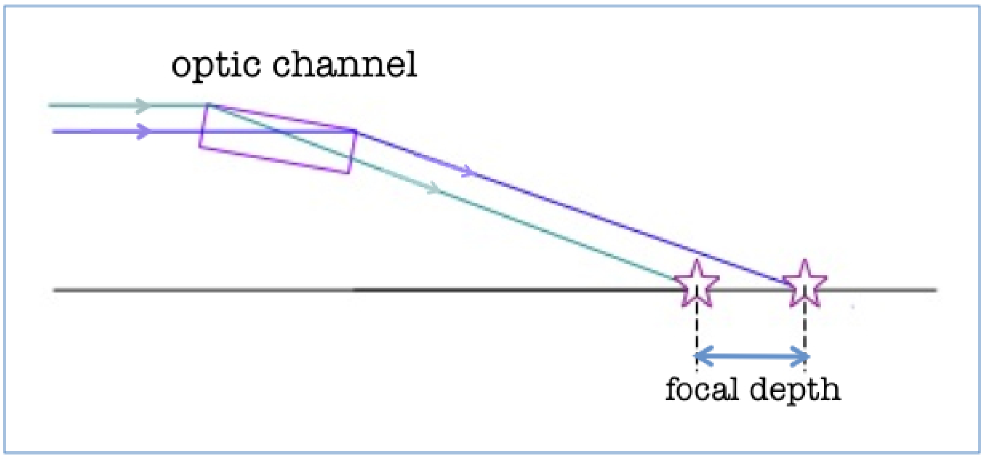

Figure 3.3 — *A slumped MCP optic focusing two parallel rays. The rays hit at different depths within the channel, but are reflected through the same angle. Hence, they reach the optical axis at different points.*

high L:D ratios, rays undergoing reflection near the entrance of a channel will experience a second reflection on the opposite wall and hence be unfocused when they reach the focal plane (see Figure 3.4), so there is a minimum depth at which photons should impact for focusing to occur. Similarly, there is a maximum depth for reflection as shown in Figure 3.4.

The minimum and maximum focusing depth for each channel in an MCP depend on the channel angle and channel width. For the 80 × 80 mm^2 JUDE optic, with $R_{MCP} = 1500$ mm, the maximum channel angle (at the edges of the optic) is $\sin^{-1}\frac{40}{1500} = 1.528°$. The maximum focusing depth for channels of width 160 μm is then $x_{max} = \frac{0.16}{\tan 1.528} = 5.998$ mm. The minimum focal depth is $x_{min} = \text{channel length} - x_{max}$. Hence at the edges of the 8 mm channel length optic in the original SRT model, the most likely channel impact depth for focusing is between 2.002 mm and 5.998 mm, with a corresponding shift in the focal length of the optic expected.

Further models of the JUDE optic were run for a variety of channel lengths, with all other parameters remaining identical to the initial model. In each case the automatic focal plane adjustment was selected, and the adjusted detector position recorded. The

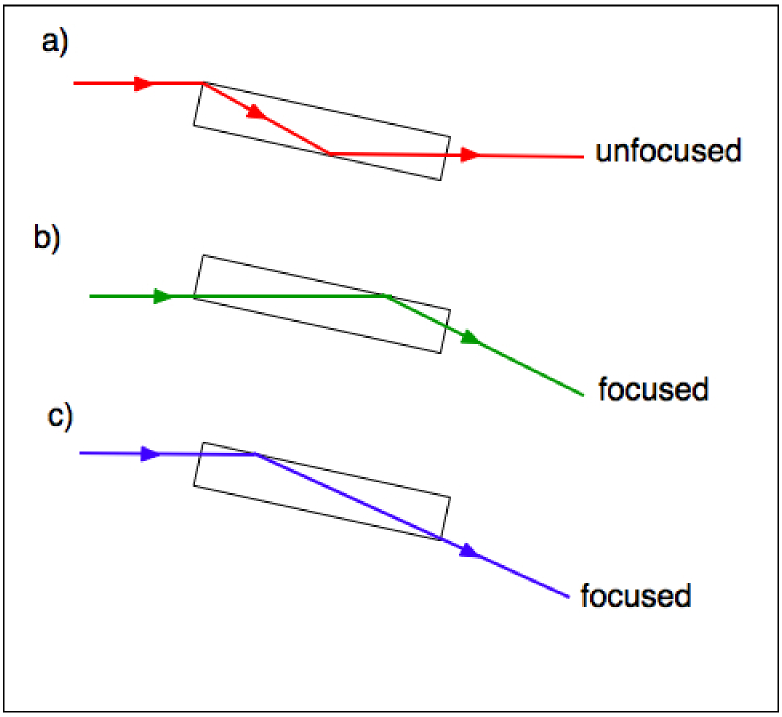

Figure 3.4 — *The effect of impact position of a photon in a tilted MCP optic channel. a) Rays impacting too near to the channel entrance undergo a second reflection further down the channel and become unfocused. b) Maximum impact depth for a single reflection in each axis. c) Minimum impact depth for a single reflection in each axis.*

predicted maximum and minimum impact depths at the optic edges were calculated for each case and added to the nominal 750 mm focal length to give the expected maximum and minimum focal lengths after adjustment. The results of these tests are shown in Table 3.2.

In each model, the measured focal length was found to lie within the expected range. This suggests that the automatic focal length adjustment is reflecting a real shift in the MCP focus rather than a problem with the code used. Further models with different optic parameters are required to confirm this, and to determine whether the exact shift is predictable.

Table 3.2 — *Comparison of predicted minimum and maximum focal lengths for MCPs with varying channel length and the measured focal length from SRT models.*

Channel length (mm)	f_{SRT} (mm)	x_{min}(mm)	x_{max} (mm)	f_{min} (mm)	f_{max} (mm)
6.0	753.4328	0.002	5.998	750.002	755.998
6.5	753.5667	0.502	5.998	750.502	755.998
7.0	753.6181	1.002	5.998	751.002	755.998
7.5	753.7782	1.502	5.998	751.502	755.998
8.0	753.9428	2.002	5.998	752.002	755.998
8.5	754.1136	2.502	5.998	752.502	755.998
9.0	754.3002	3.002	5.998	753.002	755.998
9.5	754.4865	3.502	5.998	753.502	755.998
10.0	754.6672	4.002	5.998	754.002	755.998

3.1.2 Imaging an extended source

SRT images of a point source are useful to gain an understanding of the intrinsic resolution of an instrument but, since JUDE is an imager, it is vital to investigate the instrument response to extended sources. Q allows for extended sources with the use of a deformation matrix which spreads a point source either to an angular distribution of pixels as in the case of an infinite source, or to a distribution over a certain plane at some distance from the optic, as specified by the user, for a source at finite distance. A source deformation matrix was added to the code used in Section 3.1.1, with all instrument parameters remaining as specified in Table 3.1. The radius of the source was gradually increased, and the cruxiform point spread function was seen to increase in size until, above a source radius of 1.5°, the field of view of the detector was entirely covered by the central focus of the cross, with none of the arms visible (see Figure 3.5). Since this source size corresponds to the instrument field of view (Section 2.1.2), the results show how the imager would respond to uniform illumination across the entire optic.

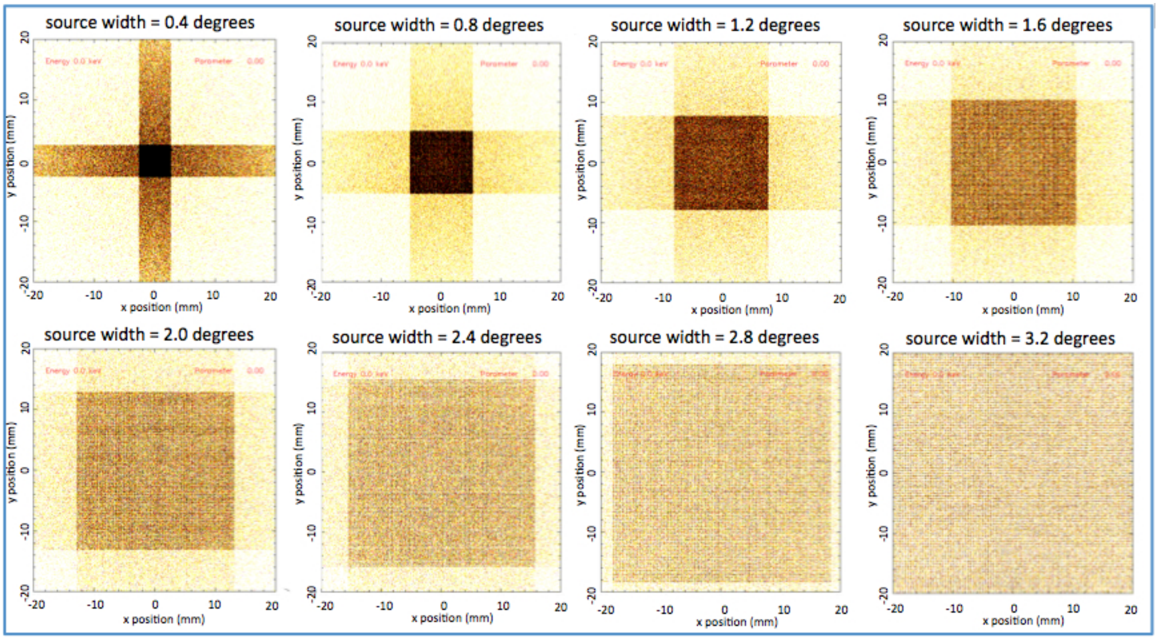

Figure 3.5 — *SRT images of extended sources as viewed by the UV imager. The source radius increases from 0.2° in the top left image to 1.6° in the bottom right image, in steps of 0.2°. The source diameter is shown above each image. 900000 rays with E = 12.4 eV were traced for each image.*

3.1.3 Modelling more realistic sources

Once a source deformation matrix has been set up in SRT, it can be manipulated to model sources of different shapes (an example of the code that can be modified to produce different source shapes can be found in Appendix B). Some examples of the modelled JUDE response to various sources are shown in Figure 3.6. It is also possible to upload an image to SRT and create a source deformation from this. The code is only able to cope with black and white images, which correspond to sources of uniform intensity. In order to test the JUDE response to a realistic source, an image of Ganymede's aurora was produced.

Feldman et al. [2000] provide images of Ganymede at 135.6 nm from *HST* STIS observations (one of these images is shown in panel (a) of Figure 3.7: this is a composite of of two STIS images with IDs o53k01010 and o53k01020). The original STIS files

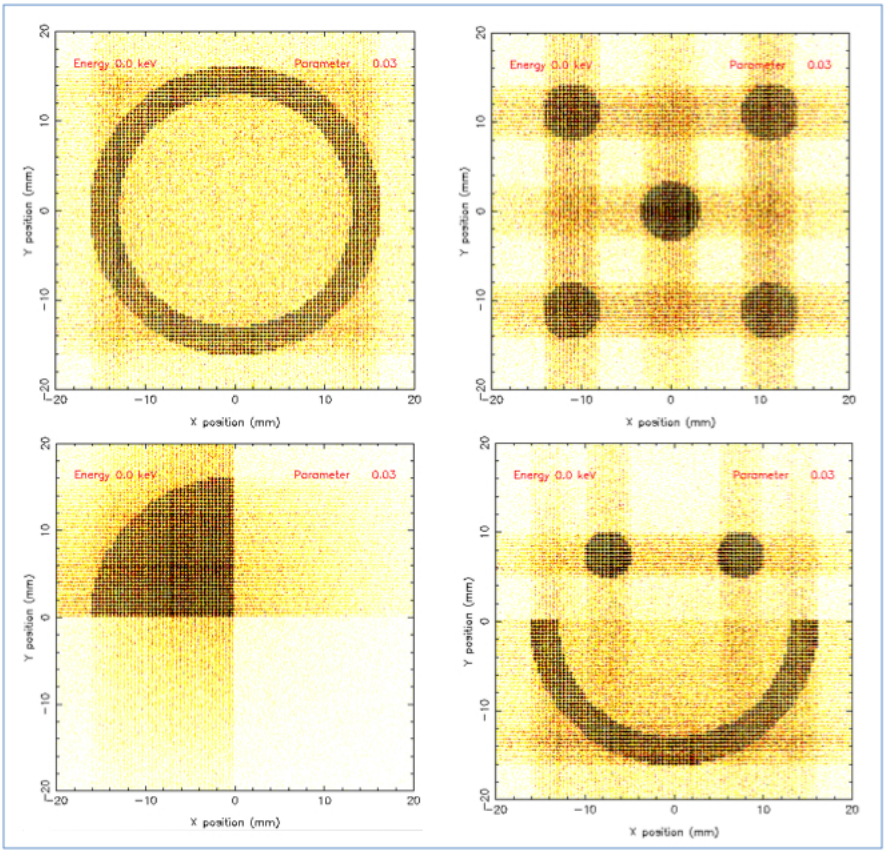

Figure 3.6 — *SRT images of sources of various shapes: top left – source is a ring of radius 1.0 to 1.25 degrees; top right – source is five circles, each of radius 0.25 degrees; bottom left – source is a quarter of a circle of radius 1.25 degrees; bottom right – source is half a ring of radius 1.0 to 1.25 degrees, plus two circles of radius 0.2 degrees. 900000 rays with E = 12.4 eV were traced for each image.*

from which these images were extracted (image IDs o53k01010 – o53k01080) were obtained from the *HST* data archive.[2] The data files contain spatial information in the y direction and a combination of spatial and spectral information in the x direction (see Chapter 5, Section 5.3.1), with each pixel along the x axis corresponding to a specific wavelength. Images at 135.6 nm were extracted from the STIS flat-fielded counts ('flt') files to match the Feldman images. These files each contained a clear horizontal stripe of signal, showing the position of Ganymede within the slit (see Figure 5.8 in Chapter 5). The eight image files were taken over 4 *HST* orbits, and each pair of images was

[2]http://archive.stsci.edu/cgi-bin/dataset_lookup

summed to allow for temporal variability over each orbit. The data extraction was performed by determining which column of pixels in each summed image corresponded to a wavelength of 135.6 nm and then extracting an 82×82 pixel [3] region centred on the pixel within this column that lay in the centre of the stripe of signal from Ganymede.

The extracted images were rotated to align jovian north along the vertical axis and Ganymede's disk overplotted, using information from the STIS file headers and the JPL HORIZONS solar system data and ephemeris computation service[4] (panel (b) of Figure 3.7). The reflected solar background was then subtracted from the newly extracted images (panel (c) of the Figure 3.7– see Chapter 5 for a detailed description of the solar subtraction). The resultant images of Ganymede's aurora were converted to black and white and used as source deformation matrices in SRT. An example of a ray traced image of Ganymede filling the field of view of JUDE is shown in panel d) of Figure 3.7.

The results shown in Figures 3.6 and 3.7 are promising, as the shape of the source is clear in each image– the background from the cross arms seen surrounding each feature is not overwhelming. However, in regions of the images where the cross-arms from various sources overlap, the background intensity rises (this is visible in the top right panel of Figure 3.6). This may lead to difficulty in source recovery from images containing a number of emission sources. The problem of deconvolving the cruxiform PSF from images obtained with MCP optics has not yet been solved, although Peele [2001] has attempted to address the issue, and concluded that source recovery is possible.

Although SRT cannot represent sources of spatially varying intensity, the response of JUDE to such sources may be approximated by co-adding SRT images, each representing a plane of fixed intensity. Figure 3.8 shows the result of an attempt to do this. As before, a black and white image of Ganymede's aurora was extracted from *HST* STIS files, but this time the image was saved four times, with the upper intensity threshold set to a different level each time so that progressively fewer pixels were selected (see Figure

[3] 82×82 pixels = 2" $\times$ 2": the slit used for the observations had a width of 2" and Ganymede had a diameter of 1.71" as seen from Earth at the time of the observations [Feldman et al., 2000].

[4] http://ssd.jpl.nasa.gov/horizons.cgi#top

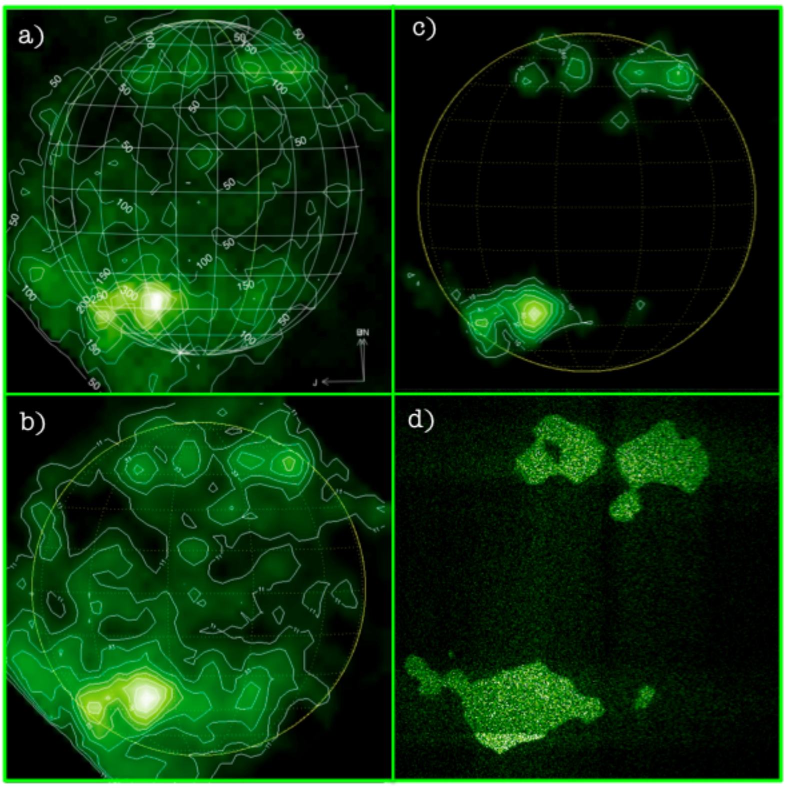

Figure 3.7 — *a) An image of Ganymede at 135.6 nm from [Feldman et al., 2000]. b) The same, but extracted from the original STIS files downloaded from the HST data archive during the work for this thesis. c) As panel b but with the contribution from reflected sunlight subtracted. d) The ray-traced image produced by using c (minus the grid and contours) as a source deformation. The brightest regions in each image represent the most intense emissions (up to ∼350 R in the original images before solar extraction). SRT does not accept sources with spatially varying intensity, hence the flat appearance of image (d).*

3.9). The four images were traced in SRT and the SRT images added together to produce the approximated source of varying spatial intensity.

The general shape of the aurora is still visible in the upper half of the summation, but the cross-arms from the small, bright region in the bottom left outshine some of the fainter features in the lower half. The brightness of this area, however, is overestimated. The thresholds of the constituent images were set so that there was an equal change in intensity between each successive image, so that the density of the rays would have

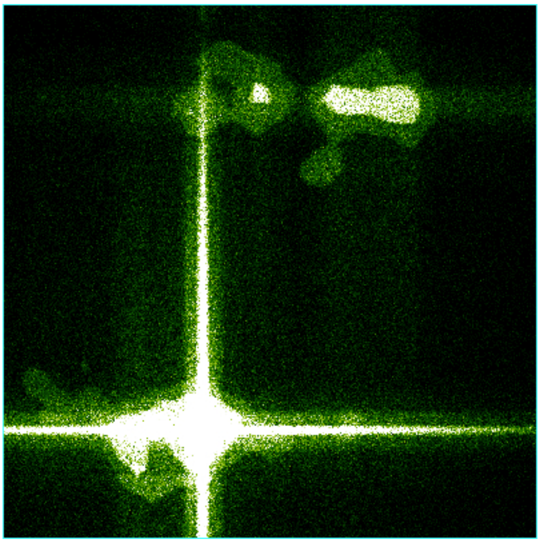

Figure 3.8 — *Sum of four SRT images of Ganymede's aurora with different thresholds. This image gives an approximation of JUDE's response to a source with a large variation in intensity.*

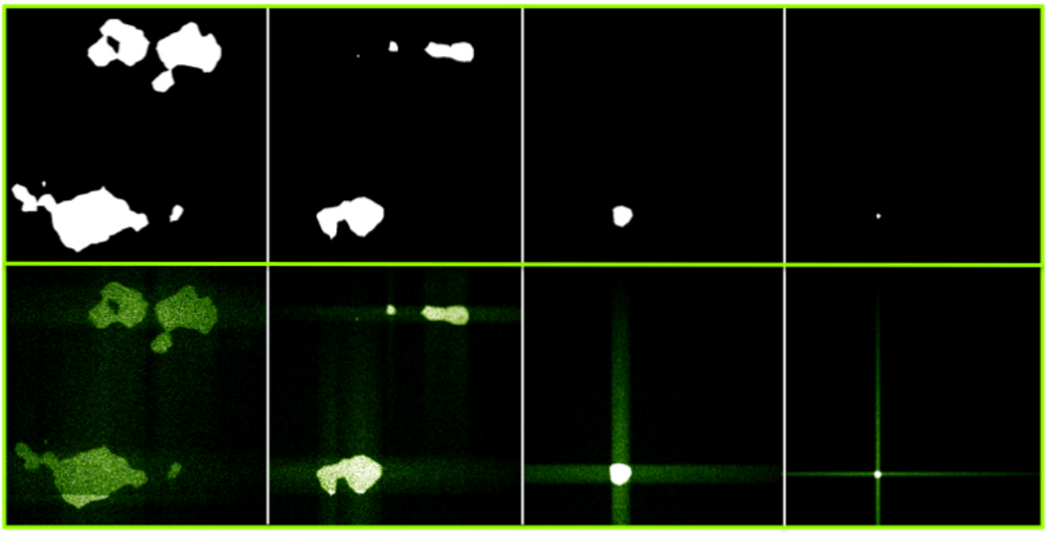

Figure 3.9 — *Top row: Black and white images of Ganymede's aurora, with the threshold set progressively higher moving towards the right. Bottom row: SRT images using the above images as source deformation matrices.*

to remain the same for each SRT run for the sum of the images to give a realistic representation of the intensity differences. However, the same number of rays was traced for each of the four constituent images, and these rays were spread only over the source deformation matrices (e.g. the white areas of the input images in Figure 3.9). Therefore, the image with the highest threshold (which produces the smallest source region) had a considerably higher ray density, and therefore intensity, than the lower threshold images. Although the intensity range is greater than the expected variation in Ganymede's 135.6 nm emissions, the result gives an insight into problems that may occur when imaging Jupiter. Jupiter's aurora is much more variable than Ganymede's, and bright cross-arms from the most intense emissions may make it difficult to resolve small, fainter emissions such as the satellite footprint aurora. Future studies will investigate the effectiveness of performing deconvolution to remove cross-arm features from JUDE images, thus restoring the imager's ability to resolve small or faint emission regions.

A composite image showing intensity variations more representative of Ganymede's aurora is shown in Figure 3.10. This was produced by normalising each of the four SRT images shown in Figure 3.9 so that the sum of intensity was the same for each one, and then summing the four normalised images. The most intense area in Figure 3.10 shows much fainter cross-arms than the same feature in Figure 3.8, implying that the recovery of fainter sources in the vicinity of the bright region should be easier for this smaller intensity variation, as expected.

3.2 Effects of diffraction on SRT results

As mentioned in Section 3.1.1, the current optic channel size provides a resolution of $\sim$0.73' ($\sim$214 km at Jupiter from Ganymede radius). The original science requirements for JUDE specified a spatial resolution goal of 100 km from a distance of 12 R_J [Bunce and Imager Consortium Members, 2009], the perijove distance in the orbit originally suggested for the Jupiter Ganymede Orbiter. This corresponds to an angular resolution of $\sim$0.007 degrees ($\sim$ 0.4'), which would require a 0.75 m focal length optic to have

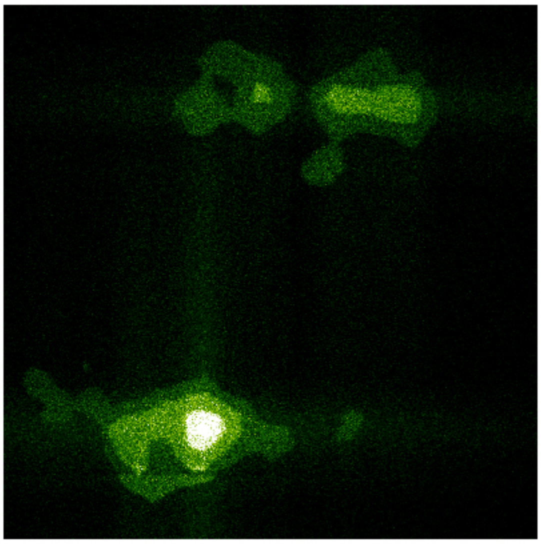

Figure 3.10 — *Sum of four normalised SRT images of Ganymede's aurora with different thresholds. This image gives an approximation of JUDE's response to a source of varying intensity.*

channel widths of $\sim$ 90 μm. However, narrower pores may actually degrade the optic resolution, as the magnitude of diffraction in the system increases.

The diffraction-limited angular resolution of an MCP optic, θ_{diff} (radians), at wavelength λ can be approximated by $\theta_{diff} \approx \lambda/D$, where *D* is the channel width [Angel, 1979]. Figure 3.11 provides a comparison between the diffraction limited resolution and the intrinsic plate resolution (the angle subtended by a channel at the focal plane) at different pore sizes, for plates with two different focal lengths. It can be seen that for the 160 μm pore, 0.75 m focal length plate used in the SRT models above, the diffraction limited resolution is $(0.049/0.012 \approx)$ 4 times worse than the intrinsic plate resolution at a wavelength of 135.6 nm (corresponding to O I emissions at Ganymede). This means that the spatial resolution when imaging Jupiter from Ganymede orbit would not be 214 km as calculated in Section 3.1.1, but around 850 km, with a consequent impact on the science that can be performed by the instrument. A pore size of 90 μm would introduce significantly larger diffraction effects to the UV images obtained by the instrument: the expected diffraction-limited resolution for 90 μm pores at 135.6 nm is 0.086°, corresponding to a spatial resolution of 1613 km when observing Jupiter from

Ganymede radius. Although the optic's focal length could be increased slightly so that wider pores could be used to provide the same resolution as 90 μm channels, it would be impractical to lengthen the instrument by much as payload space on *JUICE* is limited. In order for diffraction at 135.6 nm to be reduced to the 0.4' ($\approx 1.17\times10^{-4}$ rad) science requirement, an optic with pore width ($\lambda/\,\theta_{diff}$ =) 1.16 mm is required. The focal length of this optic should be chosen such that the angle subtended by each pore (e.g. the theoretical resolution limit of the optic) is also 0.4'. This would require a focal length of 9.94 m. Clearly this instrument configuration is unfeasible. If the MCP optic version of JUDE is to fly on *JUICE*, the science requirements must be reconsidered to determine the lowest resolution that will provide useful science, and the optic parameters will need to be optimised to try to match this resolution. A more accurate analysis of diffraction in the instrument, to confirm that the effect is as large as Figure 3.11 suggests, is described below.

3.2.1 Fraunhofer diffraction through a rectangular aperture

The effect of diffraction on JUDE images can be modelled by convolving SRT images with the diffraction pattern expected from a square aperture with side length equal to the width of the MCP optic pores. The appearance of the diffraction pattern of a distant point source is dependent on the distance between the plane containing the aperture and the screen on which the pattern is projected. If the screen is placed very close to the aperture plane, the image seen will be a recognisable image of the aperture with just slight fringing at the edges. As the screen is moved further away, the image will become more structured, as diffraction fringes become more prominent. This is Fresnel, or near-field, diffraction [Hecht, 2002]. As the screen is moved further still, the fringes will spread out more, until the observed pattern bears little resemblance to the shape of the aperture. Moving the screen after this point leads only to a change in the size of the pattern, and not its shape. This is Fraunhofer, or far-field, diffraction [Hecht, 2002].

For Fraunhofer diffraction to occur, the source as well as the screen must be far from the aperture plane. If the source is moved closer, the diffraction pattern will revert to

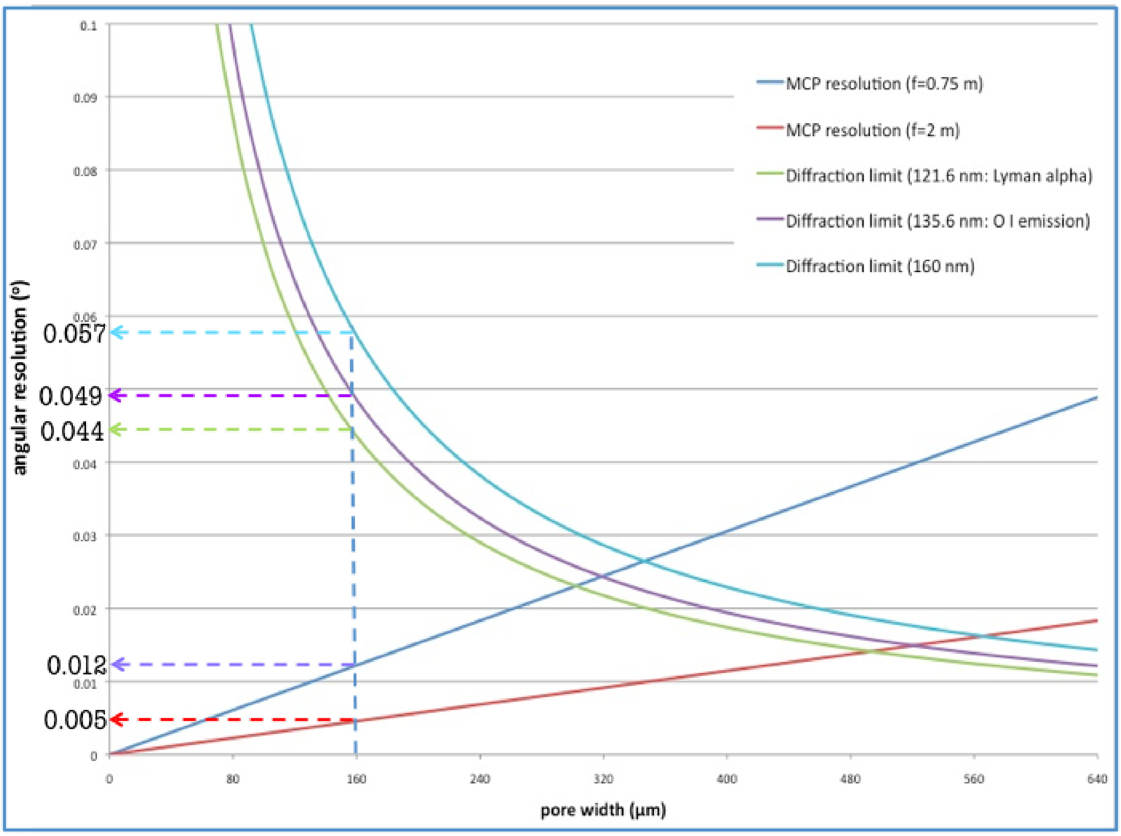

Figure 3.11 — *Angular resolution of the JUDE optics as a function of pore size. The theoretical resolution of plates with focal lengths of 2 m (red line) and 0.75 m (dark blue line) is compared to the diffraction-limited resolution at 121.6 nm (Lyman-α, responsible for Jupiter's brightest auroral emissions), 135.6 nm (corresponding to O I emissions at Ganymede) and 160 nm (towards the limit of JUDE's spectral sensitivity).*

a Fresnel pattern. Similarly, if the wavelength of light is decreased, Fresnel diffraction will be seen at larger distances than for longer wavelength diffraction. For Fraunhofer diffraction to occur at an aperture of greatest width of a, the following must be true:

$$R > a^2/\lambda, \tag{3.1}$$

where R is the distance either between the source and the aperture or the aperture and the screen, whichever is smaller [Hecht, 2002]. For JUDE, we have so far assumed values of R=750 mm, a=160 μm and λ≈130 nm. From Equation 3.1, $0.160^2/(130 \times 10^{-6})$ = 197 mm, so the diffraction pattern seen at the focal plane for this JUDE configuration

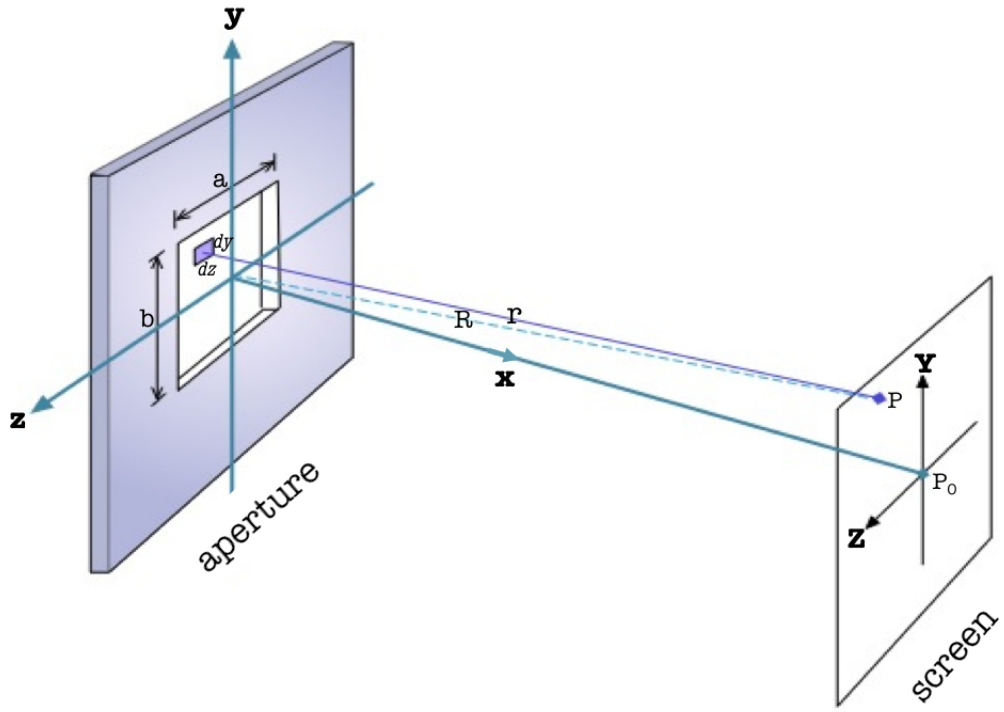

Figure 3.12 — *Rectangular aperture configuration, not to scale (r and R should be very large compared to the aperture dimensions). Based on Fig. 10.19 in [Hecht, 2002].*

will be a Fraunhofer pattern.

For a source, aperture and screen that are aligned along the X axis as in Figure 3.12, Fraunhofer diffraction through a rectangular aperture is governed by

$$I(Y,Z) = I(0)\left(\frac{\sin\alpha'}{\alpha'}\right)^2\left(\frac{\sin\beta'}{\beta'}\right)^2, \tag{3.2}$$

where $I(Y,Z)$ is the intensity of the light measured at a point on the screen with coordinates (Y,Z) and $I(0)$ is the intensity at (0,0) (see Appendix C for a derivation of Equation 3.2). α' and β' are given by

$$\alpha' = \frac{kaZ}{2R} \tag{3.3}$$

and

$$\beta' = \frac{kbY}{2R}, \tag{3.4}$$

with $k = 2\pi/\lambda$ and where R is the distance between the centre of the aperture (e.g. the point (0,0) in the aperture plane) and the point (X,Y) on the screen. a and b are the dimensions of the aperture in the z and y directions respectively.

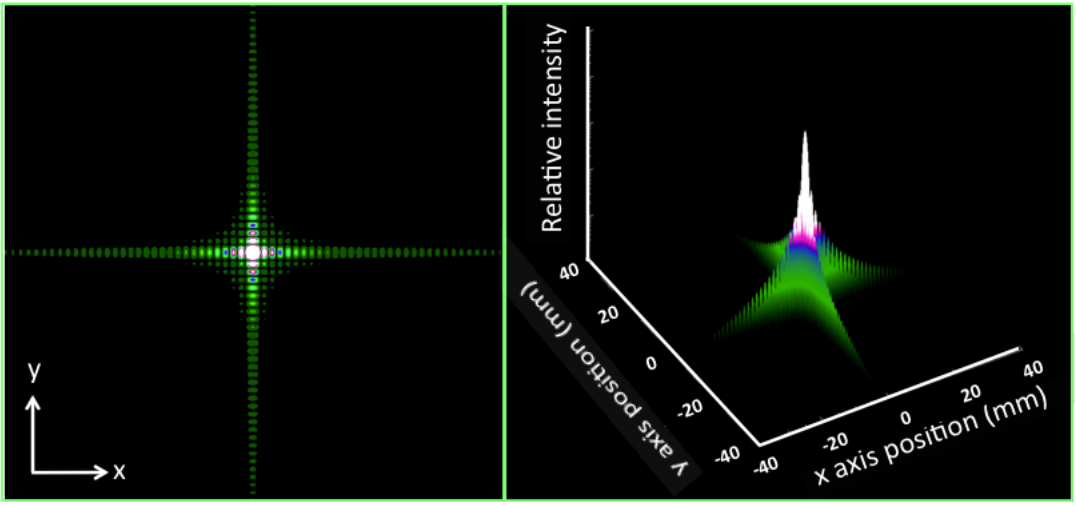

Figure 3.13 — *Left panel: diffraction pattern described by Equation* (3.2) *for the JUDE configuration (a=b=160 μm; R=750 mm, λ= 135.6 nm). Right panel: a projection of the diffraction pattern to better show the variation in intensity across the focal plane.*

Equation 3.2 was used to produce the diffraction pattern shown in Figure 3.13. This shows the expected result of viewing an distant source emitting light at 135.6 nm through a square aperture with a side length (a, b) of 160 μm (e.g. a single channel of the JUDE optic), with an aperture-focal plane distance (R) of 750 mm. The FWHM of the diffraction pattern was measured using the IDL function 'FullWid_HalfMax' [Varosi, 1994] and found to be 0.0428°, which is similar to the rough estimate of 0.049° made in Section 3.2 for 160 μm pores at 135.6 nm.

3.2.2 The effect of diffraction on the FWHM of a point source image

The diffraction pattern produced for Figure 3.13 was convolved with a JUDE SRT image of a point source at infinity, and the FWHM of the resultant image measured and compared with the FWHM of the original SRT image, in order to quantify the magnitude of diffraction experienced by the instrument. The two images are shown in Figure 3.14. The resolution of an image produced by an MCP optic is equivalent to the FWHM of the central focus. This was measured for the two images in Figure

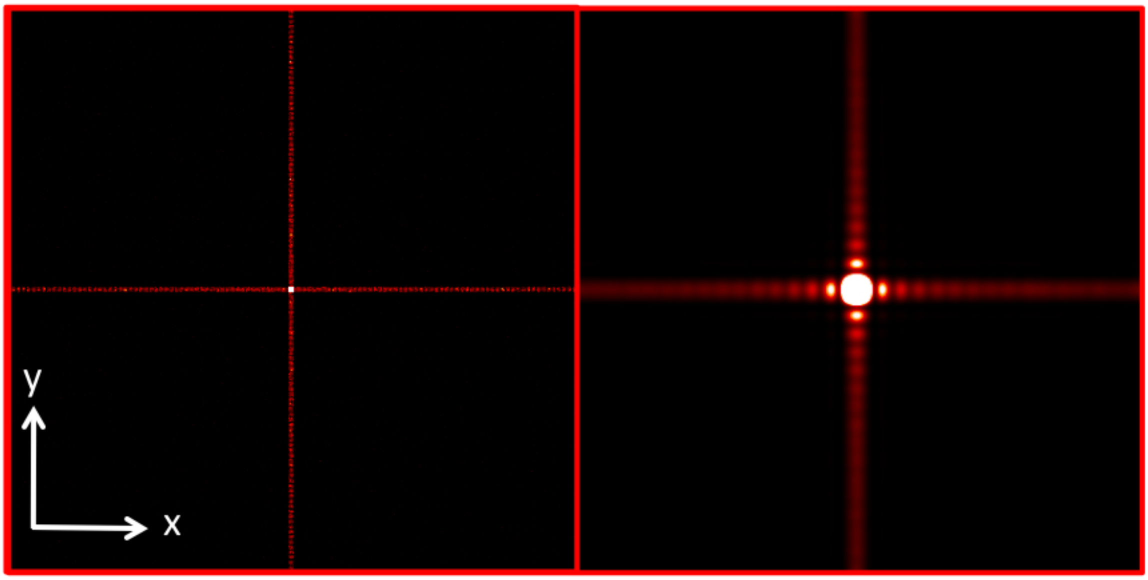

Figure 3.14 — *Left panel: SRT image of a point source focused by the JUDE MCP optic. Right panel: the same image convolved with the diffraction pattern seen in the left panel of Figure 3.13.*

3.14, using the 'FullWid_HalfMax' function. The FWHM measured for the initial SRT image was ∼3.14 pixels in the x direction and ∼3.13 pixels in the y direction. The pixel size was 0.05 mm in each direction, so the angle subtended by the pixel over the optic–detector distance was $\tan^{-1}(0.05/750)$ ≈0.23'. The FWHM therefore fits well with the expected ∼0.73' resolution of the optic (0.73/0.23≈3.17 pixels). The FWHM of the image after convolution with the diffraction pattern was approximately 11.55 pixels in each direction, or ∼2.64'. Hence the diffraction degraded the resolution of the image by a factor of ∼3.68. This is slightly better than the diffraction limit calculated for the same wavelength and pore length in Figure 3.11: $\theta_{diff} \approx \lambda/D \approx 8.59 \times 10^{-4} rad \approx 2.94'$. However, it is clearly large enough to make the requirement of a resolution of ∼100 km at Jupiter from 12 R_J unfeasible: the model suggests that the diffraction-limited spatial resolution from 12 R_J, for a 160 μm pore optic at 135.6 nm, would be ∼658 km.

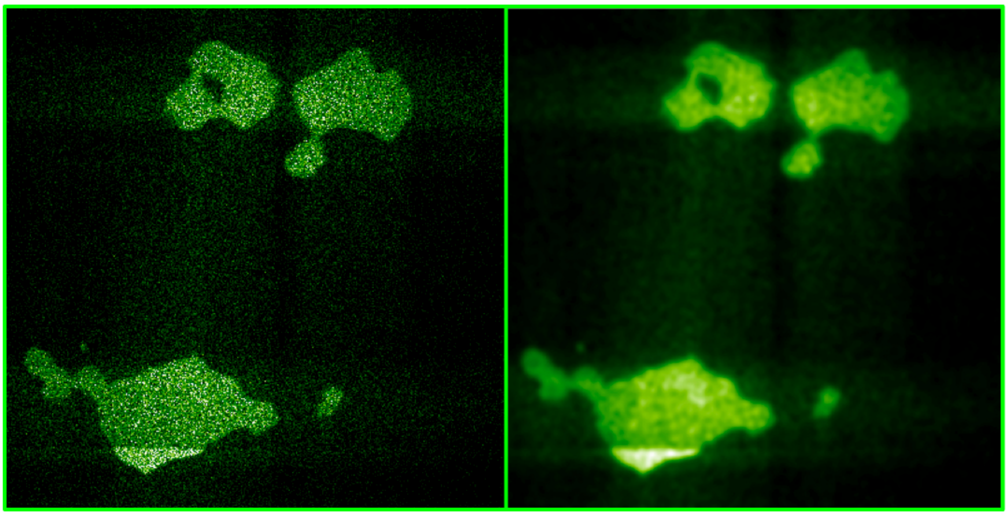

Figure 3.15 — *Left panel: SRT image of Ganymede's auroral emissions. Right panel: the same image convolved with the diffraction pattern from Figure 3.13.*

3.2.3 The effect of diffraction on an image of an extended source

The image of Ganymede shown in panel (d) of Figure 3.7 was used as the illumination source in SRT (as described in Section 3.1.3), and convolved with the diffraction pattern from Figure 3.13; the resulting image is shown in Figure 3.15. This image shows the effects of diffraction on an extended source produced by the JUDE MCP optics. The general shape of the emissions is preserved, but the image clearly shows the degrading effects of the optic. The varying-intensity image of Ganymede (Figure 3.8) was also convolved with the diffraction pattern, to give the image shown in the right panel of Figure 3.16. Again, the image is blurred by the addition of diffraction, and the bright region that was already overwhelming the fainter emissions in the lower half has been extended slightly and seems slightly intensified relative to the surrounding region. The extension of bright regions like this may make it difficult to recover any faint sources nearby; for example, at Jupiter, intense emissions from the main auroral oval may lead to difficulty in recovering faint polar emissions or the satellite footprints (see Chapter 1).

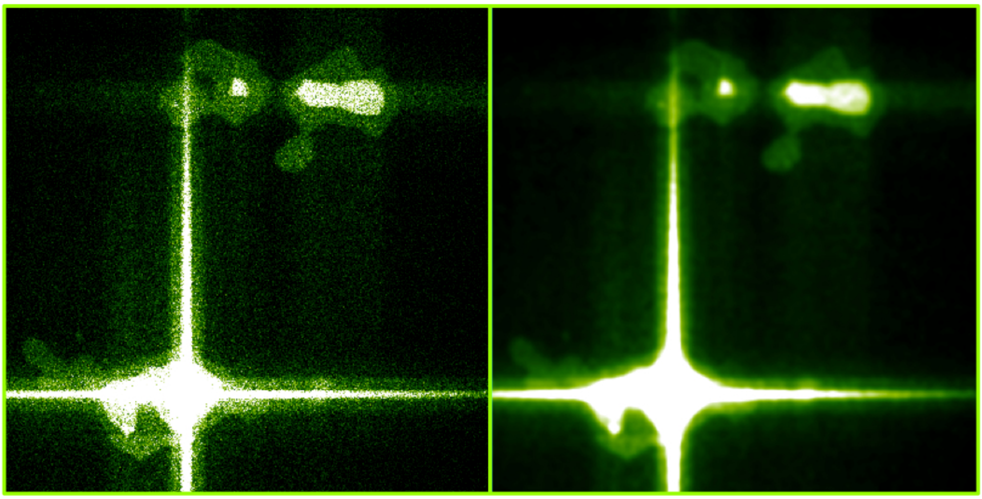

Figure 3.16 — *Left panel: Sum of four SRT images of Ganymede's auroral emissions, approximating the real variation in intensity seen in the moons emissions. Right panel: the same image convolved with the diffraction pattern from Figure 3.13.*

3.3 Effective Area of the JUDE MCP optics

3.3.1 Effective area as a function of energy

The effective area of the UV imager optics will determine the count rates at the detector when the instrument views sources of different intensities. The effective area of a slumped MCP optic is dependent on the energy of the photons encountering it, as shown in Figure 3.17, which was produced by modelling a point source at infinity. As the energy moves towards the hard X-ray region, the effective area decreases. This is because the critical angle for reflection of X-rays decreases as energy increases (Chapter 2, Equation 2.2), and so fewer rays are focused by channels towards the edges of the MCP, which are at larger angles relative to the incoming radiation.

The effective area plots within this section were generated with the standard reflectivity model used by the SRT code, assuming a perfect optic with no surface roughness on the channel walls. It was initially assumed that diffraction at the optic would not have a significant effect on the effective area (the code does not include diffraction effects), but a discussion of possible effects is given in Section 3.3.4. The SRT code is generally

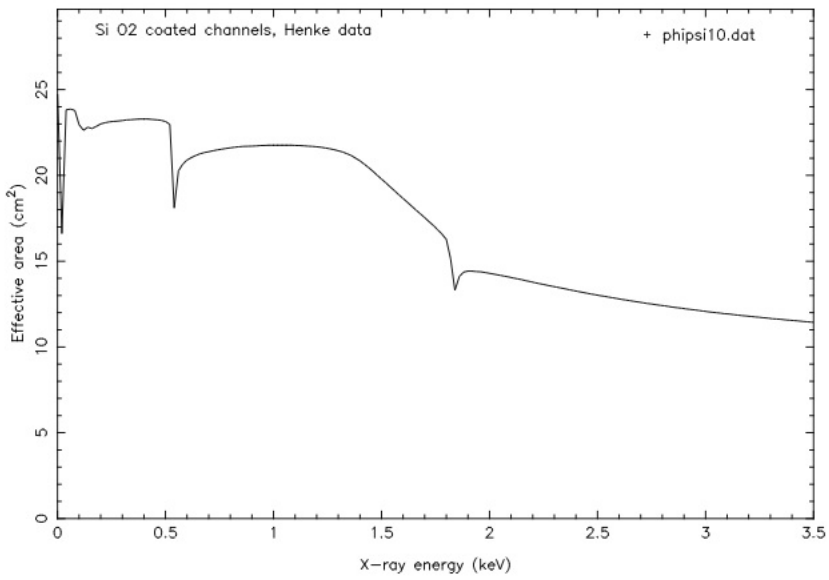

Figure 3.17 — *Relationship between effective area of MCP optic and energy of impinging photons, using Henke reflection data and an infinite point source (Optic parameters: pore width = 160 μm, pitch = 180 μm, L:D=20:1).*

used to model X-rays, and uses the semi-empirical atomic form (scattering) factor data collated by Henke et al. [1993]. The underlying assumption in using these data is that the optic material may be modelled as a collection of non-interacting atoms, so the code can combine information about the optical properties of silicon and oxygen to infer the optical properties of SiO_2. This assumption holds well at energies away from absorption edges, but is likely to give less accurate results in regions close to an edge as the chemical state of the material has a significant effect here [CXRO, 2009]. The K absorption edges of oxygen and silicon are evident in Figure 3.17, at E = 0.532 keV and E = 1.839 keV respectively [NIST, 2009].

Figure 3.18 provides a close-up view of the shape of the effective area curve in the UV energy region. A significant dip in the effective area can be seen at very low energies. This is not a real effect, but is due to the fact that the Henke data sets do not contain information for energies below 30 eV, which corresponds to wavelengths above $\sim$41 nm. Since the imager is designed to respond to radiation with wavelengths of around 120 –160 nm, an alternative data set must be used to provide the required information.

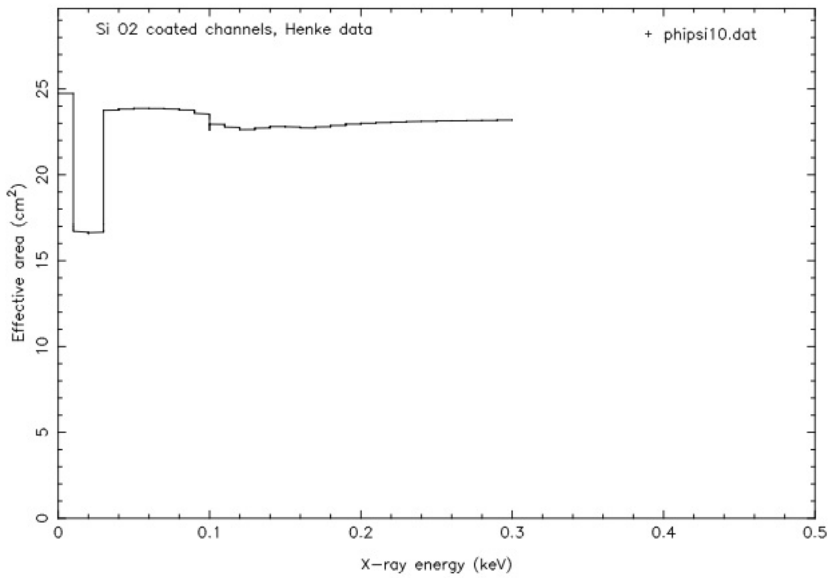

Figure 3.18 — *As Figure 3.17 but concentrating on UV and very soft X-ray photon energies, using Henke reflection data. The dip at low energies is not a real feature, but due to a lack of optical data below 30 eV for oxygen and silicon.*

Palik [1985] gives tabulated data on the real and imaginary parts of the refractive index of SiO_2 glass for energies between 0.00248 eV and 2 keV. The complex refractive index ($\tilde{n}$) of a material when interacting with plane waves of the form $\exp[-i(\omega t - \mathbf{k} \cdot \mathbf{r})]$ – where ω is the angular frequency of the wave (=$2\pi f$), **k** is the wave vector ($|\mathbf{k}| = \frac{2\pi}{\lambda}$), t is a given point in time and **r** is the position vector defining a point in space– can be expressed as either

$$\tilde{n} = n + i\kappa, \tag{3.5}$$

or

$$\tilde{n} = 1 - \delta + i\beta, \tag{3.6}$$

where n, or the equivalent $1 - \delta$, is the real part of the refractive index and κ, or β, is the imaginary part [Attwood, 2000]. These values are related to the complex atomic scattering factor of the material, f̃, at small scattering angles, by the following expressions:

$$\tilde{f} = f_1 - i f_2, \tag{3.7}$$

where f_1 and f_2 are the real and imaginary parts of the form factor respectively;

$$\delta = \frac{n_a r_e \lambda^2}{2\pi} f_1, \tag{3.8}$$

and

$$\beta = \frac{n_a r_e \lambda^2}{2\pi} f_2, \tag{3.9}$$

where n_a is the atomic density of the material, and r_e is the radius of an electron [Attwood, 2000].

Equations 3.8 and 3.9 were used to convert the SiO_2 refractive index data into a table of the atomic form factor for energies between 7.8 eV and 2000 eV, in the same format as the Henke data used by the SRT code. In order to obtain the required quantity n_a, SiO_2 was considered to be made up of atoms with the mass of one silicon and two oxygen atoms, rather than being a compound material. The density of the glass was assumed to be 3.3 g cm^{-3}, as this was the value used in the SRT templates. It was not possible to include energies of less than 7.8 eV as there was a gap in the Palik κ data from this point. However, since 7.8 eV corresponds to a wavelength of 159 nm, it was possible to obtain a much more reliable estimate of the effective area of JUDE at UV wavelengths than with the Henke data. Results from ray tracing with this new data set are shown in Figures 3.19 and 3.20, with the original Henke results overplotted for comparison. It is clear that although the Palik data suggests the effective area should fall more steeply with increasing energies above 0.5 eV than shown by the Henke data (see Figure 3.19), the two data sets agree very well below this energy (Figure 3.20).

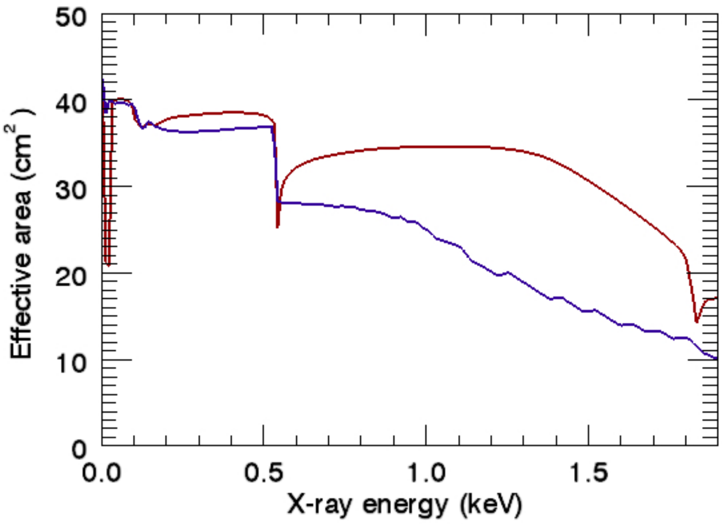

Figure 3.19 — *As Figure 3.17 but with the effective area calculated from Palik reflection data (blue line) plotted on the same axes as the original Henke results (red line). The L:D ratio for this plot was 50:1 but all other parameters were identical for those used in Figure 3.17.*

3.3.2 Effective area as a function of L:D ratio

As well as being energy-dependent, the effective area of an MCP optic varies with the ratio between the plate thickness (or channel length, L) and the width of the channels. If the ratio is too small, rays need to be travelling at a large angle relative to the channel to hit the walls and hence most rays pass straight through unfocused. However, if the ratio is too large then more rays will undergo multiple reflections within a channel, increasing the proportion of rays that are absorbed rather than focused.

The effective area as a function of channel length to diameter ratio (L:D) at UV wavelengths for a point source at infinity is shown in Figure 3.21 for plates with various pore widths and pitches. All other optic parameters are as shown in Table 3.1. The figure

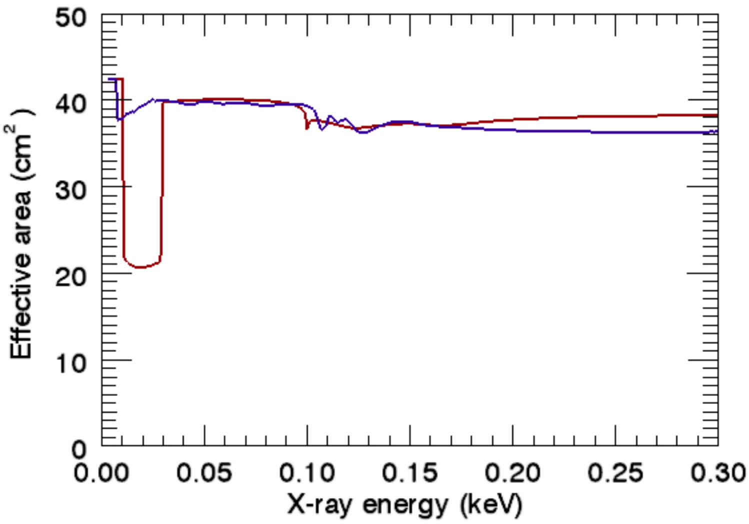

Figure 3.20 — *As Figure 3.18 but with the effective area calculated from Palik reflection data (blue line) plotted on the same axes as the original Henke results (red line). The L:D ratio for this plot was 50:1 but all other parameters were identical for those used in Figure 3.18.*

shows that a plate with 160 μm pores and wall thicknesses of 12.5% of this value (20 μm) has a larger effective area at all L:D ratios than a plate with the same pore width but wall thicknesses of 16% (25.6 μm). This is because the open area of the optic decreases as wall thickness increases. Plates with different pore widths but the same width:wall thickness ratio have the same effective areas as the open area of the optic remains the same. The plot shows that an L:D ratio of 50:1 gives the largest effective area for the JUDE optics, at 40 cm^2.

3.3.3 Effective area as a function of source size

SRT modelling shows that the effective area of an MCP optic appears to decrease as the source size increases (see Figure 3.22). The effective area calculations performed by SRT are based on the proportion of the rays from the source that can be seen in the final image at the detector. It has been shown (Figure 3.5) that as source size increases, the

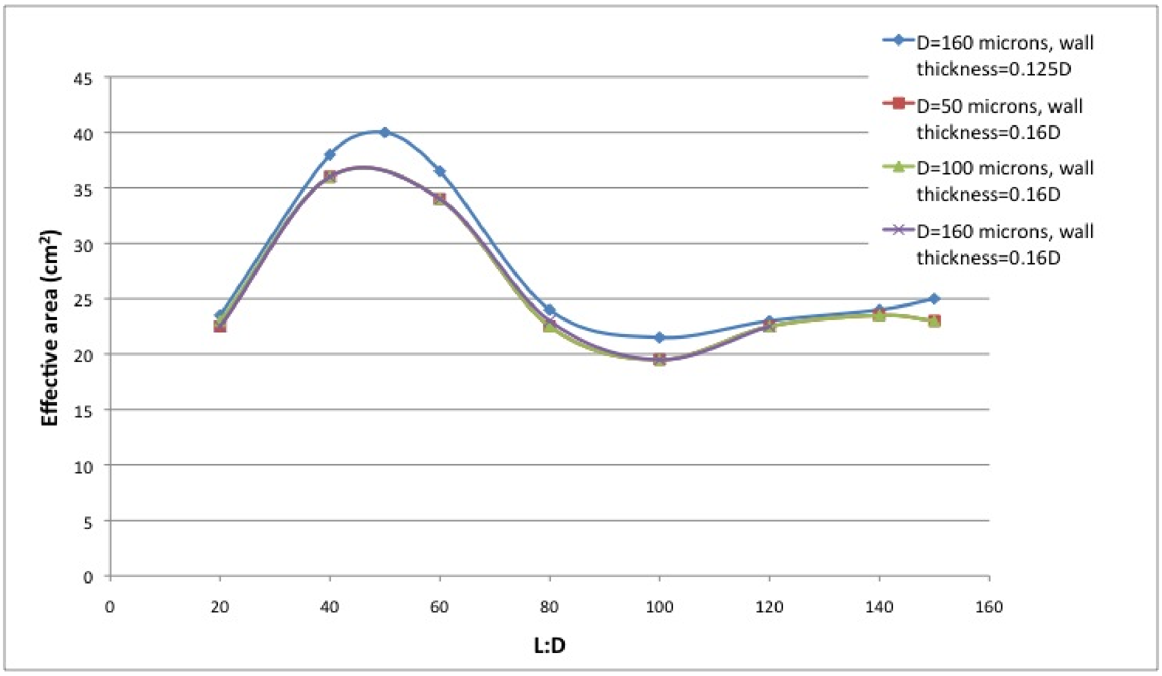

Figure 3.21 — *Relationship between effective area at UV wavelengths and L:D ratio for MCP optics with various pore widths and wall thicknesses, with all other parameters identical. Effective areas for MCPs with pores of widths 50 (red line), 100 (green line) and 160 μm (purple line) and wall thicknesses of 16% of these values are shown, along with a 160 μm pore optic with a wall thickness of 12.5% of the pore width (blue line).*

cross-arms of the point spread function begin to extend off the edges of the detector until, at a source size equal to the field of view of the instrument, only the central focus of the PSF can be seen in the image. Peele et al. [1996] state that at the optimum L:D ratio, 34.3 % of photons in an MCP optic PSF are found in the central focus, 24.3 % in each of the cross-arms and 17.2 % in the unfocused background. Hence, it is to be expected that the number of counts in an image will depend on the proportion of the PSF visible, and it follows that the SRT calculations are reflecting this rather than implying a change in the efficiency of the optic with increasing source size. A comparison between the total effective area of a simulated MCP optic image of a point source and the effective area in the central focus is shown in Figure 3.23.

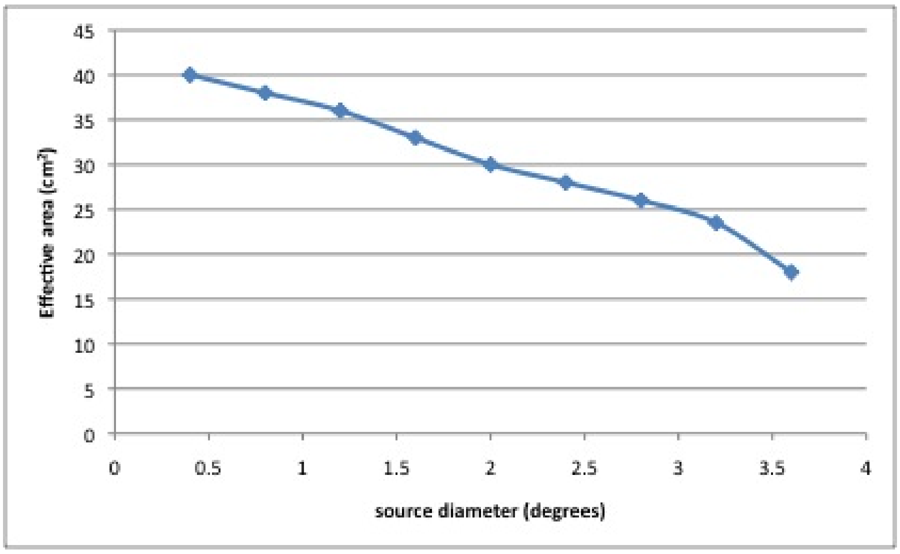

Figure 3.22 — *Apparent decrease in effective area with source size. The drop is actually due to the PSF increasing in size until, for a $\sim 3^o$ diameter source, only the central focus is seen in the image.*

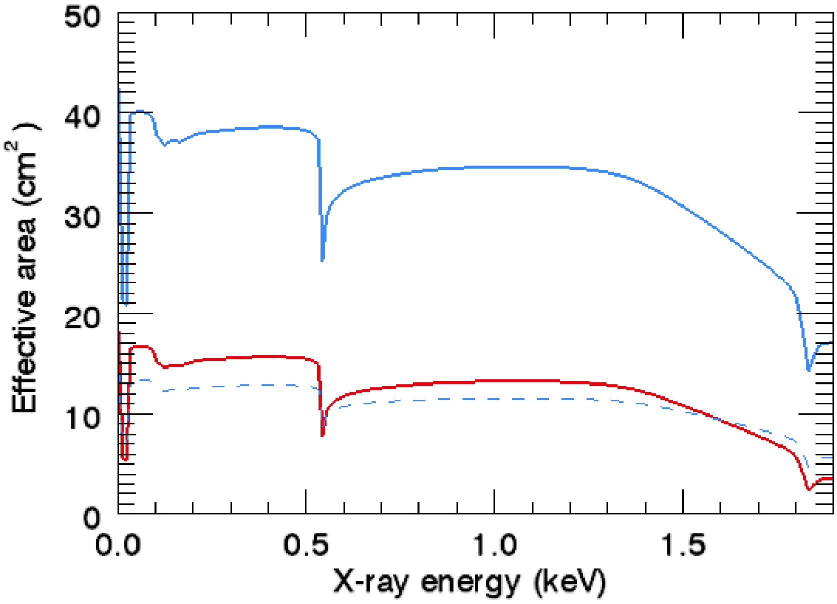

Figure 3.23 — *Total effective area (blue line) and effective area in the central focus (red line) for an MCP optic with parameters as given in Table 3.1. The dashed blue line is the total effective area at each energy multiplied by 0.343.*

3.3.4 The effect of diffraction on effective area

Diffraction at the MCP optic will alter the path of photons, leading to broadening of the focus and cross-arms, as shown in Figure 3.14. The direction of photons hitting certain areas of the optic may be altered such that they do not impinge on the detector, thus decreasing the effective area of the optic. If the MCP optic version of JUDE is chosen, this magnitude of this effect should be investigated.

3.3.5 The effect of the optic support structure on effective area

The addition of supporting structures, such as the central cross shown on the *BepiColombo* optics in Figure 2.12 (Chapter 2), will decrease the effective area slightly relative to a single MCP optic of the same area, since the supports will occupy area that would otherwise contain additional channels. However, the supports should not have a large effect on the appearance of the images produced, since photons are focused over large areas of the optic, as shown in Figure 3.24. Hence, the slight decrease in optic area associated with the use of supporting structures should not have an appreciable effect on the focused image.

3.4 Count rates in the UV imager

3.4.1 Maximum count rate achievable by the detector

Having estimated the effective area of the JUDE MCP optics, it is now possible to assess the expected count rate at the JUDE detector, since this is dependent upon effective area, among other parameters (see Section 3.4.2). The imager's science goals include studying Ganymede's UV aurora, which generally exhibit brightnesses of less than 350 R (see Section 1.3), and imaging Jupiter's aurora, which can peak at a few MR in the UV

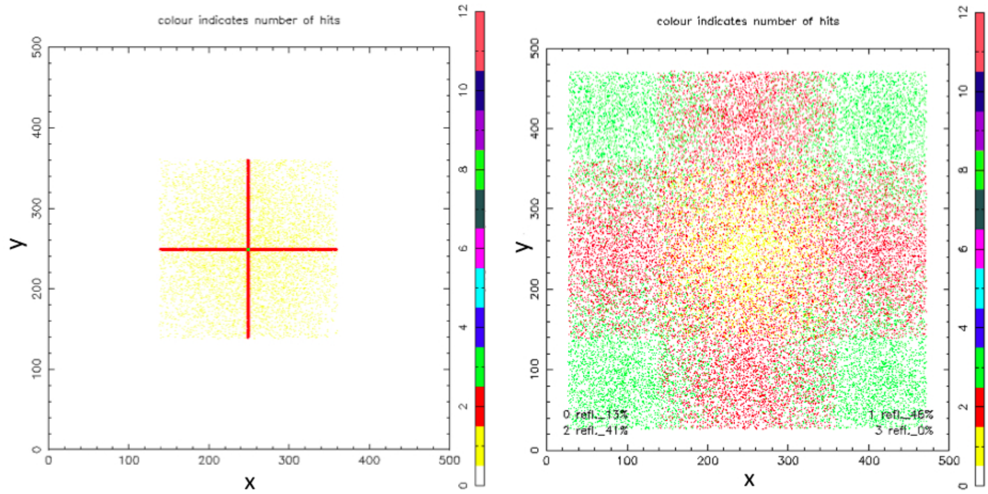

Figure 3.24 — *Left: an MCP image of an on-axis point source colour-coded according to the number of reflections each photon experienced at the optic. Right: corresponding image of the MCP optic used to produce the left image, colour-coded to show the number of reflections undergone by photons encountering different areas of the optic. Hence, the image on the right shows the origin of the different regions (central focus, cross-arms, background) of the PSF seen at the detector. The colour bars show the number of reflections +1, so that areas of no counts can be distinguished from areas where photons have passed straight through the optic pores. (x and y scales are in pixels, where 1 pixel = 0.18 mm.)*

(see Section 1.2.2), and so the instrument must be able to respond to a large dynamic range. An MCP detector has a maximum achievable count rate, since after a photon hits a channel wall and is accelerated towards the anode readout the charge in the wall must be replenished by the plate voltage before that channel may fire again [Wiza, 1979]. This maximum rate is is related to the ratio of the MCP output pulse current I_p to the strip current I_s – the current flowing within the MCP structure [Fraser et al., 1991]. These quantities are defined as follows:

$$I_p = \overline{G}N, \tag{3.10}$$

$$I_s = \frac{V_0}{R_{ch}}, \tag{3.11}$$

where $\overline{G}$ is the MCP gain, N is the count rate per channel, V_0 is the voltage across the MCP and R_{ch} is the effective resistance of each channel. The limiting $I_p : I_s$ ratio varies with number of illuminated channels and this relationship has been investigated for various plates with different numbers of channels [Fraser et al., 1993b]. The MCP to be used in the JUDE detector is a 40 mm-diameter plate containing $\sim$6.4 $\times$ 10^6 hexagonally packed 12.5 μm channels with 15 μm pitch. The limiting I_p/I_s ratio for this number of channels is approximately 0.1 (from Figure 1 in Fraser et al. [1993b]). The limiting count rate per channel for the plate is therefore given by:

$$N_{max} = \left(\frac{I_p}{I_s}\right) \frac{V_0}{\overline{G}R_{ch}} = \frac{0.1V_0}{\overline{G}R_{ch}}. \tag{3.12}$$

The Wide Field Auroral Imager (WFAI)– an instrument like JUDE but optimised for Earth-orbiting missions [Bannister et al., 2007]– uses a detector which is identical to the JUDE detector except for the radius of curvature of the MCP used. The WFAI maximum count rate was evaluated by Bannister et al. [2007] using equation 3.12, with V_0 = 1500 V, $\overline{G}$ = 1 pC and R_{MCP} = 40 MΩ. The channels making up the MCP detector have diameter 12.5 μm and are hexagonally packed with a pitch of 15 μm between the centres of adjacent channels. This implies that the channel number density is approximately 5.1 $\times$ 10^9 m^2, so for a detector with an illuminated area of diameter 40 mm there are $\sim$6.4 $\times$ 10^6 illuminated channels. Treating these as $\sim$6.4 $\times$ 10^6 resistors in parallel, the resistance of each channel can be calculated:

$$\frac{1}{R_{MCP}} = 6.4 \times 10^6 \times \left(\frac{1}{R_{ch}}\right) \Rightarrow R_{ch} = 6.4 \times 10^6 \times 40 \times 10^6 = 2.6 \times 10^{14}\Omega.$$

Hence, N_{max} is 0.6 cts s^{-1} channel^{-1}, or $\sim$4 $\times$ 10^6 cts s^{-1} over the entire detector. This maximum count rate will be adopted for the JUDE instrument.

3.4.2 Count rate due to auroral emissions at Ganymede and Jupiter

The count rate, *R*, in a detector of quantum efficiency *Q* at the focus of an MCP optic viewing emissions of brightness *I* in Rayleighs can be calculated using the equation

$$R = \frac{10^6}{4\pi} A\Omega t_w t_f QI, \tag{3.13}$$

where *A* is the effective area of the optic in cm^2 at the wavelength of the emissions, Ω is the solid angle of the instrument field of view, t_w is the transmission of the window used and t_f is the transmission of the bandpass filter [Bannister et al., 2007].

The field of view of an imager with a 2×2 array of 40×40 mm^2 MCP optics with R$_{MCP}$ of 1500 mm is approximately $3.06^o \times 3.06^o$ (Section 2.1.2). Therefore the solid angle subtended by the field of view is $3.06 \times 3.06 \times \pi^2/180^2 = 0.0029$ steradians.

The quantum efficiency of both bare and CsI-coated MCPs at UV and X-ray wavelengths has been studied previously (e.g. Simons et al. [1987]) and this data used to estimate the sensitivity of the Wide Field Auroral Imager (WFAI) [Bannister, 2009]. The WFAI calculations also included data regarding the transmission of a CaF_2 window which covers the wavelength region to be investigated with the JUDE imager (see Figure 3.25), and hence has been used in the JUDE calculations. No filter will be included for the calculations at this point, since an estimate of the upper count limit is useful for determining whether the JUDE detector will be capable of responding to the most intense emissions expected. If the count rate is found to be too high, this may inform the choice of filters for the imager, as it will provide an estimate of the filter throughput needed to reduce the count rate to an acceptable level.

3.4.2.1 Auroral emissions at Ganymede

A full description of Ganymede's UV aurora is given in Section 1.3. *HST* STIS images at 135.6 nm show that Ganymede exhibits auroral brightnesses of up to 350 R, with background emissions of brightnesses below 100 R but above the 50 R detection limit of

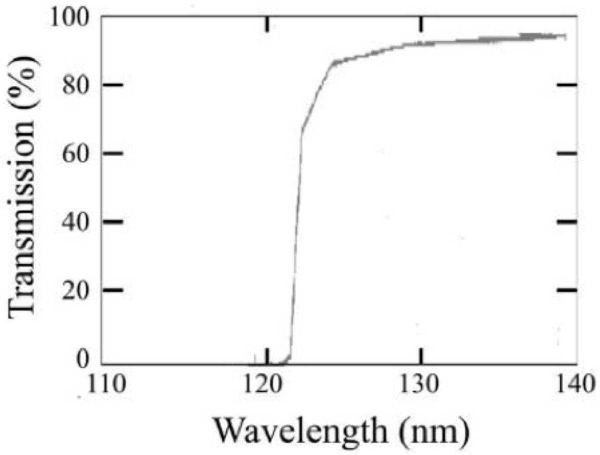

Figure 3.25 — *Transmission of a 0.5 mm* CaF_2 *filter. From Bannister et al. [2007], based on data in Laufer et al. [1965].*

the instrument seen outside of the polar regions (see Figure 1.5 in Chapter 1) [Feldman et al., 2000]. Table 3.3 gives the ratio of 135.6 nm emissions to 130.4 nm emissions for a set of Ganymede images obtained by STIS [Feldman et al., 2000]. The average ratio is $\sim$ 1.6, if image 053K01050 is ignored because of the large error associated with it. This implies that 130.4 nm emissions due to the aurora on Ganymede may have brightnesses of up to $\sim$ 219 R, with background emissions of around 31 – 62 R.

3.4.2.2 Count rate calculation- Ganymede emissions

Table 3.4 shows the results of calculations of the minimum and maximum expected count rates in the UV imager at Ganymede, based on 135.6 nm emissions between 50 and 350 R, and 130.4 nm emissions between 31 and 219 R. The calculations imply that the count rate at the detector when Ganymede's O I emissions fill the instrument field of view will be of order a few thousand to a few tens of thousands of counts per second. This is well within the maximum count rate achievable by the detector as derived in Section 3.4.1.

Table 3.3 — *Ratio of 135.6 nm to 130.4 nm emissions from images of Ganymede [Feldman et al., 2000].*

Exposure ID	I(135.6 nm)/I(130.4 nm)
O53K01010	1.6 ± 0.3
O53K01020	2.2 ± 0.4
O53K01030	1.5 ± 0.6
O53K01040	1.7 ± 0.3
O53K01050	3.2 ± 1.6
O53K01060	1.5 ± 0.2
O53K01070	1.2 ± 0.3
O53K01080	1.2 ± 0.2

Table 3.4 — *Calculation of the maximum and minimum count rates in an MCP detector imaging Ganymede's aurora.*

λ (nm)	A (cm^2)	Ω	t_w	Q	I_{max} (R)	I_{min} (R)	R(max) (s^{-1})	R(min) (s^{-1})
130.4	40	0.0029	0.921498	0.00486	219	31	9054	1282
135.6	40	0.0029	0.943182	0.003262	350	50	9940	1420
						total count rate:	18994	2702

3.4.2.3 Count rate calculation- Jupiter emissions

In order to estimate the expected count rate for observations of the Jovian aurora, spectral data collected by the Cassini UVIS instrument during a flyby of the jovian system between 1st October 2000 and 22nd March 2001 [Ajello et al., 2005] were considered. Figure 3.26 gives two examples of the spectra produced from this data.

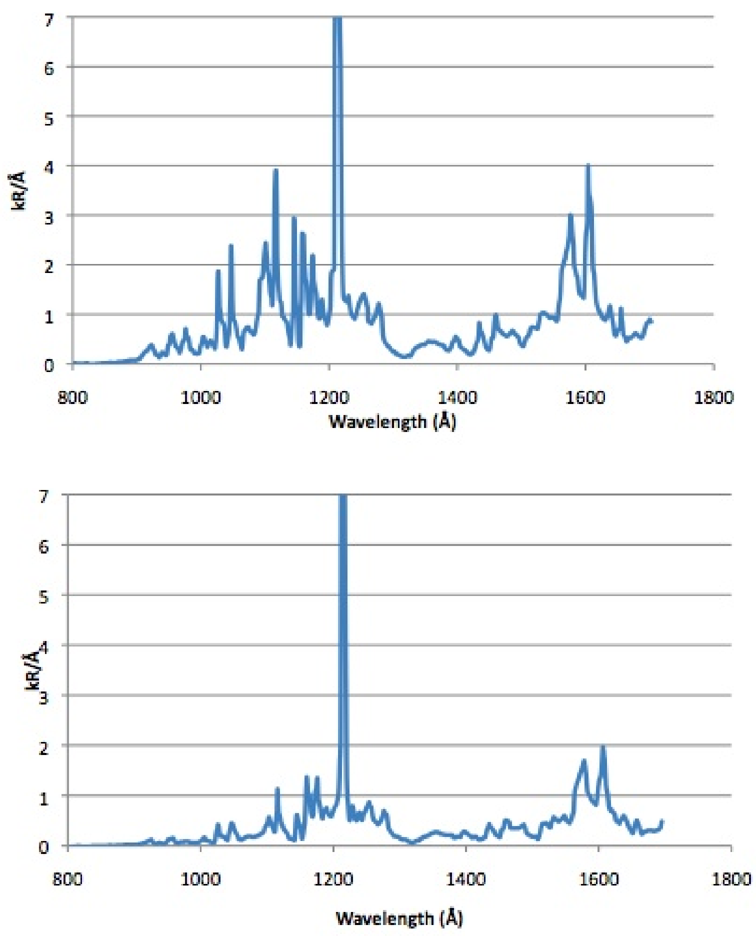

Figure 3.26 — *Two Cassini UVIS spectra of the jovian aurora (from Figure 13 in [Ajello et al., 2005]) from 2nd January 2001, used to provide maximum (top) and minimum (bottom) count rate estimates for JUDE images of the Jupiter aurora.*

The spectra shown in the figure were split into 0.1 nm bins and the brightness in R in each bin was multiplied by the transmission of the window and the quantum efficiency of the optic at the relevant wavelength, and then by the effective area and solid angle of the instrument and a factor of $10^6/4\pi$ to give the number of counts per bin (see equation 3.13). The height of the Lyman-α peak at 121.6 nm was not given for the spectra used, but other Cassini data suggested a peak height approximately 30 times larger than surrounding peaks (see Figure 3.27) [Pryor et al., 2005], so this ratio was adopted to allow a count rate estimate for this wavelength to be made. The number of counts in each bin were then summed to provide a total count rate over the range 121.3 – 170.0 nm (the transmission window cuts out any photons below 121.3 nm).

The count rates predicted by the spectra in Figure 3.26 were found to be 4.44×10^6 s^{-1} for the quieter spectra and 7.76×10^6 s^{-1} for the more active state. Both of these values are above the $\sim 4 \times 10^6$ counts s^{-1} estimate for the maximum count rate achievable by the detector.

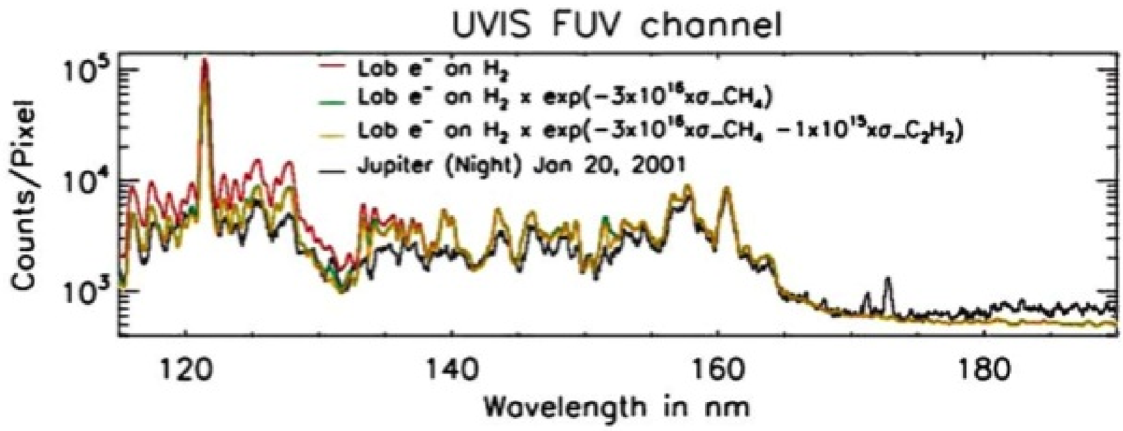

Figure 3.27 — *Comparison of Cassini UVIS count rate with laboratory models [Pryor et al., 2005], used to estimate brightness of Lyman-α emissions relative to nearby peaks.*

3.4.3 Discussion

The count rate estimates for Ganymede are well below the upper limit achievable by the detector, but the presence of H I Ly-α emissions associated with a hydrogen exosphere there may introduce a complication. These emissions have been observed with brightnesses up to a few kR [Feldman et al., 2000]. Assuming that the Ly-α emissions are at a wavelength of 121.6 nm, the count rate they produce at the detector can be estimated. The CaF_2 transmission data used indicated a transmission of 0.05 at this wavelength and the quantum efficiency of the MCP detector is $\sim 9.62 \times 10^{-3}$. Combined with the instrument effective area and solid angle, this implies that Ly α emissions of 2 kR will lead to a count rate in the detector of almost 9000 counts s^{-1}, compared to a count rate of $\sim$2700 s^{-1} for the $\sim$50 R background emissions around 130.4 – 135.6 nm (see Table 3.4). Since the MCP detector does not have intrinsic energy resolution, the images produced may be dominated by counts from Ly-α rather than OI, reducing the potential to use the OI emissions to refine models of Ganymede's atmosphere (see Chapter 1, Section 1.3). The problem can be minimised with the use of a filter to isolate the oxygen lines. However, the filter should not cover the entire instrument field of view as Jupiter's auroral emissions do not peak in the same wavelength range: Figure 3.26 shows that auroral emissions at Jupiter are weak around 130 nm, but considerably higher around 150 – 160 nm.

Jupiter's count rate estimates are clearly more problematic than Ganymede's, as even the lower estimate exceeds the maximum count rate that the detector can cope with. However, the calculations assumed that the entire field of view of the instrument would be filled by the emissions, when in reality this is unlikely to be the case, so the actual count rate should be lower. Even so, bright regions may still cause charge depletion in the detector, so a filter of some sort may be required to push the count rate down. This will need careful consideration as it will reduce the signal seen at Ganymede as well. Another strategy that may help is choosing an optic with an L:D ratio that leads to a smaller optic effective area. However, this will also decrease the Ganymede count rate, reducing the sensitivity of the instrument to Ganymede's faintest emissions. The upper count rate for Jupiter was estimated to be almost twice the maximum count rate achievable by the JUDE detector, implying that a filter with a transmission of less than 50% in the FUV would be needed to reduce the detector count rate to an acceptable level.

3.5 Summary

SRT modelling has been used to investigate the expected response of the JUDE imager to both point and extended sources, and to allow the estimation of count rates at the instruments MCP detector. The resolution of SRT images of point sources was found to correlate well with the theoretical resolution of the optics modelled, and the shapes of different emission regions were easily distinguishable in images of extended sources. However, the addition of diffraction effects to the models led to an almost 4-fold decrease in the resolution of the instrument, leading to a diffraction-limited spatial resolution of $\sim$658 km when observing Jupiter from 12 R_J. Excellent spatial resolution is a key requirement for JUDE, in order to allow small, transient features within Jupiter's aurora to be studied. This diffraction-limited resolution will have a severe impact on the imager's ability to provide high-quality observations of such features.

The count rates expected at the detector when observing Ganymede are well within the detector limit, but Jupiter's brightest emissions may lead to count rates so high that the charge in the channel walls cannot be replenished fast enough to keep up, leading to a decrease in the detector gain. Although this count rate may be decreased with the use of filters or by optimising the characteristics of the MCP optic, the diffraction problem is much more difficult to overcome. It has hence been decided that MCP optics are not suitable for this particular application, and future development of JUDE will make use of the alternative reflective optics described in Section 2.2. The reflective optics design is discussed further in Chapter 5. Before this, Chapter 4 focuses on the supporting MCP laboratory tests performed in parallel with the modelling described in the present chapter, which reinforce the conclusion that the MCP optic design is unsuitable for JUDE.

CHAPTER 4

Laboratory testing of MCP optics

This chapter describes two sets of laboratory focusing tests of MCP optics that were performed in parallel with the sequential ray tracing (SRT) modelling described in Chapter 3. Combined with the SRT studies in that chapter, these tests helped to assess the performance of the JUDE instrument in its MCP optic design.

Two different MCPs, with different pore widths, slump radii and aspect ratios (channel length : channel width), were tested. The first of these optics was a prototype Wide Field Auroral Imager (WFAI) optic, intended for observations of the Earth's aurora from a relatively low orbit. One potential application for the instrument is the two *KuaFu-B* spacecraft (see Section 4.1), which each have a preliminary orbital design of perigee 1.8 R_E and apogee 7 R_E [Tu et al., 2008]. The close proximity of the emissions of interest for auroral imaging from Low Earth Orbit led to a more lenient angular resolution requirement for WFAI than that specified for JUDE, with a goal of achieving 25 $\times$ 25 km spatial resolution from 800 km orbit (corresponding to an angular resolution of $\sim$1.79°). Hence, although the channel width of the tested MCP was of a similar magnitude to that of the JUDE optics, the radius of curvature could be significantly smaller, maximising the field of view. The second MCP optic tested was intended for use as a collimator on the Mercury Imaging X-ray Spectrometer (MIXS) for *BepiColombo* [Fraser et al., 2010]. Although its slump radius was closer to that specified in the JUDE preliminary design, the optic pores were narrower than those required to minimise diffraction on JUDE, as MIXS is an X-ray instrument and therefore does not suffer from diffraction to such an extent (this optic was tested with an X-ray source).

While neither of the MCP optics tested were of the same specifications as the prototype JUDE optics, these tests provided an insight into the operation of MCP optics in general and allowed methods of optimising the achievable resolution to be investigated. A comparison of the three MCP optics is given in Table 4.1. The WFAI MCP had a similar pore width to the JUDE optic and was tested with an FUV source. These tests could therefore give an indication of the degrading effect of diffraction on the JUDE optic's theoretical resolution, potentially confirming the results of the diffraction modelling given in Chapter 3. The MIXS-C optic had a theoretical resolution limit similar in magnitude to that of JUDE, and if this resolution could be successfully achieved during X-ray focusing tests it would show that high-resolution imaging is achievable with slumped MCP optics, albeit at shorter wavelengths than the FUV bandpass specified for JUDE.

Table 4.1 **—** *Comparison of the JUDE, WFAI and MIXS-C MCP optics*

	JUDE	WFAI	MIXS-C
Optic array area	80 × 80 mm	80 × 80 mm	80 × 80 mm
R_{MCP}	1500 mm	100 mm	550 mm
Channel width	160 μm	100 μm	20 μm
L:D ratio	50:1	10:1	55:1
Multifibre side length	TBD	∼2.204 mm	∼0.902 mm
Detector-optic distance	750 mm	50 mm	550 mm
Theoretical resolution	0.73 arcmin	6.88 arcmin	0.25 arcmin[a]

[a] when used for focusing rather than collimation (e.g. with detector-optic distance = 275 mm)

4.1 Testing the Wide Field Auroral Imager (WFAI) optic

The MCP optic design for JUDE is a modified version of another instrument currently under development at the University of Leicester, the Wide Field Auroral Imager (WFAI). This imager uses slumped MCP optics to create a large field of view, thereby allowing wide field imaging of the Earth's aurora from Low Earth Orbit, in contrast to the high orbits required to produce global-scale images with conventional satellite-based auroral imagers. The aim of the terrestrial WFAI project is to allow auroral images to be obtained simultaneously with measurements of the particle and field conditions responsible for the emissions from the same platform [Bannister et al., 2007]. One potential platform for the WFAI is the *KuaFu* mission. The original *KuaFu* mission concept was a Chinese-led mission involving three separate spacecraft designed to investigate space weather: *KuaFu-A* would observe the sun from the L1 Lagrange point, while *KuaFu-B1* and -*B2* would each make observations of the Earth from a 7 $\times$ 1.8 R$_E$ orbit [Tu et al., 2008]. Conjugate imaging of Earth's north and south auroral regions by the two *KuaFu-B* satellites could be achieved if both carried a WFAI to allow wide field imaging at the spacecraft perigee, combined with standard UV imaging at apogee. *KuaFu* has now evolved into a joint Chinese-ESA mission, with China developing *KuaFu-A* and ESA providing the two *KuaFu-B* satellites, but the mission design currently remains similar to the original concept [Milan, 2012].

A schematic of a WFAI module is shown in Figure 4.1. The module contains four slumped MCP optics, tiled in a 2 $\times$ 2 array like the prototype JUDE optics, and a detector containing two MCP electron multipliers in a chevron arrangement (see Chapter 2, Section 2.3.1.1). Each individual optic is a 40 $\times$ 40 mm^2 square pore, square packed MCP with a radius of curvature of 100 mm, and the field of view is thus 22.9° (= 360° $\times$ $\frac{40\text{mm}}{2\pi\times100\text{mm}}$). One complete WFAI module therefore has a field of view of 45.8° $\times$ 45.8°. Arrays of modules may be used to extend the field of view further as required.

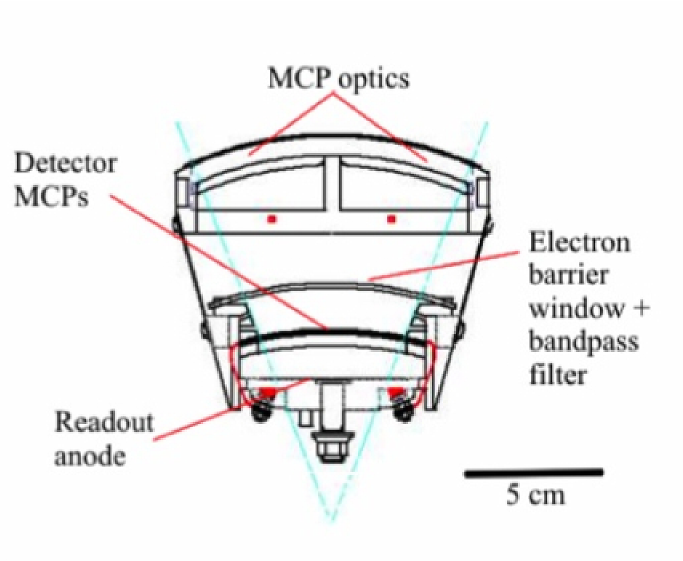

Figure 4.1 — *WFAI module schematic [Bannister et al., 2007].*

4.1.1 The Detector Test Facility

Initial focusing tests of the prototype WFAI optic and detector were performed using the detector test facility (DTF) in the University of Leicester's Space Research Centre. The DTF is a vacuum facility originally built to calibrate the MCP detectors for the *Rosat* Wide Field Camera. A schematic of the facility is shown in Figure 4.2. A number of photon sources can be used with the system to allow calibration at VUV and X-ray energies. For the WFAI, which is intended for UV (121–180 nm) imaging of Earth's aurora, a model V03 deuterium lamp produced by Cathodeon (now Heraeus Noblelight, Cambridge) was used. This consists of a vacuum UV bulb with a MgF_2 window, producing a UV continuum with a short-wavelength cut off of $\sim$112 nm. The radiation emitted by the deuterium source is constrained to a narrow beam by two pinholes, the first of which is fixed in place and has a diameter of 0.5 mm. At a distance of 8 cm along the optical axis from the first pinhole is a metal plate containing two pinholes, with diameters of 0.9 mm and 0.35 mm, either of which may be moved into the path of the radiation using a linear drive mechanism. The constrained beam of radiation next encounters a filter wheel which can hold 12 filters around its edge and is housed in a large tank set

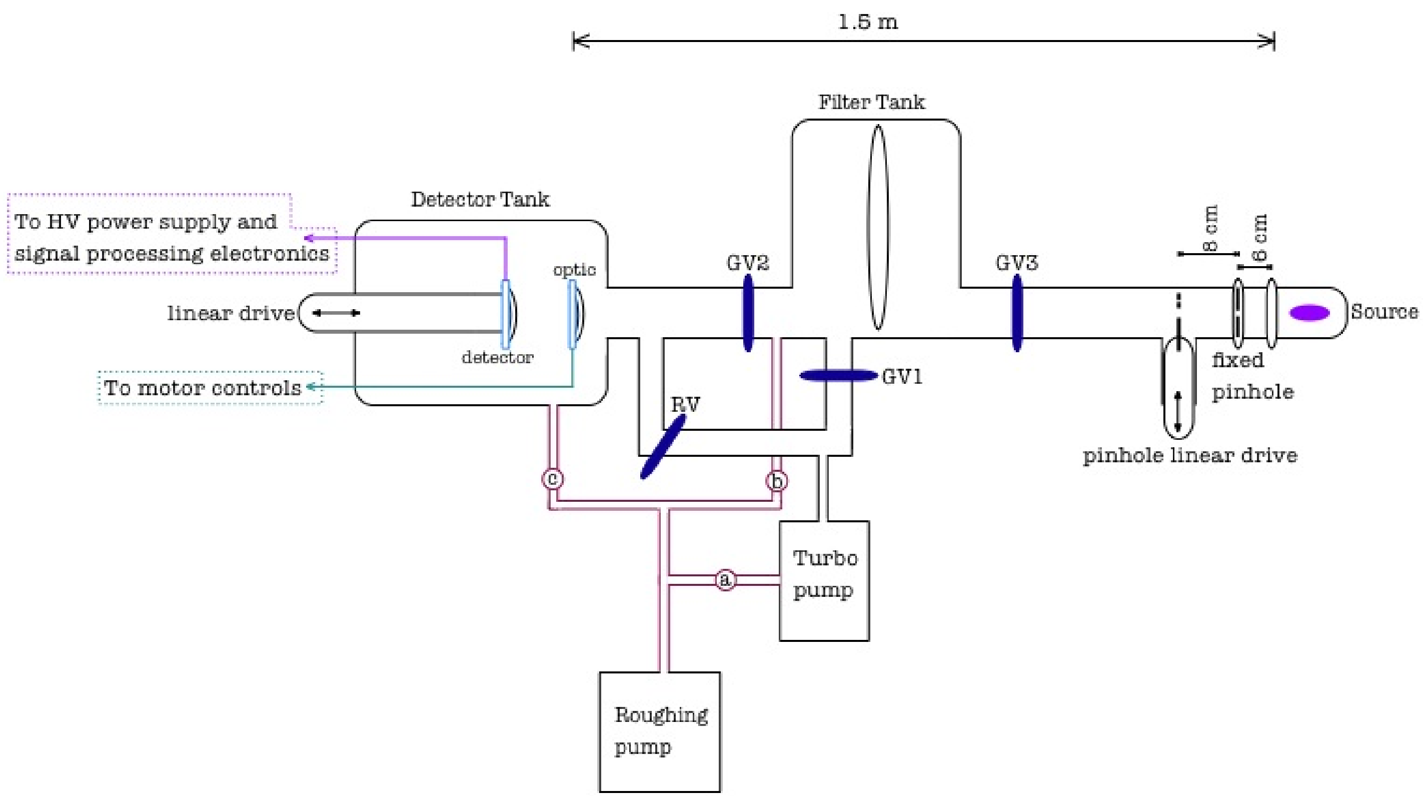

Figure 4.2 — *DTF schematic showing the positions of the source, filter tank and detector/optic tank along the beamline. The gate valves GV1, GV2, GV3 and RV can be used to isolate each of these sections. The roughing pump is used to take the pressure in the system down to* $\sim 10^{-1}$*mbar, at which point the turbo pump is turned on, allowing pressures of* $<10^{-6}$*mbar to be achieved. The taps a, b and c are used to control the flow of air around the system.*

to one side of the beamline, such that the beam passes through one filter only. The filter wheel is turned using a stepper motor which is controlled remotely by a computer, so that different filters may be selected during testing without the need to bring the system up to atmospheric pressure. The beamline ends in a second tank, which contains a fixed mount to which an MCP optic can be attached, and another mount behind this to hold an MCP detector. The detector can be moved along the optical axis with the use of a linear drive to allow the focal length of the optic to be determined experimentally. Additionally, the optic can be tilted vertically and horizontally with the use of stepper motors, allowing the off-axis imaging performance to be evaluated. The length of the DTF from source to optic is 1.5 m.

4.1.2 Focusing tests

The characteristics of the three MCPs used in the WFAI focusing tests (the optic MCP and the two MCPs contained within the detector) are summarised in Table 4.2. A high voltage power supply was used to apply a potential difference of 1500 V across each detector plate, with a voltage of 200 V in the gap between the two. The deuterium source was then turned on and images were obtained through a range of detector-optic distances, controlled using the linear drive attached to the detector mount (see Figure 4.2). The full width at half maximum (FWHM) of the cruxiform point spread function (PSF) in each image was measured to determine the angular resolution of the system at that particular detector-optic separation. An example of a screenshot generated by the Image Display interface used with the DTF is shown in Figure 4.3. The software calculates the FWHM of acquired images in two ways, first by simply taking a cut through the selected region and secondly by fitting a Gaussian curve to this cut and calculating the FWHM of the curve.

The results of the FWHM calculations are given in units of pixels, which must be converted to more useful units. The conversion between pixels and mm was performed by multiplying the FWHM by a factor known as the plate scale, which was calculated by

***Table 4.2** — WFAI MCP Characteristics*

	Detector (rear)	Detector (front)	Optic
Plate thickness (mm)	1.5	1.5	1.0
Channel width (μm)	12.5	12.5	100
Channel pitch (μm)	15	15	120
L:D	120:1	120:1	10:1
Bias angle (°)	13	0	0
MCP diameter (mm)	36	36	36
Radius of curvature (mm)	100	100	100

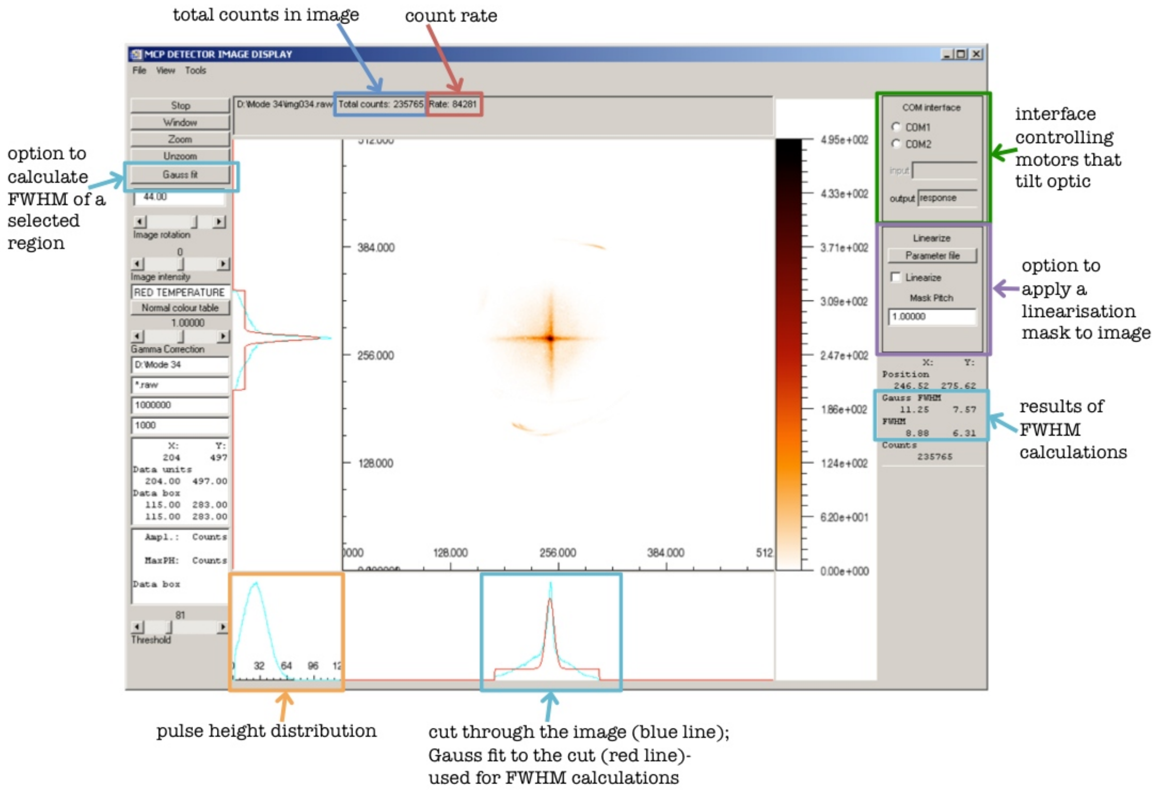

***Figure 4.3** — A screenshot of the image display interface after acquiring an image, with various features highlighted.*

dividing the known diameter of the detector in mm by the diameter of a noise image of the detector, such as that shown in Figure 4.4, in pixels. The noise image was used as it shows the full extent of the detector active area; the active area of imaging detectors is often determined using full-field illumination but this is not possible in the DTF. The diameter of the noise image was measured to be 259 pixels in the x direction and 256 pixels in the y direction, so the mean value of 257.5 mm was used (the reason for the slight distortion of the image between the two dimensions is discussed in Section 4.1.4.2), giving a plate scale of 257.5/36 $\approx$ 7.15 pixels mm^{-1}. A conversion to degrees could then be performed by considering the angle subtended by the FWHM at a distance equal to the detector-optic distance (l_i):

$$\mathrm{FWHM(deg)} = \tan^{-1}\left[\frac{\mathrm{FWHM(mm)}}{l_i\mathrm{(mm)}}\right]. \tag{4.1}$$

The results of the WFAI focal length tests are shown in Figure 4.5 as a plot of the FWHM in degrees of the image PSF as a function of the distance between the optic and the detector. The vertical error bars on the plot represent the angle subtended by one pixel in the image at the relevant detector-optic separation. There is also an error associated with the detector-optic distance itself, and the horizontal error bars in the figure reflect this: although the linear drive controlling the distance was accurate to 0.02 mm, the system wasn't properly calibrated[1] and the initial measurement of the optic position was made using a ruler, leading to an estimated reading uncertainty of $\pm$0.5 mm. However, an MCP optic has a depth of focus determined by its thickness and its radius of curvature. The WFAI depth of focus is $\sim$0.65 mm (see Appendix D), so the uncertainty will not lead to a large error in the measured focal length.

The best achievable resolution from the focusing tests was found to be at l_i= 48$\pm$0.5 mm for the y measurements (FWHM = 0.969°; Gauss FWHM = 0.816°) and at l_i=

[1]The optic was held by a mount which extended beyond the front and back surfaces of the optic. Although the position of the mount could be accurately measured, it was difficult to determine the exact position of the optic within the mount. As the tests described here were intended to be preliminary, this was not considered to be a critical issue. Unfortunately, equipment failure has made further tests impossible to date, but an investigation of the mount design will be considered before more thorough tests are performed.

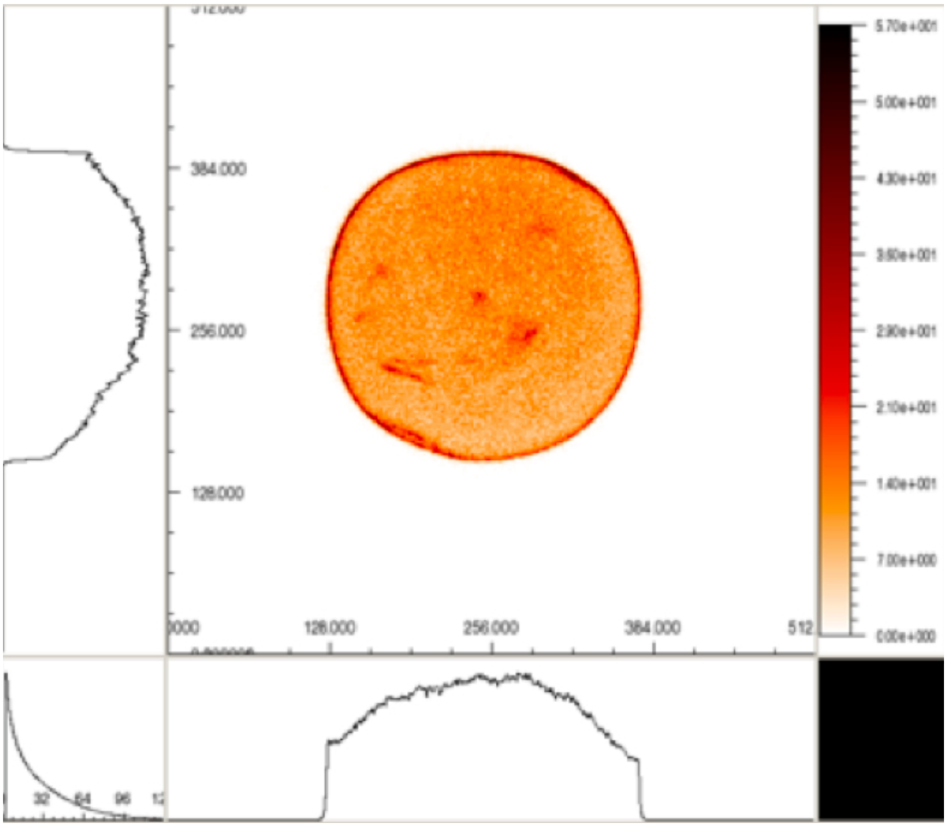

Figure 4.4 — *A noise image of the WFAI detector, i.e. an image obtained with the source switched off. This image is a ∼20 hour exposure with a noise count rate of ∼4 counts s^{-1} (≈0.39 counts cm^{-2} s^{-1}).*

49±0.5 mm for the x measurements (FWHM = 1.443°; Gauss FWHM = 1.188°). This corresponds well to the expected focal length of the system as calculated from Equation 2.3[2] (Chapter 2):

$$\begin{aligned} l_i &= \left[\frac{1}{l_s} - \frac{2}{R_{MCP}}\right]^{-1} \\ &= \left[\frac{1}{1500} - \frac{2}{-100}\right]^{-1} \\ &= 48.4\text{mm}. \end{aligned}$$

However, both resolution values are much larger than the theoretical resolution limit for the optic, given by the angle subtended by a single channel at the focal distance:

$$\theta = \tan^{-1}\left(\frac{0.1}{48.4}\right) \approx 0.118°. \tag{4.2}$$

[2]remembering that R$_{MCP}$ is negative for an MCP that is convex as seen from the source

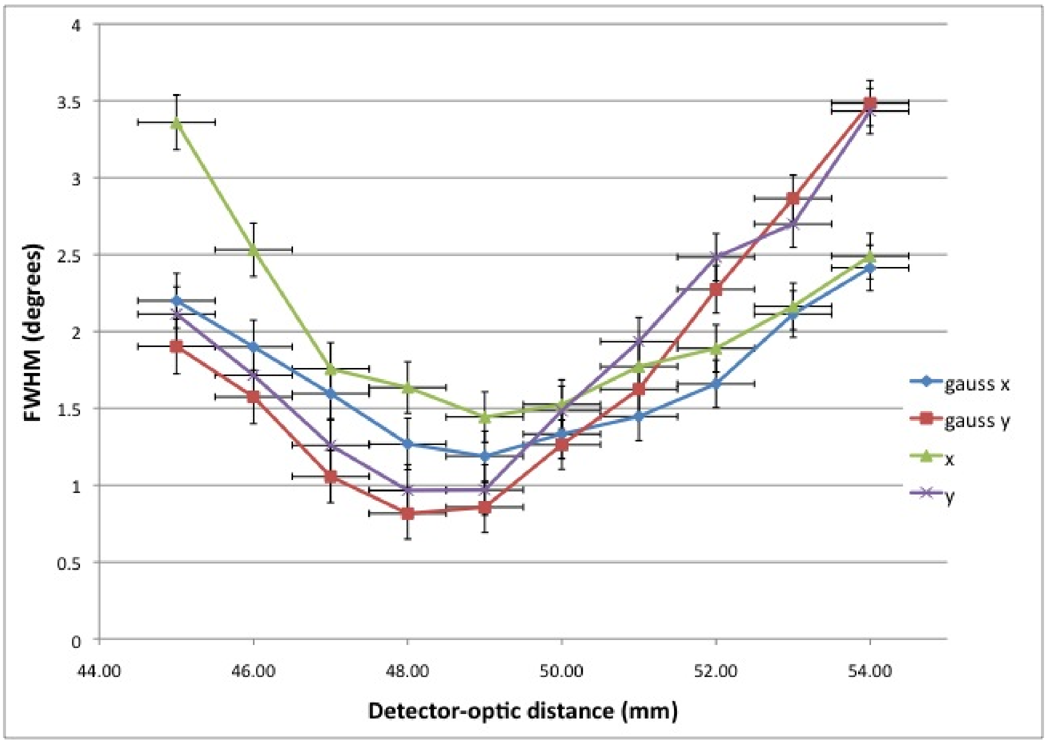

Figure 4.5 — *The results of the original FWHM calculations for the prototype WFAI module. The FWHM in degrees as a function of the detector-optic distance is shown for both the x and y directions for each of the two methods used by the image display software (raw FWHM and FWHM from a Gaussian fit).*

The main factors contributing to the degradation of the optic resolution are discussed in Section 4.1.4, along with methods of correcting for these, allowing the intrinsic MCP resolution to be measured.

4.1.3 SRT modelling of the focusing tests

SRT modelling was performed in parallel with the WFAI focusing tests, in order to confirm that the system was performing as expected, and to predict the best focus achievable at various detector-optic separations. The model input parameters are given in Table 4.3: where coordinates are given, x is the optical axis, y is the horizontal axis perpendicular to the optical axis, and z is the vertical axis. The model was designed to

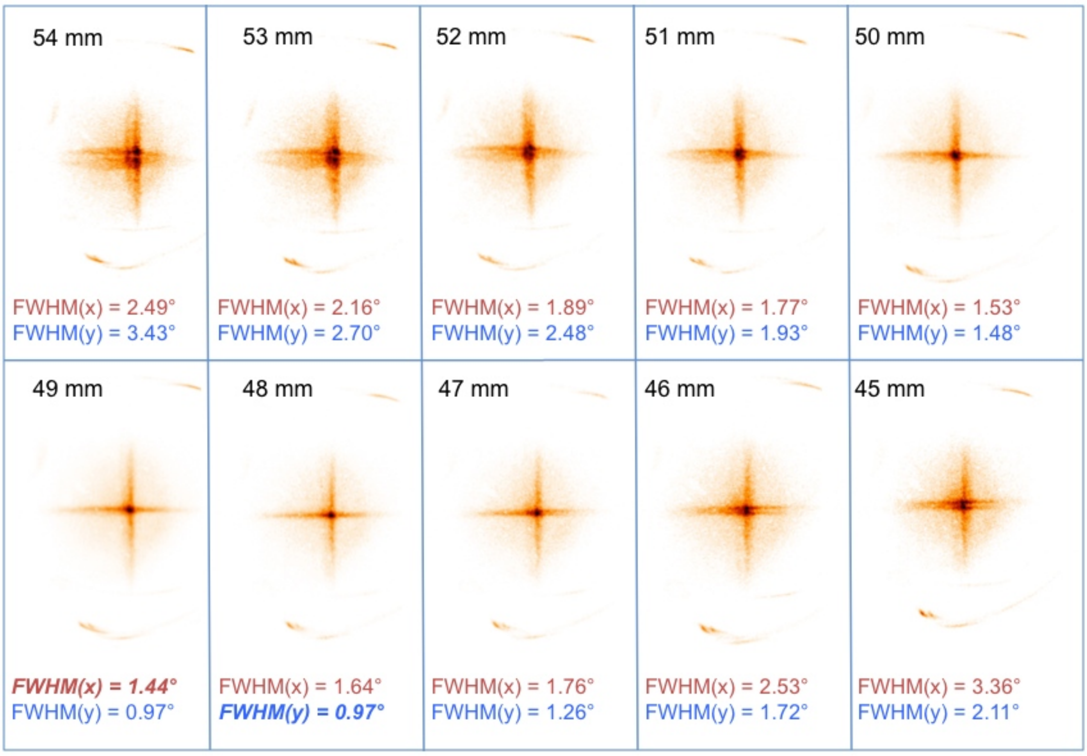

Figure 4.6 — *The point spread function of the WFAI prototype at various detector-optic distances (given at the top of each panel). The FWHM measurements for each image are given beneath the PSF, with the minimum value in each direction highlighted.*

describe the DTF geometry accurately, including the two pinholes used to constrain the UV beam. The source was defined with a diameter of 15°, as this is the cone angle of a standard V03 model UV lamp produced by Cathodeon [Cathodeon: Deuterium lamp brochure].[3] The optical properties of the MCP optic glass were derived using data from Palik [1985] as described in Chapter 3, Section 3.3.1, allowing the interaction between the optic and FUV radiation to be reliably modelled. Although the wavelength specified in the model was slightly shorter than the short-wavelength cut-off of the DTF deuterium lamp (100 nm, compared to a lamp cut-off of ∼112 nm), Figure 3.20 in Chapter 3 shows that the effective area of an MCP optic varies only slowly with wavelength at FUV wavelengths, so the results of the model should still apply to the slightly longer wavelengths used in the DTF measurements. The model was first used to simulate images

[3] http://www.teknolab.no/pdf/Cathodeon_Deuterium.pdf

with the detector and optic perfectly aligned, and then with the optic slightly tilted in both the vertical and horizontal axes perpendicular to the optical axes in an attempt to match the shape of the experimentally measured PSFs.

The images produced by the SRT model at various detector-optic separations are shown in Figures 4.7 and 4.8, each next to two corresponding DTF images: one with the optic perfectly perpendicular to the optical axis in both the y and z directions, and one with the optic tilted by $1°$ around the vertical (z) axis and by $0.2°$ around the horizontal (y) axis. To allow direct comparison between simulated and experimentally measured images, a scale has been included on each image: a scale of 11 mm was chosen for simplicity because it is approximately equal to three times the minor tick interval (32 pixels) on the experimentally obtained images with a plate scale of 8.51 pixels mm^{-1} (derived from corrections to the DTF measurements, as described in Section 4.1.4.2), and because it was close in size to the extent of the PSF cross-arms. Figure 4.7 shows the full modelled and experimental images for a detector-optic separation of 54 mm, including the axes used to indicate the image scales. Figure 4.8 shows expanded images of the PSF only for each of the modelled and experimental images obtained at separations ranging from 45 mm to 53 mm. The scale on each of these images was produced in the same way as shown in Figure 4.7.

The SRT and DTF images in each set shown in Figures 4.7 and 4.8 are similar in size, with the images from the laboratory tests being consistently slightly larger. This is to be expected, as the model specified a perfect optic free from any deformations, and any deformations present in the actual optic would degrade the focus, hence increasing the size of the PSF seen in the lab images. (A simulated PSF for an MCP with deformations of varying magnitude added can be seen in Figure 4.33: this model used different parameters and will be discussed later.) With a tilt in the optic position added, the modelled images convincingly reproduce the DTF results: the right-hand cross-arm in each image is shortest, most obviously in the unfocused images, and the PSF appears smallest, and therefore most well-focused, at a detector-optic distance of 49 mm in all images, with its size increasing inside or outside of this position, until the cross bifurcates

Table 4.3 — *Parameters used for the SRT modelling of the WFAI focusing tests*

Parameter	Value
Optic position	[0, 0, 0][a]
Source position	[1500, 0, 0]
Detector position	[-l_i, 0, 0], where l_i is the detector-optic separation
Pinhole 1 position	[1440, 0, 0]
Pinhole 1 diameter	0.5 mm
Pinhole 2 position	[1360, 0, 0]
Pinhole 2 diameter	0.9 mm
Source size	15°
Optic material	Glass (Palik data[b])
R_{MCP} (optic)	100 mm
Optic channel width	0.1 mm
Optic thickness	1.0 mm
Optic area	circle of 20 mm radius
Detector R_{curv}	100 mm
Detector area	40 mm × 40 mm
Detector pixel size	0.05 mm[c]
Number of rays	10^6
Wavelength of rays	100 nm

[a] distances in coordinates are in mm

[b] see Chapter 3, Section 3.3.1

[c] pixel size is defined for modelling only:
resistive anodes are not pixelated (see Chapter 2, Section 2.3.2.1)

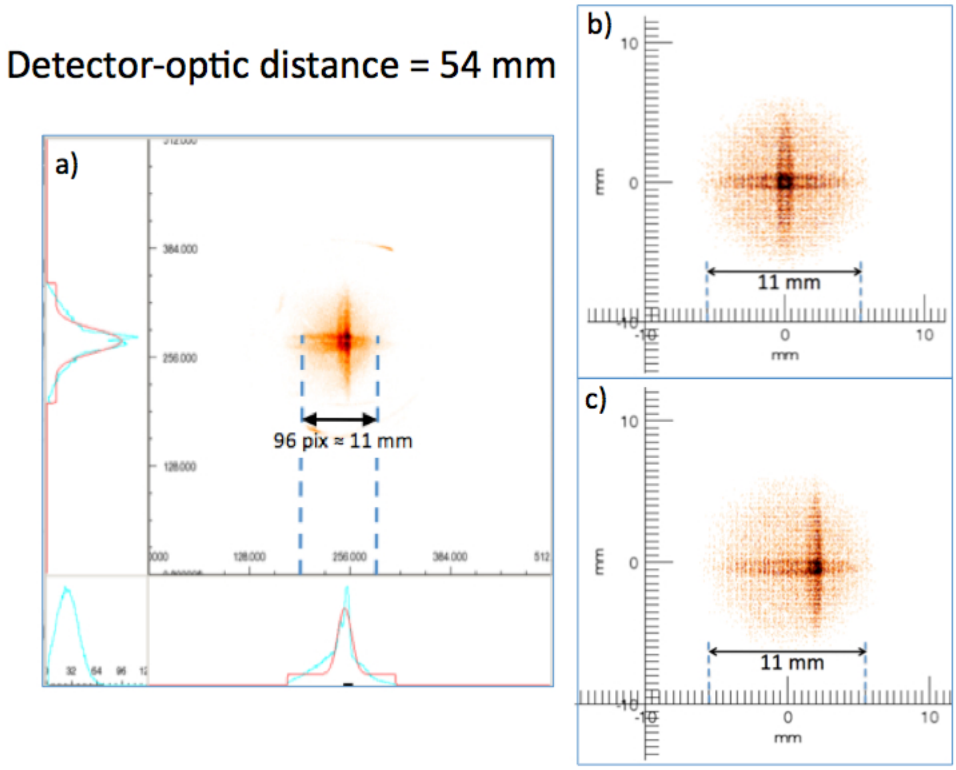

Figure 4.7 — *a) An experimentally measured image from the WFAI focusing tests, for a detector-optic separation of 54 mm, with a scale derived from the axes of the image. b) A simulated image using the WFAI parameters at the same detector-optic distance. c) As (b) but with the model optic tilted by 1° around the vertical (z) axis and by 0.2° around the horizontal (y) axis.*

to resemble a hash (#) shape at separations of 46 mm or less, or 52 mm or greater. This bifurcation is due to the different paths taken by rays focused by different regions of the optic, as shown in Figure 4.9.

The model provides a believable prediction of the operation of a perfect WFAI optic. It can thus be used to determine the best resolution that could theoretically be achieved by any real MCP optic with the WFAI MCP specifications. The FWHM of each ray-traced image was measured to allow comparison between the resolution of the theoretical perfect optic and that of the optic used in the DTF tests. Figures 4.10 and 4.11 are graphs showing the focal length for both the theoretical and real optics as a function of

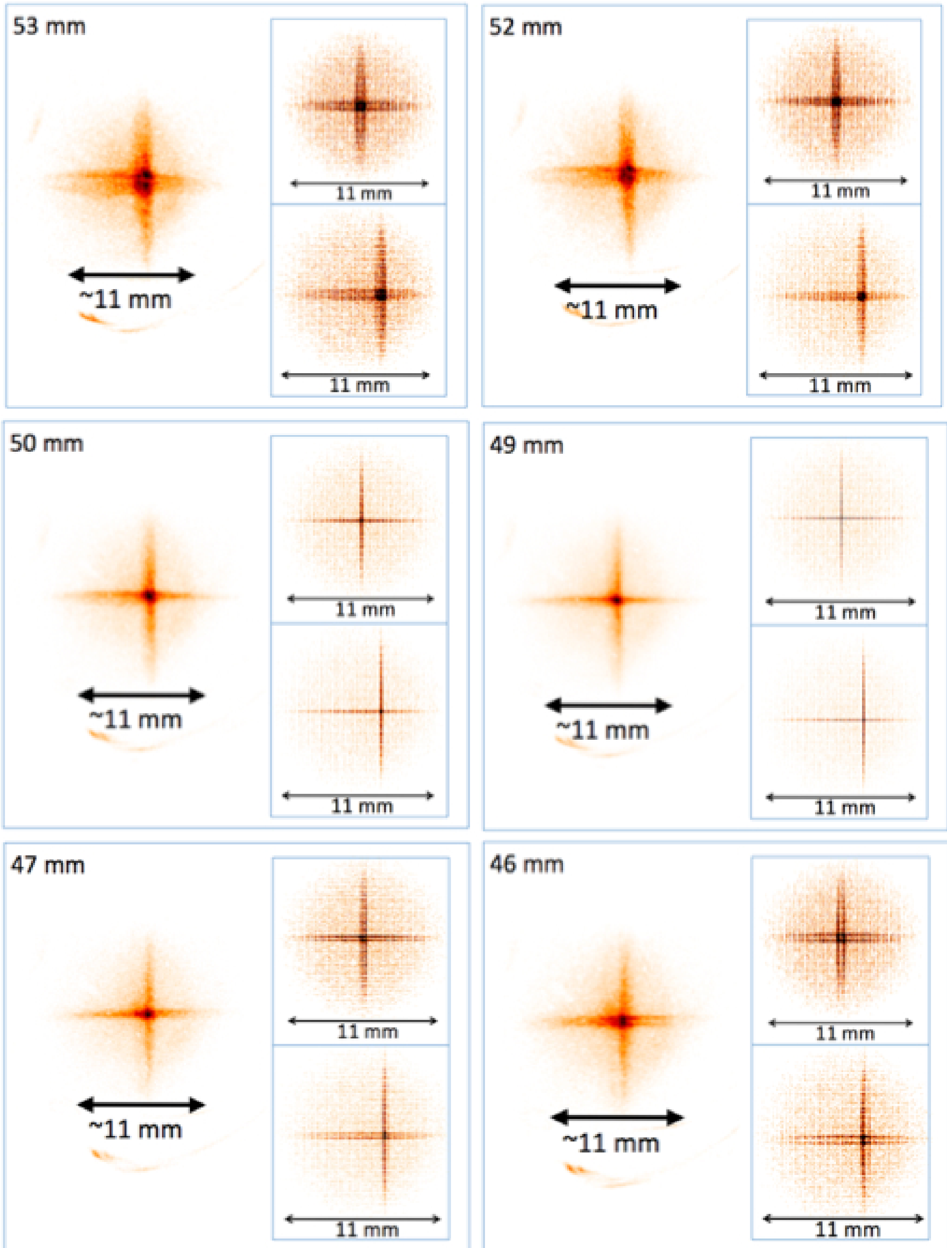

Figure 4.8 — *Comparison between measured WFAI images and simulated images produced by a model with the same parameters, for detector-optic separations varying from 53 mm (top left) to 45 mm (next page). In each case the experimental image is on the left, with a simulated image using an untilted optic in the top right corner and a simulated image using a tilted optic in the bottom right. For each of the tilted ray-traced images, the optic was tilted by 1° around the vertical (z) axis and by 0.2° around the horizontal (y) axis. The detector-optic distance given above the measured PSF in each case.*

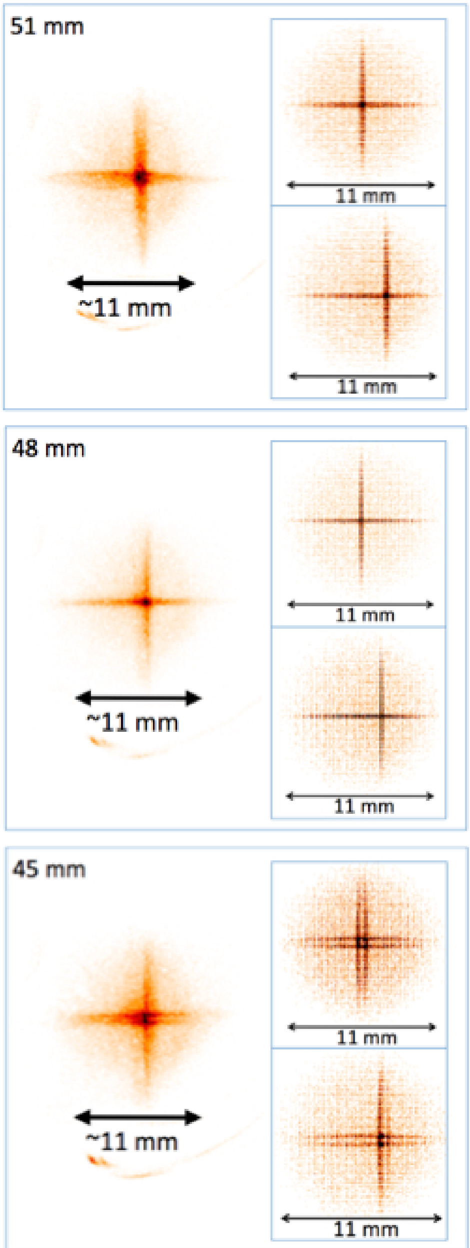

Figure 4.8 — *Cont.*

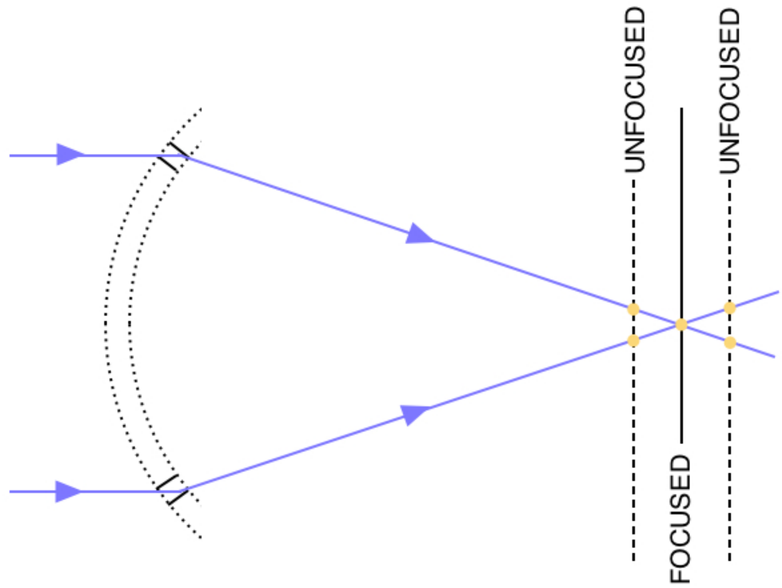

Figure 4.9 — *Diagram (not to scale) showing the origin of the bifurcation seen in unfocused MCP optic images. The rays focused by different regions of the optic intersect the detector in different places if the detector is not at the focal plane.*

detector-optic separation, for the x and y measurements in the DTF coordinate system respectively. The real data is identical to that contained in Figure 4.5, and the theoretical data was measured from the modelled images using the IDL function 'FullWid_HalfMax' [Varosi, 1994], with both the tilted and untilted images considered. The measurements from the SRT model were considerably smaller than the DTF results at every detector-optic separation, as expected given the visible difference in PSF extent in the modelled and experimentally obtained images. In the x direction, the shapes of the SRT and DTF curves are are similar for detector-optic separations of 47 mm or greater, but the raw DTF FWHM curve (the green line in Figure 4.10) is much steeper than the SRT curves below this distance. In the y direction, the DTF curves are considerably steeper than both the tilted and untilted optic SRT curves.

The smallest FWHMs were found in the modelled images corresponding to a detector placed 49 mm behind the model optic: the FWHMs (in degrees) for both the tilted and untilted optic at this separation are given in Table 4.4. In both the x and y directions, the

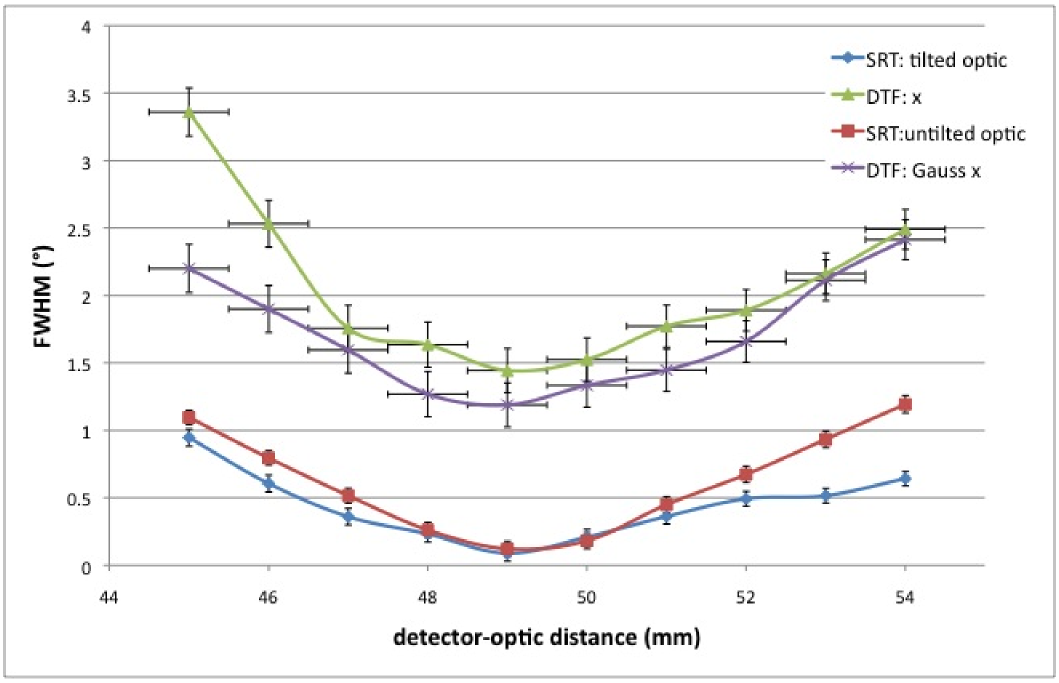

Figure 4.10 — *Comparison between DTF FWHM results and corresponding predicted FWHM results from SRT modelling for the WFAI optic. This plot shows the results measured from cuts through each image in the x direction.*

tilted optic gave best-focus images, with lower FWHMs than the untilted model. This may be due to the slight difference in the distance travelled between photons focused in each position, as shown in Figure 4.12a: the slightly larger distance travelled by photons focused by the tilted optic may be closer to the optic focal length. Another possible reason for the lower PSF in tilted optic images is the projection of the curved focal plane onto a flat image, as shown in Figure 4.12b. The difference between an area on the curved focal plane and its projection onto the flat image increases as the area of interest moves further off-axis.

The theoretical limiting resolution for the WFAI optic at l_i = 49 mm (calculated using Equation 4.2) is 0.117°, which lies within the uncertainty range of all four measured values shown in Table 4.4. A slight increase in the measured PSF size relative to the theoretical value is to be expected due to the use of an extended, rather than point, source, although the relatively large errors associated with the FWHM values given in Table 4.4

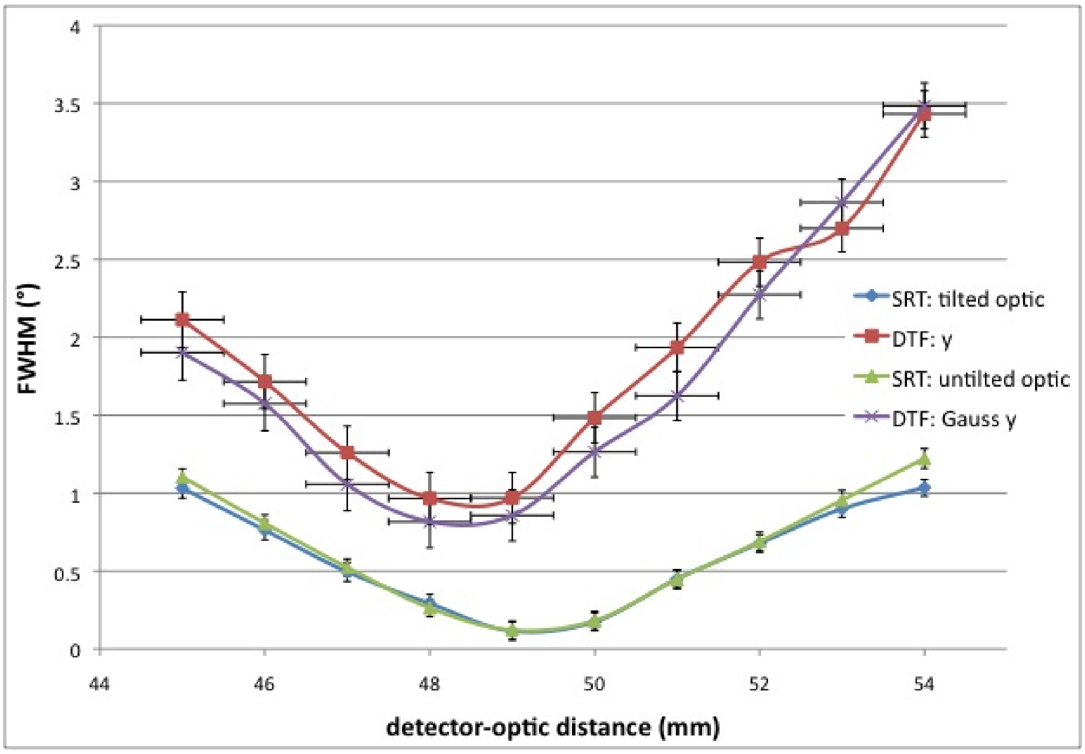

Figure 4.11 — *Comparison between DTF FWHM results and corresponding predicted FWHM results from SRT modelling for the WFAI optic. This plot shows the results measured from cuts through each image in the y direction.*

Table 4.4 — *FWHM of the WFAI PSF at l_i = 49 mm, as measured from SRT images. The error quoted is ± the angle subtended by one 0.05 mm pixel at a distance of 49 mm.*

	x FWHM (°)	y FWHM (°)
Untilted	0.121±0.058	0.121±0.058
Tilted	0.088±0.058	0.115±0.058

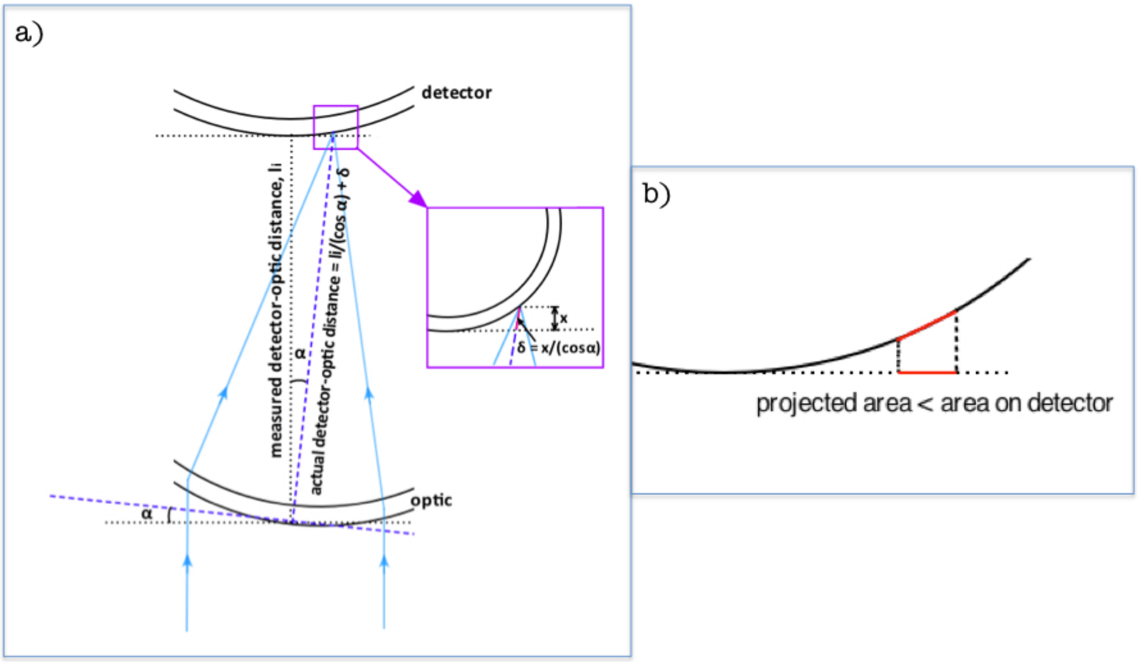

Figure 4.12 — *Possible explanations for the smaller PSF observed in tilted optic images. a) The slightly larger distance travelled by photons focused by the tilted optic may be closer to the optic focal length. b) The difference between an area on the curved focal plane and its projection onto the flat image increases as the area of interest moves further off-axis.*

mean this effect is difficult to isolate. The errors may be reduced by decreasing the pixel size used for the modelling, but software limitations mean that 0.05 mm is the current lower limit possible. The effect of source size on MCP optic images is discussed further in Section 4.1.5.

Although some difference between the FWHMs measured from the measured and laboratory images is expected due to the imperfect nature of the real WFAI optic, there are additional degradations to the PSF of DTF images produced by the imaging technique itself. These can be corrected for as described below.

4.1.4 Corrections to the measured FWHM

4.1.4.1 Correcting for the FWHM of the electronics chain

Noise can be introduced to the DTF images by the signal processing electronics chain that converts the signal from the MCP detector into the image displayed on the computer. In order to quantify this noise, a test pulse was passed through the DTF electronics chain and the FWHM of the resulting image measured. The image produced by the pulse is shown in Figure 4.13. If no noise was introduced by the electronics, the test pulse would produce an image in one pixel only. Figure 4.13 shows that this was not the case: an extended image was produced. The measured FWHM of the image was found to be 1.95 pixels in the x direction and 1.42 pixels in the y direction, or 2.02 in the x direction and 1.42 in the y direction if the Gaussian fit method was used. With the assumption that the electronics noise and the intrinsic focus FWHM combined in quadrature, the noise values were used to correct the FWHM values measured in the focusing tests as follows:

$$\mathrm{FWHM}_{\mathrm{corrected}} \approx \left(\mathrm{FWHM}_{\mathrm{image}}{}^2 - \mathrm{FWHM}_{\mathrm{electronics}}{}^2\right)^{\frac{1}{2}}. \tag{4.3}$$

This correction reduced the minimum FWHM to 1.405° in the x direction (Gaussian-fitted FWHM = 1.145°; detector-optic separation = 49 mm) and 0.937° in the y direction (Gaussian-fitted FWHM = 0.781°; detector-optic separation = 48 mm).

4.1.4.2 Linearisation

Another effect that can cause distortions in an MCP detector image arises from the use of a resistive anode readout (see Chapter 2, Section 2.3.2.1). The resistive anode encoding leads to geometric distortions, with images becoming compressed at the edges of the detector, as shown in Figure 4.14 (see Fraser and Mathieson [1981]). It is this effect that is responsible for the slight difference in the x and y measurements of the diameters of the noise image discussed in Section 4.1.2. In order to correct for the image distortions, a pinhole mask image was obtained. The optic was removed from the DTF and a metal plate containing a regularly spaced array of pinholes was placed directly in front of

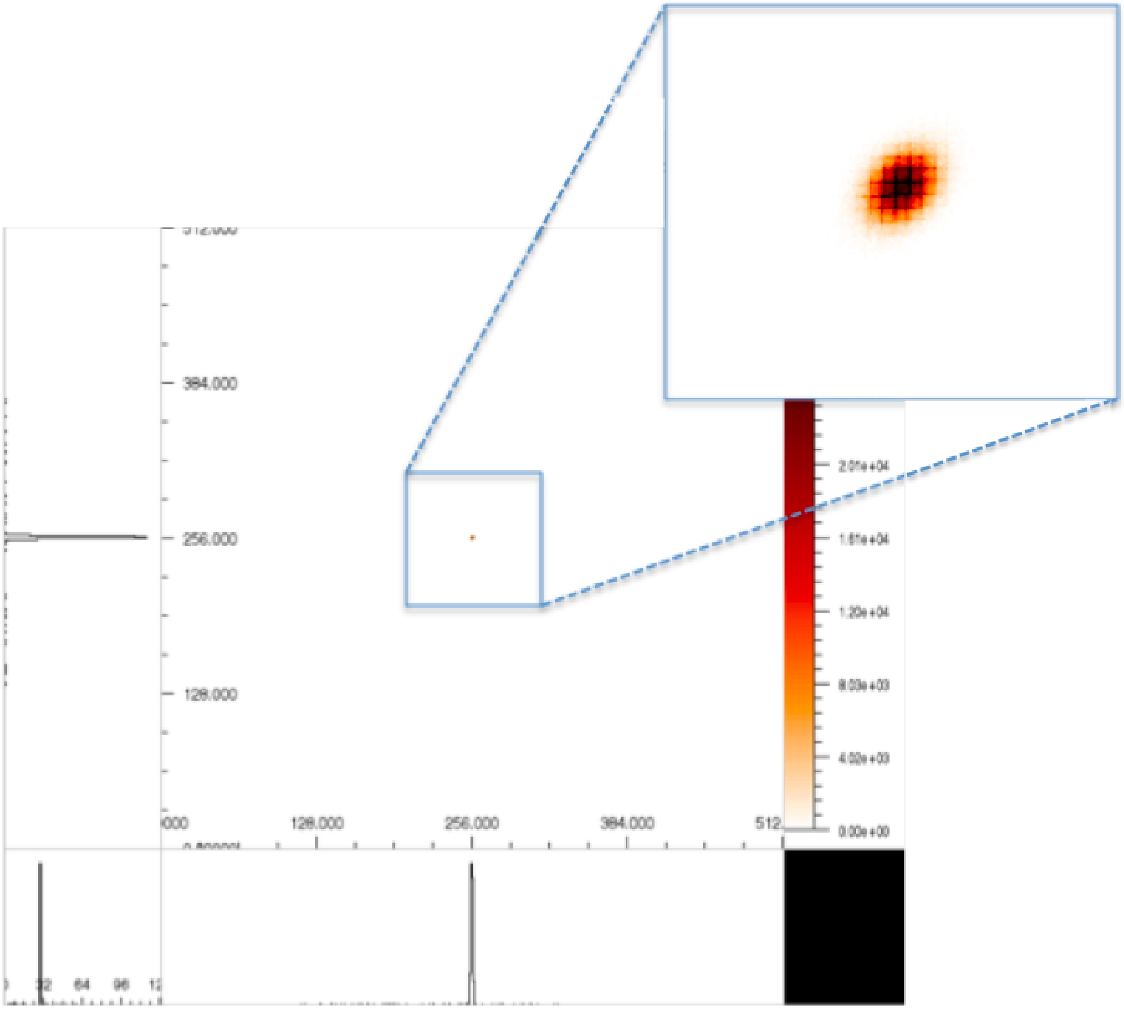

Figure 4.13 — *Image produced by passing a test pulse through the DTF electronics chain. The digitisation visible in the zoomed-in image is due to the limiting resolution of the electronics, i.e. the effective pixel size of the detector readout (see Chapter 2, Section 2.3.2.1).*

the detector and illuminated using the deuterium source. The DTF's beam-collimating pinholes were removed to allow ∼full field illumination, as was an attenuating mesh that was found to have been placed in front of the first pinhole. The image that was produced is shown in Figure 4.15. By measuring the apparent pinhole spacing in the image, and comparing it to the known pinhole spacing in the mask, it was possible to create a look-up table describing the displacements between the measured and actual positions of photon impact at any point on the anode. Distortions in any images acquired by the WFAI detector could then be corrected for by adding the relevant displacement, in the look-up table, to the position of every event measured. The look-up table produced during the WFAI focusing tests was created by Jon Lapington (University of Leicester). Its effect on the shape of the noise image shown in Figure 4.4 can be seen in Figure 4.16: the circles drawn over each image are identical and the fit with the corrected image is clearly better than that with the uncorrected image. A circular noise image is expected, as the active area of the prototype WFAI detector is circular. Hence, the linearity correction performed as expected.

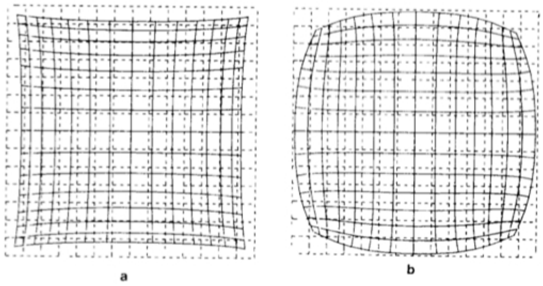

Figure 4.14 — *Examples of the transformation of a rectangular test grid by a resistive anode readout into an output with pincushion (a) or barrel (b) distortion. From Fraser and Mathieson [1981].*

Linearisation using the look-up table did not make a significant difference to the size of the PSF measured in each of the WFAI focusing tests, since the central focus of each image was very close to the centre of the detector face, where the distortion is at a minimum. However, the plate scale of the DTF images was measured from a linearised image as 8.51 pixels mm^{-1}, rather than the value of 7.15 pixels mm^{-1} measured earlier

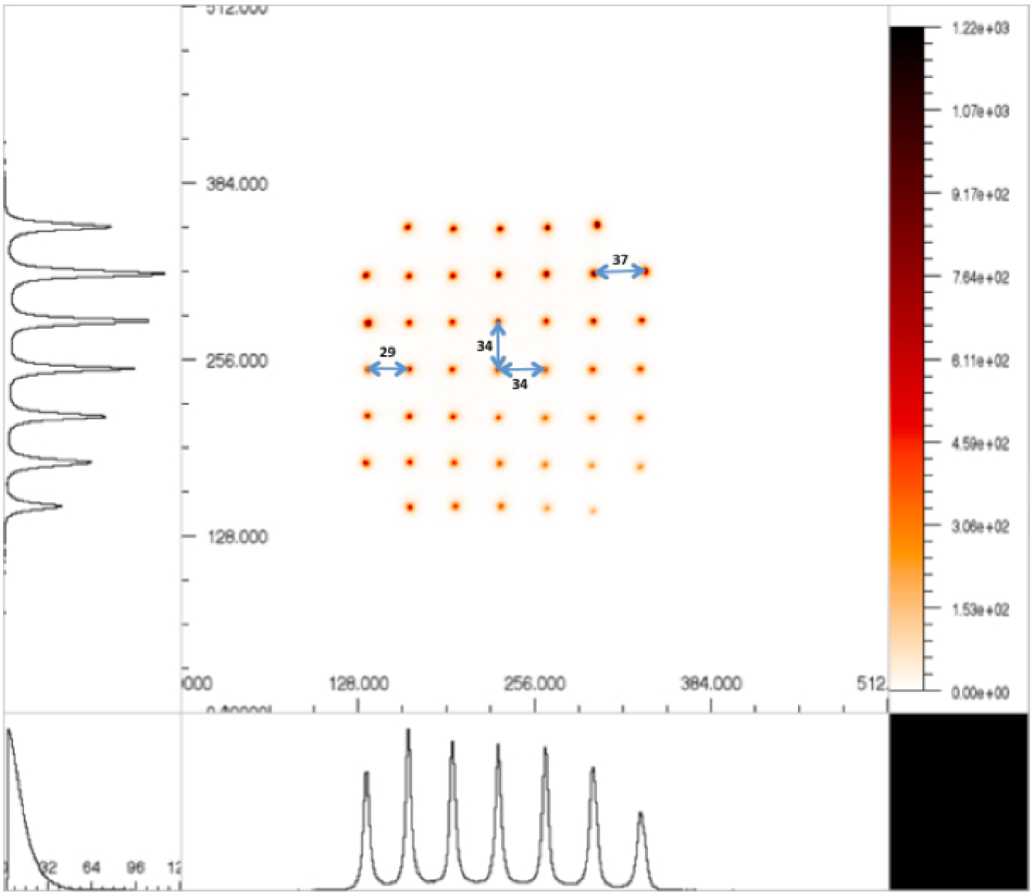

Figure 4.15 — *Image produced by placing a plate containing regularly spaced pinholes directly in front of the WFAI detector and illuminating it with the deuterium source. The WFAI optic was removed from the DTF for this part of the testing. Although the distorting effect is more obvious with larger detectors, slight differences in the pinhole spacing are observed: the values marked are distances between pinholes in pixels. The extent of the distortions is greatest around the perimeter of the imaging area.*

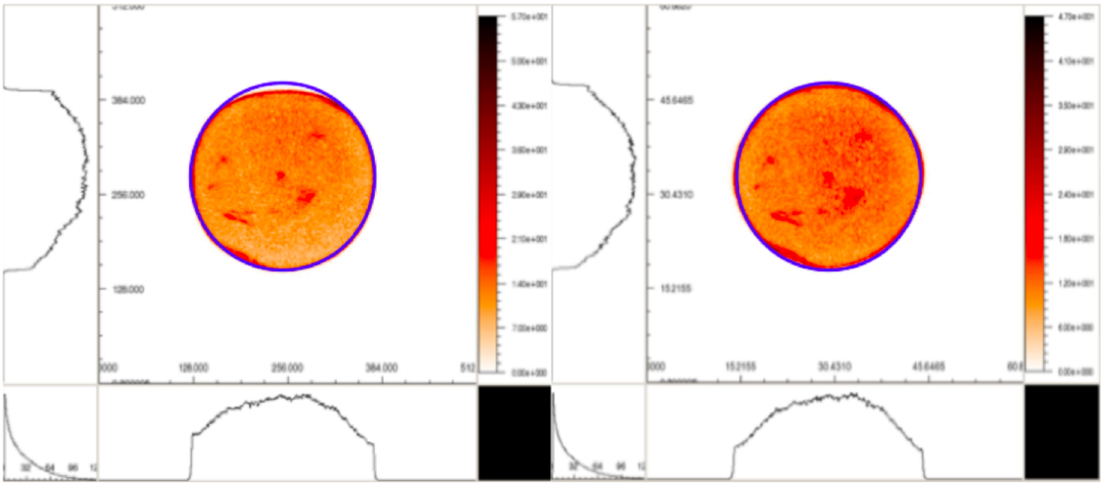

Figure 4.16 **—** *Left: the original noise image of the WFAI detector as shown in Figure 4.4. Right: the same image with the linearisation correction file applied.*

(Section 4.1.2), and so the FWHM size in mm calculated earlier for each lab image was an overestimate. Hence the angular resolution was also overestimated. The conversion between pixels and degrees was repeated using the new plate scale, and the minimum FWHM was reduced from 1.405° to 1.181° in the x direction (Gaussian-fitted FWHM = 0.962°; detector-optic separation = 49 mm) and from 0.937° to 0.787° in the y direction (Gaussian-fitted FWHM = 0.656°; detector-optic separation = 48 mm).

4.1.4.3 Correcting for diffraction effects

Another factor that can contribute to the size of the PSF measured in MCP images is the presence of diffraction effects. Diffraction becomes increasingly important as longer wavelengths are considered, since the diffraction-limited angular resolution of an MCP optic is directly proportional to the wavelength of interest (see Chapter 3, Section 3.2). The Deuterium source used in the DTF emits a spectrum dominated by H Lyman-α radiation at 121.6 nm. The diffraction limit for the 100 μm pore WFAI optic illuminated by this source is therefore $\sim$4.18’. Subtracting this in quadrature from the WFAI FWHM measurements reduces the minimum FWHM only slightly: the minimum x value is reduced from 1.181° to 1.179° (Gaussian-fitted FWHM: from 0.962° to 0.960°) and the minimum y measurement from 0.787° to 0.784° (Gaussian fitted FWHM: from 0.656° to 0.653°). This does not mean that diffraction effects are not important– for a perfect WFAI optic and an image distance of 48 mm, diffraction would degrade the angular resolution by $\sim$15%, from 0.119° to 0.138°. However, in the case of the current focusing tests, there are clearly other factors that have a more detrimental effect on the resolution than does diffraction. The presence of these additional detrimental effects means it is not possible to use the WFAI focusing tests to confirm that the magnitude of diffraction in the JUDE imager will be as predicted by the models described in Chapter 3. However, the general inability of MCP optics to achieve their theoretical resolution, as demonstrated by these tests and previous experiments [Martindale, 2011] is just as critical to the JUDE MCP optic design case as the specific degradation at FUV wavelengths caused by diffraction.

4.1.5 The contribution of the finite source size to the FWHM

4.1.5.1 The effect of source size on experimentally obtained images

Although the minimum FWHM measured during the focusing tests can be reduced by considering quantifiable sources of noise, this reduced FWHM will not reach the pore size-limited resolution calculated using Equation 4.2 because it must also contain a contribution related to the source size. In the case of the DTF, the source size is a combination of the output angle of the UV lamp and the size of the pinholes that collimate the UV beam. The spread of the UV beam in the DTF is controlled by two parallel pinholes (See Section 4.1.1 and Figure 4.2). While the first of these, with a radius of 0.5 mm, is fixed in place, the second is one of two held on the same movable plate. During the initial focusing tests, the larger of these (diameter = 0.9 mm) was selected. A second set of focusing tests was therefore begun, with the smaller (diameter = 0.35 mm) pinhole in place, producing a smaller UV beam in an attempt to reduce the FWHM of the PSF images further. The use of the smaller pinhole significantly reduced the count rate at the WFAI detector, from $\sim$150 counts s^{-1} in the earlier tests to $\sim$13 counts s^{-1} in the second set. The count rate for the noise image shown in Figure 4.4 was $\sim$4 counts s^{-1}, so the signal to noise ratio was decreased from 37.5 : 1 to 3.25 : 1 between the two focusing test runs. This was evident in the images obtained, as the PSF in the small pinhole tests was difficult to resolve above the background noise. Figure 4.17 shows one such image, taken with a detector-optic separation of 48 mm. The image intensity has been scaled, as only a faint spot in the PSF centre could be seen in the original image. The cruxiform structure is visible near the centre of the intensified image, but two of the cross arms are significantly broadened by noise counts and other noise effects can be seen around the edges of the detector area[4].

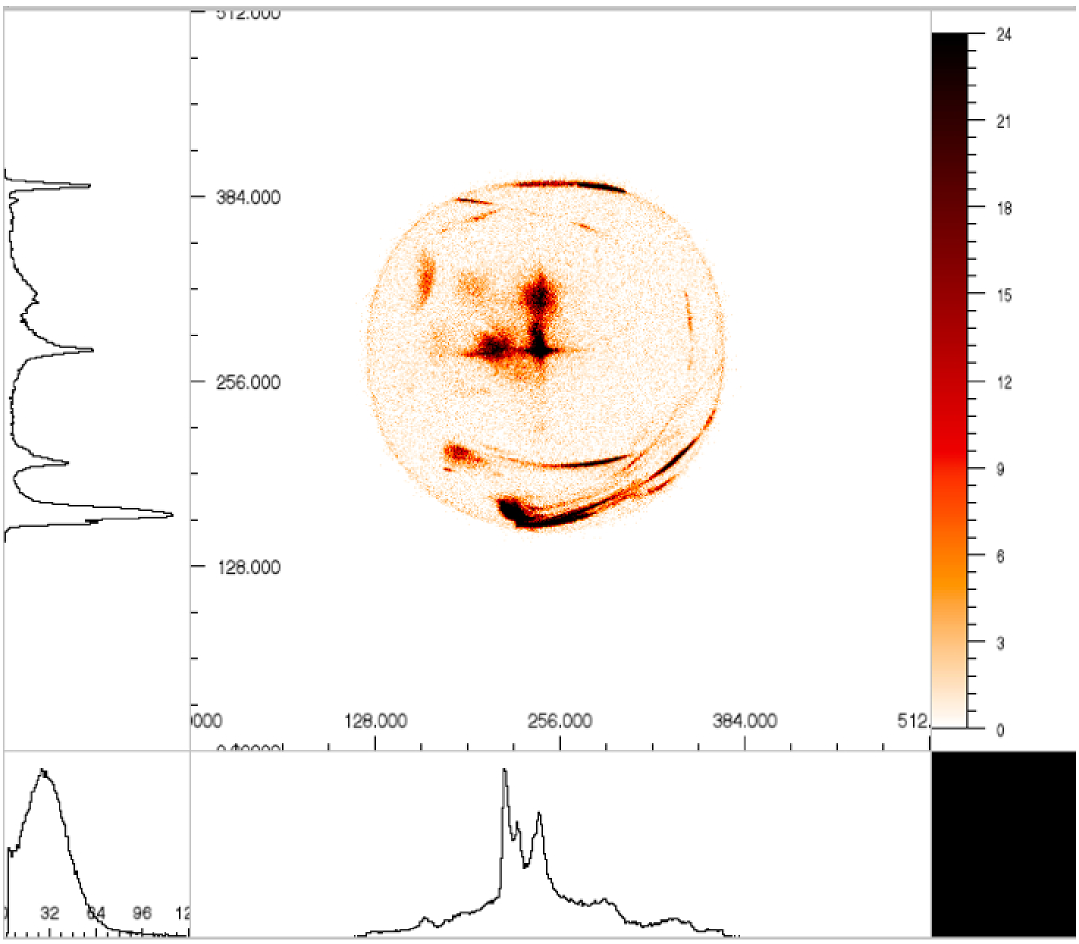

Figure 4.17 — *DTF image obtained using the 0.35 mm diameter pinhole to constrain the UV beam (image intensity has been scaled so that the PSF is visible). Detector-optic separation = 48 mm.*

[4] The noise effects are also present in the larger pinhole images, but are less obvious in these since the signal levels are higher.

In order to increase the flux through the collimating pinholes, the attenuation filter that was in place during the initial focusing tests was removed from the DTF. This successfully increased the count rate at the detector to $\sim$111 counts s^{-1} but the quality of the PSF images was not significantly improved. An example of an image obtained during this set of tests is shown in Figure 4.18. In the original image (left panel of Figure 4.18), only the central focus and one cross-arm of the PSF can be seen, and these do not appear to be any smaller than the focus and cross-arms of the equivalent image obtained with the large pinhole. The signal to noise ratio is clearly better than in Figure 4.17, as evidenced by the fact that none of the detector edge noise features can be seen. When the image was scaled to bring out low signal level features, each of the additional three cross-arms become visible to some extent (right panel of Figure 4.18), but the broadening of the strongest arm and the central focus made it impossible to obtain a reliable FWHM measurement.

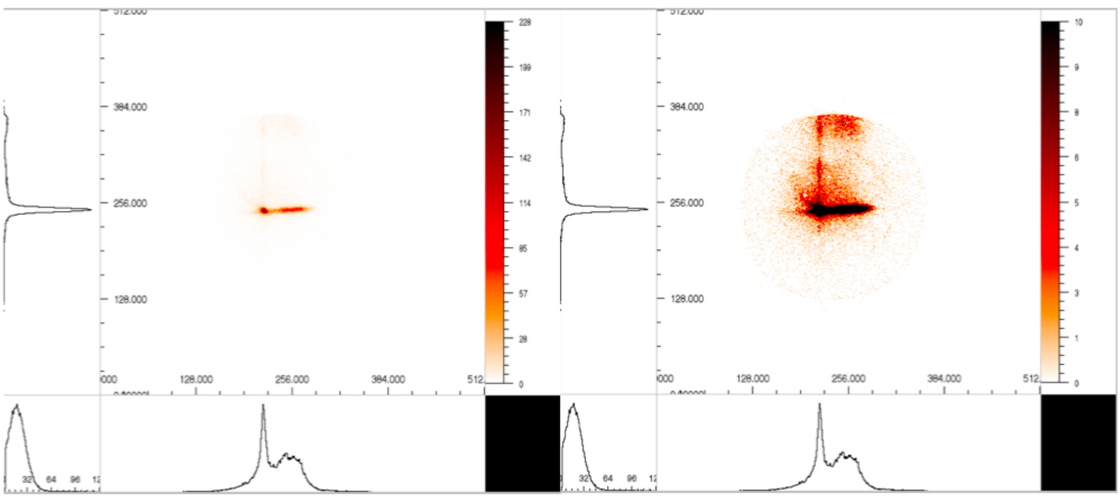

Figure 4.18 — *DTF images obtained using the 0.35 mm diameter pinhole to constrain the UV beam, after removal of the attenuating mesh. Left: original image. Right: the same image with intensity scaled so all four cross-arms can be seen.*

In order to investigate the properties of the broadened cross-arm, the image was replotted to show the mean pulse height at each point rather than the intensity. The result is shown in Figure 4.19. The lighter area surrounding the broadened cross-arm is an area of lower mean pulse height, suggesting that the detector gain was lower in that area. Low gain can have a detrimental effect on the signal to noise ratio of images obtained with MCP detectors, since the signal is split into four at the anode readout: a smaller signal gives a smaller signal to noise ratio. The voltage across each of the WFAI detector MCPs was increased from 1500 V to 1600 V to increase the gain across the whole detector, but this did not have an appreciable effect on the images obtained. Gain suppression can occur in MCP detectors when the count rate is too high, as there is not enough time for the channels to replenish their charge between events [Fraser et al., 1991]. However, at a rate of 111 counts s^{-1} this is unlikely to be a problem: the maximum WFAI count rate to allow charge recovery is 0.6 counts s^{-1} channel^{-1} (Bannister et al. [2007]; see also Chapter 3, Section 3.4.1), so the 111 counts each second would have to be concentrated over fewer than 111/0.6 = 185 channels for gain suppression to occur. For the WFAI detector, which has a channel diameter of 12.5 μm and an active area fraction of 63%, this is equivalent to an area of just 3.6×10^{-2}mm^2.

Since there was no obvious cause for the uncharacteristic appearance of the PSF observed in the small pinhole tests, the section of the DTF containing the pinholes was let up to atmospheric pressure with dry nitrogen to allow examination of both plates and to check that the holes were well aligned. At this time, the plate holding the 0.9 mm and 0.35 mm diameter pinholes was damaged, so the small pinhole focusing tests could not continue. However, ray tracing simulations have been performed to investigate the expected results of the small pinhole tests.

4.1.5.2 SRT investigations of source size effects

In order to investigate the effect of the extended DTF source, the code used to produce the untilted optic images shown in Figures 4.7 and 4.8 was altered to specify a point source at a distance of 1.5 m from the optic, rather than a 15° extended source. All other parameters remained unchanged, and images were once again obtained at detector-optic distances ranging from 45 mm to 54 mm. The FWHM of each image was measured for comparison with the corresponding extended source image. Figure 4.20 is a plot showing the FWHM measured from both the extended and point source sets of SRT images as a

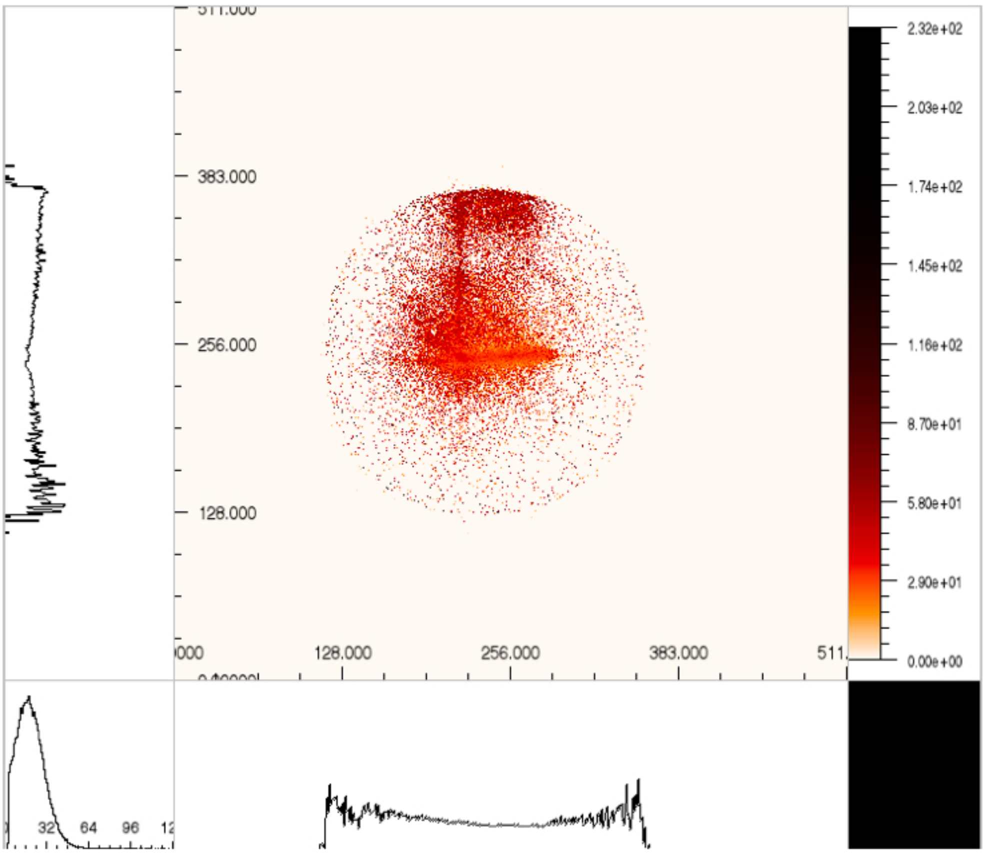

Figure 4.19 — *Mean pulse height distribution in the image shown in Figure 4.18. The area around the broadened cross-arm is made up of smaller pulses than the rest of the image, suggesting that the gain was lower in that part of the detector.*

function of detector-optic separation. The SRT model was then altered to replace the 0.9 mm diameter pinhole with a 0.35 mm diameter pinhole in the same location, and images were obtained for both point and extended sources for the same range of detector-optic separations. Figure 4.21 is the equivalent of Figure 4.20 for the small pinhole setup. In both plots, the error bars show the angular extent of one 0.05 mm pixel at the relevant image distance.

Both Figure 4.20 and Figure 4.21 show that the effect of the source size on the size of the PSF produced is greatest in the least focused images towards the extremal values of each plot. The FWHM was consistently smaller in the small pinhole images for both the extended and point source images, which was expected since the beam was more

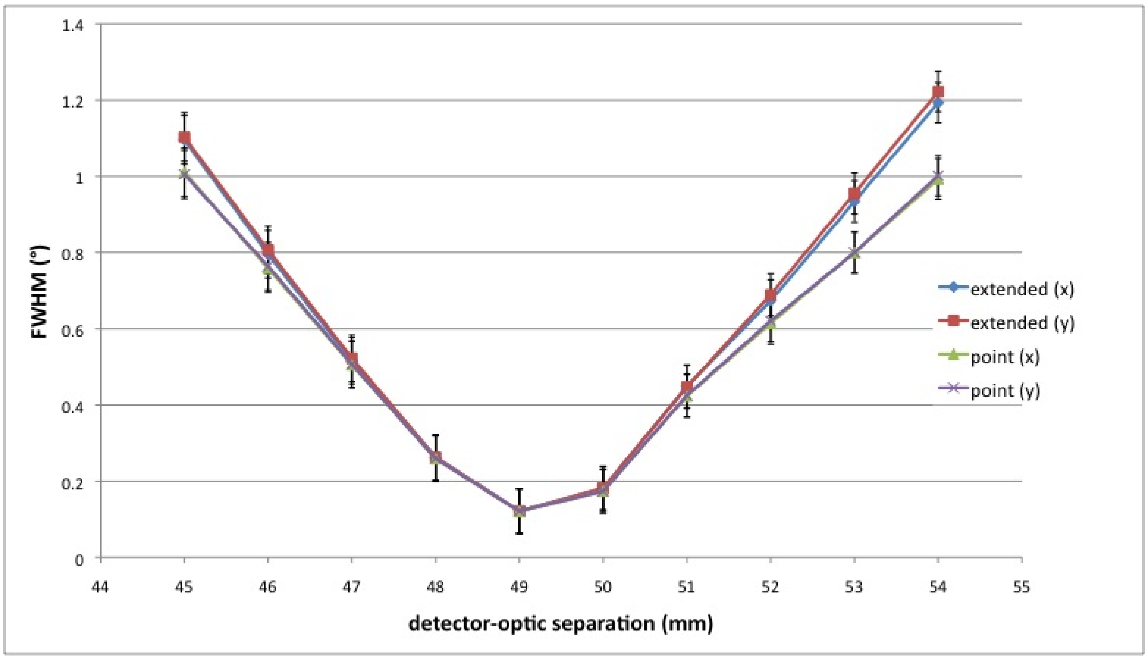

Figure 4.20 — *Comparison of FWHM measurements from SRT measurements of both point and extended sources, for the 0.9 mm pinhole configuration.*

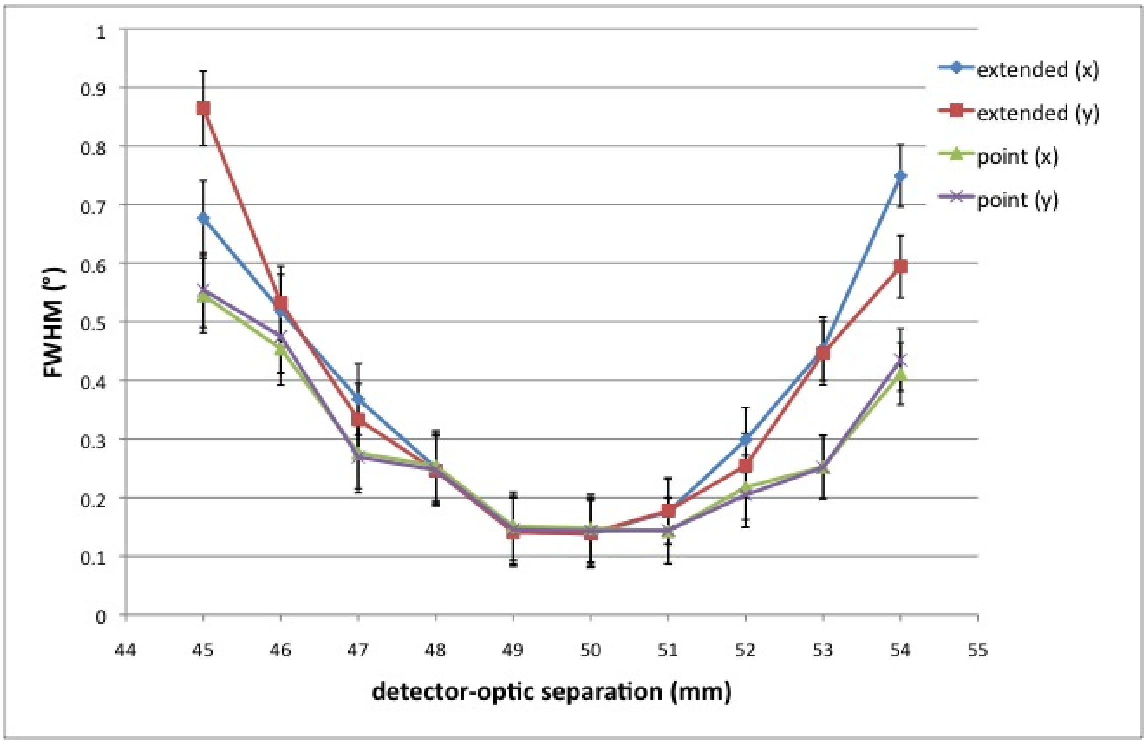

Figure 4.21 — *Comparison of FWHM measurements from SRT measurements of both point and extended sources, for the 0.35 mm pinhole configuration.*

constrained in these simulations. However, the signal to noise ratio was much worse, as the narrow beam was concentrated on the centre of the optic, where the shallow angles of the pores relative to the optical axis allow more rays to pass straight through without being reflected by the channel walls, increasing the background levels around the PSF. Figure 4.22 shows a comparison of one focused (panel a) and one unfocused (panel c) small pinhole image with the large pinhole images obtained at the same image distances (panels b and d). In each panel, the SRT image is shown alongside a cut along the x cross arms. The cruxiform PSF is particularly difficult to resolve in the unfocused small pinhole image shown in panel c. This may explain the difficulty experienced when attempting to obtain DTF images with the small pinhole selected. When a tilt in the optic of -1.0° about the vertical axis and -0.2° about the horizontal axes is added, the focused small pinhole image begins to resemble that seen in the DTF, but without the one enlarged cross arm: compare Figure 4.23 to the right panel of Figure 4.18.

An approximation of the contribution of source size to the FWHM of the large pinhole extended source images was made by subtracting the FWHM of the corresponding point source image in quadrature. The values given were then subtracted from the experimentally obtained FWHM measurements to give an estimate of the expected resolution of the real WFAI optic when viewing a point source. However, since the contribution of the source size was least for the most well-focused images, the effect this had on the estimate of the best resolution of the optic was small: the minimum y FWHM was reduced by $\sim$0.06 arcminutes, and the minimum x FWHM by $\sim$0.0024 arcminutes (the difference between the magnitude of effect in each dimension is due to the different focal lengths measured in the DTF tests: the x focal length of 49 mm was equal to the focal length measured from SRT images, where the source contribution was found to be lowest; the source contribution at the y focal length of 48 mm was slightly higher according to SRT measurements).

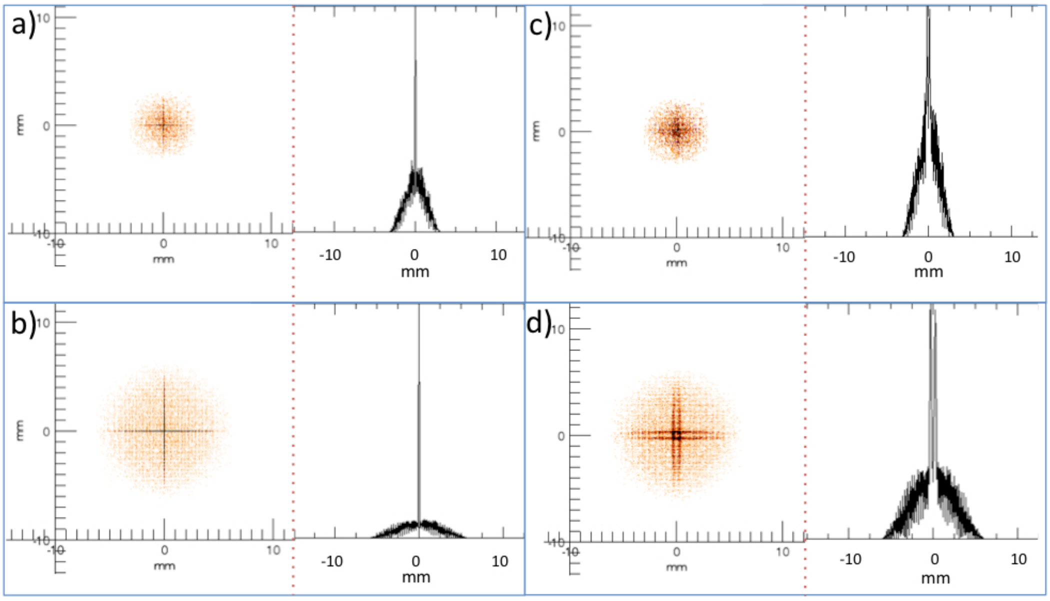

Figure 4.22 — *a) Ray-traced simulation of a focused, extended source with the 0.35 mm pinhole selected, alongside a cut through the image along the cross arms. b) As panel (a) but for an unfocused ray-traced image. c) Focused ray-traced PSF image of an extended source with the 0.9 mm pinhole selected, alongside a cut through the image along the cross arms. d) As panel (c) but for an unfocused ray-traced image.*

4.1.5.3 Deconvolution of the optic PSF from extended source images

In a real observation of an auroral emission feature, the size of sources imaged will be unknown. In this case, the intrinsic PSF of the optic must be deconvolved from the images produced by the instrument to give the source intensity distribution. This is a complex problem, particularly when the image contains multiple sources with overlapping cross-arms, but has been attempted for a similar slumped MCP optic by Peele [2001], who concluded that it was feasible. This recovery of the source information from MCP images is one of the most important issues to overcome in the development of MCP optics, including the WFAI optics currently under development.

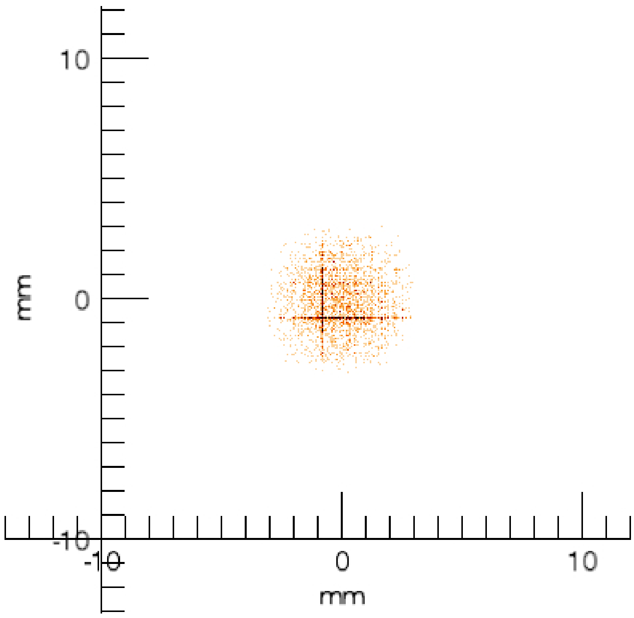

Figure 4.23 — *Focused SRT image of a 15° extended source, using a WFAI optic tilted by -1° around the vertical axis and -0.2° around the horizontal axis.*

4.1.6 Summary of corrections to the WFAI FWHM

Table 4.5 gives a summary of all the corrections to the measured WFAI resolution described within this chapter. After all corrections were applied, the DTF FWHM measurements were reduced to ∼80 % of their initial values. The SRT measurements given in the table provide an estimate of the best resolution possible for a perfect WFAI optic, which was found to account for ∼10–20 % of each final DTF FWHM measurement. The other 80–90 % of the focus extent will be due to imperfections in the MCP optic. These may include: surface roughness on the channel walls, which would reduce reflectivity or affect the angle of reflection of incident rays; deviations of the directions of channels away from the optical axis; twisting of channels introduced during the drawing stages of manufacture (see Chapter 2, Section 2.1.1.1); and misalignments of channels introduced during the stacking stages of manufacture. The slumping process may also introduce errors, such as deviations from a spherical profile: such deviations are investigated in Section 4.1.7. To date, no slumped MCP optic focusing test has been able to match the theoretical resolution of the optic used. It has been suggested that the resolution is limited by the size of the multifibres that make up the MCP [Martindale and Molyneux, 2009]: during the slump process, each multifibre may become angled toward the centre of curvature while the individual channels within the multifibre remain parallel to each other. If correct, this would have a significant broadening effect on the PSF produced by an MCP optic. In future, deformations of varying magnitude may be added to the optic in SRT models of the DTF tests, in order to investigate the extent of imperfections within the plate necessary to produce images with the observed FWHM.

***Table 4.5** — Summary of corrections to the WFAI FWHM measurements*

	FWHM (degrees)			
	x	y	Gauss x	Gauss y
Initial measurements	1.443	0.969	1.188	0.816
After electronics correction	1.405	0.937	0.145	0.781
With plate scale from pinhole mask	1.181	0.787	0.962	0.656
After diffraction correction	1.179	0.784	0.960	0.653
After source size correction	1.179	0.784	0.960	0.653
Final value / initial value	81.7 %	80.9 %	80.8 %	80.0 %
SRT best focus	0.121	0.121	–	–
SRT values / corrected DTF values	10.3 %	15.4 %	12.6 %	18.6 %

4.1.7 Optic profiling

Surface profilometry of the WFAI optic was performed to check whether the slump radius of the MCP agreed with the 100 mm value given in the specifications. Any deviation from this value would affect the focal length of the optic, and differences in curvature in different regions of the MCP may explain the difference in the x and y focal lengths measured in the WFAI focusing tests. The profilometry was also used to investigate if a dark line visible in the glass towards one edge of the optic was superficial or indicative of surface damage, possibly due to pressure from the optic mount.

Measurements were taken using a Rank-Taylor-Hobson Talysurf profilometer, which obtained surface height data by dragging a stylus with a 0.5 mm radius inductive tip across the surface of the optic and recording the variation in its vertical position. An inbuilt data analysis package was used to determine the radius of curvature from the raw profile. The package also returned information about the surface roughness, in the form of three parameters: the arithmetic mean roughness, R_a; the RMS average roughness, R_q; and the maximum roughness height, R_t. A raw surface profile, modified profile (created by subtracting the calculated radius of curvature from the raw profile) and an amplitude distribution (showing the distribution of the heights of peaks in the measured profile data) were plotted for each surface measurement. Traverses of the optic by the stylus were performed in four directions passing through the centre of the MCP, as shown by lines E, F, 1 and 2 in Figure 4.24. Four additional traverses along the edges of the plate ($\sim$2 mm from each edge) were performed (lines A–D in Figure 4.24), including one that passed over the marked portion of the plate. Measurements were performed first with the optic in its mount, and then with the top cover of the mount removed, to check whether pressure from the mount was distorting the optic at all. The results for all traverses are shown in Table 4.6.

An example of the plots generated by the Talysurf can be found in Figure 4.25. As shown in Table 4.6, the curvature of the mounted MCP optic was consistently measured to be below the 100 mm expected value, with a mean R_{MCP} of $\sim$96.3 mm, and all measurements showed the plate to be smooth to an RMS roughness of $\sim$1 μm. A significant difference was found between the curvatures measured in traverses E and F, e.g. measurements along the x and y axes. This is consistent with a difference in focal length between the two dimensions, as suggested by the laboratory focal tests, although the Talysurf measurements imply optimum image distances of 45.0 mm (y focus) or 47.1 mm (x focus) for the DTF setup (using Equation 2.3 from Chapter 2 with l_s=1500 mm), which are both shorter than the measured focal lengths. The distance between these two values is larger than the measured difference of 1 mm, but this may be explained by the variation of R_{MCP} across the optic: the regions of the plate most likely to focus photons to the central spot of the PSF are toward the corners rather than across the centre (see

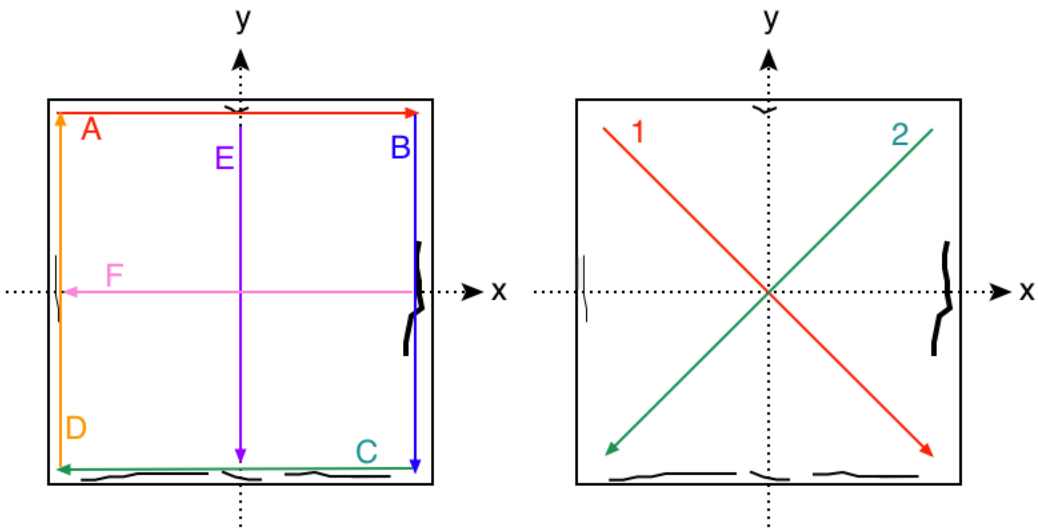

Figure 4.24 — *Diagrams showing the different measurements of the WFAI plate performed by the Talysurf. The darkest mark, at the right edge of the plate was the only mark visible when the optic was mounted. Fainter marks were seen on the other edges once the top cover of the mount had been removed.*

Table 4.6 — *R_{MCP} of the WFAI MCP optic, as measured by the Talysurf profilometer.*

Traverse	R_{MCP}: mounted (mm)	RMS roughness (μm)	uncertainty (mm)	R_{MCP}: unmounted (mm)	RMS roughness (μm)	uncertainty (mm)
A	97.3201	0.8627	$^{+0.0727}_{-0.0726}$	100.976	0.8588	$^{+0.0779}_{-0.0778}$
B	95.8521	0.8867	$^{+0.0725}_{-0.0724}$	98.1838	0.9085	$^{+0.0779}_{-0.0778}$
C	98.0962	0.8871	$^{+0.0759}_{-0.0758}$	97.6891	1.2010	$^{+0.1020}_{-0.1018}$
D	97.3861	1.2228	$^{+01032}_{-0.1030}$	97.2836	1.2738	$^{+0.1073}_{-0.1070}$
E	92.8176	0.7164	$^{+0.0549}_{-0.0548}$	97.0066	0.8817	$^{+0.0738}_{-0.0737}$
F	97.1516	0.8434	$^{+0.0708}_{-0.0707}$	101.993	0.8781	$^{+0.0813}_{-0.0811}$
1	97.0905	0.9641	$^{+0.0809}_{-0.0807}$	98.4438	0.9975	$^{+0.0860}_{-0.0859}$
2	94.9257	0.8720	$^{+0.0699}_{-0.0698}$	97.3290	0.9385	$^{+0.0791}_{-0.0790}$

Chapter 3, Section 3.3.5).

The uncertainty values given in Table 4.6 were generated by calculating the maximum and minimum radius of curvature possible for an error of $\pm$ the RMS roughness of the optic in the vertical measurement (the sagittal depth of the optic). The slump radius, R_{MCP}, measurement radius a (e.g. half the length of the traverse considered) and sagittal depth w are related by [Martin, 2000]:

$$R_{MCP} = \frac{1}{2}\left(w + \frac{a^2}{w}\right). \tag{4.4}$$

Since the radius of curvature is much greater than the sagittal depth, this can be approximated by

$$R_{MCP} \approx \frac{a^2}{2w}. \tag{4.5}$$

Hence, if the error in w is known, the maximum and minimum radius of curvature for the optic may be calculated (Figure 4.26).

Even the largest R_{MCP} measured for the mounted optic suggests a focal length shorter than that measured in the focusing tests: R_{MCP} = 98.0962 mm implies an l_i of ~47.5 mm. It is likely that there is some error in the image distances measured in the laboratory tests: although the linear drive was accurate to 0.02 mm, and hence the 1 mm change in distance between images was accurately measured, the drive was not calibrated and the initial 45 mm detector-optic distance was measured with a ruler, leading to an estimated reading error of ±0.5 mm. SRT modelling in Section 4.1.3 suggested that a $\sim 1^\circ$ tilt around the vertical axis was likely. At the edges of the optic, this corresponds to an additional error in the detector-optic distance of ±0.35 mm (= $d \sin 1^\circ$, where d = 20 mm: half the optic sidelength). Furthermore, images were obtained only at 1 mm intervals, and the best focus may lie within one of these intervals. Hence it is difficult to be sure if the focal length of the optic as predicted by the Talysurf measurements corresponds well to the PSF-derived measurements. In future it may be helpful to repeat the focusing tests, with a profile of the optic obtained first and with a smaller interval between images around the predicted focus. A more accurate method of determining the initial detector-optic separation should also be established.

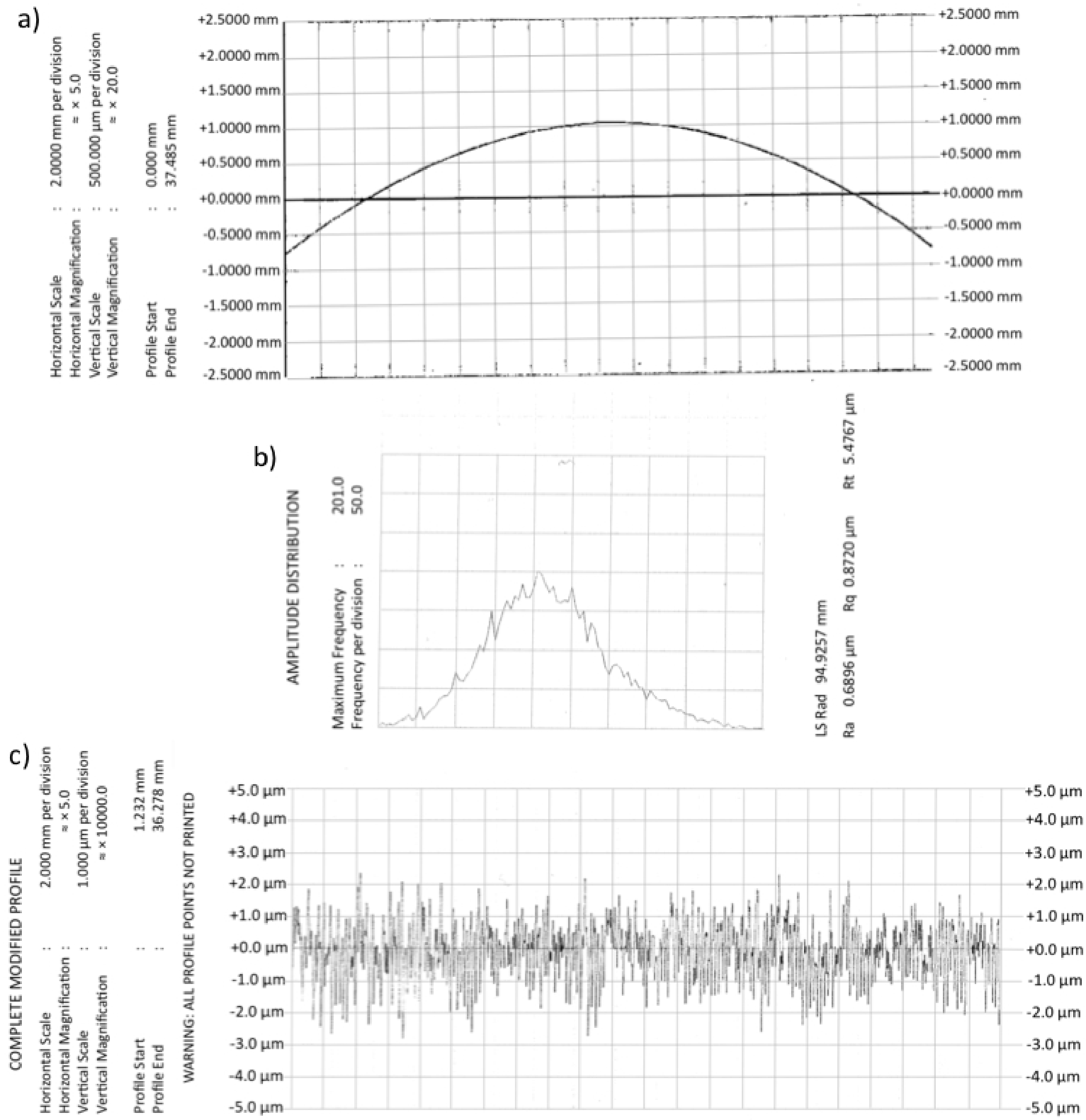

Figure 4.25 — *Scans of Talysurf plots generated for traverse 2 (as shown in Figure 4.24): a) Raw data; b) Distribution of amplitudes of peaks in raw data; c) Modified profile produced by subtracting the calculated slump radius from the raw data profile.*

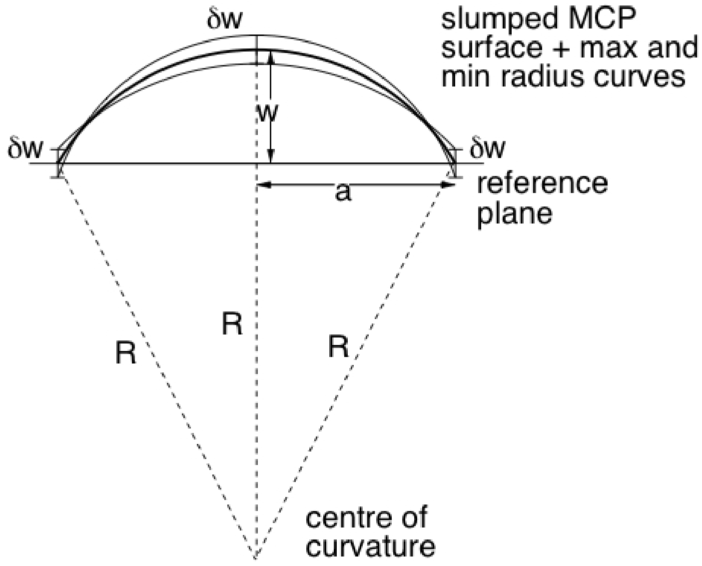

Figure 4.26 — *Estimate of error in R_{MCP} associated with a known error in sagittal height. From Martin [2000].*

Removal of the top cover of the optic mount allowed the full extent of the marked area of the plate to be seen and also uncovered other, fainter marks along each of the remaining edges, as indicated on the drawings in Figure 4.24. The Talysurf traverse along the edge that was initially thought to be damaged, marked by line B in the figure, did not reveal any unusual features, and the RMS roughness measured was similar to that for the other traverses, suggesting that the feature seen was superficial. The largest roughness values were measured for traverses C and D, which appeared less marked to the eye. This may be due to smaller, invisible cracks in the optic, or to dust or similar in the path of the stylus.

The Talysurf measurements obtained when the optic was unmounted were larger than the corresponding mounted measurement for all but two traverses– those indicated by lines C and D– with a mean R_{MCP} of $\sim$98.6 mm. This suggests that the mount was distorting the optic, with the largest effects being seen in the measurements indicated by lines E and F, for which the radius of curvature changed by $\sim$4.2 and 4.8 mm respectively. This may be due to the either the shape of the optic mount or to the four screws that hold the front on being tightened by different amounts. A profile of the mount would determine which of these was the case: the former would suggest a need for a new mounting system to be designed. This should be carried out before any future focusing tests with the WFAI MCP.

4.1.8 Future work

Since one of the DTF pinhole plates was deformed during the focusing tests, a new pinhole structure was manufactured, consisting of two metal sheets, each with a central pinhole, held together by metal supports so that the two holes were perfectly aligned. Focusing tests with the new pinhole structure have not yet begun, due to a turbomolecular pump malfunction in the DTF. A new pump has been obtained so the tests may be continued in the near future, with the aim of reducing the measured FWHM of the WFAI images further.

Future modelling work will concentrate on introducing deformations in the model optic in an attempt to match the measured resolution of the WFAI optic. This will provide an estimate of the magnitude of deformations introduced to the optic during the manufacturing process.

Additional areas of future research will include further investigations into the contribution of multifibre size on the achievable resolution of MCP optics, and on the issue of deconvolving the characteristic cruxiform PSF from MCP optic images.

4.2 Testing a *BepiColombo* MIXS collimator plate

BepiColombo is an ESA-led mission to Mercury, due for launch in 2014 and arriving at Mercury in 2020. The University of Leicester has a strong involvement in the Mercury Imaging X-ray Spectrometer (MIXS) (see Figure 4.27) on *BepiColombo* (the MIXS PI is G. W. Fraser, University of Leicester), particularly in the development, production and calibration of the optics and the calibration of the focal plane detector.

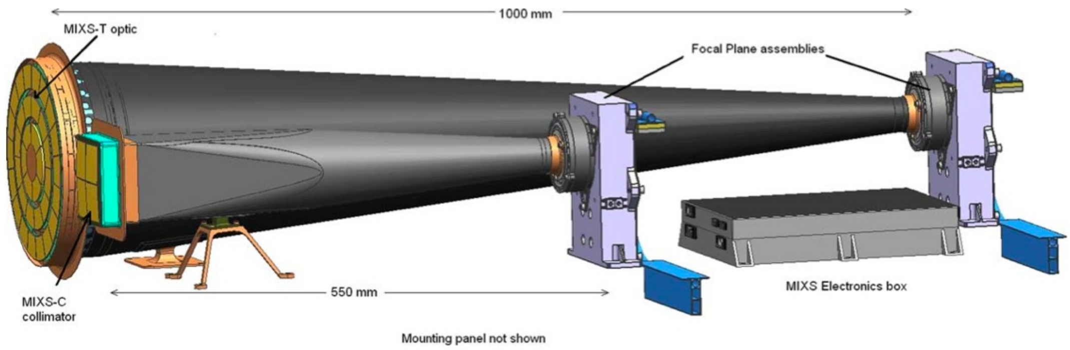

Figure 4.27 — *The* BepiColombo *MIXS instrument [Fraser et al., 2010]*

MIXS will measure fluorescent X-ray emission from the surface of Mercury, allowing its composition to be determined and the formation and evolution of the planet to be investigated [Fraser et al., 2010]. The instrument is comprised of two channels: MIXS-C is a collimator with a FOV, and therefore angular resolution, of 10.4°, corresponding to a spatial resolution at Mercury varying between 70 and 270 km over the course of each 400 km $\times$ 1500 km spacecraft orbit; MIXS-T is an imaging telescope with a 1.1° FOV and an angular resolution better than 9 arcminutes, providing a spatial resolution of better than 1 km at periherm (400 km altitude) [Fraser et al., 2010]. Both channels make use of MCP optics. MIXS-T uses radially packed, square-pore MCP optics, which are arranged to approximate a Wolter type 1 geometry (see Chapter 2, Section 2.1.1.2 for a description of Wolter type 1 geometry, and Willingale et al. [1998] for the MCP optic Wolter approximation). The MIXS-C collimator optics are an array of four slumped 40 $\times$ 40 mm square pack, square-pore glass MCPs, each with a slump radius of 550 mm, and this channel is similar in appearance to the MCP optic version of JUDE (compare the MIXS-C channel in Figure 4.27 with the JUDE design shown in Chapter 2, Figure 2.12). The most obvious difference between MIXS-C and JUDE is the position of the focal plane detector in each instrument: for JUDE, the detector is placed at a distance of $R_{MCP}/2$ so that parallel rays are focused to a point; for MIXS-C, the detector is placed at a distance of R_{MCP} where it will detect both collimated X-rays and those that have undergone grazing incidence reflection at channel walls (the large detector-optic separation means that reflected rays will be unfocused when they reach the detector and the cruxiform PSF will therefore not be seen). Another important difference is the channel width: the channels of the MIXS-C optics, at $d = 20\mu$m, are much narrower than the JUDE optic channels, which would make the MIXS-C optics unsuitable for FUV imaging due to diffraction effects scaling with λ/d. A comparison between the JUDE, MIXS-C and WFAI optics is given in Table 4.1.

4.2.1 The Tunnel Test Facility

A prototype MIXS-C optic MCP was tested in the University of Leicester's Tunnel Test Facility (TTF), a 27 m beamline with an X-ray source at one end and a detector test chamber at the other. The initial tests concentrated on finding the focal length of the MCP, using the same method employed in the WFAI focusing tests, and comparing this to the focal length predicted by theory for the MCP. The optic was then moved to a distance of twice the focal length away from the detector and tested as a collimator through a series of tilt angles, to explore its response to off-axis radiation. The detector used in the MIXS-C tests consisted of two planar MCPs with their channels oriented in a chevron arrangement, and a resistive anode readout. All of the tests were performed with X-rays of energy 0.28 keV. Figure 4.28 shows the reference axes that describe the TTF. The distance between the optic and detector was controlled by moving the detector along the x-axis, and the optic could be tilted in both the horizontal and vertical directions by changing the values of ϕ and ψ. All movements were driven by ultra high vacuum stepper motors, with step sizes of 15 μm for movements in the x, y and z axes, and 0.121" for changes in ϕ and ψ [Pearson and Martindale, 2009]. The stepper motors were controlled remotely by a computer through which the required position in steps for any selected motor could be specified.

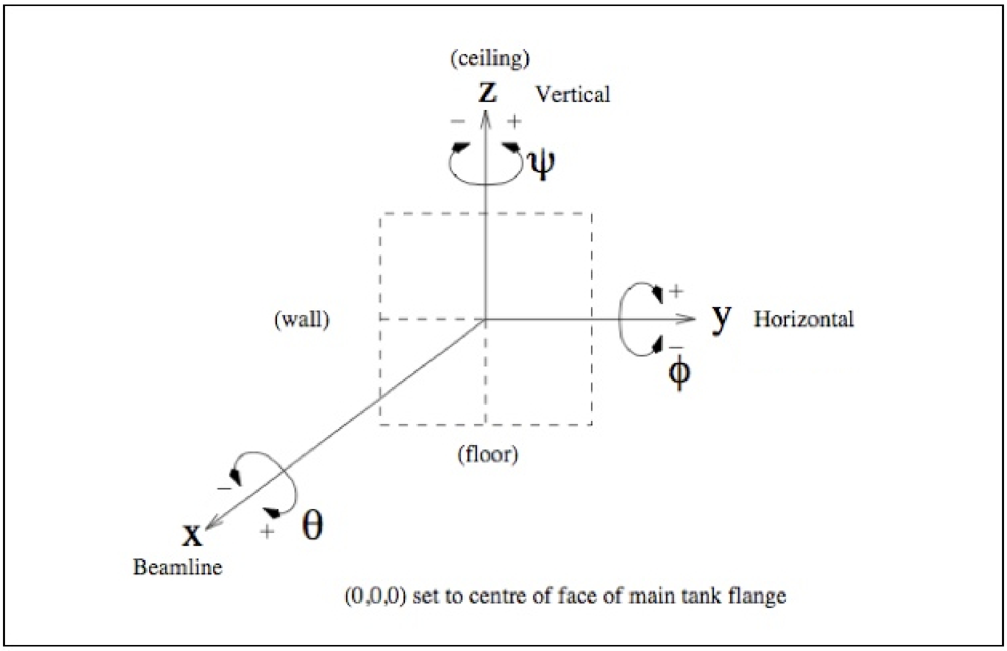

Figure 4.28 — *Reference axes used in the TTF. The detector could be moved in the X-direction, while the optic could be rotated through angles ϕ and ψ [Pearson and Martindale, 2009]*

4.2.2 Focusing tests

The optic used for the MISX-C tests had an expected R_{MCP} of 550 mm, so, using Equation 2.3 with a source distance of 27 m, the expected focal length was approximately 272 mm. In the tests, the detector-optic distance was varied in fixed steps through the expected focal distance, and images were taken at each step. Each image showed a cruciform PSF, the FWHM of which was obtained as a number of pixels in two dimensions using the imaging software, converted to mm, and then degrees. These values were plotted against the detector-optic distance (Figure 4.29) with the minimum of the graph giving the focal length of the optic. Measurements were initially in steps of 15 mm, then in 3 mm steps closer to the focal length, and the finally in steps of 1.5 mm to accurately pinpoint the focal length. Examples of focused and unfocused images are shown in Figure 4.30.

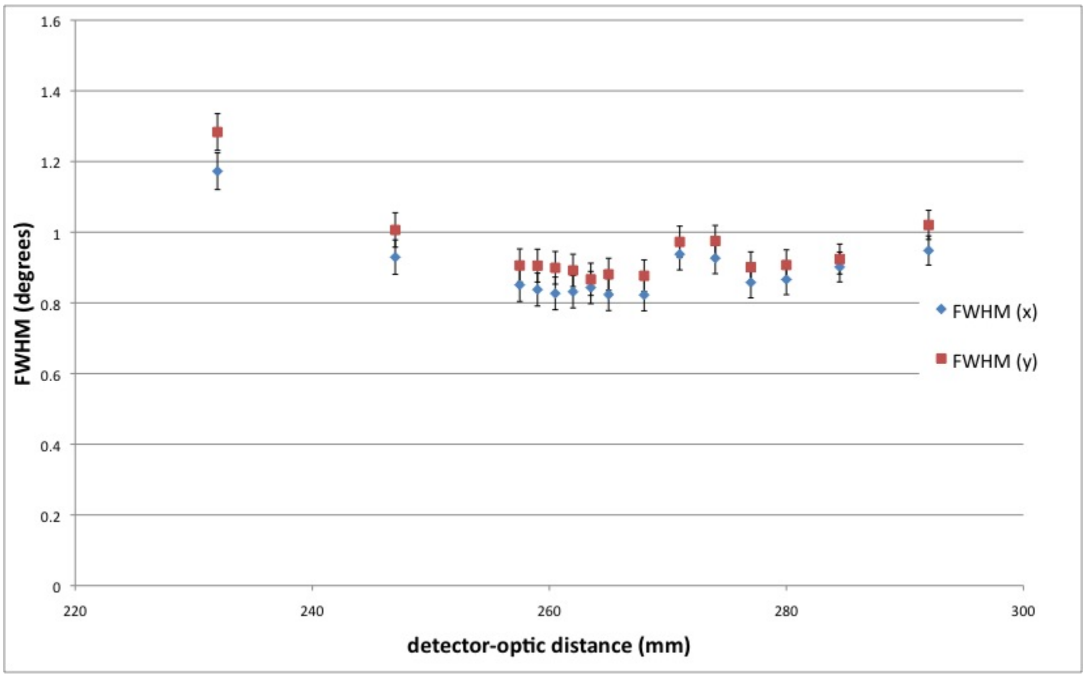

Figure 4.29 — *FWHM of MIXS-C images as a function of detector-optic distance. The vertical error bars represent the angular extent of one pixel (0.21 mm) at each distance.*

The true focal length of the MIXS-C MCP was taken to be the detector-optic separation at which the mean FWHM (e.g. FWHM(x) + FWHM(y) / 2) was lowest. This occurred at 260.5±1.5 mm,[5] where the measured FWHM was $4.13^{+0.33}_{-0.37}$ mm,[6] corresponding to an angular resolution of ∼0.82°. The optic used had 20 μm pores, so the theoretical resolution limit at 260.5 mm was ∼0.26 arcminutes – almost 200 times better than the measured resolution. The optic was known to have been badly fused – when viewed under a microscope it was clear that there were gaps between multifibres. This will have had a significant detrimental effect on the best resolution achievable by the optic. However, even in previous tests of better quality slumped plates the theoretical resolution limit was not reached. It is believed that the best achievable resolution is controlled by the

[5]The uncertainty given is the distance moved along the x axis between images. It was not thought useful to obtain images at smaller intervals than this because of the finite depth of the MCP focal plane (see Chapter 3, Section 3.1.1).

[6]The uncertainty in the measured FWHM reflects the fact that the quoted value is an average of four measurements at the focal length: the uncertainty values are the differences between the mean and the two most outlying values.

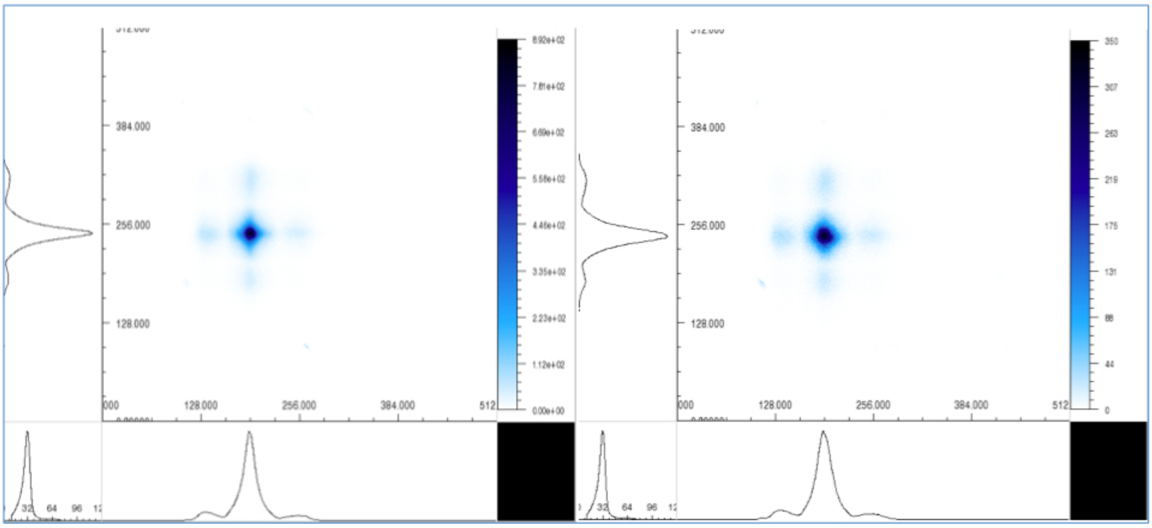

Figure 4.30 — *Left - focused image using MIXS-C optic (detector-optic distance = 260.5 mm); right- unfocused image (detector-optic distance = 292 mm). 1 pixel = 0.21 mm so the FWHM of the focused image is $\sim$ 4.13 mm, or $\sim$0.82°.*

finite size of the multifibres (0.902 mm) that make up the optic, implying a theoretical resolution limit of 11.4 arcminutes – a factor of $\sim$4 better than the measured values. The data collected in the X-ray focusing tests are therefore nominally consistent with the assumption that well fused MCPs have angular resolution approximately limited by the multifibre size (if we assume the factor of 4 degradation to be caused by poor block fusion). The possible connection between an MCP optics multifibre size and its achievable resolution is discussed below.

4.2.3 Modelling the effects of multifibre size on MCP images

The expected size of the focus in MCP images limited by the multifibre size can be calculated using the equation:

$$S = \sqrt{MF^2 + \left(\frac{Z_d X_{MCP}}{F_l}\right)^2}, \tag{4.6}$$

where MF is the size of a multifibre, Z_d is the axial position of the detector away from the expected focal point, X_{MCP} is the linear size of the optics and F_l is the focal length

(Martindale and Molyneux [2009]; the MF term was first suggested by George Fraser). This equation was applied to the data collected in the WFAI focusing tests and found to fit the shape of the data well, but the equation predicted consistently larger focuses than those measured in the test campaign: the predicted minimum was 2.2 mm, while the measured minima were ~0.9 mm in the x direction and ~0.6 mm in the y direction. Hence, Equation 4.6 becomes

$$S = \sqrt{MF^2 + \left(\frac{Z_d X_{MCP}}{F_l}\right)^2} - S_{shift}, \tag{4.7}$$

where S_{shift} is a fixed shift, the physical significance of which is currently unclear. With S_{shift} of 1.3 mm in x and 1.6 mm in y, the model fits the WFAI measurements well, as shown in Figure 4.31a. A similar fit was performed for the MIXS-C focusing tests, and the model was found to fit the data best with values of $MF = 3.9$ mm (i.e. ~4.3 × the true multifibre size, suggesting that the poor fusing of the optic makes ~4 adjacent multifibres behave as one) and $S_{shift} = 0.1$ mm for x and $S_{shift} = -0.1$ mm for y. A plot showing the fit between the MIXS-C data and model is shown in Figure 4.31b.

Although the fit between the model and the measured data is good, the physical significance of the shift term is not yet understood, and the equation used did not take into account factors such as the divergence of the beam in the test facility. Work to refine the model is ongoing.

4.2.4 MCP profiling

Talysurf measurements of the curvature of the MIXS-C optic were performed in four directions through the centre of the (unmounted) MCP, as shown in Figure 4.32: between each of the two sets of diagonally opposite corners, as shown by lines A and B, and between the midpoints of each set of parallel edges, as shown by lines C and D. The measurements were then repeated in the opposite direction to that indicated by each arrow. The results are shown in Table 4.7. The uncertainty values given were calculated

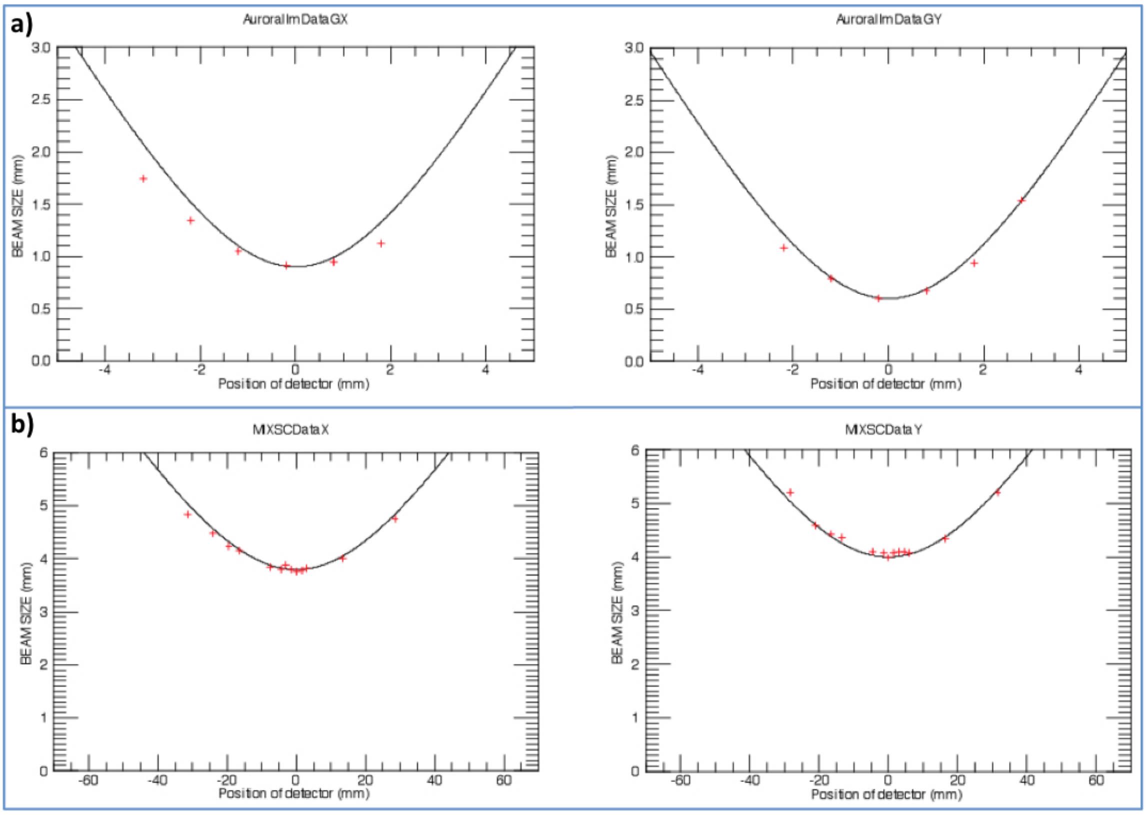

Figure 4.31 — *Plots showing comparisons between the size of PSF focus of MCP optics measured from lab images and the size predicted by Equation 4.7, as a function of the detector position along the optical axis. The zero position of the detector is normalised to correspond to the minimum of the data points and does not necessarily correspond to the expected focal point of the optic. Panel (a) shows the results of calculations using the WFAI parameters and data, and panel (b) corresponds to the MIXS-C optic. From Martindale and Molyneux [2009].*

using the method described in Section 4.1.7 for an RMS roughness of 1 μm.

The slump radius of the MCP was found to be lower than its specification of 550 mm, with the Talysurf measurements giving values of between ~521.7 mm and ~538.3 mm. This implies that the focal length of the MCP should be between 258.4 mm and 266.5 mm (using Equation 2.3 with a 27 m source distance). The result correlates well with the measured focal length of 260.5 mm, which suggests a radius of curvature of ~526.1 mm. The reason for the deviation of R_{MCP} from the nominal value in the optic specification

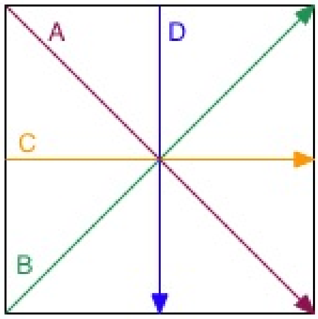

Figure 4.32 — *Diagram showing the directions of Talysurf traverses performed on the MIXS-C MCP.*

Table 4.7 — *R_{MCP} of the MIXS-C collimator MCP, as measured by the Talysurf profilometer.*

Measurement	1st result (mm)	uncertainty (mm)	2nd result (mm)	uncertainty (mm)
A	535.628	$^{+2.563}_{-2.538}$	531.759	$^{+2.525}_{-2.502}$
B	538.261	$^{+2.588}_{-2.563}$	535.088	$^{+2.557}_{-2.533}$
C	527.816	$^{+2.488}_{-2.465}$	521.668	$^{+2.430}_{-2.408}$
D	531.164	$^{+2.520}_{-2.496}$	532.602	$^{+2.533}_{-2.510}$

is not obvious, but Martindale [2008] suggests that such deviations may be caused by either manufacturing error, degradation of the slump profile during storage, or distortion introduced by uneven pressure in the mounting structure (this last factor can be ruled out for the MISX-C optic as the measurements were performed before mounting).

4.2.5 SRT modelling of MIXS-C focusing tests

Sequential ray tracing was performed in order to aid the analysis of the results from the optic testing. The model was set up with an optic radius of curvature of 531.8 mm (the mean R_{MCP} determined by the Talysurf measurements) and a source distance of 27 m. The detector-optic distance was set to 260.5 mm – the focal length as measured by the experimental tests, and X-rays with energies of 0.28 keV were specified. Deformations were applied to the optic to model misalignments between the channels, by defining a deformation matrix which applied an angular displacement to the direction of each channel. The deformation matrix is a 2-dimensional array, with each element representing a specific position on the MCP optic. Each element is assigned a value corresponding to a tilt in the channels at the relevant optic position, causing a shift in the radius of curvature, and hence focal length, for that area of the optic. The tilt values contained in the deformation matrix have a gaussian distribution, with the mean tilt and standard deviation of the distribution specified by the user so that the magnitude of the deformations can be controlled. When applied to the optic, the deformation matrix allows the effects of channel misalignments introduced in the MCP manufacturing process to be modelled. The mean displacement in this case was set to zero and the standard deviation of the deformations was increased in steps of 5 arcminutes between runs, from 5 to 60 arcminutes (the results of modelling 5 to 30 arcmin deformations are shown in Figure 4.33). The FWHM of the PSF produced by each run of the code was measured and compared to the FWHM of the images obtained using the TTF.

The FWHM of the experimental image obtained at the focal point was approximately 4.13 mm. Analysis of the ray tracing results showed that applying a deformation matrix with 25 arcmin standard deviation gave a FWHM of 3.3 mm; while 30 arcmin standard deviation deformations produced a point spread function with a FWHM of 4.4 mm. This suggests that the deformation matrix with standard deviation of 30 arcmin best describes the MCP imperfections.

4.2.6 Testing the MIXS-C MCP as a collimator

An MCP optic can be used as an X-ray collimator if the detector-optic distance is set to twice the focal length of the optic. In this configuration, rays travelling at large angles relative to channel walls are absorbed by the plate, while those at narrow angles are completely unfocused when they reach the detector. Once the X-ray focusing

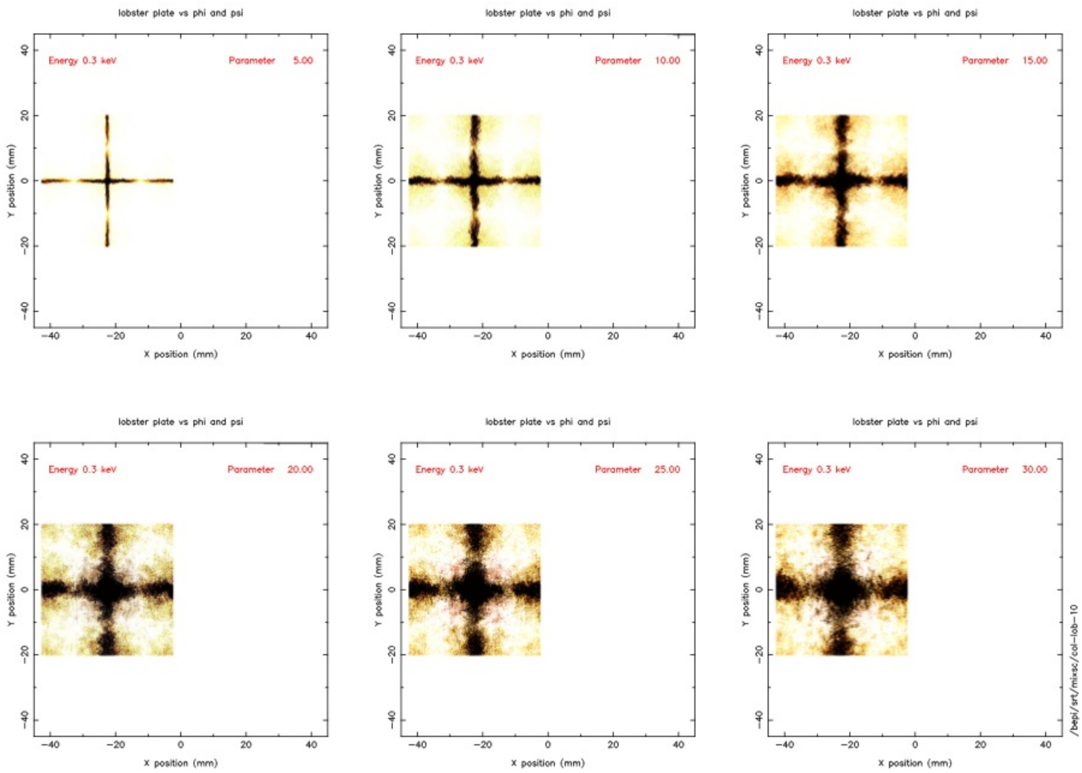

Figure 4.33 — *Ray tracing models of the PSF at the optic focus, with varying deformations added to the plate. The standard deviation of the deformations in the top left image is 5 arcminutes, and this parameter increases by 5 arcmin in each subsequent image, up to a deformation of 30 arcmin for the bottom right image.*

measurements described above were completed, the detector was moved another 260.5 mm away from the optic in order to allow testing of the plate as a collimator. The MCP was initially in a plane perpendicular to the X-ray beamline, and was then tilted in one direction only (by changing angle ψ as shown in Figure 4.28) in steps of 1°, up to 5°, beyond which point the signal to noise ratio became too small to obtain clear images. The images acquired are shown in Figure 4.34 with the approximate sizes of various features indicated on each image. The sizes are likely to be more accurate towards the centre of each image, as the images have not been corrected for the distortion introduced by the resistive anode readout (see Section 4.1.4.2).

The size of the area of the MCP that acts as a collimator is simply the area of the plate for which the angles of the channels relative to the incoming X-rays allow the rays to pass

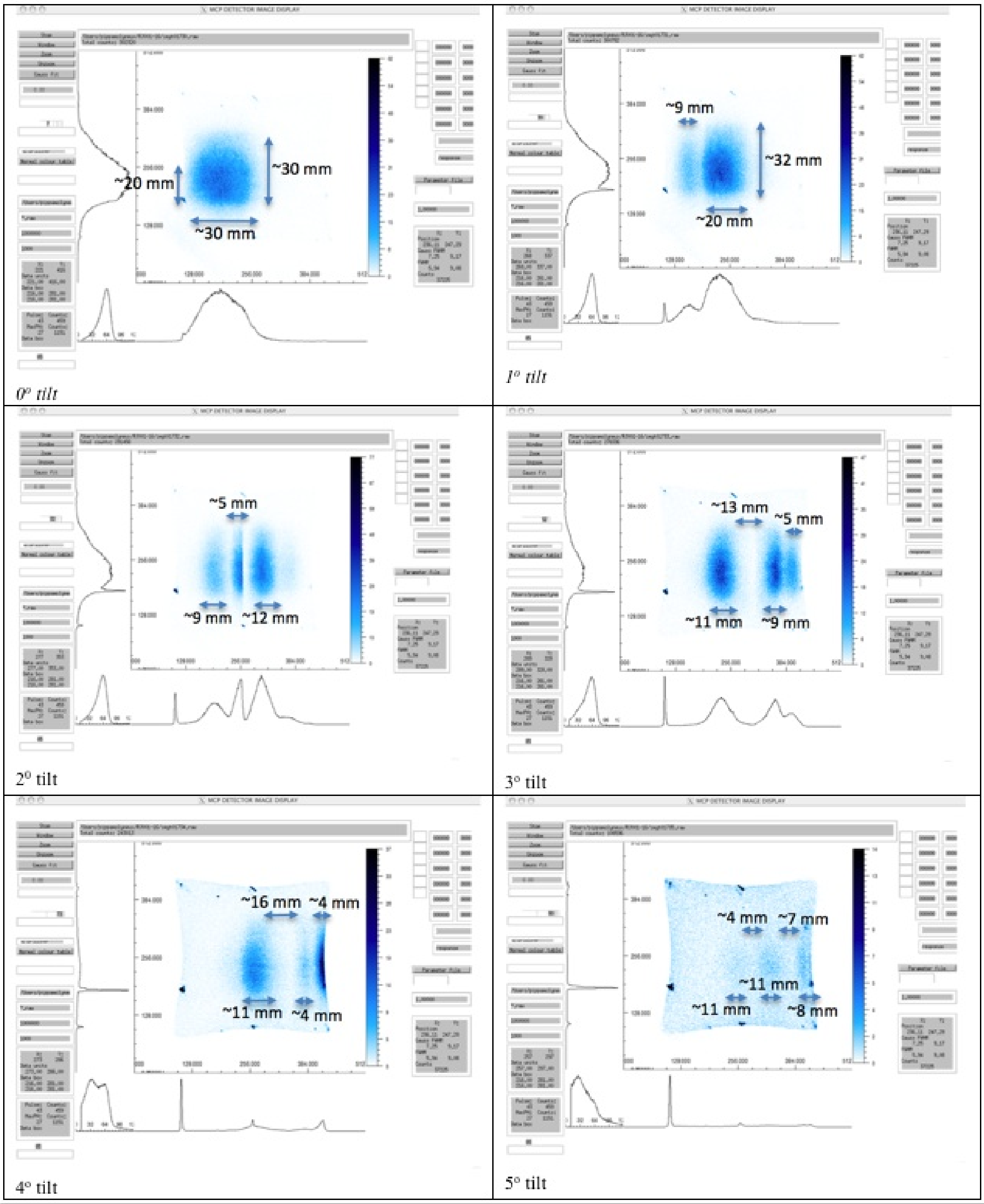

Figure 4.34 — *Images obtained using the MCP as an X-ray collimator, with the sizes of various features indicated. The angle at which the plate was tilted is given under each panel.*

through without undergoing any reflections from the channel walls. The MIXS-C MCP used had a thickness of 1.1 mm and channels of width 0.02 mm, so the maximum channel angle for collimation was $\tan^{-1}(0.02/1.1) = 1.04°$. The plate had a radius of curvature of between 521.7 mm and 538.3 mm, so when the plate was untilted the collimating area was a square with approximate side length $2 \times R_{MCP} \sin(1.04)$ =18.96 to 19.57 mm (see Figure 4.35). A more intense region with a side length similar to these values can be seen in image taken with zero plate tilt (see Figure 4.34, top left panel). This area contains counts from collimated rays, while the area around it contains rays that have experienced reflections from channel walls. This is discussed further in Section 4.2.7.

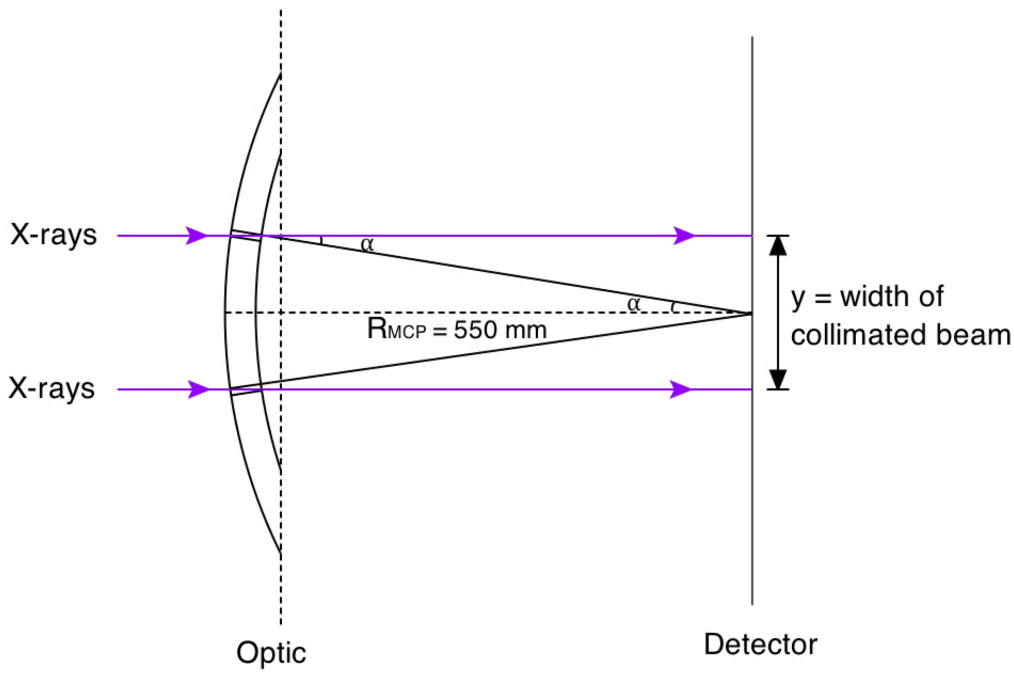

Figure 4.35 — *Diagram (not to scale) showing collimated part of the X-ray beam (α = 1.04°, $y = 2 \times 550 sin(1.04) = 19.97$mm).*

4.2.7 SRT modelling of the MIXS-C collimator tests

The collimator tests, like the X-ray focusing tests, were complimented by SRT modelling. The model parameters used were identical to those described in Section 4.2.5, except for the detector-optic distance, which was doubled. The model was run six times, with the collimator plate being rotated by an extra degree around the vertical axis between successive runs, from 0° to a tilt of 5° as in the X-ray tests. Initially no deformations were considered. The results from this model are shown in Figure 4.36. Once the initial model had produced results, deformations with standard deviation of 30 arcminutes were added to the collimator plate, as this magnitude of deformation had given the best model of the X-ray focusing results. The results of the model with deformations added are shown in Figure 4.37. Both Figure 4.36 and Figure 4.37 show horizontal banding when the optic is tilted. Each band contains rays that have been reflected a specific number of times at the optic, with higher numbers of reflections furthest from the centre of the image. This is shown in Figure 4.38, which gives the number of reflections undergone by rays in each of the bands for each optic position. The banding appearance is reduced when higher energy X-rays are considered, since these have a smaller critical angle of reflection and hence are more likely to be absorbed by the optic glass rather than being focused by multiple reflections. An example of the expected images obtained for the collimator set up with X-rays of 4 keV is shown in Figure 4.39.

The ray-tracing results fit well with the central parts of the experimental images up to a tilt of 3°, but show extra bands towards the edges of the detector that are not seen in the test images. This can be explained by considering the number of reflections an X-ray must undergo at the collimator in order to be directed towards these features. Figure 4.38 provides an analysis of the number of reflections undergone by rays in each image. It can be seen that areas further from the image centre are hit by rays which have been reflected a larger number of times. The more times a ray interacts with the walls of a channel, the greater the chance that it will be absorbed rather than reflected. The collimator described by the model had channels with zero roughness and perfect reflectivity, decreasing the proportion of rays being absorbed. In reality, absorption is much more likely.

The ray-traced image produced with the collimator tilted by 4° shows a gap between bands that is considerably larger than the gap seen in the experimentally obtained image ($>$30 mm in the model compared to $\sim$16 mm in the X-ray tests – compare Figure 4.34

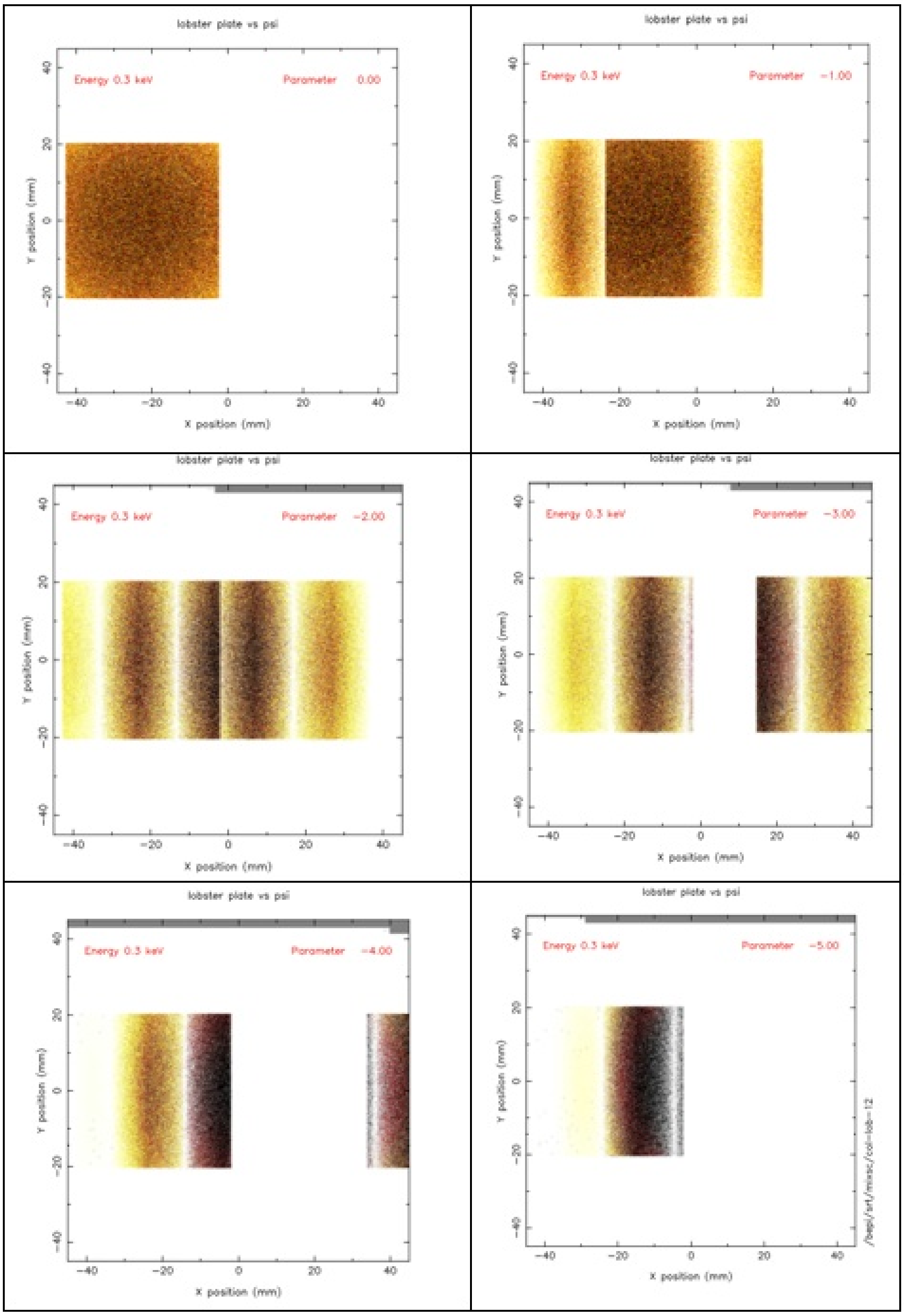

Figure 4.36 — *SRT model of the collimator tests: the tilt of the optic around the vertical axis, ψ, is increased in steps of 1 degree, from 0 the top left panel to 5 degrees in the bottom right panel.*

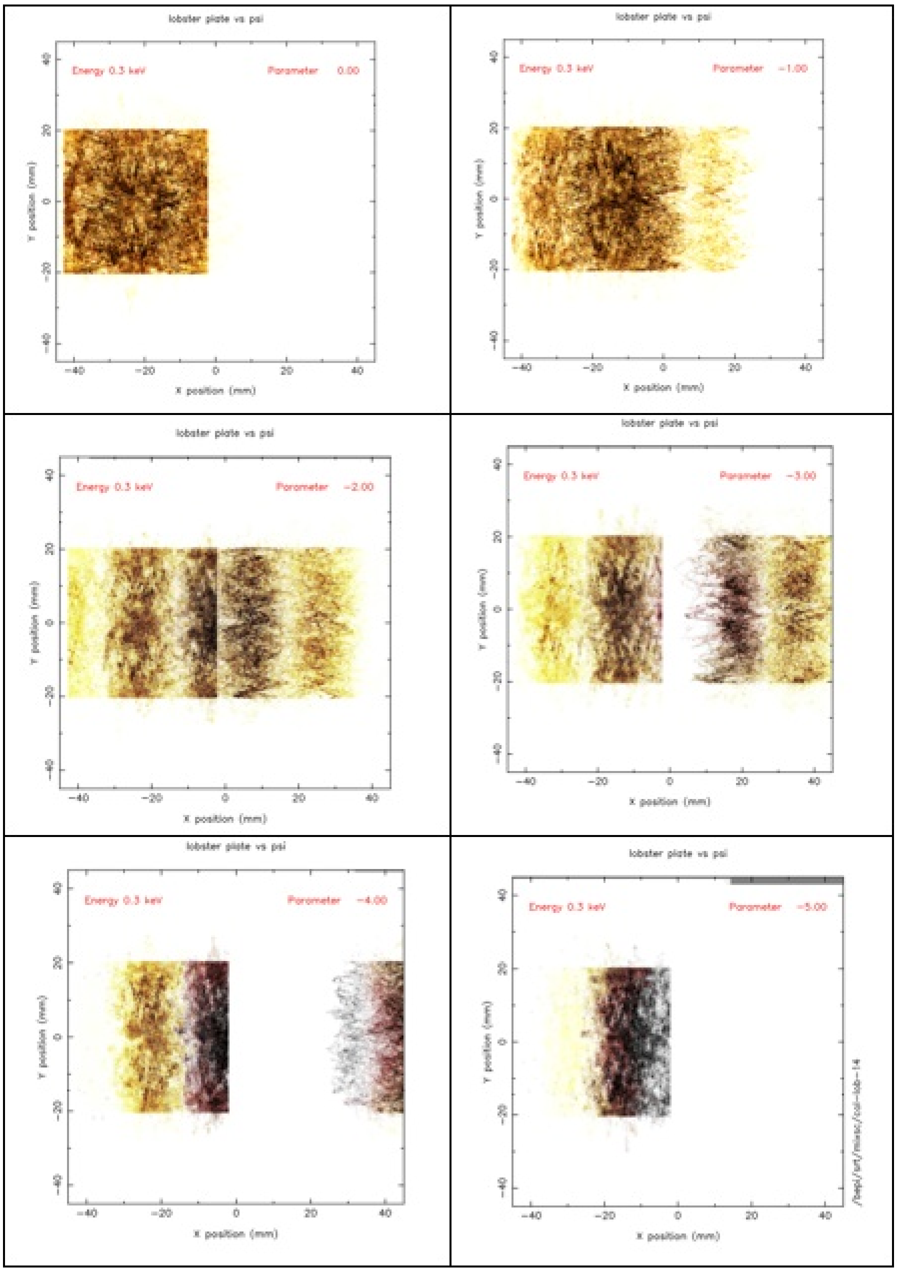

Figure 4.37 — *As Figure 4.36 but with added deformations (standard deviation of deformations is 30 arcminutes).*

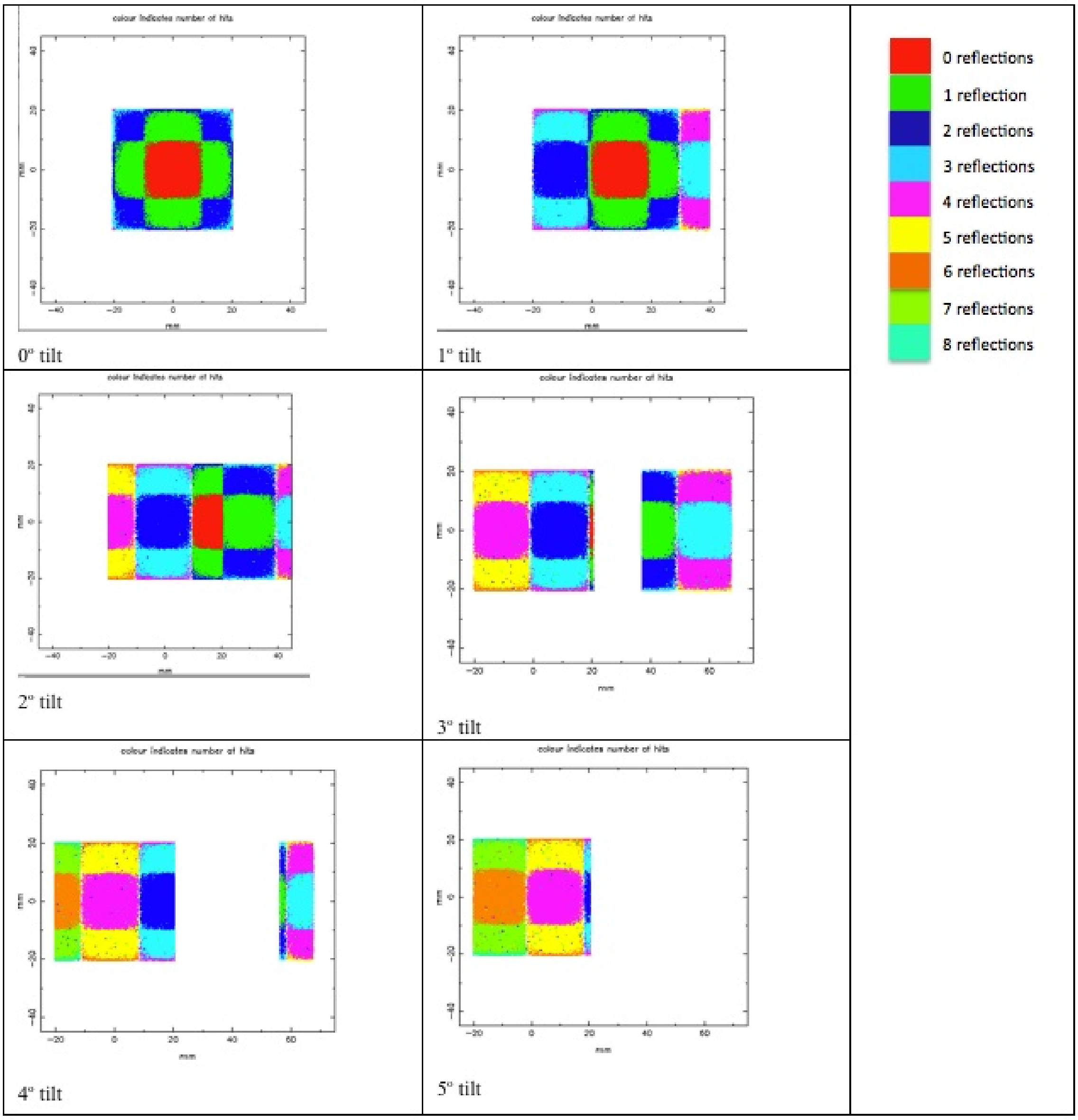

Figure 4.38 — *Similar to Figure 4.36, but each ray is colour-coded according to the number of reflections it undergoes at the optic. Red areas show rays that were not reflected (collimated rays). (The first four images have been offset to the right relative to the images shown in Figure 4.36)*

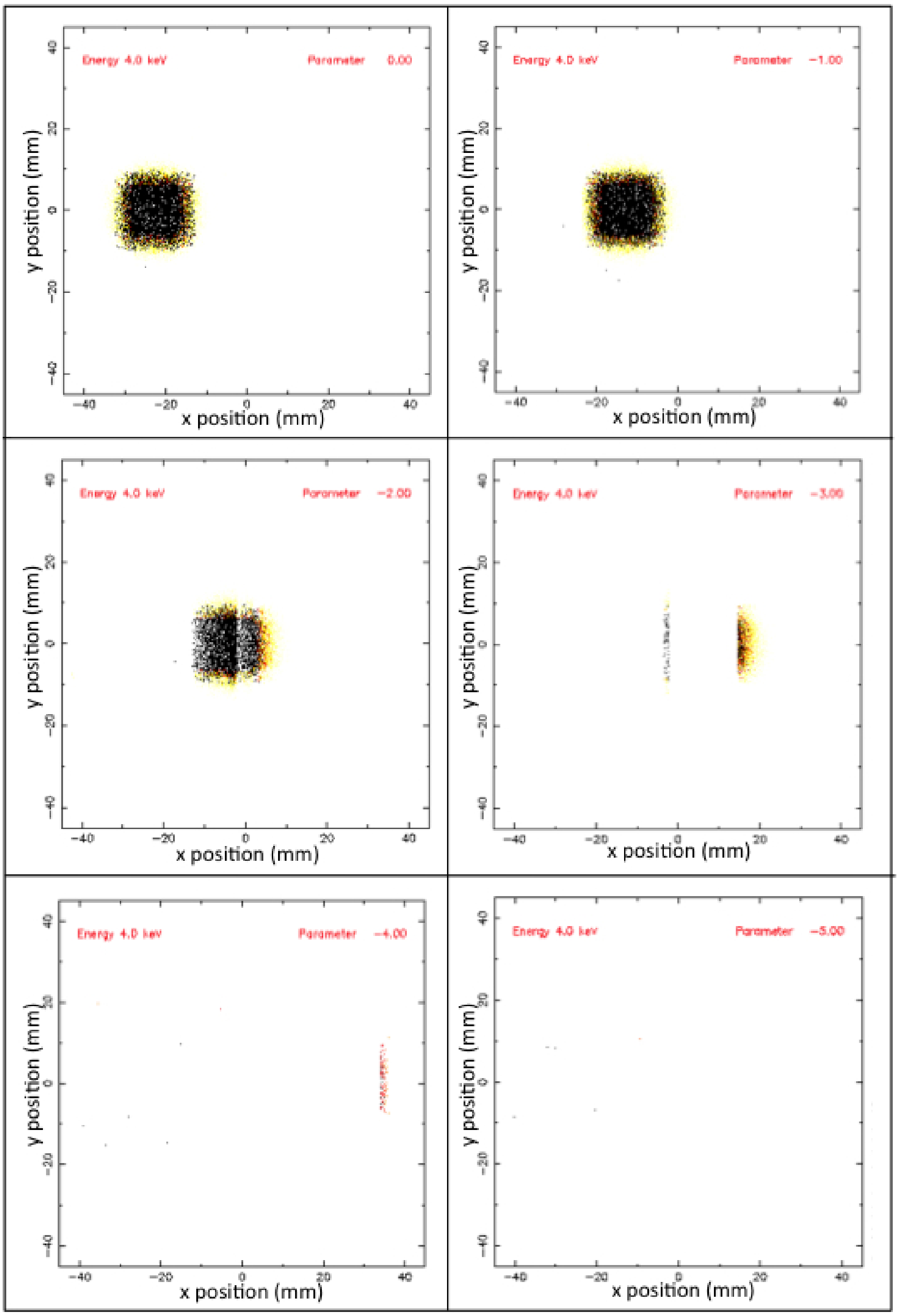

***Figure 4.39** — As Figure 4.36 but for X-rays with E = 4 keV.*

and Figure 4.36). This gap is narrowed somewhat when the 30 arcminute deformations are included ($\sim$20-25 mm in Figure 4.37) but is still larger than the experimental results suggest it should be. The compression effects due to the resistive anode readout (see Section 4.1.4.2) may have played a part in making the gap in the X-ray image appear smaller than it actually is.

The ray-traced and experimental images produced when the collimator was tilted by 5° are very different. The experimental image shows three faint bands on the right-hand side of the detector area. These features contain a slightly higher concentration of counts than the background but only the faintest one is in an area that the model predicts should have rays incident upon it. The collimator images obtained from the TTF tests were re-plotted to show the distribution of pulse heights within the images, as shown in Figure 4.40. An area of low pulse heights is visible on the right edge of the images taken with optic tilts of 3, 4, and 5°. This implies that this region of the detector is noisy, since the dark noise pulse height distribution of an MCP detector has the form of an exponential decay, with low pulse heights dominating (see Chapter 2, Section 2.3.1). Noise features will therefore be seen in these regions at a low signal : noise ratio, and since the signal : noise ratio decreases as the optic tilt is increased, the noise features can be seen most easily in the image obtained at 5° tilt.

4.2.8 Further focusing tests with a better MIXS-C MCP

Further X-ray focusing tests were performed by C. Feldman (University of Leicester) on an MCP of the same specifications as that discussed in Section 4.2.2. The new MCP was manufactured from a different block and its constituent multifibres were well-fused. Focusing tests were performed in the TTF with an 8.4 keV X-ray source. Figure 4.41 is an image from this set of tests, taken at a detector-optic distance equal to the predicted focal length of 272 mm [Feldman and Martindale, 2011]. As the X-ray source used for these tests was of a higher energy than that used in the earlier tests, the critical angle of reflection at the optic was lower. As a result, the probability of multiple reflections within

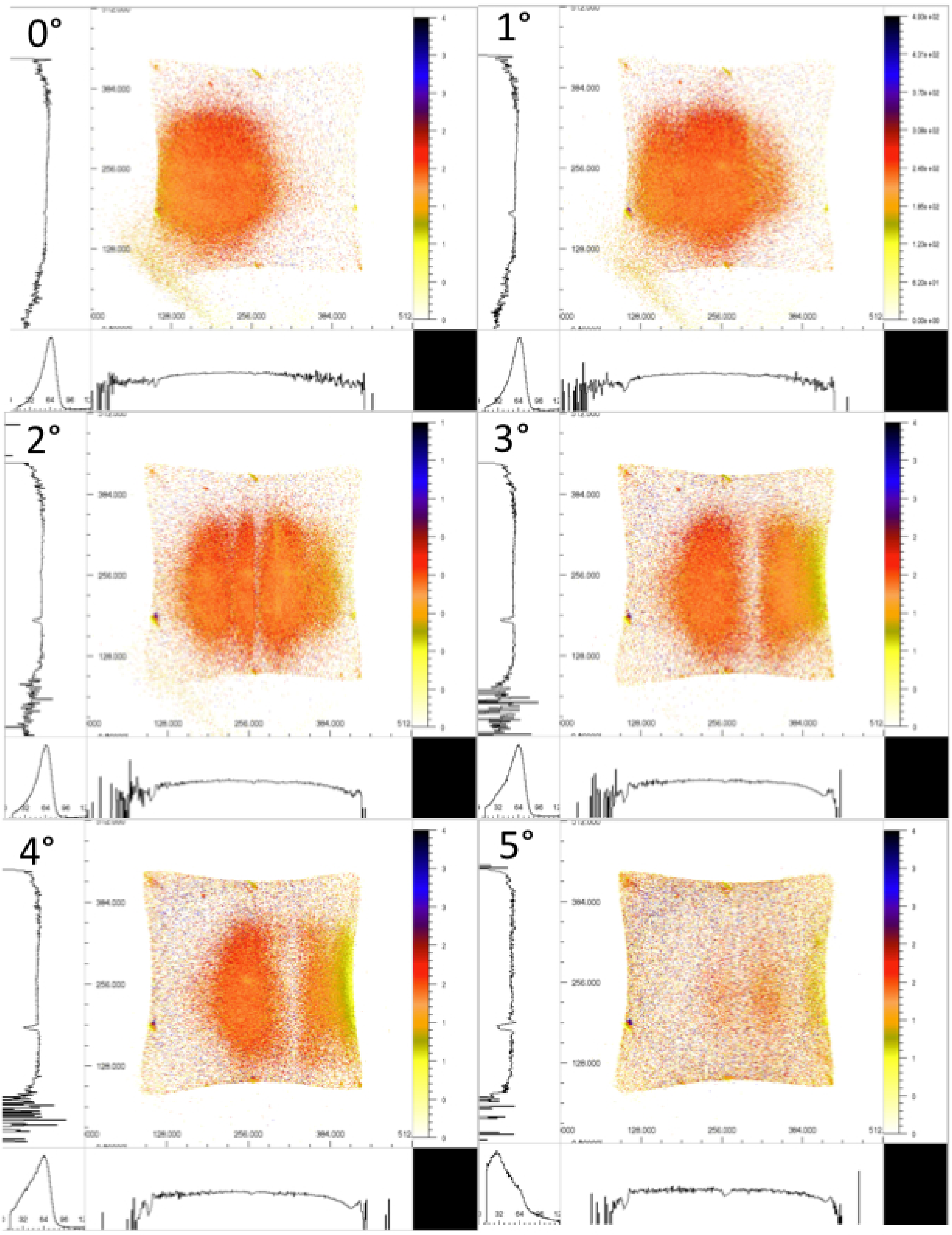

Figure 4.40 — *Mean pulse height distributions for the images shown in Figure 4.34. The images taken with the optic tilted by 3 or more degrees show a region of low mean pulse height along the right edge. This suggests that this region is a noisy area of the detector.*

channels was reduced, and the images obtained show the first reflection zone of the optic PSF only, in contrast to the images obtained with the damaged MCP, in which multiple reflection zones were visible. The bright strip at the top of Figure 4.41 should be ignored: it was caused by the X-ray beam extending outside of the optic area so that at one edge photons were able to reach the detector without encountering the optic [Feldman and Martindale, 2011].

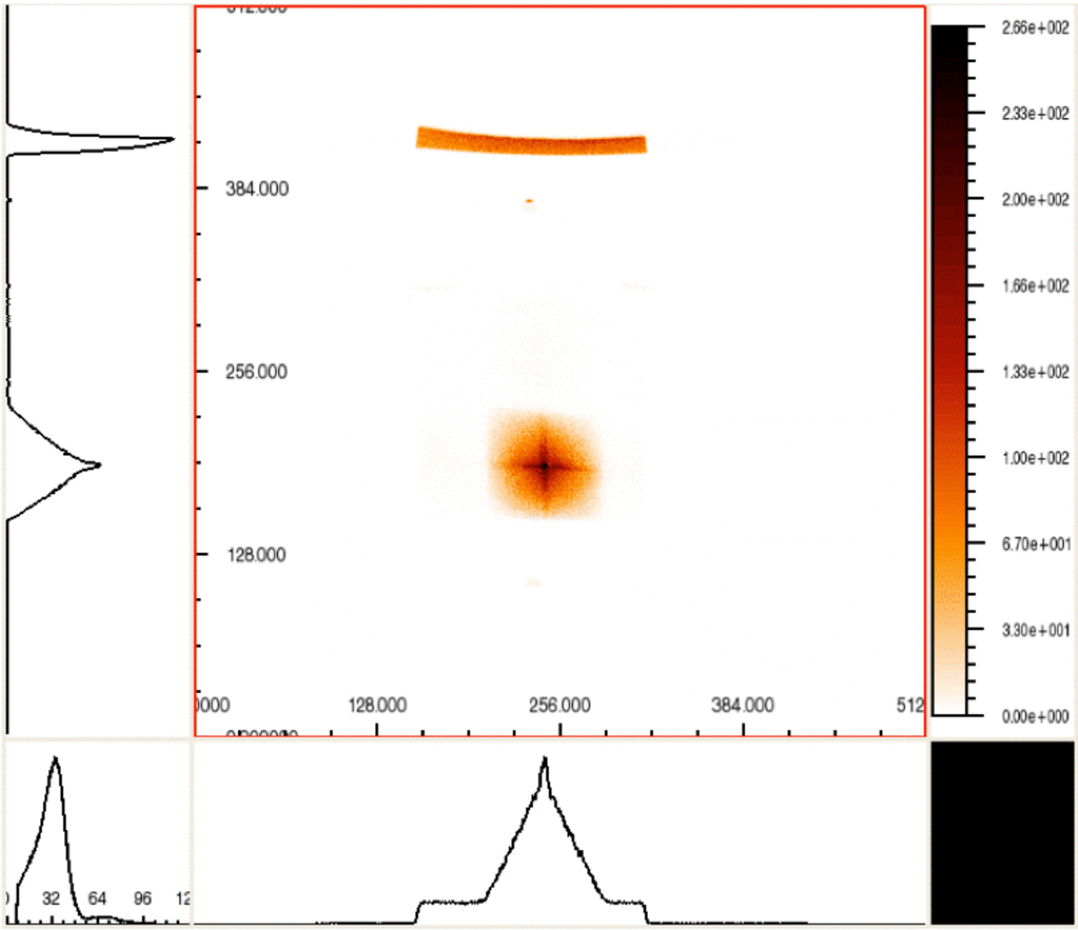

Figure 4.41 — *Focused TTF image of an 8.4 keV X-ray source obtained with a well-fused MIXS-C MCP [Feldman and Martindale, 2011].*

The linear size of the FWHM measured in images at the optimum detector-optic separation was on average 0.89 mm (∼11.2 arcmin) in the horizontal axis and 1.06 mm (∼13.4 arcmin) in the vertical axis [Feldman and Martindale, 2011]. As the MCP had a multifibres of ∼0.9 mm, this lends further weight to the idea that the multifibre size is the limiting factor in the achievable angular resolution of MCP optics.

4.3 Feasibility of JUDE MCP optic design

Neither the WFAI or MIXS-C evaluation tests described in this chapter were able to match the theoretically predicted resolutions of the MCPs. This is not a significant issue for those instruments: MIXS-C is a collimating instrument so resolution is not important, and WFAI is designed to view emissions from low Earth orbit, so its angular resolution requirement is less critical than its large field of view. However, the requirement for JUDE to match the resolution of *HST* STIS (see Chapter 1, Section 1.5.3) is vital for the imager's science case. The MCP optic version of JUDE has already been shown to suffer from diffraction effects to such an extent to render this requirement unfeasible (see Chapter 3, Section 3.2), and the fact that no slumped MCP yet tested has achieved its theoretical best resolution suggests that even the diffraction-limited resolution calculated in that section is likely to be unachievable. Hence, MCP optics do not appear to be a suitable choice for JUDE, and future work for that instrument will be based on the reflective optic design (Chapter 2, Section 2.2).

The following is a list of the factors that have lead to the decision not to develop the JUDE MCP optic design further, including references to the sections within this work that discuss these factors in detail:

- The preliminary JUDE parameters of R_{MCP} = 1500 mm and pore width = 160 μm were shown to lead to diffraction effects that would degrade the achievable resolution to $\sim$850 km at Jupiter from Ganymede orbit (Chapter 3, Section 3.2). The resolution goal for JUDE is 100 km at Jupiter from Ganymede orbit.
- If the MCP parameters were adjusted to the point where the diffraction limited resolution and the geometrically limited resolution were both equal to 0.4' to match the resolution goal, the optic would require 1.16 mm pores and a focal length of 9.94 m (R_{MCP} = $2f$ = 19.88 m), which is clearly unfeasible (Chapter 3, Section 3.2).
- Laboratory focusing tests of slumped MCP optics have not been able to achieve the

theoretical resolution of the optics (Chapter 4, Sections 4.1.2; 4.2.2; 4.2.8), with the best measured FWHM of the optic PSFs significantly larger than the theoretical values in each case.

- The preliminary reflective optic design produced at CSL in Liège has been shown to achieve the required angular resolution for JUDE, and further optimisation may improve the resolution further (Chapter 2, Section 2.2.1).

4.4 Summary

Focusing tests were performed on two slumped MCPs of different specifications: one a prototype optic for the WFAI imager and one designed for use as a collimator in the *BepiColombo* MIXS-C instrument. The minimum FWHM achievable with the WFAI optic was initially measured as 0.816°, which is $\sim$6.7 times larger than the intrinsic FWHM of a perfect optic with the same specification, according to measurements from an SRT model of the laboratory set-up. The initial FWHM result was corrected for noise introduced by the signal processing chain that converted the detector signals into images, and for distortions introduced to the images by the use of a resistive anode readout. A correction for diffraction by the optic channels was also performed, since the SRT model did not include any diffraction effects. The minimum FWHM after corrections was 0.653°– approximately 5.4 times larger than the value suggested by the ray tracing results. It is thought that the larger FWHM is due to deformations in the WFAI optic.

The minimum resolution of the MIXS-C MCP was similar to the resolution of the WFAI optic, at $\sim 0.82^{\circ}$, despite its smaller channel width and larger slump radius giving the MIXS-C MCP a theoretical resolution $\sim$27 times better than that of WFAI. This was due to a manufacturing error: the MIXS-C MCP was so badly fused that gaps between multifibres were clearly visible when the plate was viewed using an optical microscope. SRT analysis confirmed that significant deformations in the MCP channel alignment could account for the poor resolution measured. Further tests of a better MCP of the same MIXS-C specifications gave an improved resolution of $\sim$11.2 arcminutes ($\sim$0.19°), which is close to the angle subtended by one multifibre at the focal length.

To date, no focusing tests of slumped MCP optics have yet matched the theoretical resolution of the optic tested [Martindale, 2011], and the tests described in this chapter are no different. It seems that the achievable resolution may be limited by the size of the multifibres that make up the optics. A mission such as JUDE, for which excellent angular resolution is an important requirement, should therefore not be based on an MCP optic design until the problem of achieving the theoretical optic resolution has been overcome.

CHAPTER 5

Ganymede Spectroscopy

The main purpose of JUDE is to obtain wide field views of FUV emissions within the jovian system, at high spatial and temporal resolution. In situ FUV observations of Jupiter's aurora have previously been limited to spectrometers, which have provided high spectral resolution data with limited spatial and temporal resolution. Hence, it was decided that the requirement for excellent spatial and temporal resolution would drive the JUDE design, with spectral capabilities largely sacrificed in order to fulfil this requirement. Both the Leicester and Liège instrument designs therefore made use of broadband optics.

The images of Jupiter obtained by JUDE will enable the temporal and spatial nature of small, transient auroral features to be studied in more detail than ever before, allowing current models of the jovian magnetosphere-ionosphere interaction to be refined. However, the instrument should also be able to provide useful data about other ultraviolet emitters in the vicinity. As the JUICE spacecraft will spend a significant proportion of its lifetime in orbit around Ganymede, it is particularly important that the imager can enhance our understanding of this moon. Ganymede is the only moon in our solar system known to possess an intrinsic magnetosphere, and has been found to display emissions that appear to be of an auroral nature [Hall et al., 1998, Feldman et al., 2000], but these emissions have not been comprehensively studied. In order for a reliable understanding of Ganymede's aurora to be obtained, spectral isolation of the main emission lines is required. Since JUDE does not have the intrinsic capability to do this, the addition of transmission filters to the baseline design has been suggested. This chapter describes the JUDE reflective optics and outlines the different options for the positions of filters within the imager design, and provides the results of a study designed to show that Ganymede's main FUV emission lines can be successfully isolated with the use of a combination of readily available broadband FUV filters and reflective mirror coatings.

The significance of the two FUV oxygen lines in Ganymede's atmospheric emissions has been discussed in detail in Chapter 1 (Section 1.3). To summarise, the ratio between these emissions, at 130.4 nm and 135.6 nm, allows constraints to be placed on the relative abundances of O atoms and O_2 molecules within the atmosphere, leading to more accurate models of atmospheric composition.

5.1 JUDE reflective optic design

The JUDE reflective optics under development at Centre Spatial de Liège (CSL – part of the University of Liège, Belgium) consist of two off-axis mirrors, along with multilayer filter coatings which are deposited onto the mirror surfaces to provide some wavelength discrimination in the UV (see Chapter 2, Section 2.2 for an overview of the JUDE reflective optic design). A basic explanation of the theory on which multilayer coatings are based can be found below, along with a description of the methods used at CSL to deposit the coatings onto optical components.

5.1.1 Reflective multilayer coatings: general theory

In general, the reflectivity of a material decreases with decreasing wavelength, and efficient reflectivity of far and extreme ultraviolet and X-ray radiation at normal incidence is difficult to achieve. However, high reflectivity at normal incidence can be achieved at UV, and to some extent soft X-ray [Attwood, 2000], wavelengths with the use of multilayer interference coatings. These comprise thin layers of alternating high and low refractive index materials deposited onto a substrate such as glass. Reflection occurs at the interfaces between the two constituent materials in the multilayer stack, and the thickness of the materials is controlled so that the light reflected from interfaces at the wavelength of interest is in phase, and hence interferes constructively, increasing the reflectivity of the stack compared to that of a single material. The reflectivity and transmissivity of light at the interface of two materials are governed by the Fresnel equations, which are given in Appendix A. At normal incidence the reflectivity reduces to

$$R = \left(\frac{n_1 - n_2}{n_1 + n_2}\right)^2, \tag{5.1}$$

where n_1 and n_2 are the refractive indices of the two materials. It can be seen from Equation 5.1 that the reflectivity is the same when n_1 and n_2 are interchanged, so the reflectivity is the same from either side of the boundary. The use of alternating high and low refractive index materials in multilayer coatings maximises the magnitude of n_1 - n_2, hence maximising the reflectivity.

One common type of multilayer stack is a quarter wave (QW) filter. The films making up a QW stack each have an optical thickness (defined as a product of the physical thickness of the film and its refractive index) that is equal to one quarter of a reference wavelength, λ_r [Zukic and Torr, 1992]. This means that for incident radiation at λ_r, the beams reflected from any interfaces will be in phase, giving maximum reflectance.

Suitable high- and low-index materials for vacuum ultraviolet (VUV) multilayer filters identified by Zukic and Torr [1992] include BaF_2 and LaF_2 (high-index), and MgF_2 (low index). The high-index materials have UV extinction coefficients[1] which are 100 times greater than that of MgF_2, and hence absorb UV radiation to a much greater degree than the MgF_2 layers. In a QW filter, where the optical thickness of both the high- and low-index material is equal, the reflectivity is therefore limited in the VUV range by absorption in the high-index layers. To overcome this, Zukic and Torr [1992] consider stacks with an optical thickness ratio $H/L < 1$, where H and L are the optical thicknesses of the high- and low-index materials respectively. They describe a multilayer stack made up of HL pairs of total optical thickness of $\lambda_r/2$. The total phase thickness of the pair, $\delta_H + \delta_L$, is equal to π. Hence, Zukic and Torr [1992] term the stacks 'π multilayers'. Light reflected from each HL pair in a π multilayer is in phase. A QW stack is simply a special case of a π multilayer, in which the equal optical thicknesses of the layers leads to in-phase reflection at every interface. While QW multilayers are able to provide higher reflectivity with fewer layers in the visible and infrared spectral regions, where low-absorbing film materials are available, in the VUV a π multilayer with a lower H/L ratio is able to provide lower absorptance and therefore higher reflectance [Zukic and Torr, 1992].

5.1.2 Multilayer deposition methods

Thin film deposition processes can be broadly split into two groups: chemical vapour deposition (CVD), in which the film is formed by a chemical reaction between the substrate and a suitable compound; and physical vapour deposition (PVD), in which physical processes such as heating and sputtering are used to produce a vapour from a suitable source material, which is then directed toward the substrate. A discussion of the various deposition processes available can be found in text books such as Ohring [2002]. This section concentrates on the PVD techniques used to produce optical coatings at the University of Liège.

[1]The extinction coefficient is the imaginary part of the refractive index and describes the absorptivity of a material.

The Centre Spatial de Liège (CSL) has extensive experience of coating deposition and has developed extremely low roughness Al/MgF_2 reflective coatings for the VUV. The coating stacks are applied to optical components using a combination of electron-beam evaporation and dual ion beam sputtering deposition. Schematics of these two deposition techniques are shown in Figure 5.1 [Martin, 1986]. Evaporation deposition involves heating a source material to a high temperature so that it evaporates. A substrate is placed in the vapour stream, and when the evaporant encounters this it condenses and is adsorbed by the surface, forming a film. Various heat sources may be used for evaporation deposition. In the CSL system, the heat source is an electron beam focused onto the source, as shown in Figure 5.1a.

Although electron-beam evaporation is suitable for a large range of source materials, complications may occur if the source is a compound material. This is because the elements comprising a compound source material have different vaporisation pressures and temperatures, so the composition of the vapour produced, and hence the film, is usually different from that of the source [Ohring, 2002]. Therefore, if a compound film is required, a different deposition technique is often used. One suitable method is sputter deposition, in which ions or atoms with energies of several keV bombard the solid surface of the source material, releasing atoms, molecules or clusters of molecules, which are then deposited on the substrate to form a film (see e.g. Reichelt and Jiang [1990]). The sputter deposition equipment available at Liège is a dual ion beam system (Figure 5.1b). The first ion beam in such a system is usually an energetic beam of inert gas ions [Weissmantel, 1982], which is focused onto the source to sputter the film material. The second ion beam, sometimes called the assist beam, is focused onto the substrate: this bombardment can remove contaminants from the substrate, and the energy transferred from the second beam to the growing film gives the film atoms more surface mobility, allowing them to move to different sites, producing denser and better bonded films [Colligon, 2004]. The assist beam may also be used to alter the composition of the film: the movement of atoms within the film, along with the implantation of ions from the assist ion beam, encourages chemical reactions that allow films of myriad compound materials to be produced [Colligon, 2004].

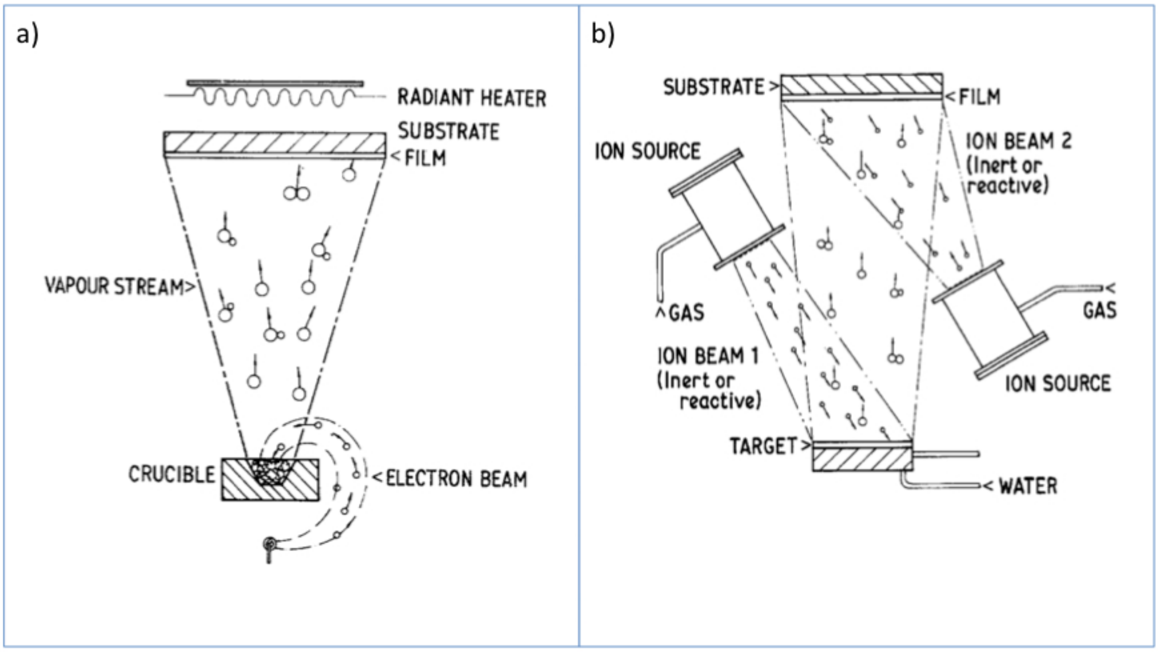

Figure 5.1 — *Schematics of the thin film deposition equipment available at CSL, from Figures 4 and 5 in Martin [1986]. a) Electron-beam evaporation: the film material is heated to evaporation by an electron beam, and condenses onto the substrate. The temperature of the substrate can be controlled using the radiant heater, which allows the condensation of the film to be controlled. b) Dual-ion-beam sputtering: the film material is sputtered from a target by an ion beam and condenses onto the substrate (the target is cooled with water to remove excess heat imparted by the sputtering ions). Certain properties of the growing film, such as its composition, can be controlled using a second ion source focused onto the substrate (see e.g. Colligon [2004]).*

5.1.3 Transmission of Liège coatings

In the JUDE baseline design, both of the focusing mirrors have the same coating to maximise reflectivity in the ∼125–145 nm wavelength band, and the combination of the two gives a transmission function as shown by the line labelled 'solution 1' in Figure 5.2. Also under study is a more complex design, in which a coated MgF_2 beam-splitter is used to create two observation channels: one with a similar throughput to the baseline design, well-suited to study Ganymede's aurora, and one which has a wider

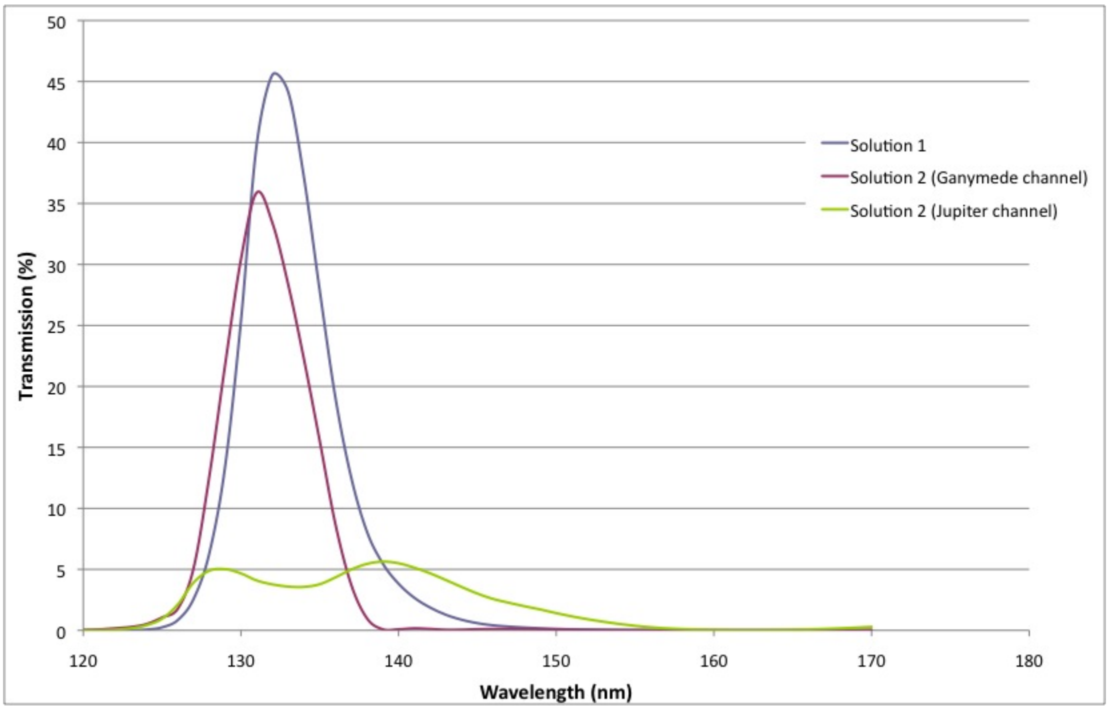

Figure 5.2 — *Transmission of coatings under study for the JUDE UV imager [Fleury-Frenette, 2009].*

transmission function to allow a larger range of Jupiter's auroral emission spectrum to be studied. These transmission curves can also be seen in Figure 5.2, labelled 'solution 2 (Ganymede channel)' and 'solution 2 (Jupiter channel)' respectively. Although the design incorporating the beamsplitter may be preferable in terms of optimising the data collected at both Jupiter and Ganymede, it would add complexity to the system, along with the mass of an extra detector for the additional channel.

5.1.4 Transmission filters for isolating OI emission lines

The possibility of isolating Ganymede's two FUV OI emissions at 130.4 nm and 135.6 nm using a combination of the Liège optical coatings and standard UV transmission filters has been suggested, and calculations to determine whether this isolation could be accurately performed are described in Section 5.2. Three filters with transmission peaks near 130 nm (peak wavelengths: 122 nm, 130 nm and 147 nm) were chosen for further investigation based on information provided by Acton Optics and Coatings [Acton: Optics brochure, 2008], a division of Princeton Instruments. This type of product has been used for FUV auroral imaging in the past, with Acton providing FUV transmission filters for the Earth-observing *Dymanics explorer 1* satellite. The transmission curves of the three filters can be seen in Figure 5.3. Standard UV bandpass filters provided by Acton with peak wavelengths below 190 nm are of an open-faced design, consisting of a substrate with an optical filter coating on one surface [Princeton Instruments, 2009]. For peak wavelengths up to 150 nm, the substrate is MgF_2.

If the isolation of the OI lines is found to be feasible, the two transmission filters that are ultimately chosen will be incorporated into optical design directly in front of the MCP detector. If the more complex, two-channel design is developed, the filters may cover the entire field of view of the Ganymede channel. The simplest option in this case would be for each of the filters to cover half of the focal plane, as shown in Figure 5.4a. However, Ganymede's atmosphere may be spatially variable, so it may be more useful to split the focal plane further into sections of alternating filters to investigate the variation in the 135.6 nm / 130.4 nm ratio over the instrument field of view, as in the alternating strip pattern shown in Figure 5.4b.

If the simpler, single-channel baseline JUDE design is chosen for further development, the transmission filters should not cover the focal plane entirely, as the detector will also need to respond to Jupiter's auroral emissions, which are low at $\sim$130 nm (see Chapter 1, Figure 1.3). One possibility in this case is to perform Ganymede spectroscopy with the two transmission filters in a central stripe across the instrument focal plane, leaving the portions above and below this unfiltered for observations of Jupiter's aurora, as shown in Figure 5.5. The JUDE focal plane design with the transmission filters included has not been finalised. For the purposes of the calculations in this chapter, the dual-channel design was assumed, in series with two transmission filters of equal area. The way in which the filter areas are spread across the focal plane does not affect the calculation, as long as it is known which section of the detector corresponds to which filter so that the count rates in each section are not corrected for the wrong filter transmission.

5.2 Initial calculations of Ganymede's FUV OI ratio

5.2.1 Choice of transmission filters

The throughput of each of the Princeton Instruments filters described in Section 5.1.4 as a function of wavelength, along with that of each of the Liège coatings, was extracted

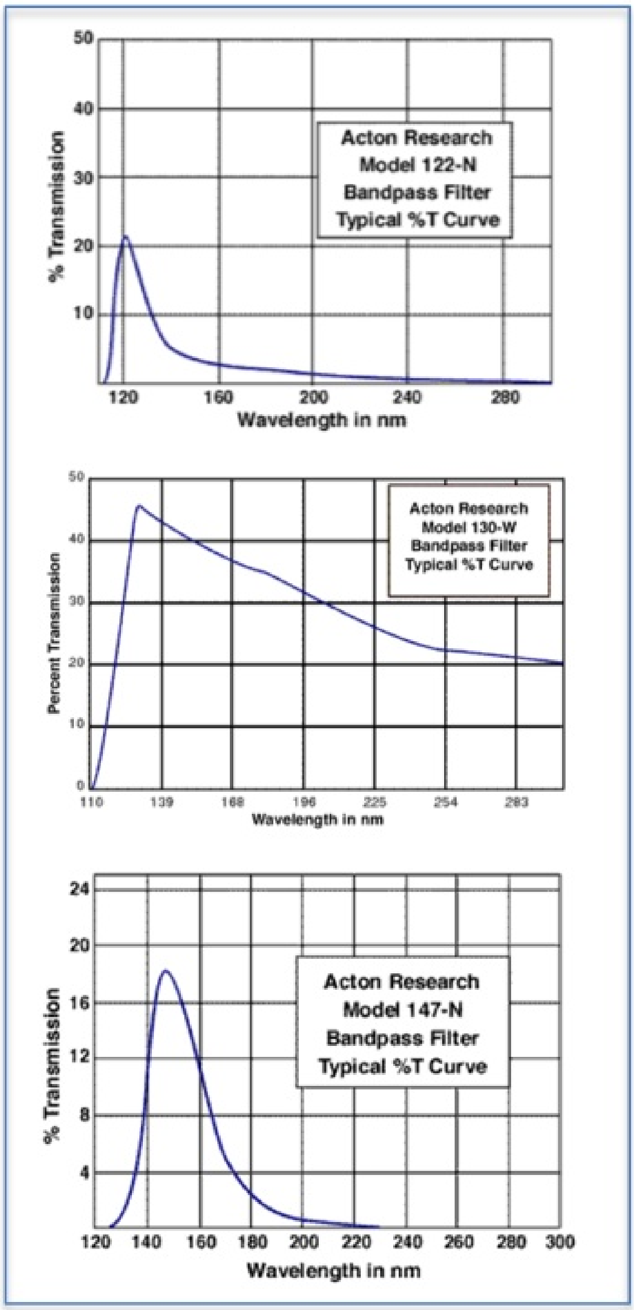

Figure 5.3 — *Transmission curves for various Princeton Instruments filters [Princeton Instruments, 2009]: top: peak at 122 nm; middle: peak at 130 nm; bottom: peak at 147 nm.*

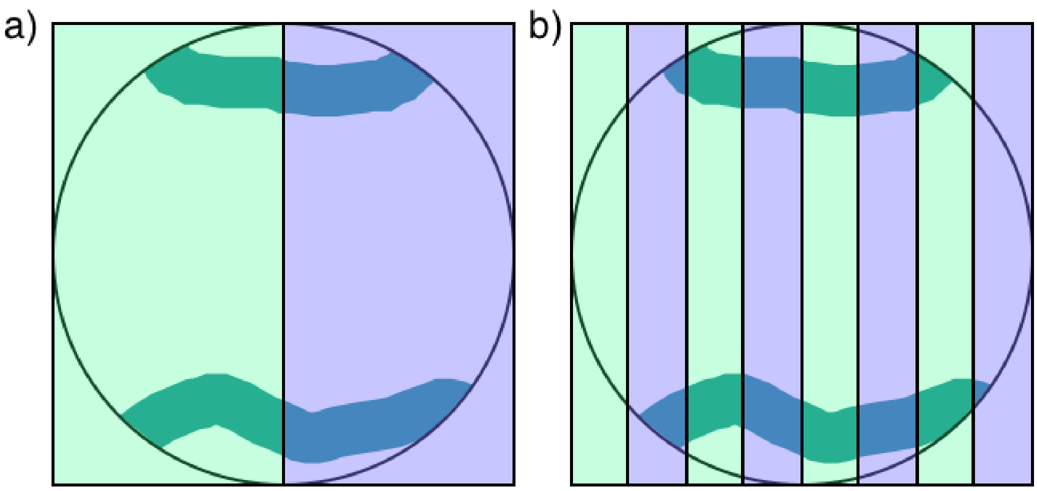

Figure 5.4 — *Possible designs for filter positions at the focal plane of the JUDE Ganymede channel, shown with Ganymede filling the instrument field of view. Different coloured stripes indicate different coating bandpasses.*

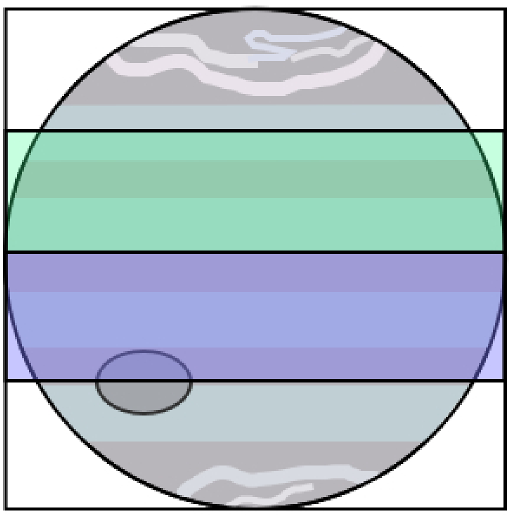

Figure 5.5 — *Possible design for UV filter positions at the baseline JUDE focal plane, shown with Jupiter filling the instrument field of view. The two transmission filters cover the central region of the focal plane for Ganymede spectroscopy, leaving unfiltered regions at the top and bottom of the field of view for observations of Jupiter's aurora.*

from the throughput curves shown in Figures 5.2 and 5.3 and interpolated to a resolution of 0.1 nm (1 Å) across the range 129 nm – 137 nm. The throughput of each filter in every wavelength bin was then multiplied by the throughput of each of the coatings at that wavelength, to give the combined throughputs for all of the possible optic configurations as a function of wavelength. The combined throughput was then multiplied by an FUV spectrum of Ganymede to provide an estimate of count rates seen at the JUDE detector for each of these instrument configurations. The spectrum used for initial calculations was obtained by the Goddard High-Resolution Spectrograph (GHRS) on the Hubble Space Telescope (HST) (see Figure 5.6 [Hall et al., 1998]). The count rate spectra produced by these calculations are given in Figure 5.7. For the Ganymede channel (the red line in Figure 5.7), the 122 nm and 147 nm filters show the greatest difference in count rate distribution for the spectrum studied, with the 130.4 nm emissions dominating through the 122 nm filter, and the 135.6 nm emissions dominating for the 147 nm filter. These two filters were chosen for further study.

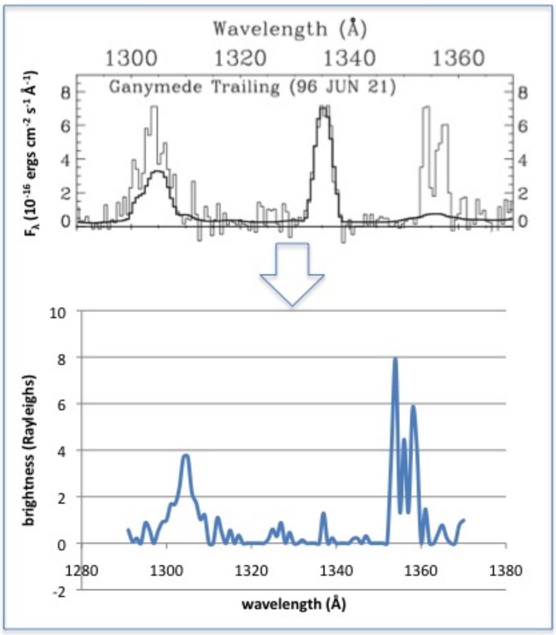

Figure 5.6 — *Top: Ganymede emissions as measured by Hubble GHRS – dark line is a model of reflected sunlight [Hall et al., 1998]. Bottom: The same data with reflected sunlight subtracted, and flux converted to Rayleighs.*

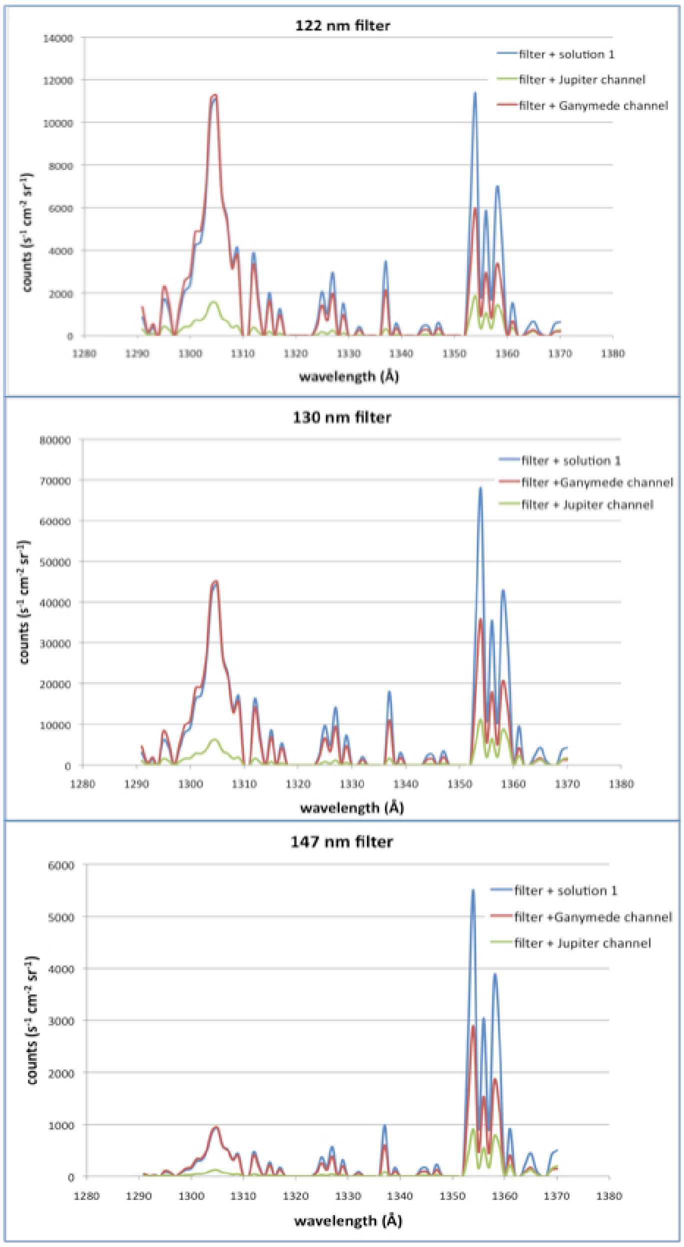

Figure 5.7 — *Count rates seen at the JUDE detector through each of the three Princeton Instruments filters, for the two optic designs described in Section 5.1.3. In each panel, the red line shows the count rates measured through a combination of the Ganymede channel (dual channel JUDE design) and the relevant filter, the green line shows the count rates measured through a combination of the Jupiter channel (dual channel JUDE design) and the same filter, and the blue line shows the count rates measured through a combination of the baseline (single channel design) channel and the filter.*

5.2.2 Emission ratio calculation background

Assuming that all FUV emissions other than the 135.6 nm and 130.4 nm lines are negligible, as suggested by the low background in the [Hall et al., 1998] spectrum shown in Figure 5.6, the total number of counts through each of the two transmission filters chosen is given by

$$t_{130.4(a)}G_{130.4} + t_{135.6(a)}G_{135.6} = F_{total(a)}, \tag{5.2}$$

and

$$t_{130.4(b)}G_{130.4} + t_{135.6(b)}G_{135.6} = F_{total(b)}, \tag{5.3}$$

where t is the transmission of the filter at the wavelength specified by the subscript, and (a) and (b) represent the 122 nm and 147 nm filters respectively. The G terms refer to the count rates of the emissions through the Ganymede channel of the instrument, and the F terms represent the count rate through the Ganymede channel plus the relevant filter (a or b). If the transmission of the filters and the total count rates through each are known, the number of counts through the Ganymede channel at 130.4 nm can be calculated by

$$G_{130.4} = \frac{F_{total(b)} - \frac{t_{135.6(b)}F_{total(a)}}{t_{135.6(a)}}}{t_{130.4(b)} - \frac{t_{135.6(b)}t_{130.4(a)}}{t_{135.6(a)}}}, \tag{5.4}$$

and from this the count rate at 135.6 nm can be determined:

$$G_{135.6} = \frac{F_{total(a)} - t_{130.4(a)}G_{130.4}}{t_{135.6(a)}}. \tag{5.5}$$

The count rates can then be divided by the Ganymede channel transmission at the relevant wavelengths to give the raw count rates from Ganymede's aurora, and these can be used to calculate the 135.6 nm / 130.4 nm ratio.

5.2.3 Count rates from GHRS spectrum

5.2.3.1 O I lines only

The count rate, C, measured by the JUDE detector at a particular wavelength is given by

$$C = G t_{GC} t_f, \tag{5.6}$$

where G is the count rate from Ganymede's emissions at that wavelength, t_{GC} is the transmission of the Ganymede channel, and t_f is the transmission of the filter placed in front of the portion of the detector in which each count is observed. Equation 5.6 was evaluated over the entire Ganymede spectrum for each of the two transmission filters chosen, using count rates from the GHRS observation of Ganymede [Hall et al., 1998] (see Figure 5.6). The 130.4 nm and 135.6 nm emissions seen in the GHRS spectrum were each spread out over $\sim$1 nm (see Section 5.2.4). For this reason, regions of 1.2 nm around 130.4 nm, and 0.9 nm around 135.6 nm were used in the calculations, and count rates through the Ganymede channel were summed over these regions. Calculations of the expected count rates through the Ganymede channel were then performed using Equations 5.4 and 5.5 and compared to these values. Counts at any other wavelength were ignored for the initial calculation. The F_{total} values required by the equations would normally be the total count rate through the combination of the Ganymede channel and the relevant filter across all wavelengths, but for this initial assessment the values were given by summing the counts in the two selected spectral regions only. The transmission of each filter at the required wavelengths was approximated by taking the mean transmission over each of the two selected regions. The calculated count rates were divided by the mean transmission of the Ganymede channel over the relevant spectral region to give estimates of the raw counts from Ganymede. The results of the initial calculations are shown in Table 5.1. The calculation was found to give an accurate estimate of the 135.6 nm / 130.4 nm ratio: the difference between the calculated value and the actual value extracted directly from the spectrum was just 1.61% of the actual value.

Table 5.1 — *Comparison of calculated count rates (s^{-1} cm^{-2} sr^{-1}) through the JUDE Ganymede channel with actual count rates, 130.4 nm and 135.6 nm only (GHRS spectrum).*

	Calculated value	Actual value	Difference as % of actual value
Counts through Ganymede channel (130.4 nm)	563227	560988	0.399
Counts through Ganymede channel (135.6 nm)	267911	273853	2.170
Raw counts (130.4 nm)	1747099	1721354	1.496
Raw counts (135.6 nm)	2491977	2416350	3.130
135.6 nm / 130.4 nm	1.426	1.404	1.610

5.2.3.2 All emissions

Although the initial result of the ratio calculation was promising, the method used ignored the presence of background events ('noise') in the spectra. In reality, it will not be possible to separate signal and noise counts measured by the JUDE detector across the UV spectrum as the detector does not have intrinsic energy resolution. Therefore, the process described in Section 5.2.3.1 was repeated, but this time all emissions (e.g. counts at all wavelengths) were included in the F_{total} values required by Equations 5.4 and 5.5. The results are shown in Table 5.2. The inclusion of noise counts meant that the calculated count rates around 130.4 nm and 135.6 nm were much less accurate (>20% different from the actual value, compared to a <3% difference when only those particular regions were considered – compare Tables 5.1 and 5.2). However, the calculated 135.6 nm / 130.4 nm ratio was accurate to a similar degree, with an error of 1.506% of the actual value.[2]

Table 5.2 — *Comparison of calculated count rates (s^{-1} cm^{-2} sr^{-1}) through the JUDE Ganymede channel with actual count rates, all emissions (GHRS spectrum).*

	Calculated value	Actual value	Difference as % of actual value
Counts through Ganymede channel (130.4 nm)	722073	560988	28.714
Counts through Ganymede channel (135.6 nm)	332937	273853	21.575
Total counts (lines plus noise)	1055010	1062355	0.691
Raw counts (130.4 nm)	2239830	1721354	30.120
Raw counts (135.6 nm)	3096824	2416350	28.161
Total raw counts (lines plus noise)	5336654	5152664	3.571
135.6 nm / 130.4 nm	1.383	1.404	1.506

[2]The percentage error in the ratio calculation is given by 100 $\times$ $|$ calculated value - actual value $|$ / actual value.

5.2.4 The need for more representative atmospheric spectra

The results of the FUV ratio calculations using the GHRS Ganymede spectrum suggest that the calculation method is sound. However, this spectrum is not representative of the emissions that will be encountered by the JUDE imager at Ganymede, because the emission lines seen in the GHRS spectrum are broadened as a result of that instrument's response to extended sources. The GHRS aperture used for the Ganymede observation had an extent of 1.74" $\times$ 1.74", and the detector consisted of diodes each with an angular size of 0.22" and dispersion of 0.0572 nm [Hall et al., 1998]. Hence, an extended object filling the aperture and emitting light at a single wavelength will appear to be emitting over a $\sim$0.46 nm (= 8 diode) region centred around the actual emission wavelength. The only other FUV Ganymede spectra currently available are the Feldman et al. [2000] STIS spectra. The dispersion in these spectra is much larger: the slit used, which had a width similar to the angular extent of Ganymede at the time of the observations, spanned $\sim$4.8 nm (see Section 5.3.1). It was therefore necessary to produce model spectra of Ganymede's atmosphere in order to perform a realistic test of the emission ratio calculation. The models were based on count rates extracted from the eight available STIS spectra, in order to cover a range of realistic emission ratios.

5.3 Spectral model of Ganymede's atmosphere

A model of Ganymede's FUV spectrum was produced, assuming that the only emissions within the 128 nm to 138 nm region were the OI lines at 130.4 nm and 135.6 nm. The OI emission region around 130.4 nm is a triplet with components at 130.217 nm, 130.486 nm and 130.603 nm, while the 135.6 nm emissions consist of a doublet at 135.560 nm and 135.851 nm [Wiese et al., 1996]. The width of the emission lines is governed by the energy of the oxygen responsible for the emissions. However, little is known about Ganymede's atmosphere, including its temperature, so the energy of the excited O atoms is not easily characterised. Two line width estimates were therefore considered, at the suggestion of Jean-Claude Gérard (University of Liège). Firstly, Doppler broadening of the lines was considered, assuming an equilibrium temperature of 600 K. In this case, the FWHM of the broadened lines is given by Equation 5.7 (derived in various text books, including Foot [2005]):

$$\Delta\lambda_{FWHM} = \sqrt{\frac{8kT\ln 2}{mc^2}}\lambda_0, \tag{5.7}$$

where k is the Boltzmann constant, T is the temperature, m is the mass of an oxygen atom, c is the speed of light in a vacuum and λ_0 is the central wavelength of the emission line. This equation is valid for the case where the O atoms are in thermodynamical equilibrium, so their velocity distribution is Maxwellian. However, the process leading to the excitation of the 130.4 nm and 135.6 nm oxygen multiplets is believed to be dissociative excitation of O_2 (see Chapter 1, Section 1.3.3), and consequently, it is quite possible that the excited O atoms are not in equilibrium [Gérard, 2011]. A second line width estimate was therefore made, assuming that the two O atoms produced by the excitation of each O_2 molecule are not in equilibrium and carry a total of 10 eV kinetic energy. This energy can be converted into a velocity using the standard kinetic energy formula $E = \frac{1}{2}mv^2$. An upper limit for the line width can be calculated by assuming that the O atoms, each carrying 5 eV kinetic energy, travel in opposite directions with their velocities directly toward or away from the observer. The Doppler shift in the emission line wavelength in each case can be calculated using Equation 5.8:

$$\Delta\lambda = \frac{v}{c}\lambda_0, \tag{5.8}$$

and the maximum line width is the difference between the two Doppler-shifted emission wavelengths. The line widths calculated for each OI multiplet using for each of the two approximations are given in Table 5.3. The non-equilibrium line widths are a factor of $\sim$6 larger than the equivalent lines in the thermodynamic equilibrium case, but in either case the widths are small.

Table 5.3 **—** *Estimated line widths for OI multiplet emissions at Ganymede*

Wavelength (nm)	Line widths (nm) Thermodynamic equilibrium case	 Non-equilibrium case
130.217	0.000571	0.00337
130.486	0.000572	0.00338
130.603	0.000572	0.00338
135.560	0.000594	0.00351
135.851	0.000595	0.00352

In the approximation that Ganymede's atmosphere is optically thin, the intensities of the multiplet component lines are in the ratio of their transition properties [Gérard, 2011], which are given in Table 5.4 (values taken from Wiese et al. [1996]). To create the Ganymede FUV spectral model, data were extracted from *HST* STIS observations of Ganymede and the count rates for the regions around 130.4 nm and 135.6 nm calculated and redistributed to the constituent multiplet lines according to the ratios in Table 5.4. The number of counts in each line was then distributed into a gaussian, initially with a FWHM as calculated for O atoms in thermodynamic equilibrium at 600 K (Table 5.3, middle column), and then in a separate procedure using the FWHM calculated for O atoms that are not in equilibrium (Table 5.3, right column). In this way, two spectra were produced for each of the STIS images, to allow the accuracy of the 130.4 nm : 135.6 nm calculation to be investigated for two different atmospheric approximations. A more detailed description of the extraction of count rates from *HST* STIS files is given in Section 5.3.1.

Table 5.4 — *Transition probabilities for OI emissions around 130.4 nm and 135.6 nm [Wiese et al., 1996].*

Wavelength (nm)	Transition probability (s^{-1})
130.217	3.41×10^8
130.486	2.03×10^8
130.603	6.76×10^7
135.560	4.20×10^3
135.851	1.36×10^3

5.3.1 Extracting count rate spectra from STIS data files

Eight STIS observations of Ganymede were performed over four contiguous *HST* orbits on October 30th, 1998 [Feldman et al., 2000][3]. An example of one of the STIS spectral images obtained during this observation campaign is shown in Figure 5.8. STIS is an imaging spectrograph, so its data files contain information about both the spectra of emissions and their spatial distribution. Slits of various widths and heights may be used as STIS apertures, and the distribution of any objects within the area of the slit is conserved in the image produced. Light entering the selected slit is collimated by an off-axis elliptical mirror and the parallel beam is directed to a grating wheel, where one of 16 possible diffraction gratings is selected according to the wavelength range of interest and the spectral dispersion required. The light dispersed by the grating is then focused onto one of three detectors, with each pixel along the horizontal axis of the detector corresponding to a specific wavelength within the dispersed image (a detailed description of the STIS design is given in Woodgate et al. [1998]). The image produced is therefore made up of various images of the STIS slit at wavelengths given by the position of each slit image along the x axis, and spectra can be extracted by taking a cut along the

[3]The image IDs for the eight STIS observations are o53k01010 – o53k01080. The data sets can be downloaded by entering these IDs into the form at http://archive.stsci.edu/cgi-bin/dataset_lookup.

x direction. However, the finite width of the slit means that the spectral information is convolved with the spatial distribution of the emitting objects within the slit, so an object filling the slit and emitting at a certain wavelength will produce a spectral line that is broadened to the width of the slit.

The image shown in Figure 5.8 is a 1201 pixel $\times$ 1201 pixel fluxed two-dimensional image (x2d) file: a calibrated data file in which the signal is given in units of ergs s^{-1} cm^{-2} Å^{-1} arcsec^{-2}. Each pixel in the image is 0.0244" $\times$ 0.0244", and the dispersion is 0.584 Å pixel^{-1}. In total, the image extends from 115 nm to 172 nm, with a height of 25". The width of the slit used to acquire the image was 2", and at the time of the observations Ganymede was 4.25 AU from Earth, so its diameter was 1.71" [Feldman et al., 2000]. The signal due to emissions from Ganymede can be seen as a horizontal stripe across the image in the upper half. The vertical stripe of enhanced signal toward the left edge of the image is due to geocoronal Lyman-α emissions at 121.6 nm.

The 1201 pixel $\times$ 71 pixel stripe containing signal from Ganymede was extracted from each x2d data file. The signal in each column was averaged to give a mean signal per pixel value for each 0.584 Å wavelength bin. A background spectrum for each image was obtained by finding the average signal for each wavelength across two 1201 pixel $\times$ 151 pixel regions, one above and one below the image of Ganymede. The signal was then converted to photons cm^{-2} s^{-1} Å^{-1} by dividing by the photon energy for each wavelength bin (using the equation $E = \frac{hc}{\lambda}$) and multiplying by the area of Ganymede's disk in arcseconds ($A = \pi \left(\frac{1.71}{2}\right)^2$). An example of an extracted spectrum after noise has been subtracted is shown in Figure 5.9 (the signal flux has been rebinned by 4 pixels to match Figure 2 in Feldman et al. [2000]).

The flux values given in Figure 5.9 include a contribution from reflected solar radiation, which was modelled by convolving a solar spectrum obtained by the Upper Atmosphere Research Satellite (*UARS*) SOLar STellar Irradiance Comparison Experiment (SOLSTICE) instrument on the day of the STIS Ganymede observations[4] (see Figure 5.10) with a top-hat function of Ganymede radius so that the spectral lines

[4]SOLSTICE data downloaded from http://mirador.gsfc.nasa.gov/, November 2010

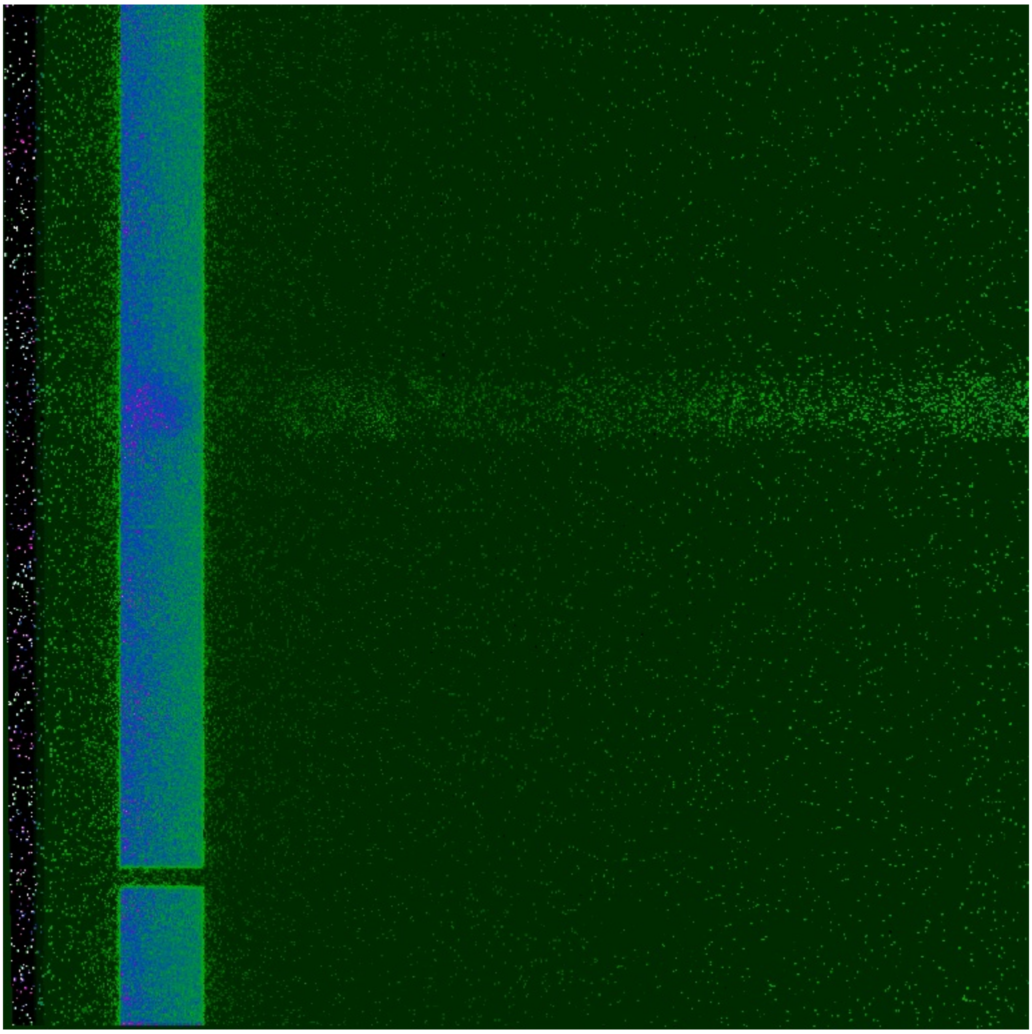

Figure 5.8 — *An example of a STIS spectral image (image ID o53k01010). The horizontal axis extends from 115 to 172 nm and the image is 25" high. The bright vertical stripe towards the left is geocoronal Lyman-α emission. The horizontal band visible near the bottom of the Ly-α stripe is the shadow of a 0.5" fiducial bar in the slit. The horizontal stripe in the upper portion of the image is produced by emissions from Ganymede.*

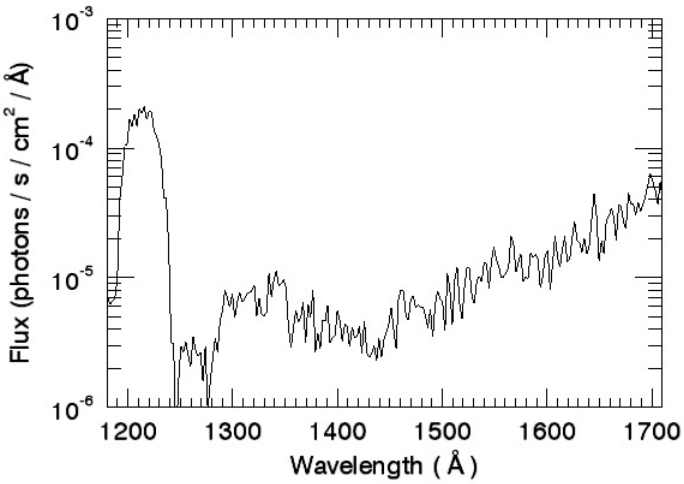

Figure 5.9 — *Spectrum extracted from the image shown in Figure 5.8 (ID o53k01010).*

were broadened to the same degree as the STIS images. Before the convolution could be performed, the SOLSTICE spectrum had to be converted from a solar flux at 1 AU ($F_\odot$), to the flux reflected by Ganymede's surface (F_G), using Equation 5.9:

$$F_G(\lambda) = \frac{F_\odot(\lambda)p(\lambda)\Omega_G}{\pi d^2}, \tag{5.9}$$

where Ω_G is the solid angle of Ganymede as seen from Earth, p is the planetary albedo of Ganymede and d is the Sun-Jupiter distance in AU [Feldman et al., 2000]. The albedo used for the calculation was 2.3% – the value derived by Feldman et. al, who assumed an albedo that is constant with wavelength. The resulting spectrum is shown in Figure 5.11. This spectrum was then scaled to fit each of the STIS Ganymede spectra (see Figure 5.12), with the assumption that all signal at wavelengths greater than 138 nm was due to reflected sunlight [Feldman et al., 2000]. The solar component of each spectrum could then be subtracted to give Ganymede's FUV emission spectrum, as shown in Figure 5.13. This is the same method used by Feldman et al. [2000] in their analysis of the same STIS images.

The spectra extracted from the STIS Ganymede observations provided information about the UV flux from Ganymede's atmosphere, but in order to determine the amount of flux in each of the OI emission lines, the spatial distribution of the emissions had to

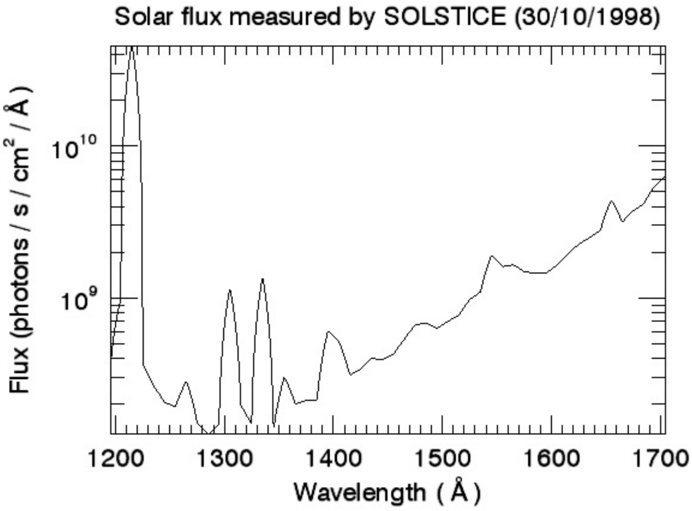

Figure 5.10 — *Solar spectrum at 1 AU, obtained by the SOLar STellar Irradiance Comparison Experiment (SOLSTICE) on UARS.*

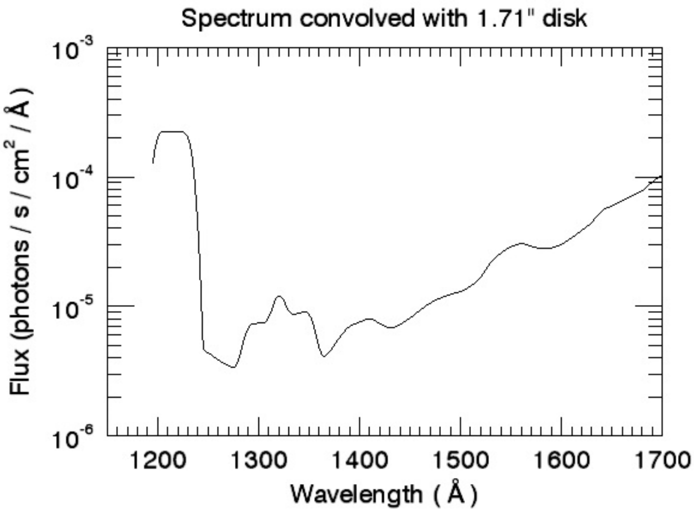

Figure 5.11 — *Reflected solar flux at Ganymede, extrapolated from SOLSTICE spectrum (see Figure 5.10) and assuming an albedo of 2.3% [Feldman et al., 2000]. The spectrum has been convolved with a uniform reflecting disk of Ganymede radius.*

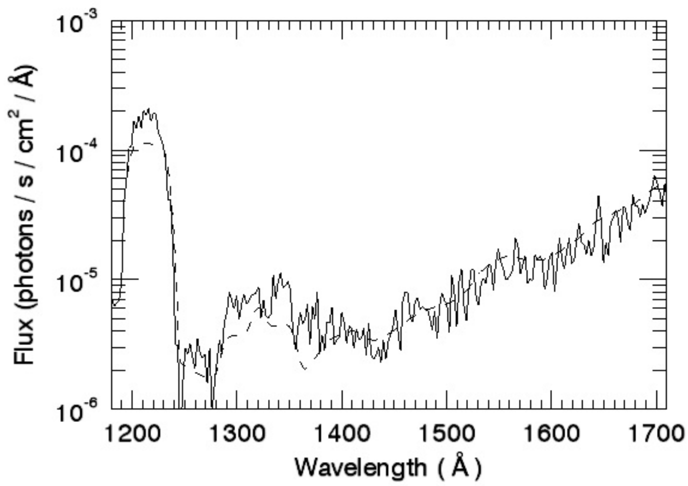

Figure 5.12 — *As Figure 5.9 but with the reflected solar component of Ganymede's spectrum (Figure 5.11) overlaid and scaled to fit.*

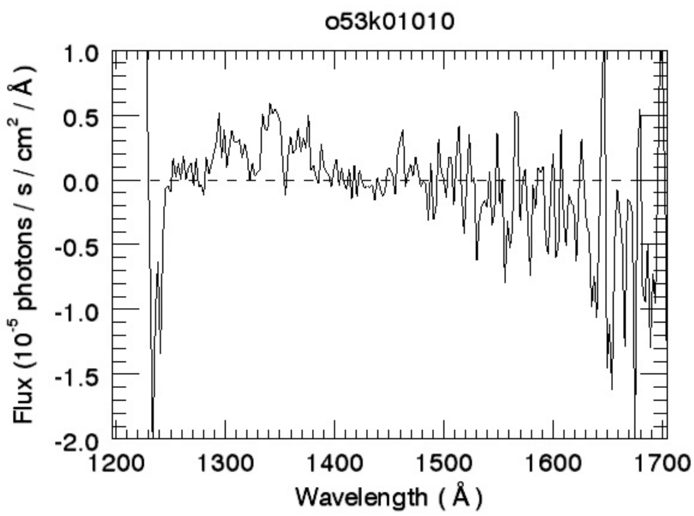

Figure 5.13 — *Ganymede's emission spectrum as extracted from image o53k01010, after subtraction of the reflected solar component.*

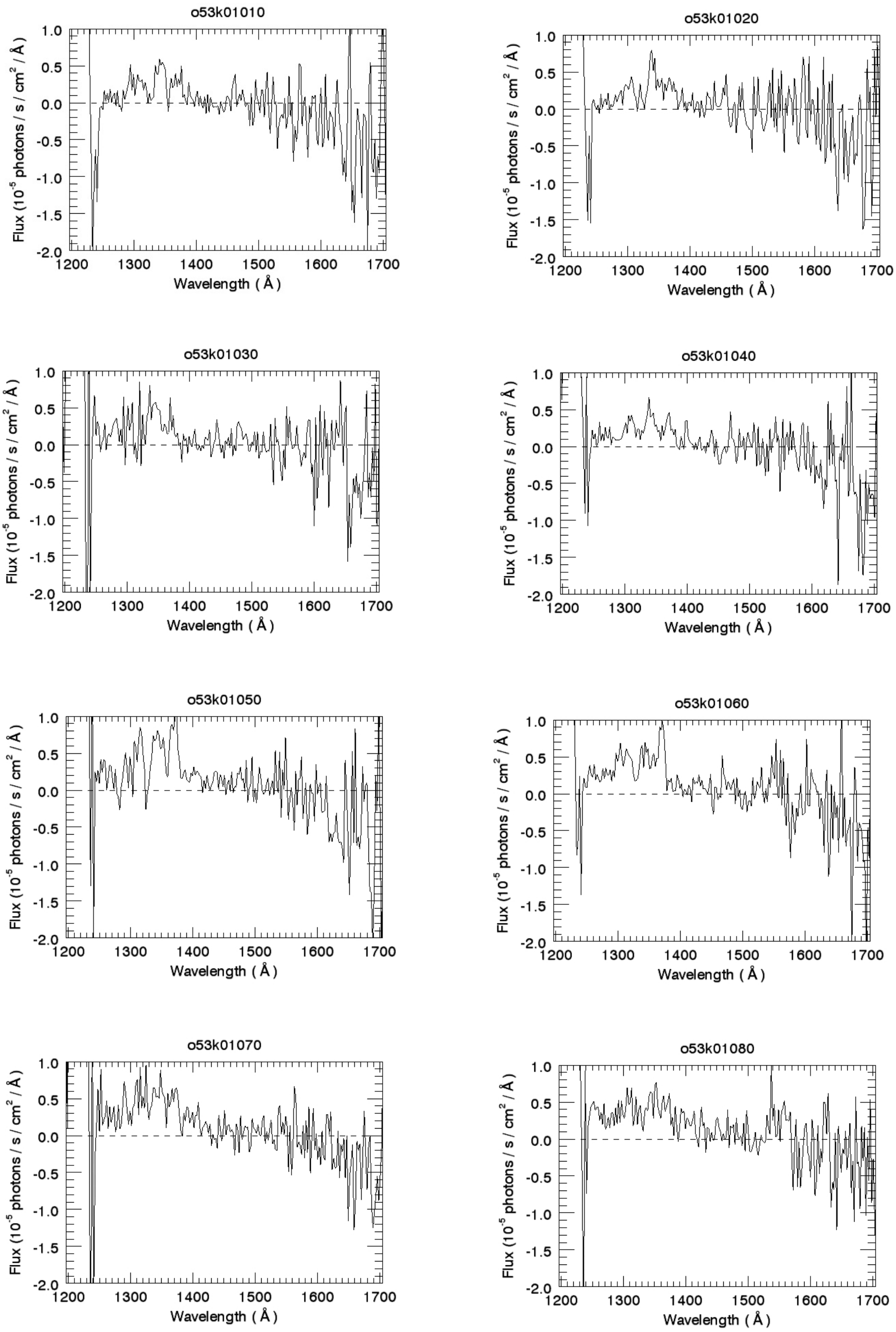

Figure 5.14 — *As Figure 5.13 for all of the 30/10/1998 STIS images: from o53k01010 (top left) to o53k01080 (bottom right).*

be considered. The slit used for the observations had a width of 2", which corresponds to ∼82 pixels. With a dispersion of 0.584 Å pixel^{-1}, this means that emissions at any specific wavelength which are spatially distributed over the width of the slit will appear to be spread over ∼4.8 nm. Hence, emissions at 130.4 nm may appear anywhere between 128.0 and 132.8 nm in the STIS spectra, and emissions at 135.6 nm may appear between 133.2 and 138.0 nm. Since these emission regions do not overlap, and no other FUV emissions were expected in the 128.0–138.0 nm part of the spectra, the 130.4 nm flux for each of the extracted spectra was calculated by summing over 128.0–132.8 nm and the 135.6 nm flux by summing over 133.2–138.0 nm, ignoring negative flux values, which may be caused by a number of factors, including the coarseness of the subtracted solar spectrum and a possible error in the fit of this spectrum to the extracted Ganymede spectra. The two flux values were then distributed into the constituent multiplet emission lines, according to the ratios given in Section 5.3, to produce models of the raw Ganymede emission spectra at the time of each STIS observation. The model produced for image o53k01010, assuming non-equilibrium so the line widths are 0.0034 nm (130.4 nm emissions) or 0.0035 nm (135.6 nm emissions), is shown in Figure 5.15. Figure 5.16 provides a zoomed-in view of each of the two multiplets in the same spectrum, so that the Gaussian shape of the emission lines can be seen.

5.4 135.6 nm / 130.4 nm ratio calculations using modelled spectra

A set of OI ratio calculations were performed with the modelled Ganymede emission spectra, using the same method described in Section 5.2.3. The results are shown in Table 5.5. The emission ratios measured directly from the spectra were generally very different from the ratios derived by Feldman et al. [2000] for the same x2d files (see Chapter 3, Table 3.3), with only the ratios measured from images o53k01070 and o53k01080 matching the published values. This may be due to slight differences in the method of extracting the spectral information from the original STIS files– for example, different

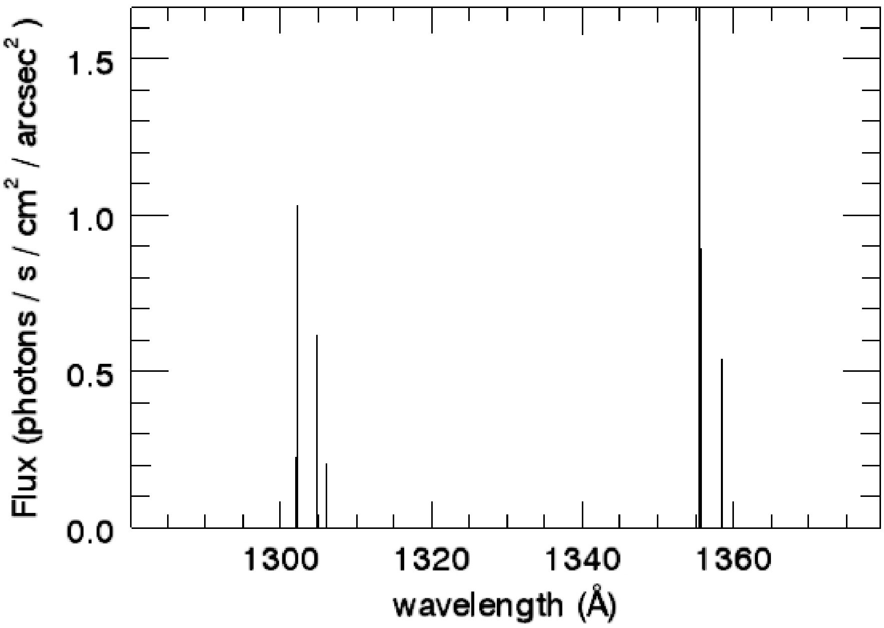

Figure 5.15 **—** *Modelled emission spectrum using flux values from STIS image o53k01010, with line widths of FWHM 0.0034 nm (130.4 nm emissions) and 0.0035 nm (135.6 nm emissions).*

areas of the images may have been used for the background subtraction, and the solar spectrum was fitted to each extracted spectrum by eye, allowing more scope for variation. However, the range of ratios measured here, 1.2 – 2.8, is similar to that measured by Feldman et al., 1.2 – 3.2, so the model spectra are able to provide an indication of the accuracy of the ratio calculation method across a range of ratio values likely to be observed at Ganymede. Table 5.5 shows that the calculations performed using the model spectra gave emission ratios that varied by less than a percent from the known ratio in each case. There was not a significant difference between the agreement of results using the equilibrium and non-equilibrium spectra, and the most accurate result was found for an emission ratio of $\sim$1.6. However, the spectra used included no noise contribution, and the accuracy of the results is therefore to be expected. The agreement between the calculated and measured emission ratios was better for the model spectra than for the GHRS spectra without noise described in Section 5.2.3 (results of the GHRS calculations

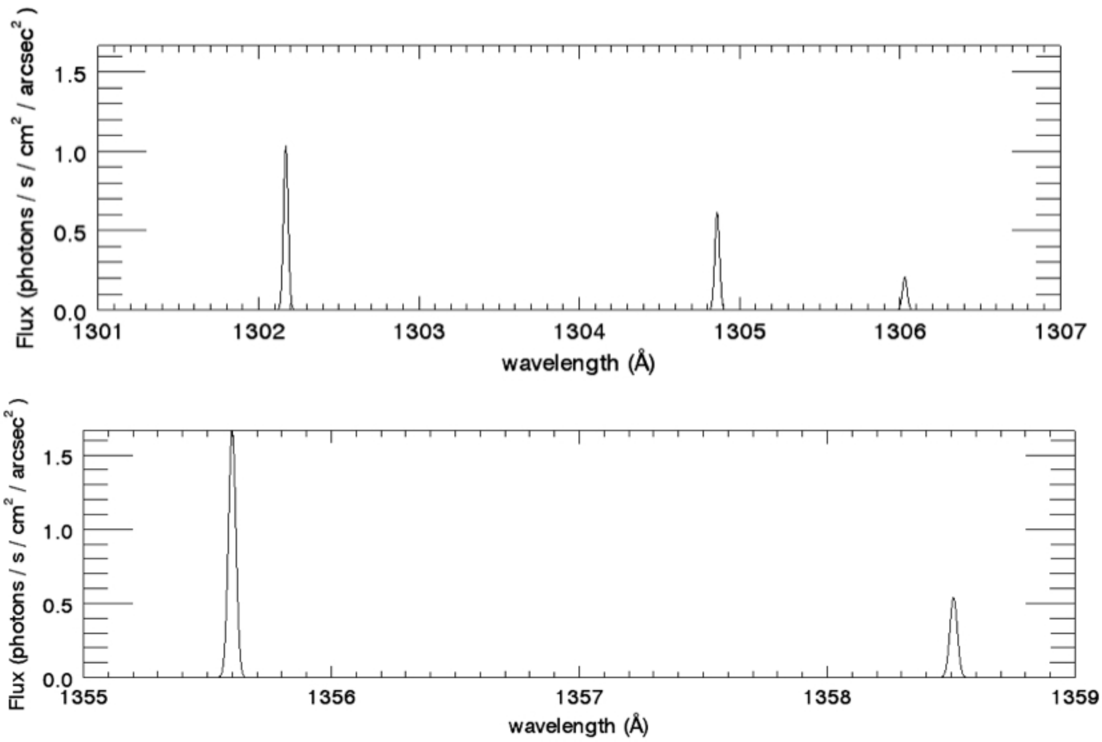

Figure 5.16 — *Close-up view of the multiplets at 130.4 nm and 135.6 nm, from the spectrum in Figure 5.15.*

are shown in Tables 5.1 and 5.2). This may be due to the emission regions in the model being narrower. The regions over which the throughput of the filters were averaged for the calculations were reduced from 1.2 nm (centred around 130.4 nm) and 0.9 nm (centred around 135.6 nm) for the GHRS calculations to 0.6 nm and 0.4 nm respectively for the model spectra calculations. This reduces the possibility of variations of the optic's transmissions affecting the results. The throughput curves for the Ganymede channel coating and the two filters are shown in Figure 5.17.

***Table 5.5** — Results of emission ratio calculation for spectral models based on STIS observations of Ganymede*

Image ID	FWHM = 0.0034 nm			FWHM = 0.00057 nm		
	Measured ratio	Actual ratio	Difference as % of actual value	Measured ratio	Actual ratio	Difference as % of actual value
o53k01010	1.1959	1.2018	0.496	1.1960	1.2020	0.496
o53k01020	1.2529	1.2589	0.473	1.2531	1.2590	0.473
o53k01030	2.7727	2.7905	0.639	2.7730	2.7908	0.640
o53k01040	1.2487	1.2546	0.474	1.2488	1.2547	0.474
o53k01050	1.6147	1.6213	0.409	1.6148	1.6215	0.409
o53k01060	1.3170	1.3230	0.452	1.3171	1.3231	0.452
o53k01070	1.2078	1.2137	0.491	1.2079	1.2138	0.491
o53k01080	1.2039	1.2098	0.493	1.2040	1.2099	0.493

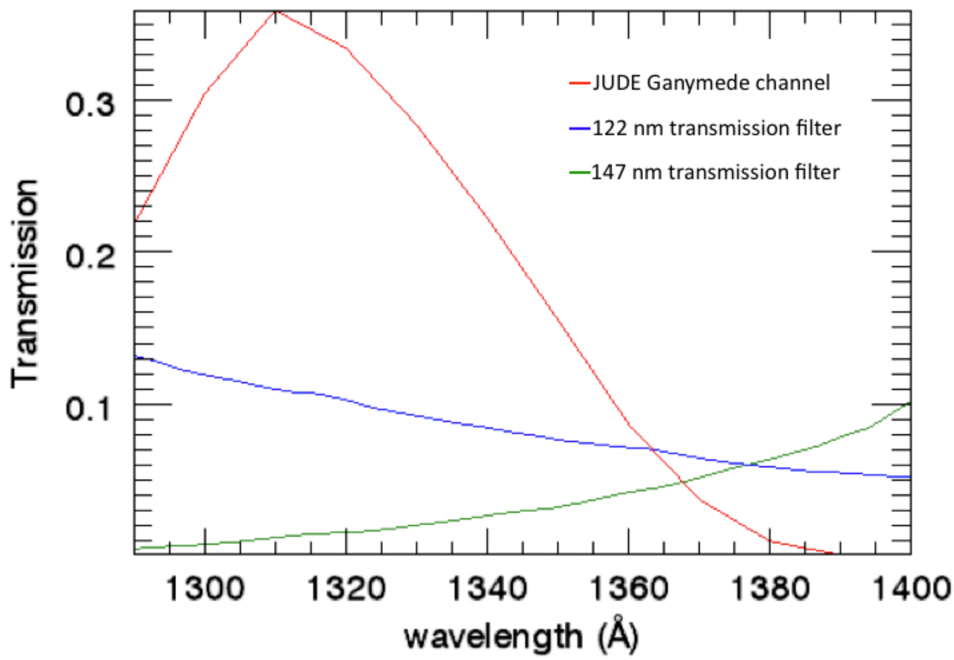

Figure 5.17 **—** *Throughput curves for the JUDE optical components relevant to the FUV OI emission ratio calculations.*

5.4.1 Further calculations with noise added

The ratio calculation tests on the modelled spectra were repeated, with Poisson noise added to each spectrum using the IDL RANDOMN random number generator function. The mean noise was set such that the overall signal : noise ratio was $\sim$2 : 1, to assess the accuracy of the calculation in a worst-case scenario. For comparison, only $\sim$20% of the counts in the GHRS spectrum shown in Figure 5.6 are found outside the two main emission regions around 130.4 nm and 135.6 nm, so the actual signal : noise ratio encountered by JUDE should be significantly better than that modelled here. An example of one of the modelled spectra before and after the addition of noise is shown in Figure 5.18.

The results of the ratio calculations for modelled spectra with noise are given in Tables 5.6 (for the non-equilibrium case: spectra with line widths of 0.0034 – 0.0035 nm) and 5.7 (for the thermodynamic equilibrium case: spectra with line widths of 0.00057 –

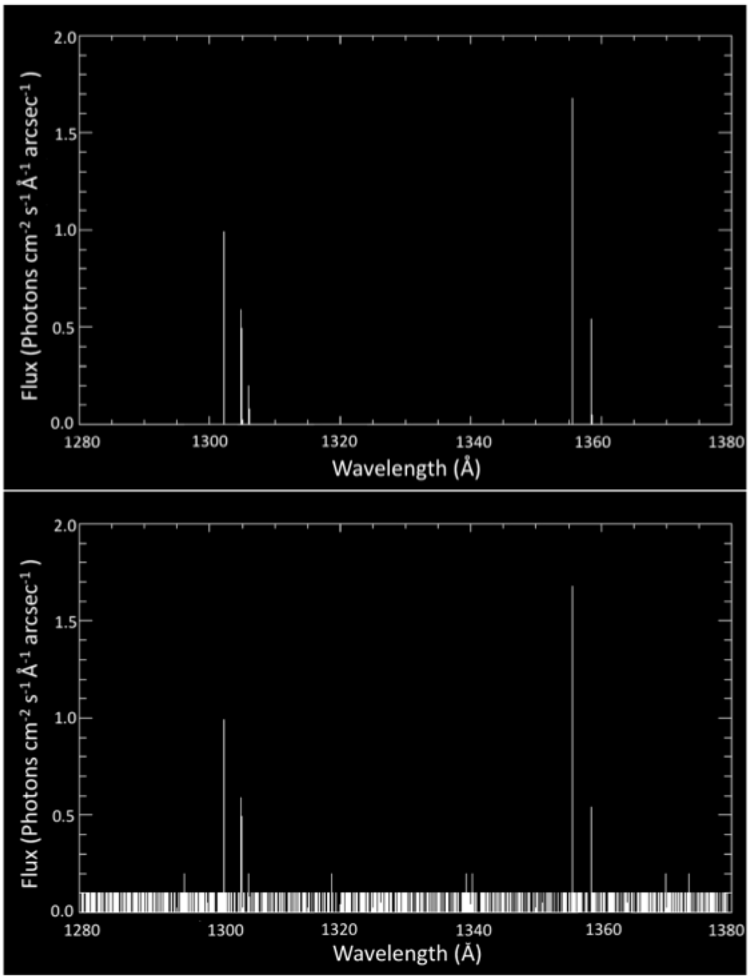

Figure 5.18 — *Top: modelled spectrum based on STIS image o53k01020, with line widths of FWHM=0.0034 nm. Bottom: the same spectrum with random noise added to each wavelength bin such that the total noise is equal to half the original signal.*

0.00059 nm). The known emission ratio for each spectrum is slightly different to that for the equivalent spectrum with no noise (see Table 5.5), because noise was added to every wavelength bin, including those in the emission regions. The accuracy of the ratio calculation was diminished compared to the accuracy of the earlier, noiseless calculations, as expected. The most accurate result for both the equilibrium and non-equilibrium atmospheric models was found for an emission ratio of $\sim$1.5, with a difference of 1.4% and 1.8% between the real and measured results in these two cases respectively. The least accurate result for both models was found for a ratio of $\sim$2.6, with errors of 16–17%.

Table 5.6 — *Results of emission ratio calculation for spectral models based on emissions from oxygen atoms which are not in thermodynamic equilibrium (e.g. the FWHM of emission lines is ∼0.0034 nm), with noise.*

Image ID	Measured ratio	Actual ratio	Difference as % of actual value	Signal : Noise
o53k01010	1.2310	1.1692	5.285	2.14 : 1
o53k01020	1.2531	1.2156	3.082	1.90 : 1
o53k01030	2.1625	2.6071	17.05	1.99 : 1
o53k01040	1.2995	1.2058	7.771	1.99 : 1
o53k01050	1.5035	1.5317	1.844	1.88 : 1
o53k01060	1.3463	1.2754	5.562	2.02 : 1
o53k01070	1.2500	1.1632	7.457	2.07 : 1
o53k01080	1.2380	1.1720	5.630	2.09 : 1

5.5 Conclusions

The calculations described above show that determination of the 130.4 nm / 135.6 nm emission ratio of Ganymede's atmosphere is possible using a combination of JUDE reflective multilayer coatings and UV transmission filters, as long as a good knowledge of the throughput of these optical components is obtained. However, the accuracy of the ratio calculation will decrease if any noise emissions at wavelengths other than that of the two FUV OI emissions are detected by the imager. The accuracy of the calculation for a noisy spectrum appears to vary with the magnitude of the ratio, so it will be useful in future to create a comprehensive set of atmospheric models, spanning the range of ratios expected, in order to determine whether the error for any particular ratio value at a set noise level can be predicted. The level of error that is acceptable for the ratio results to provide constraints on the atmospheric composition should also be determined before the final JUDE optical configuration is decided.

Table 5.7 — *Results of emission ratio calculation for spectral models based on emissions from oxygen atoms which are in thermodynamic equilibrium (e.g. the FWHM of emission lines is ∼0.00057 nm), with noise.*

Image ID	Measured ratio	Actual ratio	Difference as % of actual value	Signal : Noise
o53k01010	1.2408	1.1689	6.155	2.07 : 1
o53k01020	1.2909	1.2269	5.212	1.92 : 1
o53k01030	2.1443	2.5486	15.86	1.94 : 1
o53k01040	1.3294	1.2152	9.395	2.09 : 1
o53k01050	1.5244	1.5466	1.438	1.94 : 1
o53k01060	1.3160	1.2801	2.807	2.00 : 1
o53k01070	1.2554	1.1729	7.038	1.93 : 1
o53k01080	1.2223	1.1663	4.806	1.93 : 1

A potential complication of the 130.4 nm / 135.6 nm isolation by JUDE is the effect of radiation on the UV optics. Although the multilayer coatings have their heritage in UV optics designed for the *Juno* mission to Jupiter, and have hence been designed to cope with radiation in the Jupiter environment, ionising radiation may lead to effects such as optical darkening in the transmission filters (e.g. Speit et al. [1992]). Any change in the throughput of the optical components will affect the ratio calculations, so it is vital to investigate the radiation dose each component is likely to experience during the mission, and how this will affect the throughput.

5.6 Summary

The current JUDE baseline design is based on reflective UV optics designed at the University of Liège, Belgium. Generally, materials become less reflective with decreasing wavelength, and UV reflection at normal incidence is unlikely. The Liège optics therefore include multilayer coatings: UV radiation reflected from the interfaces between the layers interferes constructively, increasing the efficiency of reflection relative to that of a single layer. The baseline optical design for JUDE consists of a single channel through which emissions from both Jupiter and Ganymede can be observed. However, a more complex design with separate channels optimised for each of these two objects has been suggested. An investigation was performed to determine whether the Ganymede channel of this design, in conjunction with two UV transmission filters in front of the instrument focal plane, could be used to isolate the ratio of OI emissions in Ganymede's atmosphere at 130.4 nm and 135.6 nm. Knowledge of this ratio would provide information about the composition of Ganymede's atmosphere, which is not well characterised at present.

Initially, a model of the JUDE response to a spectrum from a *HST* GHRS observation of Ganymede was created to test the possibility of isolating the 135.6 nm / 130.4 nm ratio, using only a knowledge of the throughput curves of the optical components and the count rates observed through the two transmission filters. Although the results were promising, the spectrum used was unrepresentative of Ganymede's raw emissions, as it included a convolution with the GHRS instrument response which broadened the emission lines. For this reason, model spectra were produced based on count rates from *HST* STIS observations. The linewidths of the emissions within the spectra were dependent on the energy of the oxygen in Ganymede's atmosphere and, since the atmosphere is not well understood, two estimates were made: one for oxygen in thermodynamic equilibrium and one for the non-equilibrium case.

The results of the ratio calculations based on the model spectra showed no significant difference in accuracy between calculations using the equilibrium model and those using the non-equilibrium model, since in both cases the linewidths were very small: much less than 0.1 nm. When random noise was added to the spectra, the accuracy of the calculated ratio varied with the magnitude of the ratio– the error on a ratio of $\sim$2.6 : 1 was approximately ten times larger than than the error on a ratio of $\sim$1.5 : 1. Future work will concentrate on investigating the relationship between the magnitude of the emission ratio and the magnitude of error in calculations at that ratio. A thorough understanding of the potential effects of radiation in the Jupiter environment on the throughputs of the UV coatings and filters will also be required, as the ratio calculation method depends on knowledge of these parameters.

CHAPTER 6

Summary, Conclusions and Future Work

The work described in this thesis was performed to determine whether an FUV imager using MCP optics would be capable of achieving 100 km spatial resolution when observing Jupiter from Ganymede orbit. It has been shown that diffraction would degrade the resolution of such optics by a factor of $\sim$4 when observing emissions at 135.6 nm wavelength (Chapter 3), making the 100 km resolution goal unfeasible. Laboratory measurements of the resolution of two similar MCP optics failed to match the theoretical limit determined by the optic pore size and slump radius (Chapter 4). These two results lead to the conclusion that MCP optics are not suitable for high-resolution FUV imaging within the jovian system.

6.1 JUDE

Auroral images provide information about a planet's atmospheric composition, the conditions within its magnetosphere at the time of the observation, and, when combined with charged particle and field information from other instruments, the coupling between the solar wind, magnetosphere, ionosphere and atmosphere. Far ultraviolet imagers are well-suited to auroral science, as the solar background in the FUV is greatly reduced compared to the visible background, meaning imaging is possible in both the nightside and dayside hemispheres. Jupiter's FUV aurora has been the subject of various investigations by the UV instruments on the Hubble Space Telescope (*HST*), and previous missions to the planet have carried ultraviolet spectrometers which have led to an increased understanding of the emissions (see Chapter 1, Section 1.1.2). However, no mission to Jupiter has included on its payload any FUV imagers capable of obtaining large-scale images of the aurora with high temporal resolution and continuity of coverage. Such an imager would increase our understanding of the fainter, more variable auroral emissions, leading to better models of the processes responsible for them. It would also allow other, fainter UV emissions within the jovian system, such as Ganymede's aurora, to be investigated in detail for the first time.

The JUpiter ICy moon Explorer (*JUICE*) is a European mission to the Jupiter system, competing with two other large European missions (*Athena* and *NGO*) for a 2022 launch. By the time the spacecraft is operational, *HST* will have reached the end of its mission lifetime, and its successor, the James Webb Space Telescope, will not carry any UV imaging instruments [Gardner et al., 2006]. No other Earth-orbiting telescopes with UV planetary imaging capability are planned at present, so it is likely that imaging of Jupiter's UV aurora from Earth orbit will cease. Hence, there is a strong case for a dedicated FUV imager on board *JUICE*, particularly if this new instrument is able to produce higher resolution images than *HST* STIS– the instrument responsible for the most highly resolved images at present. An in situ imager would also have a significant advantage over Earth orbiting imagers as the higher flux experienced when imaging emissions from within the jovian system would allow images to be obtained with greatly reduced integration times, allowing fainter or more transient emissions to be studied.

The Jupiter system Ultraviolet Dynamics Experiment (JUDE) is an FUV imager designed for possible inclusion on the *JUICE* mission. Two designs were investigated for the instrument, one based on UV reflective optics and one based on novel microchannel plate (MCP) optics. This thesis concentrated on the MCP optic design, with a description of the instrument given in Chapter 2, and a feasibility study was performed based on both modelling of the instrument response and laboratory investigations of the achievable resolutions of similar MCP optics. The results of the study are described in Chapters 3 (modelling) and 4 (laboratory measurements). Two major problems with the design were discovered. Firstly, modelling of diffraction effects suggested that the combination of a small (160 μm $\times$ 160 μm) aperture and a relatively long ($\sim$130 nm) wavelength of interest would lead to a degradation of a factor of almost four in the best resolution achievable by the optic (see Chapter 3, Section 3.2). Secondly, to date no MCP optic has been shown to achieve its theoretical resolution limit in laboratory focusing tests (see Chapter 4). The resolution of an MCP optic is, in theory, the angle subtended by each individual channel at the focal plane. Hence, an improvement of the resolution is possible by decreasing the channel width or increasing the focal length (by increasing the radius of curvature of the optic). Neither of these options is appropriate for JUDE, as a decrease in channel width would increase the diffraction effects seen in images, and an increase in focal length would lead to greater mass and volume, making the instrument less competitive. The ability to match the spatial resolution of *HST* STIS is seen as a critical requirement for JUDE, and since the MCP optic design cannot achieve this goal, the reflective optic design was selected for further development.

The baseline JUDE reflective optic design makes use of multilayer reflective coatings deposited onto nickel-plated aluminium mirrors, giving a bandpass of $\sim$120–150 nm. The option to modify the design to include a beam-splitter has been suggested: with this function in place, the beam would be split and directed to two channels, one optimised for observing Ganymede's oxygen emissions, with a peak transmission around 130 nm and a long-wavelength cut off of $\sim$140 nm, and one for Jupiter observations, with a lower transmission but slightly wider bandpass, extending to ~155 nm, as Jupiter's emissions are particularly low in the region around 130–135 nm (see Chapter 1, Figure 1.3). This option would add complexity to the optical design of the instrument, and increase its mass and volume, as a second detector likely to be required. However, the dedicated Ganymede channel would provide the possibility of isolating each of the two FUV OI emission lines visible in the moons atmosphere, at 130.4 nm and 135.6 nm. The ratio of these emissions can provide information about the composition of Ganymede's atmosphere, which at present is not well characterised. To date, the only measurements of the emissions have been taken from the few *HST* observations of Ganymede (e.g. Feldman et al. [2000], and have been hindered by low fluxes and the limited spatial resolution of the instruments used.

In order to test the possibility of isolating the Ganymede OI emissions, two transmission filters were considered for use in series with the mirror coating proposed for the JUDE Ganymede channel. If the transmission of both filters at 130.4 and 135.6 nm was well known, along with the count rates through each filter (assuming the radiation had first encountered the Ganymede channel coating), the count rate through the Ganymede channel at each of the two wavelengths of interest could be determined by solving two simultaneous equations (see Chapter 5). The raw count rate at each wavelength, and therefore the ratio between the two, could then be calculated by dividing these values by the transmission of the Ganymede channel coating at the relevant wavelength. This method was tested in Chapter 5 using modelled spectra based on *HST* STIS observations of Ganymede, and the difference between the actual count rates and those calculated using the simultaneous equations method was consistently below 1% of the actual value. This result is encouraging, but the method relies on an excellent knowledge of the filter and coating transmissions, which may be affected by the intense radiation of the jovian system. Hence, modelling of the expected radiation dose of the instrument over the course of the *JUICE* mission, and a thorough investigation into the effects this may have on the optical components, will be an essential part of the future work on the instrument design.

Another factor that must be considered before the JUDE design is finalised is the orientation of any transmission filters used. For the Ganymede line ratio calculations, both of the filters must encounter flux from the aurora at the same time, as the ratio is thought to be variable (see Table 1 in Feldman et al. [2000]). The best orientation for this will depend in large part on the spacecraft yaw steering, which must be performed in order to keep the solar panels illuminated at all times. More detailed information about the yaw steering is therefore necessary before the filter design is finalised.

As well as the finalisation of the optical design, consideration should be given to the type of data collected by JUDE and how it is stored. A number of operating modes have been suggested for the imager, to enable data collection at various spatial and temporal resolutions across the range of intensities it is expected to encounter: from features with brightnesses $<$100 R at Ganymede, to the few MR upper limit for intense features at Jupiter. The imaging modes are summarised in Chapter 2, but the best way to switch between modes has not yet been decided. Possible methods include imaging in each mode consecutively in a fixed cycle, or adapting the instrument electronics to respond differently to emissions of different intensities.

6.2 Other applications for the MCP optic design

Although the MCP optic design was found to be unsuitable for JUDE, it may still be suitable for applications with less strict spatial resolution requirements, as its compactness and ability to achieve wide fields of view are desirable features for any space-based imager. Two potential future instruments making use of MCP optics are discussed below.

6.2.1 WFAI

The Wide Field Auroral Imager (WFAI) was discussed briefly in Chapter 4, which contains the results of UV focusing tests performed using a prototype WFAI MCP optic and detector. The main aim of WFAI is to allow large scale imaging of the Earth's FUV auroral emissions from low Earth orbit, so that images can be combined with detailed particle and field measurements from the same platform, leading to more refined models of the interactions between the Earth's magnetosphere, ionosphere and atmosphere. In this application, the diffraction of FUV radiation within the optic channels is less problematic than for the MCP JUDE design, since the emissions of interest are much closer so good spatial resolution is easier to achieve. One potential mission for which WFAI may be particularly well suited is the *KuaFu* project (Tu et al. [2008] – although the mission design has changed slightly since the publication of that paper, and is now a collaboration between China and ESA), which is designed to investigate space weather and its effects on the Earth. The mission consists of three spacecraft: the Chinese-led *KuaFu-A*, which will observe the sun from the L1 Lagrange point; and ESA's *KuaFu-B1* and *KuaFu-B2*, which will each orbit the Earth in elliptical polar orbits. The inclusion of a WFAI on the *KuaFu-B* satellites would allow large-scale auroral images to be obtained at the spacecraft perigee, in contrast to conventional space-based imagers which must be at apogee to obtain a global view of the aurora. The use of two Earth-orbiting satellites would allow conjugate imaging of both the north and south auroras for the first time.

As an FUV imager, WFAI has a similar wavelength of interest to JUDE. Like Ganymede, the Earth's FUV emissions include the OI lines at 130.4 nm and 135.6 nm, as well as HI Lyman-α at 121.6 nm and the N_2 Lyman Birge Hopfield (LBH) bands which extend throughout the FUV region (see, for example, Meier [1991]). As for Ganymede, the ratios of intensities of Earth's FUV emissions can provide more useful information than simple maps of intensity. For example, the ratio of the 135.6 nm oxygen emissions to the LBH emissions around 183.8 nm has been shown to be a good indicator of the characteristic energies of the precipitating particles responsible for the emissions [Germany et al., 1990]. If it is decided that the ratio information would be desirable for WFAI observations, the work on the JUDE filters described in Chapter 5 could be easily modified to apply to any transmission filters chosen for investigation. Similarly, the models developed to describe the JUDE instrument response (Chapter 3) can be modified to describe an instrument with the optic and detector parameters specific to WFAI, allowing that instruments performance to be determined.

6.2.2 An X-ray imager for the jovian system

As well as being a source of FUV radiation, the Jupiter system contains a number of X-ray sources, including the planets polar regions (see e.g. Metzger et al. [1983]), its disk [Waite Jr. et al., 1997], the Io plasma torus [Elsner et al., 2002], and the surfaces of Io, Europa and possibly Ganymede [Elsner et al., 2002]. The emissions from the Io torus and the Galilean moons are particularly faint when viewed from Earth orbit, and Elsner et al. [2005] conclude that X-ray observations from within the jovian system would lead to much progress in the understanding of the surface composition of the satellites, as well as the auroral processes and global magnetospheric electrical circuits in the system, and potentially the interior structure of Jupiter. They suggest Ganymede orbit as the ideal location for an X-ray instrument. Since *JUICE* will spend a significant period of its lifetime in Ganymede orbit, the idea of designing an X-ray imager based on MCP optics for the mission has been raised. Such an imager would not suffer as significant a degradation in resolution due to diffraction as does JUDE in the UV, since the observation wavelengths would be much smaller. The current inability of slumped MCPs to achieve their theoretical resolution may be a problem, however, so research into the sizes of interesting X-ray features in the Jupiter system leading to an angular resolution requirement for the instrument is vital to determine whether an MCP based X-ray imager would be capable of fulfilling any of the scientific goals of the *JUICE* mission. If the instrument could be shown to be capable of useful remote sensing of Europa from Ganymede orbit, it would have a particularly strong case for inclusion on the *JUICE* mission, as the cancellation of the NASA Jupiter Europa Orbiter (see Chapter 1) has greatly reduced the potential to study this moon from within the jovian system.

6.2.3 Deconvolution of MCP point spread function from images

An important area of future work for any imager making use of MCP optics is the deconvolution of the optic point spread function (PSF) from the images produced. A square packed, square pore MCP optic has a characteristic cruxiform PSF, as explained in Chapter 2 (Section 2.1.1.3). As a result of this, extended cross-arm features are seen in all images produced by such optics, and these must be removed to obtain a true image of the source being observed (see e.g. Peele [2001]). The process of removing the cross-arms can become particularly complicated when the image contains several emission regions with overlapping cross-arm features. The development of an algorithm to deconvolve the optic PSF from images is vital for instruments based on square packed, square pore MCP optics to be seriously considered for use on both Earth-orbiting and planetary space missions.

6.3 Closing remarks

The overarching goal of this thesis was to determine the feasibility of a novel MCP optic based FUV imager for observations within the Jupiter system. Although the MCP optic design was found to be unsuitable for this particular application, due to its inability to achieve the 100 km spatial resolution limit requirement for the imager, MCP optics still offer a number of considerable advantages over more conventional UV and X-ray imaging systems, as they are able to achieve large fields of view and large effective areas in imagers with a relatively low mass, particularly when compared to large X-ray telescopes such as *Chandra* and *XMM-Newton*. Future work to optimise the resolution achievable by slumped MCP optics, and to produce a reliable method of deconvolving the optic PSF from the images produced, will serve to increase the attractiveness of the MCP optic imager design to missions requiring a compact, wide-field UV or X-ray imager with high spatial and temporal resolution.

APPENDIX A

Fresnel reflection

A.1 Standard Fresnel equations

Fresnel reflection between two dielectric media (air and glass in the case of an MCP optic) is governed by the Fresnel equations, which allow the percentages of reflected and transmitted waves to be calculated. The percentage of light that is reflected– the reflectance, R– is given by

$$R = r^2 = \left(\frac{E_r}{E_i}\right)^2, \tag{A.1}$$

where E_r and E_i are the electric field amplitudes of the reflected and incident light respectively, and r is a quantity called the reflection coefficient. The percentage of transmitted light– the transmittance, T– is dependent on the change in refractive index between the two materials:

$$T = \left(\frac{n_2 \cos\theta_t}{n_1 \cos\theta_i}\right)\left(\frac{E_t}{E_i}\right)^2 = \left(\frac{n_2 \cos\theta_t}{n_1 \cos\theta_i}\right) t^2. \tag{A.2}$$

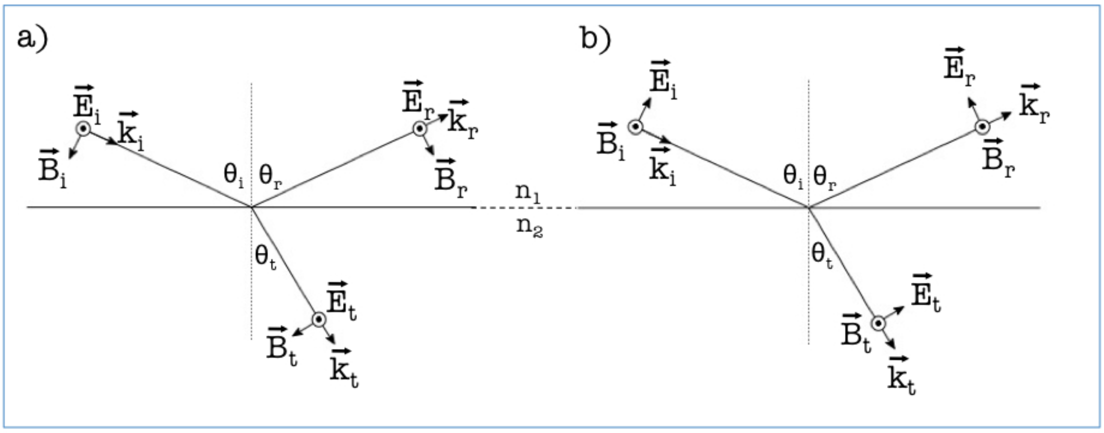

Figure A.1 **—** *Reflectance an transmittance of electromagnetic waves at the boundary between two media with refractive indices n_1 and n_2. a) The waves E-field is perpendicular to the plane of incidence; b) the waves E-field is parallel to the plane of incidence.*

E_t is the electric field amplitude of the transmitted light, n_1 and n_2 are the refractive indices of the two materials, θ_t and θ_i are the angles of transmission and reflection respectively, and t is called the transmission coefficient [Hecht, 2002].

For light whose electric field is perpendicular to the plane of incidence, as shown in Figure A.1a), the reflection and transmission coefficients can be calculated using the following equations:

$$r_\perp = -\frac{\sin(\theta_i - \theta_t)}{\sin(\theta_i + \theta_t)}; \tag{A.3}$$

$$t_\perp = +\frac{2\sin\theta_t\cos\theta_i}{\sin(\theta_i + \theta_t)}. \tag{A.4}$$

If the electric field is parallel to the plane of incidence, as shown in Figure A.1b), the reflection and transmission coefficients can be calculated using the following equations [Hecht, 2002]:

$$r_\parallel = +\frac{\tan(\theta_i - \theta_t)}{\tan(\theta_i + \theta_t)}; \tag{A.5}$$

$$t_{\parallel} = +\frac{2\sin\theta_t\cos\theta_i}{\sin(\theta_i+\theta_t)\cos(\theta_i-\theta_t)}. \tag{A.6}$$

At normal incidence, where θ_i=0 and θ_t=0, Snell's law can be used to reduce these relations to:

$$r_{\perp} = -\frac{n-1}{n+1}; \tag{A.7}$$

$$r_{\parallel} = +\frac{n-1}{n+1}; \tag{A.8}$$

$$t_{\perp} = +\frac{2}{n+1}; \tag{A.9}$$

$$t_{\parallel} = +\frac{2}{n+1}, \tag{A.10}$$

where $n = n_2/n_1$.

A.2 Henke's Fresnel equations

The X-ray reflectivity equations used by the SRT models described in Chapter 3 are forms of the Fresnel equations derived by Henke [1972] to describe ultrasoft X-ray grazing-incidence reflection and refraction at the surface of a material. The equations are expressed in terms of the real and imaginary parts of the materials dielectric constant, α and γ, the angle of incidence of the X-ray beam, ϕ, and a characteristic function a, defined by

$$a^2 = \frac{1}{2}\left(\sin^2\phi - \alpha + \sqrt{\left(\sin^2\phi - \alpha\right)^2 + \gamma^2}\right). \tag{A.11}$$

Henke [1972] defines two ratios $R_{||}$ and $R_{\perp}$, called the Fresnel coefficients. These are the ratios of reflected intensity to incident intensity for incident beams polarised with their electric vectors parallel to and perpendicular to the plane of incidence respectively:

$$R_{\perp} = \frac{4a^2\left(\sin\phi - a\right)^2 + \gamma^2}{4a^2\left(\sin\phi + a\right)^2 + \gamma^2}; \tag{A.12}$$

$$\frac{R_{||}}{R_{\perp}} = \frac{4a^2\left(a - \cos\phi\cot\phi\right)^2 + \gamma^2}{4a^2\left(a + \cos\phi\cot\phi\right)^2 + \gamma^2}. \tag{A.13}$$

The reflection coefficient for an unpolarised beam is then:

$$R = \frac{R_{\perp}}{2}\left(1 + \frac{R_{||}}{R_{\perp}}\right). \tag{A.14}$$

APPENDIX B

Manipulating an extended source in SRT

B.1 Example: source in the shape of a smiley face

B.1.1 Code in full

```
sdi=1
nd=10
deform(sdi,1,1,nd,nd)
rsrce=dtor(1.5)
xsam=rsrce*2/nd
x=(index([_real](nd))-1)*xsam-rsrce
ii=index([_real](nd,nd))-1
xx=mod(ii,nd)*xsam-rsrce
```

```
yy=int(ii/nd)*xsam-rsrce
xx1=mod(ii,nd)*xsam-(rsrce+0.01)
yy1=int(ii/nd)*xsam-(rsrce-0.01)
xx2=mod(ii,nd)*xsam-(rsrce-0.01)
rr=rtod(sqrt(xx*xx+yy*yy))
rr1=rtod(sqrt(xx1*xx1+yy1*yy1))
rr2=rtod(sqrt(xx2*xx2+yy1*yy1))
one=(rr1<0.2)
two=(rr2<0.2)
three=((rr>1.0)and(rr<1.25)and(yy<0))
zx=abs((one)or(two)or(three))
defmat(sdi,1,x,x,zx)
```

B.1.2 Step-by-step example

- *sdi=1*: sdi is a source deformation index. If sdi is 0 there is no deformation.
- *nd=10* : nd is the number of pixels the source will be stretched into in each direction (x and y).
- *deform(sdi,1,1,nd,nd)* : sets up a deformation. The bracketed terms are (deformation index, a term that is always 1 for matrices, number of sub-matrices, number of x samples, number of y samples)
- *rsrce=dtor(1.5)* : sets up a source of radius 1.5° and converts its size to radians.
- *xsam=rsrce*2/nd*: calculates the size of each pixel in radians (size of source/ number of pixels)
- *x=(index([_real](nd))-1)*xsam-rsrce* : creates an array of integers from 1 to nd, then takes 1 off each number, multiplies it by the size of a pixel and takes off the source radius. This gives the x coordinate of each pixel in radians, with x=0 being at the centre of the source. For a 1.5° radius source split into 10 pixels in each direction:

$$x = [0, \quad 1, \quad 2, \quad 3, \quad 4, \quad 5, \quad 6, \quad 7, \quad 8, \quad 9] \times 5.24\times10^{-3} - 0.0262$$

$$= [-0.0262, \quad -0.02096, \quad -0.01572, \quad -0.01048, \quad -0.00524, \quad 0, \quad 0.00524, \quad 0.01048, \quad 0.01572, \quad 0.02096]$$

- *ii=index([_real](nd,nd))-1* : sets up a 10×10 array of integers from 1 to 100, then takes 1 off each number to give:

$$ii = \begin{bmatrix} 0, & 1, & 2, & 3, & 4, & 5, & 6, & 7, & 8, & 9, \\ 10, & 11, & 12, & 13, & 14, & 15, & 16, & 17, & 18, & 19, \\ 20, & 21, & 22, & 23, & 24, & 25, & 26, & 27, & 28, & 29, \\ 30, & 31, & 32, & 33, & 34, & 35, & 36, & 37, & 38, & 39, \\ 40, & 41, & 42, & 43, & 44, & 45, & 46, & 47, & 48, & 49, \\ 50, & 51, & 52, & 53, & 54, & 55, & 56, & 57, & 58, & 59, \\ 60, & 61, & 62, & 63, & 64, & 65, & 66, & 67, & 68, & 69, \\ 70, & 71, & 72, & 73, & 74, & 75, & 76, & 77, & 78, & 79, \\ 80, & 81, & 82, & 83, & 84, & 85, & 86, & 87, & 88, & 89, \\ 90, & 91, & 92, & 93, & 94, & 95, & 96, & 97, & 98, & 99, \end{bmatrix}$$

- *xx=mod(ii,nd)*xsam-rsrce* : divides each number in the array ii by nd and returns the remainder, which is then multiplied by the pixel size, before the source radius is taken off to give an array that will represent the x coordinate of each pixel in the source array:

$$xx = \begin{bmatrix} 0, & 1, & 2, & 3, & 4, & 5, & 6, & 7, & 8, & 9, \\ 0, & 1, & 2, & 3, & 4, & 5, & 6, & 7, & 8, & 9, \\ 0, & 1, & 2, & 3, & 4, & 5, & 6, & 7, & 8, & 9, \\ 0, & 1, & 2, & 3, & 4, & 5, & 6, & 7, & 8, & 9, \\ 0, & 1, & 2, & 3, & 4, & 5, & 6, & 7, & 8, & 9, \\ 0, & 1, & 2, & 3, & 4, & 5, & 6, & 7, & 8, & 9, \\ 0, & 1, & 2, & 3, & 4, & 5, & 6, & 7, & 8, & 9, \\ 0, & 1, & 2, & 3, & 4, & 5, & 6, & 7, & 8, & 9, \\ 0, & 1, & 2, & 3, & 4, & 5, & 6, & 7, & 8, & 9, \\ 0, & 1, & 2, & 3, & 4, & 5, & 6, & 7, & 8, & 9 \end{bmatrix} \times 5.24\times10^{-3} - 0.0262$$

$$= \begin{bmatrix} -0.0262, & -0.02096, & -0.01572, & -0.01048, & -0.00524, & 0, & 0.00524, & 0.01048, & 0.01572, & 0.02096, \\ -0.0262, & -0.02096, & -0.01572, & -0.01048, & -0.00524, & 0, & 0.00524, & 0.01048, & 0.01572, & 0.02096, \\ -0.0262, & -0.02096, & -0.01572, & -0.01048, & -0.00524, & 0, & 0.00524, & 0.01048, & 0.01572, & 0.02096, \\ -0.0262, & -0.02096, & -0.01572, & -0.01048, & -0.00524, & 0, & 0.00524, & 0.01048, & 0.01572, & 0.02096, \\ -0.0262, & -0.02096, & -0.01572, & -0.01048, & -0.00524, & 0, & 0.00524, & 0.01048, & 0.01572, & 0.02096, \\ -0.0262, & -0.02096, & -0.01572, & -0.01048, & -0.00524, & 0, & 0.00524, & 0.01048, & 0.01572, & 0.02096, \\ -0.0262, & -0.02096, & -0.01572, & -0.01048, & -0.00524, & 0, & 0.00524, & 0.01048, & 0.01572, & 0.02096, \\ -0.0262, & -0.02096, & -0.01572, & -0.01048, & -0.00524, & 0, & 0.00524, & 0.01048, & 0.01572, & 0.02096, \\ -0.0262, & -0.02096, & -0.01572, & -0.01048, & -0.00524, & 0, & 0.00524, & 0.01048, & 0.01572, & 0.02096, \\ -0.0262, & -0.02096, & -0.01572, & -0.01048, & -0.00524, & 0, & 0.00524, & 0.01048, & 0.01572, & 0.02096 \end{bmatrix}$$

- *yy=int(ii/nd)*xsam-rsrce* : divides each number in the array ii by nd and returns the integer part of the answer, which is then multiplied by the pixel size. The source radius is taken off to give an array that will represent the y coordinate of each pixel in the source array:

$$
\mathrm{yy}=\begin{bmatrix}
0, & 0, & 0, & 0, & 0, & 0, & 0, & 0, & 0, & 0,\\
1, & 1, & 1, & 1, & 1, & 1, & 1, & 1, & 1, & 1,\\
2, & 2, & 2, & 2, & 2, & 2, & 2, & 2, & 2, & 2,\\
3, & 3, & 3, & 3, & 3, & 3, & 3, & 3, & 3, & 3,\\
4, & 4, & 4, & 4, & 4, & 4, & 4, & 4, & 4, & 4,\\
5, & 5, & 5, & 5, & 5, & 5, & 5, & 5, & 5, & 5,\\
6, & 6, & 6, & 6, & 6, & 6, & 6, & 6, & 6, & 6,\\
7, & 7, & 7, & 7, & 7, & 7, & 7, & 7, & 7, & 7,\\
8, & 8, & 8, & 8, & 8, & 8, & 8, & 8, & 8, & 8,\\
9, & 9, & 9, & 9, & 9, & 9, & 9, & 9, & 9, & 9
\end{bmatrix} \times 5.24\times10^{-3} - 0.0262
$$

$$
=\begin{bmatrix}
-0.0262, & -0.0262, & -0.0262, & -0.0262, & -0.0262, & -0.0262, & -0.0262, & -0.0262, & -0.0262, & -0.0262,\\
-0.02096, & -0.02096, & -0.02096, & -0.02096, & -0.02096, & -0.02096, & -0.02096, & -0.02096, & -0.02096, & -0.02096,\\
-0.01572, & -0.01572, & -0.01572, & -0.01572, & -0.01572, & -0.01572, & -0.01572, & -0.01572, & -0.01572, & -0.01572,\\
-0.01048, & -0.01048, & -0.01048, & -0.01048, & -0.01048, & -0.01048, & -0.01048, & -0.01048, & -0.01048, & -0.01048,\\
-0.00524, & -0.00524, & -0.00524, & -0.00524, & -0.00524, & -0.00524, & -0.00524, & -0.00524, & -0.00524, & -0.00524,\\
0, & 0, & 0, & 0, & 0, & 0, & 0, & 0, & 0, & 0,\\
0.00524, & 0.00524, & 0.00524, & 0.00524, & 0.00524, & 0.00524, & 0.00524, & 0.00524, & 0.00524, & 0.00524,\\
0.01048, & 0.01048, & 0.01048, & 0.01048, & 0.01048, & 0.01048, & 0.01048, & 0.01048, & 0.01048, & 0.01048,\\
0.01572, & 0.01572, & 0.01572, & 0.01572, & 0.01572, & 0.01572, & 0.01572, & 0.01572, & 0.01572, & 0.01572,\\
0.02096, & 0.02096, & 0.02096, & 0.02096, & 0.02096, & 0.02096, & 0.02096, & 0.02096, & 0.02096, & 0.02096
\end{bmatrix}
$$

- *xx1=mod(ii,nd)*xsam-(rsrce+0.01)* : like xx, this gives x coordinates of pixels for a source array, but in this case the array is centred around rsrce+0.01 rather than rsrce (i.e. x=0 moves towards the right). This array will be used to create the right eye:

$$
\mathrm{xx1} = \mathrm{xx} - 0.01 = \begin{bmatrix}
-0.0362, & -0.03096, & -0.02572, & -0.02048, & -0.01524, & -0.01, & -0.00476, & 0.00048, & 0.00572, & 0.01096,\\
-0.0362, & -0.03096, & -0.02572, & -0.02048, & -0.01524, & -0.01, & -0.00476, & 0.00048, & 0.00572, & 0.01096,\\
-0.0362, & -0.03096, & -0.0572, & -0.02048, & -0.01524, & -0.01, & -0.00476, & 0.00048, & 0.00572, & 0.01096,\\
-0.0362, & -0.03096, & -0.02572, & -0.02048, & -0.01524, & -0.01, & -0.00476, & 0.00048, & 0.00572, & 0.01096,\\
-0.0362, & -0.03096, & -0.02572, & -0.02048, & -0.01524, & -0.01, & -0.00476, & 0.00048, & 0.00572, & 0.01096,\\
-0.0362, & -0.03096, & -0.02572, & -0.02048, & -0.01524, & -0.01, & -0.00476, & 0.00048, & 0.00572, & 0.01096,\\
-0.0362, & -0.03096, & -0.02572, & -0.02048, & -0.01524, & -0.01, & -0.00476, & 0.00048, & 0.00572, & 0.01096,\\
-0.0362, & -0.03096, & -0.02572, & -0.02048, & -0.01524, & -0.01, & -0.00476, & 0.00048, & 0.00572, & 0.01096,\\
-0.0362, & -0.03096, & -0.02572, & -0.02048, & -0.01524, & -0.01, & -0.00476, & 0.00048, & 0.00572, & 0.01096,\\
-0.0362, & -0.03096, & -0.02572, & -0.02048, & -0.01524, & -0.01, & -0.00476, & 0.00048, & 0.00572, & 0.01096
\end{bmatrix}
$$

- *yy1=int(ii/nd)*xsam-(rsrce-0.01)* : as yy, but the array is centred around rsrce-0.01, so y=0 moves upwards in the array. This array will be used to create the eyes:

$$yy1= yy + 0.01 = \begin{bmatrix} -0.0162, & -0.0162, & -0.0162, & -0.0162, & -0.0162, & -0.0162, & -0.0162, & -0.0162, & -0.0162, & -0.0162, \\ -0.01096, & -0.01096, & -0.01096, & -0.01096, & -0.01096, & -0.01096, & -0.01096, & -0.01096, & -0.01096, & -0.01096, \\ -0.00572, & -0.00572, & -0.00572, & -0.00572, & -0.00572, & -0.00572, & -0.00572, & -0.00572, & -0.00572, & -0.00572, \\ -0.00048, & -0.00048, & -0.00048, & -0.00048, & -0.00048, & -0.00048, & -0.00048, & -0.00048, & -0.00048, & -0.00048, \\ 0.00476, & 0.00476, & 0.00476, & 0.00476, & 0.00476, & 0.00476, & 0.00476, & 0.00476, & 0.00476, & 0.00476, \\ 0.01, & 0.01, & 0.01, & 0.01, & 0.01, & 0.01, & 0.01, & 0.01, & 0.01, & 0.01, \\ 0.01524, & 0.01524, & 0.01524, & 0.01524, & 0.01524, & 0.01524, & 0.01524, & 0.01524, & 0.01524, & 0.01524, \\ 0.02048, & 0.02048, & 0.02048, & 0.02048, & 0.02048, & 0.02048, & 0.02048, & 0.02048, & 0.02048, & 0.02048, \\ 0.02572, & 0.02572, & 0.02572, & 0.02572, & 0.02572, & 0.02572, & 0.02572, & 0.02572, & 0.02572, & 0.02572, \\ 0.03096, & 0.03096, & 0.03096, & 0.03096, & 0.03096, & 0.03096, & 0.03096, & 0.03096, & 0.03096, & 0.03096 \end{bmatrix}$$

- *xx2=mod(ii,nd)*xsam-(rsrce-0.01)* : as xx, but the array is centred around rsrce-0.01, so x=0 moves towards the left of the array. This array will be used to create the left eye:

$$xx2 = xx + 0.01 = \begin{bmatrix} -0.0162, & -0.01096, & -0.00572, & -0.00048, & 0.00476, & 0.01, & 0.01524, & 0.02048, & 0.02572, & 0.03096, \\ -0.0162, & -0.01096, & -0.00572, & -0.00048, & 0.00476, & 0.01, & 0.01524, & 0.02048, & 0.02572, & 0.03096, \\ -0.0162, & -0.01096, & -0.00572, & -0.00048, & 0.00476, & 0.01, & 0.01524, & 0.02048, & 0.02572, & 0.03096, \\ -0.0162, & -0.01096, & -0.00572, & -0.00048, & 0.00476, & 0.01, & 0.01524, & 0.02048, & 0.02572, & 0.03096, \\ -0.0162, & -0.01096, & -0.00572, & -0.00048, & 0.00476, & 0.01, & 0.01524, & 0.02048, & 0.02572, & 0.03096, \\ -0.0162, & -0.01096, & -0.00572, & -0.00048, & 0.00476, & 0.01, & 0.01524, & 0.02048, & 0.02572, & 0.03096, \\ -0.0162, & -0.01096, & -0.00572, & -0.00048, & 0.00476, & 0.01, & 0.01524, & 0.02048, & 0.02572, & 0.03096, \\ -0.0162, & -0.01096, & -0.00572, & -0.00048, & 0.00476, & 0.01, & 0.01524, & 0.02048, & 0.02572, & 0.03096, \\ -0.0162, & -0.01096, & -0.00572, & -0.00048, & 0.00476, & 0.01, & 0.01524, & 0.02048, & 0.02572, & 0.03096, \\ -0.0162, & -0.01096, & -0.00572, & -0.00048, & 0.00476, & 0.01, & 0.01524, & 0.02048, & 0.02572, & 0.03096 \end{bmatrix}$$

- *rr=rtod(sqrt(xx*xx+yy*yy))* : creates a source array which uses pythagoras' theorem to calculate the distance from the centre of the source to each pixel in the array, using the pixel coordinates from the arrays xx and yy. The distances are converted from radians to degrees:

$$rr = \begin{bmatrix} 2.1229, & 1.9224, & 1.7506, & 1.6168, & 1.5309, & 1.5011, & 1.5309, & 1.6168, & 1.7506, & 1.9224, \\ 1.9224, & 1.6984, & 1.5011, & 1.3427, & 1.2379, & 1.2009, & 1.2379, & 1.3427, & 1.5011, & 1.6984, \\ 1.7506, & 1.5011, & 1.2738, & 1.0825, & 0.9494, & 0.9007, & 0.9494, & 1.0825, & 1.2738, & 1.5011, \\ 1.6168, & 1.3427, & 1.0825, & 0.8492, & 0.6713, & 0.6005, & 0.6713, & 0.8492, & 1.0825, & 1.3427, \\ 1.5309, & 1.2379, & 0.9494, & 0.6713, & 0.4246, & 0.3002, & 0.4246, & 0.6713, & 0.9494, & 1.2379, \\ 1.5011, & 1.2009, & 0.9007, & 0.6005, & 0.3002, & 0.0000, & 0.3002, & 0.6005, & 0.9007, & 1.2009, \\ 1.5309, & 1.2379, & 0.9494, & 0.6713, & 0.4246, & 0.3002, & 0.4246, & 0.6713, & 0.9494, & 1.2379, \\ 1.6168, & 1.3427, & 1.0825, & 0.8492, & 0.6713, & 0.6005, & 0.6713, & 0.8492, & 1.0825, & 1.3427, \\ 1.7506, & 1.5011, & 1.2738, & 1.0825, & 0.9494, & 0.9007, & 0.9494, & 1.0825, & 1.2738, & 1.5011, \\ 1.9224, & 1.6984, & 1.5011, & 1.3427, & 1.2379, & 1.2009, & 1.2379, & 1.3427, & 1.5011, & 1.6984 \end{bmatrix}$$

- *rr1=rtod(sqrt(xx1*xx1+yy1*yy1))* : creates a source array as for rr, but using coordinates from xx1 and yy1. The centre of this array is shifted up and towards the right relative to rr:

$$rr1 = \begin{bmatrix} 2.2723, & 2.0020, & 1.7416, & 1.4961, & 1.2744, & 1.0908, & 0.9674, & 0.9286, & 0.9844, & 1.1207, \\ 2.1671, & 1.8817, & 1.6019, & 1.3309, & 1.0755, & 0.8501, & 0.6846, & 0.6286, & 0.7083, & 0.8881, \\ 2.0998, & 1.8039, & 1.5097, & 1.2183, & 0.9327, & 0.6601, & 0.4264, & 0.3289, & 0.4635, & 0.7083, \\ 2.0743, & 1.7741, & 1.4739, & 1.1737, & 0.8736, & 0.5736, & 0.2741, & 0.0389, & 0.3289, & 0.6286, \\ 2.0920, & 1.7947, & 1.4987, & 1.2047, & 0.9148, & 0.6346, & 0.3857, & 0.2741, & 0.4264, & 0.6846, \\ 2.1518, & 1.8641, & 1.5811, & 1.3058, & 1.0444, & 0.8103, & 0.6346, & 0.5736, & 0.6601, & 0.8501, \\ 2.2504, & 1.9771, & 1.7129, & 1.4627, & 1.2349, & 1.0444, & 0.9148, & 0.8736, & 0.9327, & 1.0755, \\ 2.3830, & 2.1269, & 1.8838, & 1.6595, & 1.4627, & 1.3058, & 1.2047, & 1.1737, & 1.2183, & 1.3309, \\ 2.5443, & 2.3061, & 2.0841, & 1.8838, & 1.7129, & 1.5811, & 1.4987, & 1.4739, & 1.5097, & 1.6019, \\ 2.7292, & 2.5086, & 2.3061, & 2.1269, & 1.9771, & 1.8641, & 1.7947, & 1.7741, & 1.8039, & 1.8817 \end{bmatrix}$$

- *rr2=rtod(sqrt(xx2*xx2+yy1*yy1))* : creates a source array as for rr, but using coordinates from xx2 and yy1. The centre of this array is shifted up and towards the left relative to rr:

$$rr2 = \begin{bmatrix} 1.3127, & 1.1207, & 0.9844, & 0.9286, & 0.9674, & 1.0908, & 1.2744, & 1.4961, & 1.7416, & 2.0020, \\ 1.1207, & 0.8881, & 0.7083, & 0.6286, & 0.6846, & 0.8501, & 1.0755, & 1.3309, & 1.6019, & 1.8817, \\ 0.9844, & 0.7083, & 0.4635, & 0.3289, & 0.4264, & 0.6601, & 0.9327, & 1.2183, & 1.5097, & 1.8039, \\ 0.9286, & 0.6286, & 0.3289, & 0.0389, & 0.2741, & 0.5736, & 0.8736, & 1.1737, & 1.4739, & 1.7741, \\ 0.9674, & 0.6846, & 0.4264, & 0.2741, & 0.3857, & 0.6346, & 0.9148, & 1.2047, & 1.4987, & 1.7947, \\ 1.0908, & 0.8501, & 0.6601, & 0.5736, & 0.6346, & 0.8103, & 1.0444, & 1.3058, & 1.5811, & 1.8641, \\ 1.2744, & 1.0755, & 0.9327, & 0.8736, & 0.9148, & 1.0444, & 1.2349, & 1.4627, & 1.7129, & 1.9771, \\ 1.4961, & 1.3309, & 1.2183, & 1.1737, & 1.2047, & 1.3058, & 1.4627, & 1.6595, & 1.8838, & 2.1269, \\ 1.7416, & 1.6019, & 1.5097, & 1.4739, & 1.4987, & 1.5811, & 1.7129, & 1.8838, & 2.0841, & 2.3061, \\ 2.0020, & 1.8817, & 1.8039, & 1.7741, & 1.7947, & 1.8641, & 1.9771, & 2.1269, & 2.3061, & 2.5086 \end{bmatrix}$$

- *one=(rr1<0.2)* : selects any pixels within the array rr1 that have a value of less than 0.2 degrees (i.e. pixels within 0.2 degrees of the source centre). These pixels are highlighted in green in rr1 above.

- *two=(rr2<0.2)* : selects any pixels within the array rr2 that have a value of less than 0.2 degrees (i.e. pixels within 0.2 degrees of the source centre). These pixels are highlighted in green in rr2 above.

- *three=((rr>1.0)and(rr<1.25)and(yy<0))* : selects pixels in the array rr that have values between 1.0 and 1.25 degrees. Any pixels corresponding to y coordinates from the array yy that are greater than 0 are then discarded, leaving the pixels highlighted in rr above.

- *zx=abs((one)or(two)or(three))* : This is the final source array, in which the pixels are selected using the rules above to create the source shape required:

$$
\mathrm{zx} = \begin{bmatrix}
0, & 0, & 0, & 0, & 0, & 0, & 0, & 0, & 0, & 0, \\
0, & 0, & 0, & 0, & 0, & 0, & 0, & 0, & 0, & 0, \\
0, & 0, & 0, & 0, & 0, & 0, & 0, & 0, & 0, & 0, \\
0, & 0, & 0, & 0.0389, & 0, & 0, & 0, & 0.0389, & 0, & 0, \\
0, & 0, & 0, & 0, & 0, & 0, & 0, & 0, & 0, & 0, \\
0, & 0, & 0, & 0, & 0, & 0, & 0, & 0, & 0, & 0, \\
0, & 1.2379, & 0, & 0, & 0, & 0, & 0, & 0, & 0, & 1.2379, \\
0, & 0, & 1.0825, & 0, & 0, & 0, & 0, & 0, & 1.0825, & 0, \\
0, & 0, & 0, & 1.0825, & 0, & 0, & 0, & 1.0825, & 0, & 0, \\
0, & 0, & 0, & 0, & 1.2379, & 1.2009, & 1.2379, & 0, & 0, & 0
\end{bmatrix}
$$

- *defmat(sdi,1,x,x,zx)* : creates the deformation sub-matrix that will spread a point source into the shape specified by zx. The bracketed terms are (deformation index, sub-matrix index, x pixels, y pixels, deformation displacement matrix). The image created with this source shape and a JUDE MCP optic is shown in Figure B.1.

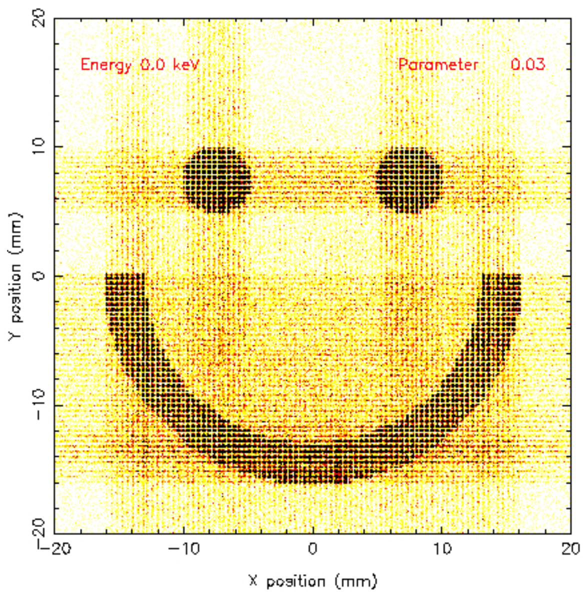

Figure B.1 — *Ray-traced image of the source described above through the JUDE MCP optics. The only parameter that differs from those in the example code is nd, which is 100 for this image, rather than 10.*

APPENDIX C

Diffraction by a rectangular aperture

This chapter contains the derivation of Equation (3.2), which describes the Fraunhofer diffraction pattern seen on a screen that is placed far from a rectangular aperture. The source, which lies along the same optical axis as the aperture plane and screen, must also be far from the aperture in order for the Fraunhofer description to apply.

C.1 Fraunhofer diffraction at a rectangular aperture

Consider Figure C.1. A monochromatic source lies at a large distance from the aperture (in the -x direction as shown in the figure), so that the rays it emits are approximately parallel by the time they reach the aperture, i.e. the wavefronts encountering the aperture are planar. A differential area with dimensions of $dy \times dz$ lies in the plane of the aperture, and according to the Huygens–Fresnel Principle[1]can be considered to be covered with

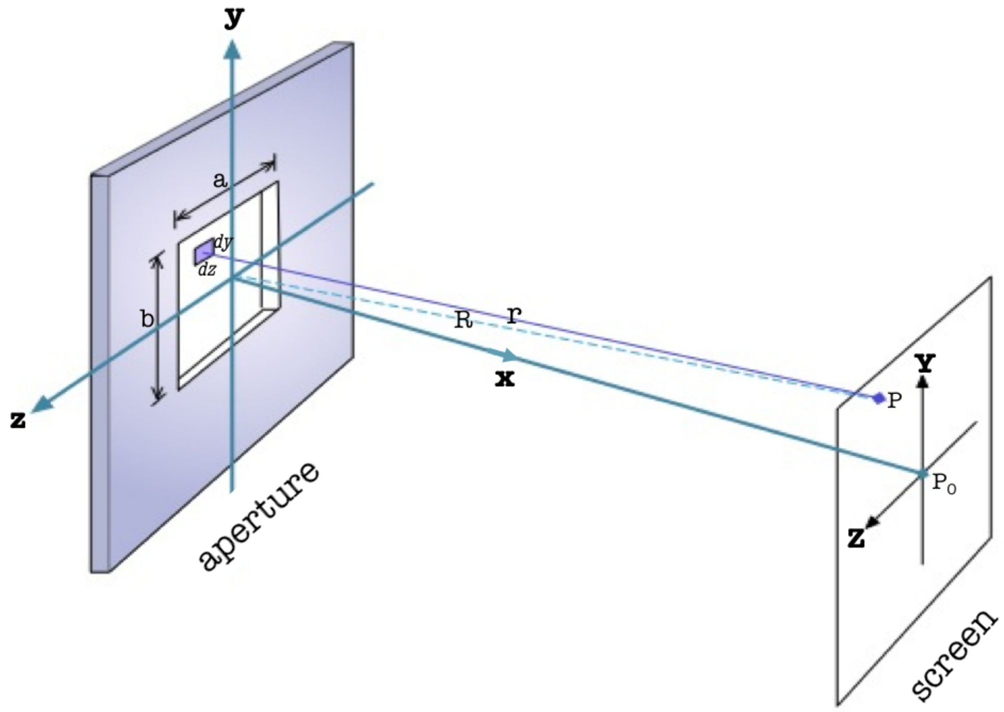

Figure C.1 — *Rectangular aperture configuration, not to scale (r and R should be very large compared to the aperture dimensions). Based on Fig. 10.19 in [Hecht, 2002].*

coherent secondary point sources. Both dy and dz are large compared to the wavelength of the light emitted by the source, so the relative phase differences between the point sources are negligible. Similarly, the gaps between the secondary sources are negligibly small, and they approximate a single continuous source. A screen lies on the opposite side of the aperture to the primary source, parallel to the plane of the aperture and at a distance that is much larger than the aperture dimension, to fulfil the criteria for Fraunhofer diffraction.

To determine the diffraction pattern observed at the screen, we need to consider the distribution of the electric field carried by the wavefronts arriving at the screen. The optical disturbance at a point P on the screen due to a spherical wave emitted by the area

[1]The Huygens–Fresnel Principle: "Every unobstructed point on a wavefront, at a given instant, serves as a source of secondary spherical wavelets (with the same frequency as that of the primary wave). The amplitude of the optical field at any point beyond is the superposition of all these wavelets (considering their amplitudes and relative phases)" [Hecht, 2002].

$dy \times dz$ is

$$dE = \frac{\varepsilon_A}{r} e^{i(\omega t - kr)}\, dy\, dz, \tag{C.1}$$

where ε_A is the source strength per unit area (assumed to be uniform over the extent of the aperture) [Hecht, 2002]. The term (ε_A/r) gives the amplitude of the wave. Since the screen is far from the aperture, $r{\sim}R$, so we can replace the amplitude term with (ε_A/R). The other term containing r is kr, which gives the phase of the wave. In this case we cannot replace r with R, as small differences between the two will have a larger effect on the result, since the wavenumber, $k = 2\pi/\lambda$, is a large number. From Figure C.1 we can see that r can be expressed as:

$$r = [X^2 + (Y-y)^2 + (Z-z)^2]^{1/2}. \tag{C.2}$$

Since $R = [X^2 + Y^2 + Z^2]^{1/2}$, Equation (C.2) can be expanded and rewritten as

$$\begin{aligned} r &= \left[X^2 + Y^2 - 2Yy + y^2 + Z^2 - 2Zz + z^2\right]^{1/2} \\ &= \left[R^2 - 2(Yy + Zz) + (y^2 + z^2))\right]^{1/2} \\ &= R\left[1 - \frac{2(Yy+Zz)}{R^2} + \frac{(y^2+z^2)}{R^2}\right]^{1/2}. \end{aligned} \tag{C.3}$$

The distance R is much larger than the x and y dimensions of the aperture, so the last term in the bracket can be discarded:

$$r = R\left[1 - \frac{2(Yy+Zz)}{R^2}\right]^{1/2}. \tag{C.4}$$

Equation (C.4) can be evaluated using a Maclaurin series expansion:

$$\begin{aligned} f(x) &= f(0) + x.f'(0) + \frac{x^2}{2!}f''(0)... \\ \Rightarrow (1+x)^n &= 1 + xn + \frac{x^2}{2!}n(n-1)... \\ \Rightarrow \left[1 - \frac{2(Yy+Zz)}{R^2}\right]^{1/2} &= 1 - \frac{Yy+Zz}{R^2} + \frac{3}{2}\left[\frac{Yy+Zz}{R^2}\right]^2 ..., \end{aligned} \tag{C.5}$$

so that

$$r \approx R\left[1 - \frac{(Yy+Zz)}{R^2}\right]. \tag{C.6}$$

This can be substituted back into Equation (C.1) (remembering that r can be replaced with R in the amplitude term) to give

$$\begin{aligned} dE &= \frac{\varepsilon_A}{R} e^{i(\omega t - kR[1-(Yy+Zz)/R^2])}\, dy\, dz \\ &= \frac{\varepsilon_A}{R} e^{i(\omega t - kR + k(Yy+Zz)/R)}\, dy\, dz \\ &= \frac{\varepsilon_A}{R} e^{i(\omega t - kR)} e^{ik(Yy+Zz)/R}\, dy\, dz. \end{aligned} \tag{C.7}$$

Hence, the total disturbance arriving at P, $\tilde{E}$, is

$$\begin{aligned} \tilde{E} &= \frac{\varepsilon_A}{R} e^{i(\omega t - kR)} \iint\limits_{aperture} e^{ik(Yy+Zz)/R}\, dy\, dz \\ &= \frac{\varepsilon_A}{R} e^{i(\omega t - kR)} \int\limits_{-a/2}^{+a/2} e^{ikZz/R} dz \int\limits_{-b/2}^{+b/2} e^{ikYy/R} dy. \end{aligned} \tag{C.8}$$

The integral over the aperture in the z direction can be evaluated as follows:

$$\begin{aligned} \int\limits_{-a/2}^{+a/2} e^{ikZz/R} dz &= \left[\frac{R}{ikZ} e^{ikZz/R} \right]_{-a/2}^{+a/2} \\ &= \frac{R}{ikZ} e^{ikZa/2R} - \frac{R}{ikZ} e^{-ikZa/2R}. \end{aligned} \tag{C.9}$$

If we define a new quantity $\alpha' = kaZ/2R$, Equation (C.9) becomes

$$\begin{aligned} \int\limits_{-a/2}^{+a/2} e^{ikZz/R} dz &= \frac{R}{ikZ} \left[e^{i\alpha'} - e^{-i\alpha'} \right] \\ &= a \left[\frac{e^{i\alpha'} - e^{-i\alpha'}}{2\alpha' i} \right] \\ &= a \left(\frac{\sin \alpha'}{\alpha'} \right). \end{aligned} \tag{C.10}$$

Similarly, the integral over the aperture in the y direction is

$$\int\limits_{-b/2}^{+b/2} e^{ikYy/R} dy = b \left(\frac{\sin \beta'}{\beta'} \right), \tag{C.11}$$

where $\beta' = kbZ/2R$, so

$$\tilde{E} = \frac{\varepsilon_A}{R} e^{i(\omega t - kR)} ab \left(\frac{\sin \alpha'}{\alpha'} \right) \left(\frac{\sin \beta'}{\beta'} \right). \tag{C.12}$$

The intensity, I, of the light observed at P is related to the disturbance of the field by $I =< (\Re\tilde{E})^2 >_T$ [Hecht, 2002]. Hence the intensity seen at the screen is

$$\begin{aligned} I(Y,Z) &= \frac{\varepsilon_A^2 a^2 b^2}{2R^2} \left(\frac{\sin\alpha'}{\alpha'}\right)^2 \left(\frac{\sin\beta'}{\beta'}\right)^2 \\ &= I(0) \left(\frac{\sin\alpha'}{\alpha'}\right)^2 \left(\frac{\sin\beta'}{\beta'}\right)^2 . \end{aligned} \tag{C.13}$$

APPENDIX D

Depth of focus of slumped MCP optics

The length of channels in an MCP optic determine the depth of the optic focus, as rays may undergo reflection at any point within the length of a channel. Figure D.1 shows the extreme case of rays focused at the entrance and exit of a channel in a slumped MCP optic. The geometry of the optic can be used to estimate the focal depth, x. From the diagram, it can be seen that

$$\begin{aligned} x &= \frac{h}{\tan 2\alpha} + l\cos\alpha - \frac{h + l\sin\alpha}{\tan 2\alpha} \\ &= l\cos\alpha - \frac{l\sin\alpha}{\tan 2\alpha}, \end{aligned} \tag{D.1}$$

where h is the height of the focusing channel above the optical axis, l is the length of the channel, and α is the angle of the channel to the focal plane (so that $\alpha = \tan^{-1}\frac{h}{R_{MCP}}$).

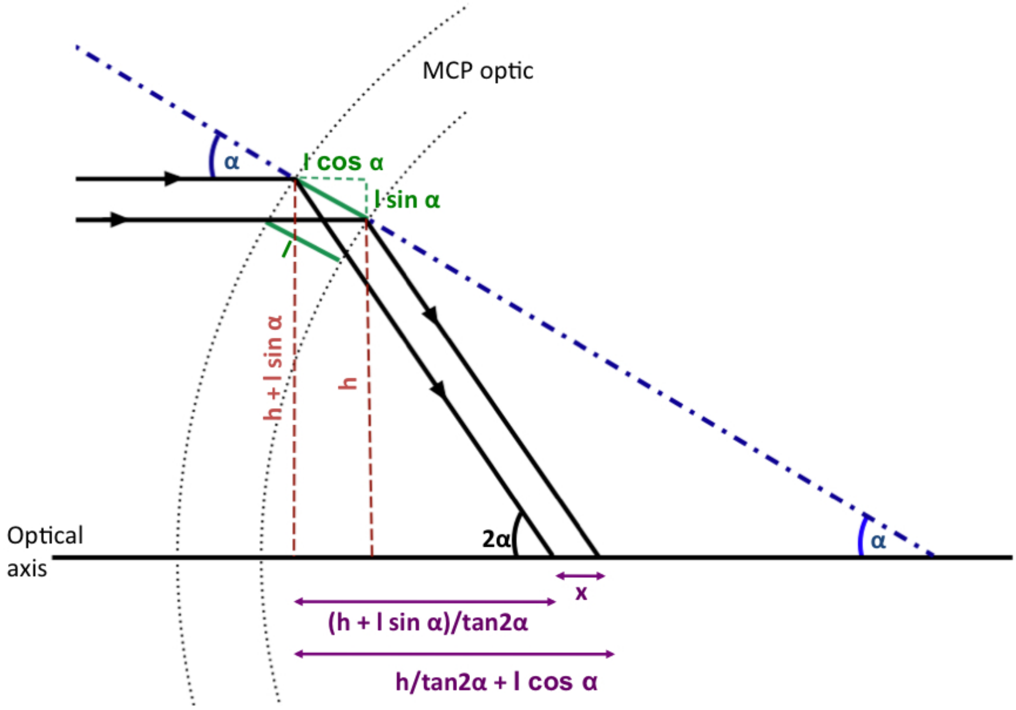

Figure D.1 **—** *Diagram of extreme paths possible for rays focused by an MCP optic channel, showing measurements that can be used to calculate the depth of focus. (Not to scale.)*

D.1 Focal depth of WFAI optic

The WFAI optic has a channel length $l = 1$ mm and a radius of curvature $R_{MCP} = 100$ mm. The depth of focus, x, was evaluated for channels with various values of h, using Equation D.1. The results are given in Table D.1. The results imply that for a WFAI optic of radius 20 mm, the depth of focus is $\sim$0.65 mm.

N. B. The depth of focus calculations here are slightly simplified: they do not take into account the fact that the presence of channel walls leads to maximum and minimum positions for single reflections within a channel, as discussed in Chapter 3, Section 3.1.1, which will narrow the focal depth for photons incident in regions near the edges of the optic.

Table D.1 — *WFAI focal depth calculated for regions of the optic of height h above the optical axis.*

h (mm)	x (mm)
1.0	0.650
2.0	0.650
3.0	0.650
4.0	0.650
5.0	0.650
6.0	0.650
7.0	0.651
8.0	0.651
9.0	0.651
10.0	0.651
11.0	0.652
12.0	0.652
13.0	0.652
14.0	0.652
15.0	0.653
16.0	0.653
17.0	0.654
18.0	0.654
19.0	0.655
20.0	0.655

Bibliography

KuaFu Payload Definition Group. KuaFu-B Payload Definition Document, December 2007.

Acton: Optics brochure. *Optics and Coatings 120 nm – 1064 nm*. Acton Optics and Coatings, 2008. Retrieved from `http://www.princetoninstruments.com/Uploads/Princeton/Documents/Brochures/Optics\%20Brochure_12_08_REVD0_web.pdf`, 9/1/2012.

J. Ajello, D. Shemansky, W. Pryor, K. Tobiska, C. Hord, S. Stephens, I. Stewart, J. Clarke, K. Simmons, W. McClintock, C. Barth, J. Gebben, D. Miller, and B. Sandel. Galileo orbiter ultraviolet observations of Jupiter aurora. *Journal of Geophysical Research*, 103(E9):20125–20148, 1998.

J. M. Ajello, S. K. Srivastava, and Y. L. Yung. Laboratory studies of UV emissions of H_2 by electron impact. The Werner and Lyman–band systems. *Physical Review A*, 25: 2485–2498, 1982.

J. M. Ajello, W. Pryor, L. Esposito, I. Strweart, W. McClintock, J. Gustin, D. Grodent, J.-C. Gérard, and J. T. Clarke. The Cassini Campaign observations of the Jupiter aurora by the Ultraviolet Imaging Spectrograph and the Space Telescope Imaging Spectrograph. *Icarus*, 178:327–345, 2005.

B.-G. Andersson. *FUSE Observer's Guide – Version 8.0*, August 2006.

J. R. P. Angel. Lobster eyes as X-ray telescopes. *The Astrophysical Journal*, 233:364–373, 1979.

C. D. Anger, T. Fancott, J. McNally, and H. S. Kerr. ISIS-II Scanning Auroral Photometer. *Applied Optics*, 12(8):1753–1766, 1973.

C. D. Anger, J. S. Murphree, A. Vallance Jones, R. A. King, A. L. Broadfoot, L. L. Cogger, F. Creutzberg, R. L. Gattinger, G. Gustafsson, F. R. Harris, J. W. Haslett, E. J. Llewellyn, J. C. McConnell, D. J. McEwen, E. H. Richardson, G. Rostoker, B. R. Sandel, G. G. Shepherd, D. Venkatesan, D. D. Wallis, and G. Witt. Scientific results from the Viking ultraviolet imager: an introduction. *Geophysical Research Letters*, 14 (4):383–386, 1987.

D. Attwood. *Soft X-Rays and Extreme Ultraviolet Radiation*. Cambridge University Press, 2000.

G. E. Ballester, J. T. Clarke, J. T. Trauger, W. M. Harris, K. R. Stapelfeldt, D. Crisp, R. W. Evans, E. B. Burgh, C. J. Burrows, S. Casertano, J. S. Gallagher III, R. E. Griffiths, J. J. Hester, J. G. Hoessel, J. A. Holtzman, J. E. Krist, V. Meadows, J. R. Mould, R. Sahai, P. A. Scowen, A. M. Watson, and J. A. Westphal. Time-resolved observations of Jupiter's far-ultraviolet aurora. *Science*, 274:409–413, 1996.

N. P. Bannister. WFAI sensitivity estimates, 2009.

N. P. Bannister, E. J. Bunce, S. W. H. Cowley, R. Fairbend, G. W. Fraser, F. J. Hamilton, J. S. Lapington, J. E. Lees, M. Lester, S. E. Milan, J. F. Pearson, and R. Willingale. A Wide Field Auroral Imager (WFAI) for low Earth orbit missions. *Annales Geophysicae*, 25:519–532, 2007.

N. P. Bannister, E. J. Bunce, P. Molyneux, R. M. Ambrosi, J. Sykes, J. S. Lapington, J.-C. Gérard, D. Grodent, B. Marquet, E. Renotte, K. Fleury-Frenette, Y. Houbrechts,

J. T. Clarke, N. Østgaard, and K. Kauristie. Jupiter system Ultraviolet Dynamics Experiment (JUDE): A UV Imager for the Jupiter Ganymede Orbiter. Design and development report, 2010.

A. Bhardwaj and G. R. Gladstone. Auroral emissions of the giant planets. *Reviews of Geophysics*, 38(3):295–353, 2000.

K. Birkeland. *The Norwegian Aurora Polaris Expedition 1902-1903. Vol. 1, On the Cause of Magnetic Storms and the Origin of Terrestrial Magnetism*. Aschehoug, 1908.

B. Bonfond. The Io UV footprint: Location, inter-spot distances and tail vertical extent. *Journal of Geophysical Research*, 114:A07224, 2009.

B. Bonfond, J.-C. Gérard, D. Grodent, and J. Saur. Ultraviolet Io footprint short timescale dynamics. *Geophysical Research Letters*, 24(L06201), 2007.

B. Bonfond, D. Grodent, J.-C. Gérard, T. Stallard, J.T. Clarke, M. Yoneda, A. Radioti, and J. Gustin. Auroral evidence of Io's control over the magnetosphere of Jupiter. *Geophysical Research Letters*, 39:L01105, 2012.

K. A. Bostroem, A. Aloisi, R. Bohlin, R. Diaz, V. Dixon, P. Goudfrooij, P. Hodge, D. Lennon, C. Long, S. Niemi, R. Osten, C. Proffitt, N. Walborn, T. Wheeler, M. Wolfe, B. York, and W. Zheng. *STIS Instrument Handbook – Version 10.0 (Baltimore: STScI)*, 2010.

A. Boutonnet, J. Schoenmaekers, and D. Garcia. JGO: Consolidated report on mission analysis [draft]. Technical report, ESA, July 2010.

A. L. Broadfoot, B. R. Sandel, D. E. Shemansky, S. K. Atreya, T. M. Donahue, H. W. Moos, J. L. Bertaus, J. E. Blamont, J. M. Ajello, D. F. Strobel, J. C. McConnell, A. Dalgarno, R. Goody, M. B. McElroy, and Y. L. Yung. Ultraviolet Spectrometer Experiment for the Voyager mission. *Space Science Reviews*, 21:183–205, 1977.

E. J. Bunce and Imager Consortium Members. A UV Imager Instrument Study, 2009. Response to the ESA call for Declarations of Interest in Science Instrumentation for the Europa Jupiter System Mission (EJSM/Laplace) Cosmic Vision L Class Mission Candidate.

E. J. Bunce, P. M. Molyneux, N. P. Bannister, J. S. Lapington, M. Lester, E. Renotte, J.-C. Gérard, and D. Grodent. A Far-UV Imager for the Jupiter Ganymede Orbiter, 2009. Poster for the EJSM science meeting, 17th–19th May 2010 at ESTEC, Noordwijk.

R. Buzzi, J. Eder, G. Grisoni, G. Parodi, and K. van Katvijk. The development of the XMM mirror shell integration process and optical performance prediction. In C. Stavrinidis, A. Rolfo, & E. Breitbach, editor, *Spacecraft Structures, Materials and Mechanical Testing*, volume 468 of *ESA Special Publication*, pages 63–68, 2001.

R. W. Carlson. A tenuous carbon dioxide atmosphere on Jupiter's moon Callisto. *Science*, 283:820–821, 1999.

Cathodeon: Deuterium lamp brochure. *Deuterium lamps*. Cathodeon, 2011. Retrieved from `http://www.teknolab.no/pdf/Cathodeon_Deuterium.pdf`, 14/11/2011.

H. N. Chapman, K. A. Nugent, S. W. Wilkins, and T. J. Davis. Focusing and collimation of X-rays using microchannel plates: an experimental investigation. *Journal of X-Ray Science and Technology*, 2:117–126, 1990.

H. N. Chapman, K. A. Nugent, and S. W. Wilkins. X-ray focusing using square channel-capillary arrays. *Review of Scientific Instruments*, 32:1542–1561, 1991.

K. Clark, T. Magner, R. Pappalardo, M. Blanc, R. Greeley, J.-P. Lebreton, C. Jones, and J. Sommerer. Jupiter Europa Orbiter Mission Study 2008: Final Report. Technical report, NASA, January 2009. Task Order #NMO710851.

J. T. Clarke, H. W. Moos, S. K. Atreya, and A. L. Lane. Observations from Earth orbit and variability of the polar aurora on Jupiter. *The Astrophysical Journal*, 241:L179–L182, 1980.

J. T. Clarke, J. Trauger, and J. H. Waite Jr. Doppler shifted H Ly α emission from Jupiter's aurora. *Geophysical Research Letters*, 16(6):587–590, 1989.

J. T. Clarke, G. Ballester, J. Trauger, J. Ajello, W. Pryor, K. Tobiska, J. E. P. Connerney, G. R. Gladstone, J. H. Waite Jr., L. Ben Jaffel, , and J.-C. Gérard. Hubble Space Telescope imaging of Jupiter's UV aurora during the Galileo orbiter mission. *Journal of Geophysical Research*, 103(E9):20217–20236, 1998.

J. T. Clarke, J. Ajello, G. Ballester, L. Ben Jaffel, J. Connerney, J.-C. Gérard, G. R. Gladstone, D. Grodent, W. Pryor, J. Trauger, and J. H. Waite Jr. Ultraviolet emissions from the magnetic footprints of Io, Ganymede and Europa on Jupiter. *Nature*, 415: 997–1000, 2002.

J. T. Clarke, D. Grodent, S. W. H. Cowley, E. J. Bunce, P. Zarka, J. E. P. Connerney, and T. Satoh. Jupiter's Aurora. In F. Bagenal, T. Dowling, and W McKinnon, editors, *Jupiter – the planet, satellites and magnetosphere*, chapter 26. Cambridge University Press, 2004.

J. S. Colligon. Ion-assisted sputter deposition. *Philosophical transactions of the royal society A*, 392:103–116, 2004.

Committee on the Planetary Science Decadal Survey. Vision and Voyages for Planetary Science in the Decade 2013–2022. Technical report, National Research Council of the National Academies, 2011.

S. W. H. Cowley and E. J. Bunce. Origin of the main auroral oval in Jupiter's coupled magnetosphere-ionosphere system. *Planetary and Space Science*, 49:1067–1088, 2001.

S. W. H. Cowley, E. J. Bunce, T. S. Stallard, and S. Miller. Jupiter's polar ionospheric flows: theoretical interpretation. *Geophysical Research Letters*, 30(5), 2003.

CXRO. X-Ray interactions with matter – Introduction. `http://henke.lbl.gov/optical_constants/intro.html`, 2009. retrieved July 2009.

P. A. Delamere and F. Bagenal. Solar wind interaction with Jupiter's magnetosphere. *Journal of Geophysical Research*, 115, 2010.

P. A. Delamere, A. Steffl, and F. Bagenal. Modeling temporal variability of plasma conditions in the Io torus during the Cassini era. *Journal of Geophysical Research*, 109:A10216, 2004.

S. T. Durrance, G. A. Kriss, W. P. Blair, J. W. Kruk, and B. R. Espey. *The Hopkins Ultraviolet Telescope Handbook – Version 1.1*, 1994.

M. Ehle, M. Breitfellner, R. Gonzales Riestra, M. Guainazzi, P. Rodriguez, M. Santos-Lleo, N. Schartel, L. Tomas, E. Verdugo, and M. Dahlem. *XMM-Newton Users' Handbook – Issue 2.1*, March 2003.

EJSM-Laplace Joint Science Definition Team. EJSM-Laplace: Assessment Study Report (Yellow book). Technical report, ESA, February 2011. ESA/SRE(2011)1.

R. F. Elsner, G. R. Gladstone, J. H. Waite, F. J. Crary, R. R. Howell, R. E. Johnson, P. G. Ford, A. E. Metzger, K. C. Hurley, E. D. Feigelson, G. P. Garmire, A. Bhardwaj, D. C. Grodent, T. Majeed, A. F. Tennant, and M. C. Weisskopf. Discovery of soft X-ray emission from Io, Europa, and the Io plasma torus. *The Astrophysical Journal*, 572: 1077–1082, 2002.

R. F. Elsner, B. D. Ramsey, J. H. Waite Jr., P. Rehak, J. F. Cooper, and D. A. Swartz. Discovery of soft X-ray emission from Io, Europa, and the Io plasma torus. *Icarus*, 178:417–428, 2005.

ESA. IUE – Instruments. `http://sci.esa.int/science-e/www/object/index.cfm?fobjectid=31311`, 2005. retrieved 7/6/2011.

L. W. Esposito, C. A. Barth, J. E. Colwell, G. M. Lawrence, W. E. McClintock, A. I. F. Stewart, H. U. Keller, A. Korth, H. Lauche, M. C. Festou, A. L. Lane, C. J. Hansen, J. N. Maki, C. W. Hord, R. A. West, H. Jahn, R. Reulke, K. Warlich, D. E. Shemansky, and Y. L. Yung. The Cassini Ultraviolet Imaging Spectrograph Investigation. *Space Science Reviews*, 115:299–361, 2004.

A. Eviatar, D. F. Strobel, B. C. Wolven, P. D. Feldman, M. A. McGrath, and D. J. Williams. Excitation of the Ganymede ultraviolet aurora. *The Astrophysical Journal*, 555:1013–1019, 2001.

C. Feldman and A. Martindale. Collimator MCP X-ray testing on SE001-A14. Technical report, University of Leicester, 2011.

P. D. Feldman, M. A. McGrath, D.F. Strobel, H. W. Moos, K. D. Retherford, and B. C. Wolven. HST/STIS ultraviolet imaging of polar aurora on Ganymede. *The Astrophysical Journal*, 535:1085–1090, June 2000.

Karl Fleury-Frenette. Personal communication, 2009.

C. J. Foot. *Atomic physics*. Oxford University Press, 2005.

L. A. Frank and J. D. Craven. Imaging results from Dynamics Explorer 1. *Reviews of Geophysics*, 26(2):249–283, 1988.

G. W. Fraser. The soft X-ray quantum detection efficiency of microchannel plates. *Nuclear Instruments and Methods*, 195:523–538, 1982.

G. W. Fraser. *X-ray detectors in astronomy*. Cambridge University Press, 1989.

G. W. Fraser and E. Mathieson. Signal location by uniform resistive anodes. a) square anodes in the DC limit. *Nuclear Instruments and Methods*, 179:591–604, 1981.

G. W. Fraser and J. F. Pearson. Soft X-ray energy resolution with microchannel plate detectors of high quantum detection efficiency. *Nuclear Instruments and Methods*, 219:199–212, 1984.

G. W. Fraser, J. F. Pearson, and J. E. Lees. Caesium bromide X-ray photocathodes. *Nuclear Instruments and Methods*, 256:401–405, 1987.

G. W Fraser, M. T. Pain, J. E. Lees, and J. F. Pearson. The operation of microchannel plates at high count rates. *Nuclear Instruments and Methods A*, 306:247–260, 1991.

G. W. Fraser, A. N. Brunton, J. E. Lees, J. F. Pearson, and W. B. Feller. X-ray focusing using square-pore microchannel plates: First observation of cruxiform image structure. *Nuclear Instruments and Methods in Physics Research A*, 324:404–407, 1993a.

G. W. Fraser, J. D. Carpenter, D. A. Rothery, J. F. Pearson, A. Martindale, J. Huovelin, J. Treis, M. Anand, M. Anttila, M. Ashcroft, J. Benkoff, P. Bland, A. Bowyer,

A. Bradley, J. Bridges, C. Brown, C. Bulloch, E. J. Bunce, U. Christensen, M. Evans, R. Fairbend, M. Feasey, F. Giannini, S. Hermann, M. Hesse, M. Hilchenbach, T. Jorden, K. Joy, M. Kaipiainen, I. Kitchingman, P. Lechner, G. Lutz, A. Malkki, K. Muinonen, J. Näränen, P. Portin, M. Prydderch, J. San Juan, E. Sclater, E. Schyns, T. J. Stevenson, L. Strüder, M. Syrjasuo, D. Talboys, P. Thomas, C. Whitford, and S. Whitehead. The Mercury Imaging X-ray Spectrometer (MIXS) on BepiColombo. *Planetary and Space Science*, 58:79–95, 2010.

G.W. Fraser, M. T. Pain, and J. E. Lees. Microchannel plate operation at high count rates: further studies. *Nuclear Instruments and Methods in Physics Research*, A327: 328–336, 1993b.

J. P. Gardner, J. C. Mather, M. Clampin, R. Doyon, M. A. Greenhouse, H. B. Hammel, J. B. Hutchings, P. Jakobsen, S. J. Lilly, K. S. Long, J. I. Lunine, M. J. McCaughrean, M. Mountain, J. Nella, G. H. Rieke, M. J. Rieke, H.-W. Rix, E. P. Smith, G. Sonneborn, M. Stiavelli, H. S. Stockman, R. A. Windhorst, and G. S. Wright. The James Webb space telescope. *Space Science Reviews*, 123:485–606, 2006.

J.-C. Gérard. Personal communication, 2011.

J. C. Gérard, D. Grodent, R. Prangè, J. H. Waite, G. R. Gladstone, V. Dols, F. Paresce, A. Storrs, L. Ben Jaffel, and K. A. Franke. A remarkable auroral event on Jupiter observed in the ultraviolet with the Hubble Space Telescope. *Science*, 266:1675–16708, 1994.

J.-C. Gérard, A. Saglam, D. Grodent, and J. T. Clarke. Morphology of the ultraviolet Io footprint emission and its control by Io's location. *Journal of Geophysical Research*, 111(A04202), 2006.

G. A. Germany, M. R Torr, P. G. Richards, and D. G. Torr. The dependence of modeled OI 1356 and N_2 Lyman Birge Hopfield auroral emissions on the neutral atmosphere. *Journal of Geophysical Research*, 95(A6):7725–7733, 1990.

R. Giacconi and B. Rossi. A 'telescope' for soft X-ray astronomy. *Journal of Geophysical Research*, 65:773–775, 1960.

G. R. Gladstone. Personal communication, 2012.

G. R. Gladstone, S. A. Stern, D. C. Slater, M. Versteeg, M. W. Davis, K. D. Retherford, L. A. Young, A. J. Steffl, H. Throop, J. W. Parker, H. A. Weaver, A. F. Cheng, G. S. Orton, J. T. Clarke, and J. D. Nichols. Jupiter's Nightside Airglow and Aurora. *Science*, 318(5848):229–231, 2007.

D. Grodent, J. T. Clarke, J. H. Waite Jr., S. W. H. Cowley, J.-C. Gérard, and J. Kim. Jupiter's polar auroral emissions. *Journal of Geophysical Research*, 108(A10):1366, 2003.

D. Grodent, J.-C. Gérard, A. Radioti, B. Bonfond, and A. Saglam. Jupiter's changing auroral location. *Journal of Geophysical Research*, 113, 2008.

D. Grodent, B. Bonfond, A. Radioti, J.-C. Gérard, X. Jia, J. D. Nichols, and J. T. Clarke. Auroral footprint of Ganymede. *Journal of Geophysical Research*, 114(A07212), 2009.

J. Gustin, P. D. Feldman, J.-C. Gérard, D. Grodent, A. Vidal-Madjar, L. Ben Jaffel, J.-M. Desert, H. W. Moos, D. J. Sahnow, H. A. Weaver, B. C. Wolven, J. M. Ajello, J. H. Waite, E. Roueff, and H. Abgrall. Jovian auroral spectroscopy with FUSE: analysis of self-absorption and implications for electron precipitation. *Icarus*, 171:336–355, 2004.

D. T. Hall, D. F. Strobel, P. D. Feldman, M. A. McGrath, and H. A. Weaver. Detection of an oxygen atmosphere on Jupiter's moon Europa. *Nature*, 373:677–679, February 1995.

D. T. Hall, P. D. Feldman, M. A. McGrath, and D. F. Strobel. The far-ultraviolet oxygen airglow of Europa and Ganymede. *The Astrophysical Journal*, 499:475–481, 1998.

E. Hecht. *Optics*. Addison Wesley, fourth edition, 2002. International edition.

B. L. Henke. Ultrasoft X-ray reflection, refraction, and production of photoelectrons (100-1000 eV region). *Physical Review A*, 6(1):94–104, 1972.

B. L. Henke, E. M. Gullickson, and J. C. Davis. X-ray interactions: photoabsorption, scattering, transmission, and reflection at E = 50–30,000 eV, Z = 1–92. *Atomic data and nuclear data tables*, 54:181–342, 1993.

C. A. Higgins, T. D. Carr, F. Reyes, W. B. Greenman, and G. R. Lebo. A redefinition of Jupiter's rotation period. *Journal of Geophysical Research*, 102(A10):22033–22041, 1997.

T. W. Hill. The jovian auroral oval. *Journal of Geophysical Research*, 106:8101–8107, 2001.

C. W. Hord, W. E. McClintock, A. I. F. Stewart, C. A. Barth, L. W. Esposito, G. E. Thomas, B. R. Sandel, D. M. Hunten, A. L. Broadfoot, D. E. Shemansky, J. M. Ajello, A. L. Lane, and R. A. West. Galileo Ultraviolet Spectrometer Experiment. *Space Science Reviews*, 60:503–530, 1992.

W.-H. Ip. Europa's oxygen exosphere and its magnetospheric induction. *Icarus*, 120: 317–325, 1996.

X. Jia, R. J. Walker, M. G. Kivelson, K. K. Khurana, and J. A. Linker. Three-dimensional MHD simulations of Ganymede's magnetosphere. *Journal of Geophysical Research*, 113:A06212, 2008.

JUICE Science Study Team. JUICE: Assessment Study Report (Yellow book). Technical report, ESA, December 2011. ESA/SRE(2011)18.

A. T. Kenter, J. H. Chappel, K. Kobayashi, R. P. Kraft, G. R. Meehan, S. S. Murray, M. V. Zombeck, G. W. Fraser, J. F. Pearson, J. E. Lees, A. N. Brunton, S. E. Pearce, M. Barbera, A. Collura, and S. Serio. Performance and Calibration of the AXAF High Resolution Camera I: Imaging Readout. *Proceedings of SPIE*, 3114(26), 1997.

M. G. Kivelson, K. K. Khurana, F. V. Coroniti, S. Joy, C. T. Russell, R. J. Walker, J. Warnecke, L. Bennett, and C. Polanskey. The magnetic field and magnetosphere of Ganymede. *Geophysical Research Letters*, 24(17):2155–2158, 1997.

M. G. Kivelson, K. K. Khurana, and M. Volwerk. The Permanent and Inductive Magnetic Moments of Ganymede. *Icarus*, 157:507–522, 2002.

A. J. Kliore, A. Anabtawi, R. G. Herrera, S. W. Asmar, A. F. Nagy, D. P. Hinson, and F. M. Flasar. Ionosphere of Callisto from Galileo radio occultation observations. *Journal of Geophysical Research*, 107(A11):1407, 2002.

M. F. Land, F. A. Burton, and V. B. Meyer-Rochow. The optical geometry of euphausiid eyes. *Journal of Comparative Physiology A: Neuroethology, Sensory, Neural, and Behavioral Physiology*, 130:49–62, 1979.

J. S. Lapington. High speed imaging using a capacitive division technique. *Nuclear Instruments and Methods*, 2012. In Press.

A. H. Laufer, J. A. Pirog, and J. R. McNesby. Effect of temperature on the vacuum ultraviolet transmittance of lithium fluoride, calcium fluoride, barium fluoride, and sapphire. *Journal of the Optical Society of America*, 55:64–66, 1965.

C. Laver, I. de Pater, H. Roe, and D. F. Strobel. Temporal behavior of the SO 1.707 μm ro-vibronic emission band in Io's atmosphere. *Icarus*, 189:401–408, 2007.

J. E. Lees, G. W. Fraser, and D. Dinsdale. Direct beta autoradiography using microchannel plate (MCP) detectors. *Nuclear Instruments and Methods in Physics Research A*, 392:349–353, 1997.

N. Lindlein and Gerd. Leuchs. Geometrical Optics. In Träger, F., editor, *Springer Handbook of Lasers and Optics*, chapter 2. Springer, 2007.

W. Liu and A. Dalgarno. The ultraviolet spectra of the jovian aurora. *The Astrophysical Journal*, 467:446–453, 1996.

A. T. Y. Lui, D. Venkatesan, G. Rostoker, J. S. Murphree, C. D. Anger, L. L. Cogger, and T. A. Potemra. Dayside auroral intensifications during an auroral substorm. *Geophysical Research Letters*, 14(4):415–418, 1987.

A. P. Martin. *Exploitation of Microchannel Plate Optics*. PhD thesis, University of Leicester, 2000.

C. Martin and S. Bowyer. Quantum efficiency of opaque CsI photocathodes with channel electron multiplier arrays in the extreme and far ultraviolet. *Applied Optics*, 21:4206–4207, 1982.

P. J. Martin. Review: Ion-based methods for optical thin film deposition. *Journal of materials science*, 21:1–25, 1986.

A. Martindale. *Novel X-ray instrumentation for astronomy*. PhD thesis, University of Leicester, 2008.

A. Martindale. Private communication, December 2011.

A. Martindale and P. Molyneux. The effect of the finite size of multifibres. Technical report, University of Leicester, 2009.

S. Matousek. The Juno new frontiers mission. *Acta Astronautica*, 61:932–939, 2007.

Maybhate et al. *ACS Instrument Handbook – Version 10.0 (Baltimore: STScI)*, 2010.

M. A. McGrath, E. Lellouch, D. F. Strobel, P. D. Feldman, and R. E. Johnson. Satellite Atmospheres. In F. Bagenal, T. Dowling, and W McKinnon, editors, *Jupiter – the planet, satellites and magnetosphere*, chapter 19. Cambridge University Press, 2004.

M. McMaster, J. Biretta, S. Baggett, L. Bedin, G. Brammer, C. Burrows, S. Casertano, M. Chiaberge, M. Clampin, V. Dixon, H. Ferguson, A. Fruchter, R. Gilliland, D. Golimowski, S. Gonzage, R. Griffiths, I. Heyer, J. Holtzman, S. Hulbert, A. Koekemoer, V. Kozhurina-Platais, J. Krist, L. Lubin, J. Mack, J. MacKenty, M. Mutchler, K. Noll, M. Sirianni, M. Stevens, M. Stiavelli, A. Suchkov, J. Surdej, M. Wiggs, and B. Whitmore. *WFPC2 Instrument Handbook – Version 10.0 (Baltimore: STScI)*, 2008.

R. R. Meier. Ultraviolet spectroscopy and remote sensing of the upper atmosphere. *Space Science Reviews*, 58:1–185, 1991.

S. B. Mende, H. U. Frey, T. J. Immel, J.-C. Gerard, B. Hubert, and S. A. Fuselier. Global imaging of proton and electron aurorae in the far ultraviolet. *Space Science Reviews*, 109:211–254, 2003.

A. E. Metzger, D. A. Gilman, J. L. Luthey, K. C. Hurley, H. W. Schnopper, F. D. Seward, and J. D. Sullivan. The detection of X-rays from Jupiter. *Journal of Geophysical Research*, 88:7731–7741, 1983.

S. Milan. Personal communication, 2012.

J. S. Murphree, M. L. Johnson, L. L. Cogger, and D. J. Hearn. Freja UV imager observations of spatially periodic auroral distortions. *Geophysical Research Letters*, 21(17):1887–1890, 1994.

P. T. Newell, K. Liou, C.-I. Meng, M. J. Brittnacher, and G. Parks. Dynamics of double-theta aurora: Polar UVI study of January 10-11, 1997. *Journal of Geophysical Research*, 104(A1):95–104, 1999.

NIST. X-Ray Form Factor, Attenuation, and Scattering Tables. `http://physics.nist.gov/PhysRefData/FFast/html/form.html`, 2009. retrieved July 2009.

K. S. Noll, R. E. Johnson, A. L. Lane, D. L. Domingue, and H. A. Weaver. Detection of Ozone on Ganymede. *Science*, 273:341–343, 1996.

C. Noren, I. Kanik, J. M. Ajello, P. McCartney, O. P. Makarov, W. E. McClintock, and V. A. Drake. Emission cross section of O I (135.6 nm) at 100 eV resulting from electron-impact dissociative excitation of O_2. *Geophysical Research Letters*, 28(7): 1379–1382, 2001.

A. Nota, R. Jedrzejewski, M. Voit, and W. Hack. *FOC Instrument Handbook – Version 7.0 (Baltimore: STScI)*, 1996.

M. Ohring. *The materials science of thin films: Deposition and structure*. Academic press, second edition, 2002.

E.D. Palik, editor. *Handbook of Optical Constants of Solids*. Academic Press, Inc., 1985.

L. Pallier and R. Prangè. More about the structure of the high latitude jovian aurora. *Planetary and Space Science*, 49:1159–1173, 2001.

J. F. Pearson and A. Martindale. Tunnel test facility operating manual. Technical report, University of Leicester, 2009.

A. G. Peele. Deconvolution of an extended object viewed by a lobster-eye telescope. *Nuclear Instruments and Methods*, 459:354–364, 2001.

A. G. Peele, K. A. Nugent, A. V. Rode, K. Gabel, M. C. Richardson, R. Strack, and W. Siegmund. X-ray focusing with lobster-eye optics: a comparison of theory with experiment. *Applied Optics*, 35(22):4420–4425, 1996.

R. Prangè, D. Rego, L. Pallier, J. E. P. Connerney, P. Zarka, and J. Queinnec. Detailed study of FUV Jovian auroral features with the post-COSTAR HST faint object camera. *Journal of Geophysical Research*, 103(E9):20195–20215, 1998.

G. J. Price. *Microchannel plates in astronomy*. PhD thesis, University of Leicester, 2001.

Princeton Instruments. Acton Optics and Coatings. `http://www.princetoninstruments.com/products/optical_filters/curve_library.aspx`, 2009.

W. R. Pryor, A. I. F. Stewart, L. W. Esposito, W. E. McClintock, J. E. Colwell, A. J. Jouchoux, A. J. Steffl, D. E. Shemansky, J. M. Ajello, R. A. West, C. J. Hansen, B. T. Tsuruntani, W. S. Kurth, G. B. Hospordarsky, D. A. Gurnett, K. C. Hansen, J. H. Waite Jr., F. J. Crary, D. T. Young, N. Krupp, J. T. Clarke, D. Grodent, and M. K. Dougherty. Cassini UVIS observations of Jupiter's auroral variability. *Icarus*, 178:312–326, 2005.

A. Radioti, D. Grodent, J.-C. Gèrard, B. Bonfond, and J. T. Clarke. Auroral polar dawn spots: Signatures of internally driven reconnection processes at jupiter's magnetotail. *Geophysical Research Letters*, 35:L03104, 2008.

D. Rego, R. Prangè, and L. Ben Jaffel. Auroral Lyman α and H_2 bands from the giant planets 3. Lyman α spectral profile including charge exchange and radiative transfer effects and H_2 color ratios. *Journal of Geophysical Research*, 104(E3):5939–5954, 1999.

K. Reichelt and X. Jiang. Review: The preparation of thin films by physical vapour deposition methods. *Thin solid films*, 191:91–126, 1990.

K. D. Retherford, S. A. Stern, D. C. Slater, G. R. Gladstone, M. W. Davis, J. W. Parker, M. H. Versteeg, A. J. Steffl, T. K. Greathouse, and N. J. Cunningham. SwRI's ALICE line of ultraviolet spectrographs. *Proceedings of SPIE*, 7441, 2009.

F. L. Roesler, H. W. Moos, R. J. Oliversen, R. C. Woodward Jr., K. D. Retherford, F. Scherb, M. A. McGrath, W. H. Smyth, P. D. Feldman, and D. F. Strobel. Far-ultraviolet imaging of Io's atmosphere with HST/STIS. *Science*, 283:353–357, 1999.

J. B. Rogerson, L. Spitzer, J. F. Drake, K. Dressler, E. B. Jenkins, D. C. Morton, and D. G. York. Spectrophotometric results from the *Copernicus* satellite. I. Instrumentation and performance. *The Astrophysical Journal*, 181:L97–L102, 1973.

J. D. Rummel, P. D. Stabekis, D. L. DeVincenzi, and J. B. Barengoltz. COSPAR'S planetary protection policy: A consolidated draft. *Advances in Space Research*, 30(6): 1567–1571, 2002.

K. Rypdal and T. Brundtland. The Birkeland Terrella Experiments and their Importance for the Modern Synergy of Laboratory and Space Plasma Physics. *Journal de Physique IV*, 7:C4–113–C4–132, 1997.

J. Saur, D. F. Strobel, and F. M. Neubauer. Interaction of the Jovian magnetosphere with Europa: Constraints on the neutral atmosphere. *Journal of Geophysical Research*, 103 (E9):19947–19962, 1998.

J. Saur, F. M. Neibauer, J. E. P. Connerney, P Zarka, and M. G. Kivelson. Plasma Interaction of Io with its Plasma Torus. In F. Bagenal, T. Dowling, and W McKinnon, editors, *Jupiter – the planet, satellites and magnetosphere*, chapter 22. Cambridge University Press, 2004.

O. H. W. Siegmund, E. Everman, J. V. Vallerga, J. Sokolowski, and M. Lampton. Ultraviolet quantum detection efficiency of potassium bromide as an opaque photocathode applied to microchannel plates. *Applied Optics*, 26:3607–3614, 1987.

D. G. Simons, G. W. Fraser, P. A. J. De Korte, J. F. Pearson, and L. De Jong. UV and XUV quantum detection efficiencies of CsI-coated microchannel plates. *Nuclear Instruments and Methods in Physics Research*, A261:579–586, 1987.

H. J. Smith, J. P. Rodman, and W. A. Sloan. On Jovian Hα Auroral Activity. *The Astronomical Journal*, 68:79, 1963.

D. J. Southwood and M. G. Kivelson. A new perspective concerning the influence of the solar wind on the jovian magnetosphere. *Journal of Geophysical Research*, 106: 6123–6130, 2001.

B. Speit, E. Rädlein, G. H. Frischat, A. J. Marker, and J. S. Hayden. Radiation resistant optical glasses. *Nuclear Instruments and Methods B*, 65:384–386, 1992.

J. R. Spencer, W. M. Calvin, and M. J. Person. Charge-coupled device spectra of the Galilean satellites: Molecular oxygen on Ganymede. *Journal of Geophysical Research*, 100(E9):19049–19056, 1995.

T. Stallard, S. Miller, G. Millward, and R. D. Joseph. On the dynamics of the jovian ionosphere and themosphere: 1. the measurement of ion winds. *Icarus*, 154:475–491, 2001.

A. J. Steffl, A. I. F. Stewart, and F. Bagenal. Cassini UVIS observations of the Io plasma torus. 1. Initial results. *Icarus*, 172:78–90, 2004.

S. A. Stern, D. C. Slater, J. Scherrer, J. Stone, G. Dirks, M. Versteeg, M. Davis, G. R. Gladstone, J. W. Parker, L. A. Young, and O. H. W. Siegmund. ALICE: The Ultraviolet Imaging Spectrograph Aboard the New Horizons Pluto-Kuiper Belt Mission. *Space Science Reviews*, 140:155–187, 2008.

D. F. Strobel, J. Saur, P. D. Feldman, and M. A. McGrath. Hubble Space Telescope Space Telescope Imaging Spectrograph search for an atmosphere on Callisto: A jovian unipolar inductor. *The Astrophysical Journal*, 581:L51 – L54, 2002.

STScI. Hubble Space Telescope Primer for Cycle 20. `http://www.stsci.edu/hst/proposing/documents/primer/Ch_48.html`, 2011.

J. Tennyson. *Astronomical Spectroscopy: An Introduction to the Atomic and Molecular Physics of Astronomical Spectra*. Imperial College Press, 2005.

N. Thomas, F. Bagenal, T. W. Hill, and J. K. Wilson. The Io Neutral Clouds and Plasma Torus. In F. Bagenal, T. Dowling, and W McKinnon, editors, *Jupiter – the planet, satellites and magnetosphere*, chapter 23. Cambridge University Press, 2004.

J. G. Timothy and R. L. Bybee. One-dimensional photon-counting detector array for use at EUV and soft X-ray wavelengths. *Applied Optics*, 14:1632–1644, 1975.

C.-Y. Tu, R. Schwenn, E. Donovan, E. Marsch, J. S. Wang, L.-D. Xia, and Y.-W. Zhang. Space weather explorer – The KuaFu mission. *Advances in Space Research*, 41:190–209, 2008.

F. Varosi. `http://www.astro.washington.edu/docs/idl/cgi-bin/getpro/library21.html?FULLWID_HALFMAX`, 1994. Retrieved 4/8/2011.

A. R. Vasavada, A. H. Bouchez, A. P. Ingersoll, B. Little, C. D. Anger, and the Galileo SSI Team. Jupiter's visible aurora and Io footprint. *Journal of Geophysical Research*, 104(E11):27133–27142, 1999.

M. F. Vogt, M. G. Kivelson, K. K. Khurana, R. J. Walker, B. Bonfond, D. Grodent, and A. Radioti. Improved mapping of Jupiter's auroral features to magnetospheric sources. *Journal of Geophysical Research*, 116:A03220, 2011.

J. H. Waite Jr., J. T. Clarke, T. E. Cravens, and C. M. Hammond. The Jovian aurora: electron or ion precipitation? *Journal of Geophysical Research*, 93(A7):7244–7250, 1988.

J. H. Waite Jr., G. R. Gladstone, W. S. Lewis, P. Drossart, T. E. Cravens, A. N. Maurellis, B. H. Mauk, and S. Miller. Equatorial X-ray emissions: Implications for Jupiter's high exospheric temperatures. *Science*, 276:104–108, 1997.

J. H. Waite Jr., G. R. Gladstone, W. S. Lewis, R. Goldstein, D. J. McComas, P. Riley, R. J. Walker, P. Robertson, S. Desai, J. T. Clarke, and D. T. Young. An auroral flare at jupiter. *Nature*, 410:787–789, 2001.

J. R. Walsh. Extraction of Point Source Spectra from STIS . In *1997 HST Calibration Workshop*, pages 156–160, 1997.

J. W. Weiss. Appendix 2 – Planetary Parameters. In F. Bagenal, T. Dowling, and W McKinnon, editors, *Jupiter – the planet, satellites and magnetosphere*. Cambridge University Press, 2004.

C. Weissmantel. Ion-based growth of special films: techniques and mechanisms. *Thin solid films*, 92:55–63, 1982.

W. L. Wiese, J. R. Fuhr, and T. M. Deters. *Atomic transition properties of carbon, nitrogen and oxygen – a critical data compilation*. AIP press, 1996.

R. Willingale. The grazing incidence telescope. *Nuclear Instruments and Methods in Physics Research*, 221:1–13, 1984.

R. Willingale. Q Help Index. `http://www.star.le.ac.uk/~rw/q_v6/`, 2009. Information about the Q data analysis system and its use in sequential ray tracing.

R. Willingale, G. W. Fraser, A. N. Brunton, and A. P. Martin. Hard X-ray imaging with microchannel plate optics. *Experimental Astrophysics*, 8:281–296, 1998.

J. L. Wiza. Microchannel Plate Detectors. *Nuclear Instruments and Methods*, 162:587–601, 1979.

H. Wolter. Spiegelsysteme streifenden Einfalls als abbildende Optiken für Rüntgenstrahlen. *Annalen der Physik*, 445:94–114, 1952.

B. E. Woodgate, R. A. Kimble, C. W. Bowers, S. Kraemer, M. E. Kaiser, A. C. Danks, J. F. Grady, J. J. Loiacono, M. Brumfield, L. Feinberg, T. R. Gull, S. R. Heap, S. P. Maran, D. Lindler, D. Hood, W. Meyer, C. Vanhouten, V. Argabright, S. Franka, R. Bybee, D. Dorn, M. Bottema, R. Woodruff, D. Michika, J. Sullivan, J. Hetlinger, C. Ludtke, R. Stocker, A. Delamere, D. Rose, I. Becker, H. Garner, J. G. Timothy, M. Blouke, C. L. Joseph, G. Hartig, R. F. Green, E. B. Jenkins, J. L. Linsky, J. B. Hutchings, H. W. Moos, A. Boggess, F. Roesler, and D. Weistrop. The Space Telescope

Imaging Spectrograph Design. *Publications of the Astronomical Society of the Pacific*, 110:1183–1204, 1998.

Y. L. Yung, G. R. Gladstone, K. M. Chang, J. M. Ajello, and S. K. Srivastava. H_2 fluorescence spectrum from 1200 to 1700 Å by electron impact: laboratory study and application to Jovian aurora. *The Astrophysical Journal*, 254:L65–L69, 1982.

M. Zukic and D. G. Torr. Multiple reflectors as narrow-band and broadband vacuum ultraviolet filters. *Applied Optics*, 31:1588–1596, 1992.